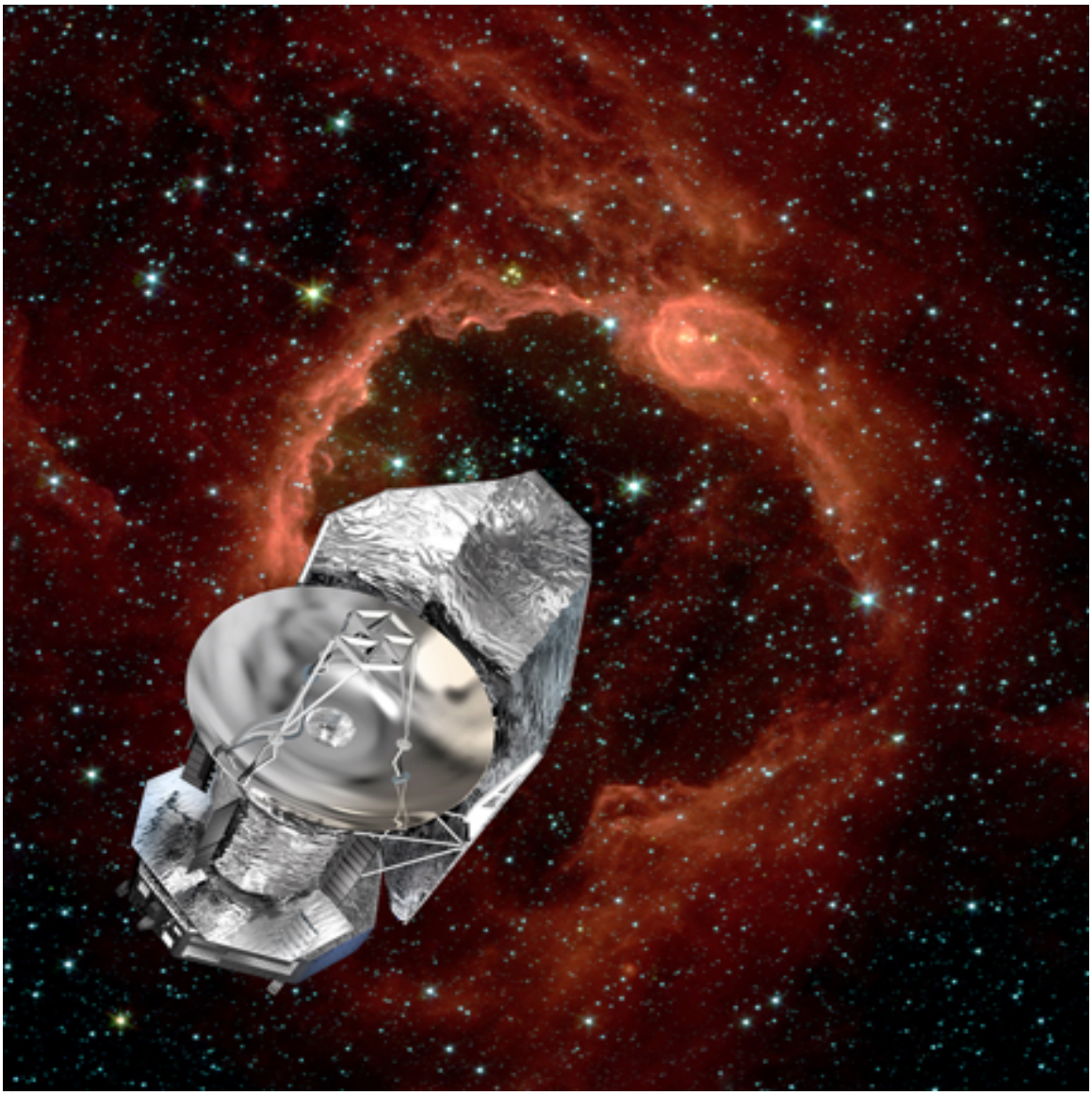

This thesis was typeset with LaTeX, using a modified version of the University of California Ph.D. dissertation class file, `ucthesis.cls`. Unless otherwise noted, all figures in this thesis were created by the author using IDL, APLpy, HIPE and ds9.

**Cover photograph** Artist's impression of *Herschel* in space. Credit: ESA – D. Ducros, 2009 (*Photo: ESA/PACS & SPIRE Consortium/HOBYS Key Programme Consortia*). *Herschel* is an ESA space observatory with science instruments provided by European-led Principal Investigator consortia and with important participation from NASA.

# A Study of the Physics of the Interstellar Medium using the Herschel-SPIRE Instrument

Gibion Makiwa

B.Sc. Hons in Physics, University of Zimbabwe, 1999
M.Sc. Applied Physics, University of Zimbabwe, 2006
M.Sc. Physics, University of Lethbridge, 2011

A Thesis
Submitted to the School of Graduate Studies
of the University of Lethbridge
in Partial Fulfilment of the
Requirements of the Degree

Philosophiæ Doctor

in

Earth, Space, and Physical Science

Department of Physics & Astronomy
University of Lethbridge
Lethbridge, Alberta, Canada

# A Study of the Physics of the Interstellar Medium using the Herschel-SPIRE Instrument

Gibion Makiwa

Approved:

---

Dr. David A. Naylor, Supervisor, Department of Physics & Astronomy — Date

---

Dr. Adriana Predoi-Cross, Department of Physics & Astronomy — Date

---

Dr. René T. Boeré, Department of Chemistry & Biochemistry — Date

---

Dr. René Plume, Department of Physics & Astronomy, University of Calgary — Date

---

Dr. Ken Vos, Chair, Thesis Examination Committee — Date

## Dedication

This thesis is dedicated to my wife Gladys and our daughters Rejoice and Esther. It is also dedicated to all those from the Evangelical Free Church of Lethbridge who have helped us spiritually, emotionally and physically. I am humbled by the love you have shown us since we came to Lethbridge five years ago. May the Love of our Lord Jesus Christ always be with you all.

## Abstract

Stars form in cold and dense regions of the interstellar medium where Rayleigh scattering heavily attenuates short wavelength radiation but allows long wavelength radiation to escape. Long-wavelength radiation from star forming regions, after travelling many lightyears to reach us, is absorbed by the water vapour in the Earth's atmosphere before it can reach ground-based telescopes. Thus, prior to the far-infrared space telescope, *Herschel*, our view of the submillimeter universe was through very narrow spectral windows that are only accessible from high mountain sites. *Herschel*, with its three instruments, was designed to operate in the far-infrared and observe radiation from star forming regions. Unlike ground based telescopes, *Herschel* has provided the first unfettered access to the entire far-infrared electromagnetic spectrum.

In this work, I have analyzed *Herschel* observations of three starless cores (L1521E, L1521F and L1689B), one Class 0 protostar (IRAS16293-2422) and one Class I protostar (Elias 29). These observations were obtained with the Spectral and Photometric Imaging Receiver (SPIRE) photometer and spectrometer. The measured low-spectral resolution spectra of starless cores have been used to obtain more accurate spectral energy distributions (SEDs) which have enabled the calculation of dust temperatures, emissivity spectral indices, and masses associated with these cores.

The map-making capability of the SPIRE instrument provided fully sampled spectral maps of IRAS16293-2422 and Elias 29. A wealth of molecular line emission was detected from both protostars. These include $^{12}$CO, $^{13}$CO, C$^{18}$O, C I, $H_2O$, $HCO^+$ and CS. Integrated

line intensity maps show that both line and continuum emission from IRAS16293-2422 originate from a compact region surrounding the protobinary system. An SED constructed from flux density points obtained with various instruments has been fitted with radiative transfer models to obtain physical parameters associated with IRAS16293-2422. Integrated line intensity maps for Elias 29 have confirmed the previously reported result that there are three components along the line of sight. The spatial extent of molecular emission from these sources is an important constraint in radiative transfer models that are used to better understand the physical conditions in the early stages of star formation.

Far-infrared broadband observations of starless cores, Class 0 and Class I protostars obtained with the *Herschel*-SPIRE instrument have provided for the first time the ability to study the first stages of star formation. Continuum observations of starless cores have been used to construct SEDs from which more accurate dust temperatures and emissivity indices have been derived. Fully Nyquist sampled observations have been used to study the spatial extent of dust and line emission from Class 0 and Class I protostars.

## Acknowledgements

Firstly I would like to thank my supervisor Prof. David Naylor for accepting me as a masters student and then as a PhD student. I still remember the first e-mail conversations that we had while I was still in South Africa and the first phone call he made to me. The past five years have been a time for me to grow as a scientist. Thank you David for the academic, financial and emotional support throughout this process.

I would also like to thank Dr. Adriana Predoi-Cross for sharing the e-mail I sent her with David. Without Adriana I would not have known David. I believe my coming to Lethbridge was not a coincidence but was in God's plan. My favourite scripture in the Bible says it all. (*And we know that all things work together for good to those who love God, to those who are the called according to His purpose* - Romans 8:28, NKJV).

I would like to thank my supervisory committee members, Prof. David Naylor, Prof. Adriana Predoi-Cross and Prof. René Boeré for their guidance and support throughout the past five years. I was always encouraged by their interest in my work. I also thank them for reading my thesis and providing constructive comments. I thank Prof. René Plume for agreeing to serve as external examiner for my thesis defence and for his invaluable comments.

I would like to thank Brad Gom, Peter Davis, Trevor Fulton, Edward Polehampton, Locke Spencer and Richard Querel for all the support from the day I joined David's research group. Thanks Brad for all the support you provide to all members of David's research group. When I joined the group, IDL was a foreign language to me. I am grateful to Brad, Locke and Richard for helping me understand the language. Peter, Trevor and Ed have helped in various ways including processing data for the SPIRE FTS beam profile. Thanks

Ed for reading the initial drafts of the beam profile paper. Thanks Locke for proof-reading my thesis.

It has been great to share the office with Matthijs van der Wiel for the past three years. Thank you for all the conversations that we have had during this period. I have learnt a great deal of Astrophysics from you. Thank you for reading my thesis chapters and all the thoughtful comments.

David always says that it takes a family to raise a graduate student. I would like to thank past and present members of David's research group who have encouraged me on this journey. These include: Greg Tompkins, Tanner Heggie, Scott Jones, Yuan Zhang, Regan Dahl, Darren Hayton, Ben Sadeghi, Coskun (Josh) Oba, Matt Sherwood, Grace Trimboli, Ian Veenendaal and Sherif AbdElazim. Thank you all for the encouragements and emotional support. Thanks, Tanner, for everything.

I would like to thank all the members of the department of Physics and Astronomy at the University of Lethbridge. You have all played various roles in my growth as a scientist. I thank Dr. Ken Vos for chairing both my MSc and PhD exam committees. I thank Sheila Matson for the encouragement and prayers. It always felt good to hear you stressing the importance of prayer during our conversations. I also thank Sheila Matson, Laurie Scott and Susan Hill for all the help you provided when I needed something from the departmental office. Thanks Susan for helping organize supervisory committee meetings on behalf of René.

I would like to thank the Dean of School of Graduate Studies, Dr. Rob Wood and his staff for financial and emotional support. I thank Katheen Schrage for guiding me through the application process to come to the University of Lethbridge. Thank you for your

understanding and for treating graduate students with respect. I thank Deirdre Coburn for processing all the scholarships and awards that I received for the past three years.

Lastly, I would like to thank my wife, Gladys, and our two daughters, Rejoice and Esther for all the support and care. This journey has been difficulty for all of you. I had wanted to spend more quality time with you but that was not possible because I had to study even when I was supposed to be resting at home. Thank you for your understanding.

# Contents

# List of Tables

# List of Figures

# List of Abbreviations

| | |
|---|---|
| 2MASS | Two Micron All Sky Survey. 137 |
| ALMA | Atacama Large Millimeter Array. 98, 100, 160 |
| AOS | acousto-optical spectrometer. 133 |
| AU | astronomical unit. 8, 11, 97, 98, 106, 129, 139, 152 |
| CNM | Cold Neutral Medium. 5 |
| CSO | Caltech Submillimeter Observatory. 133 |
| DAS | Digital Autocorrelation Spectrometer. 133 |
| Dec | declination. 64, 103, 139 |
| DIGIT | Dust, Ice and Gas in Time. 137 |
| ESA | European Space Agency. 3, 35, 51, 100, 138 |
| FOV | field of view. 62 |
| FTS | Fourier transform spectrometer. 67, 112, 117 |
| FUV | Far Ultra-violet. 8 |
| FWHM | Full Width Half Maximum. 41, 44, 63, 76, 114, 139 |
| GMC | Giant Molecular Cloud. 9, 10, 54 |
| *Herschel* | *Herschel Space Observatory*. 3, 50, 71, 72, 74, 75, 93, 96, 117, 132, 133, 152, 157, 159 |
| HIFI | Heterodyne Instrument for the Far Infrared. 3, 35, 51, 72, 75, 101, 117, 120, 138, 152, 159, 160 |
| HIM | Hot Ionized Medium. 4 |
| HIPE | Herschel Interactive Processing Environment. 35, 43, 47, 50, 51, 61, 75, 77, 100, 102, 103, 106, 108, 138, 139, 142 |

*IRAS* *Infrared Astronomical Satellite*. 3, 64, 70, 124, 137
*ISO* *Infrared Space Observatory*. 3, 123, 124, 133, 135, 137, 152
IDL Interactive Data Language. 43
iFTS imaging Fourier transform spectrometer. xvii, 3, 14, 25, 26, 28, 32–35, 37, 38, 40, 41, 43, 44, 47, 49–52, 54, 59, 61–64, 67, 69, 71, 72, 75–77, 83–85, 92, 93, 95–97, 101, 106, 109, 114, 117, 120, 123, 129, 131, 133, 138, 142, 146, 152, 158–160
IRAC Infrared Array Camera. 76, 78, 80, 137, 158
ISM Interstellar Medium. 2, 4–6, 9, 25, 30, 31, 101, 138, 150, 157
ISRF interstellar radiation field. 71

JCMT James Clerk Maxwell Telescope. 77, 97, 133, 135, 158

LIME Line Modeling Engine. 160
LSR local standard of rest. 108
LTE local thermodynamic equilibrium. 28, 30
LW Long-Wave. 77
LWS long wavelength spectrometer. 123, 124, 133, 152

MIPS Multiband Imaging Photometer for Spitzer. 76, 77, 79, 80, 82, 124, 137, 158

NASA National Aeronautics and Space Administration. 35, 51, 100, 138
NHKT nominal housekeeping timeline. 35, 37
NRAO National Radio Astronomy Observatory. 133

OBSID Observation Identification Number. 74, 75, 100, 101, 138
OVRO Owens Valley Radio Observatory. 134

PACS Photodetecting Array Camera and Spectrometer. 3, 71, 74, 75, 100, 137, 138
PAH Polycyclic Aromatic Hydrocarbon. 7, 8
PANIC Persson's Auxiliary Nasmyth Infrared Camera. 134
PLW photometer long wavelength. 72, 100

PMW photometer medium wavelength. 72, 100
PPN Proto-Planetary Nebula. 54
PSF Point spread function. xxxi, 34, 40–44, 61–63, 68, 158
PSW photometer short wavelength. 72, 77, 100, 109

RA right ascension. 64, 103, 139
RMS root mean square. 35
RSRF relative spectral response function. 38

*Spitzer* *Spitzer Space Telescope*. 76, 77, 85, 90–93, 137, 158
SCUBA Submillimeter Common-User Bolometer Array. 77, 79, 80, 82, 85, 90–93, 97, 108, 124, 158
SDT spectrometer detector timeline. 35
SED spectral energy distribution. 10, 23, 32, 71–73, 83, 85, 90–93, 123, 126, 129, 131, 133, 137, 152, 159, 160
SLW spectrometer long wavelength. xvii, 44, 47, 51–54, 59, 61, 63, 64, 67, 68, 72, 101, 103, 106, 110, 114, 139, 148, 151, 160
SMECT spectrometer mechanism timeline. 35, 37
SPIRE Spectral and Photometric Imaging Receiver Array. xvii, 3, 14, 25, 26, 28, 32–35, 37–40, 43, 44, 47, 49–52, 54, 59, 61–64, 67, 69, 71, 72, 74–80, 82–85, 90–93, 95–97, 100, 101, 103, 106, 109, 114, 117, 120, 123, 124, 129, 131, 133, 138, 139, 142, 146, 151, 152, 157–160
SPP SPIRE pointing product. 35, 37
SSW spectrometer short wavelength. xvii, 44, 47, 51–54, 59, 61, 64, 67, 68, 72, 101, 103, 106, 109, 110, 114, 139, 148, 151, 160
SW Short-Wave. 77
SWS short wavelength spectrometer. 133, 135, 152

UV Ultra-violet. 131, 137

WCS World Coordinate System. 59, 61, 103, 108, 112, 142
WIM Warm Ionized Medium. 5
WISH Water in star-forming regions with Herschel. 117, 152
WNM Warm Neutral Medium. 5

YSO Young Stellar Objects. 120, 126

# List of Equations

# Thesis Format

This thesis uses the following conventions:

**Equations** Equation units are included in square brackets after the equation (e.g., [km/s] indicates that an equation has units of kilometres per second). If the units of a numbered equation are not given the equation is unitless.

**Units** An attempt has been made to use SI units and constants. There are exceptions where non-SI units are more commonly used in this field. One example of this is the use of $cm^{-1}$ (wavenumber) for frequency. Another exception is the units used for angles. Radians (rad.), degrees (deg./°), arcminutes (′), and arcseconds (″) will all be used depending on the context of the discussion. If the unit of an angle is not stated in an equation, and the angular units do not cancel out, the angle is assumed to be in radians. Standard astronomical units such as the AU (1 AU = 1.495 $\times 10^{13}$ m), parsec (1 pc = 3.086 $\times 10^{18}$ cm), Solar mass (1 $M_{\odot}$= 1.989 $\times 10^{33}$ g), Solar luminosity (1 $L_{\odot}$=3.826 $\times 10^{26}$ W) and Jansky (1 Jy = $10^{-26}$ $W/m^2/Hz$) will also be used.

# Chapter 1

# Introduction

## 1.1 Overview

Stars are the building blocks of galaxies. Most of the visible light we see in the sky at night comes from stars. Leblanc (e.g. LeBlanc, 2011) defines a star as a self-gravitating celestial object in which there is, or there once was (in the case of dead stars), sustained thermonuclear fusion of hydrogen in their core. How stars form is a question many astronomers are working hard to answer. In order to answer this question we have to focus on what fills the space between stars: interstellar gas and dust, cosmic rays, electromagnetic radiation, magnetic fields, gravitational fields and dark matter (e.g. Draine, 2010). Interstellar dust is comprised of small-sized solid particles ($\sim$ 1 $\mu$m). Interstellar gas is comprised of ions, atoms and molecules in gas phase which are usually far from thermodynamic equilibrium. Gas collisions establish Maxwell-Boltzmann velocity distributions. Because of this, the temperature normally used to describe interstellar gas is 'kinetic temperature', the temperature at which gas particles in thermal equilibrium would have the observed Maxwell-Boltzmann

velocity distribution.

Stars are born in dense and cold regions of the Interstellar Medium (ISM) (Shu et al., 1987). There is a series of phases a star has to pass through after its birth from these dense clouds of gas and dust until it dies (Ward-Thompson, 2011). During its lifetime, a star influences its surrounding environment differently depending on its mass and luminosity. It heats up the surrounding material and sweeps up gas by stellar winds and outflows triggering the formation of new stars and/or dispersing surrounding clouds that might have collapsed to form stars. At the end of its life, a star undergoes a series of stages of mass-loss to become a giant or super-giant. High-mass stars – those with mass greater than eight times the mass of the sun ($M_{\odot}$) – undergo a violent mass-loss phase which results in supernova. During these mass-loss stages the ISM is enriched with heavy elements. These heavy elements provide a unique mechanism that can cool the ISM to form new stars and are the basis for the formation of metal-rich planets like the Earth. Star formation is therefore an important area of research in astrophysics.

Advances in our understanding of the process of star formation are intimately related to such fields as the formation of planetary systems, stellar evolution and energetics of the interstellar gas and dust. The currently accepted theory of star formation is not definitive due to the complexity of the physical processes involved. Although our understanding of the basic physical laws and processes involved are well advanced, we still lack a detailed understanding of how these processes interact to form stars. A challenge in star formation research is the vast length scales involved – from parsec scales in molecular clouds down to solar radii scales – which demands high spatial resolution.

In order to answer questions surrounding the formation of stars, one has to study their birth place: the cold and dense clouds of gas and dust dispersed throughout galaxies. Unfortunately the large amounts of gas and dust obscure our view of the processes taking place at the centre of a cloud until the already formed star is able to blow away all the surrounding layers of gas and dust. The short wavelength radiation emitted by the hot nuclei of clouds is absorbed by dust particles and reemitted as long wavelength far-infrared light. The Earth's atmosphere is, however, opaque to this part of the electromagnetic spectrum. The water vapour in the atmosphere absorbs the faint radiation from the star-forming regions making it impossible to observe in certain wavebands. This problem is solved by using space borne instruments like the European Space Agency (ESA)'s *Herschel Space Observatory* (*Herschel*) launched on the 14th of May 2009 (Pilbratt et al., 2010).

*Herschel* was designed to cover the far-infrared region of the electromagnetic spectrum using three instruments: the Spectral and Photometric Imaging Receiver Array (SPIRE) (Griffin et al., 2010), the Photodetecting Array Camera and Spectrometer (PACS) (Poglitsch et al., 2010) and the Heterodyne Instrument for the Far Infrared (HIFI) (de Graauw et al., 2010). SPIRE consists of a two-band imaging Fourier transform spectrometer (iFTS) and a three-band photometer. With its 3.5 m diameter passively cooled primary mirror, *Herschel* provides a major advance in spatial resolution. Diameters of the first infrared telescopes, *Infrared Astronomical Satellite* (*IRAS*) (Neugebauer et al., 1984) and *Infrared Space Observatory* (*ISO*) (Kessler et al., 1996), were limited to 60 cm due to the requirement to place the entire telescope in a cryostat. Before *Herschel* ran out of cooling cryogens on the 29th of April 2013, its three instruments had made over 37,000 successful observations

in about 23,500 hours covering almost 10 % of the sky (http://herschel.esac.esa.int/esupport/index.php?_m=news&_a=viewnews&newsid=156). In this thesis, I will present results obtained from analyzing Herschel observations of a sample of star forming regions. More information about *Herschel* will be provided in Chapter 3.

## 1.2 The Interstellar Medium

As stated in the previous section, the ISM is composed of gas and dust. Hydrogen and Helium are the most abundant gas components in the ISM, constituting 70 % and 28 % by mass respectively (Yamada & Winnewisser, 2011). The remaining 2 % comes from heavy elements – elements with mass greater than that of Helium. It is thought that 1 % of the mass of the ISM is in the form of dust particles.

### 1.2.1 Interstellar gas

The ISM of the Milky Way Galaxy is dynamic and has a wide range of temperatures and densities as shown in Table 1.1. The densities of the different phases of the ISM in the table are given as hydrogen number densities ($n_{\rm H}$) for the simple reason that hydrogen is the most abundant element in the Universe. A brief overview of the different phases of the ISM will be provided below. A more detailed description is given by Draine (2010) and Tielens (2005).

Coronal gas (or Hot Ionized Medium (HIM)) is high temperature gas that has been shock-heated by blast waves from supernova explosions. The gas has been collisionally ionized and is traced by X-ray emission and UV absorption lines of highly ionized species

Table 1.1: The different phases of interstellar gas (Draine, 2010). [H I: atomic hydrogen, H II: ionized hydrogen]

| Phase | Temperature (K) | $n_{\rm H}$ (cm$^{-3}$) |
|---|---|---|
| Coronal gas (HIM) | $10^5$-$10^6$ | ∼0.04 |
| H II gas | $10^4$ | 0.3-$10^4$ |
| Warm H I (WNM) | ∼5000 | 0.6 |
| Cool H I (CNM) | ∼100 | 30 |
| Diffuse $H_2$ | ∼50 | ∼100 |
| Dense $H_2$ | 10-50 | $10^3$-$10^6$ |
| Cool stellar outflows | 50-$10^3$ | 1-$10^6$ |

such as O IV, N V, S VI and O IV. H II gas regions are those in which hydrogen has been photoionized by hot massive O-type stars. When the photoionized gas is a relatively dense cloud close to the star, the ionized gas is referred to as an H II region and when it is lower density inter cloud material, it is referred to as a diffuse H II region (or Warm Ionized Medium (WIM)). H II gas can be traced by the H$\alpha$ recombination line, optical and UV ionic absorption lines against background sources and by the dispersion of pulsar signals passing through the WIM (Tielens, 2005).

The warm H I (or Warm Neutral Medium (WNM)) and cold H I (or Cold Neutral Medium (CNM)) constitute the neutral phase of the ISM. The WNM and CNM consists of atomic gas heated to $T \sim 10^{3.7}$ K and $T$ ∼100 K, respectively. They can both be traced by the H I 21 cm line in both emission and absorption and also in optical and UV atomic

absorption lines of various elements towards bright background stars.

Diffuse and dense $H_2$ regions together constitute the molecular phase of the ISM. The diffuse $H_2$ regions have relatively large densities and column densities to allow the existence of $H_2$ molecules in cloud interiors through self-shielding and can be traced by the H I 21 cm line in emission and absorption, the CO 2.6 mm emission and optical/UV absorption lines. Dense $H_2$ regions are dark gravitationally bound clouds which block most of the optical radiation from background sources. They can be observed through CO line emission, dust continuum emission and C I fine structure line emission. In these dense "dark" and cold regions, the dust is usually coated with ice mantles consisting of $H_2O$, CO and other molecules. Even though these regions are referred to as dense ($n_H \sim 10^3$ – $10^6$ cm$^{-3}$), their gas pressures are lower than can be achieved using state-of-the-art vacuum pumps[1]. It is in these dense $H_2$ regions that stars are born.

The last phase of the ISM in Table 1.1 is the cool stellar outflows. These come from evolved stars which are in the process of losing mass. A combination of high mass-loss rates of $10^{-4}$ $M_\odot$yr$^{-1}$ and low outflow velocities ($\lesssim 30$ kms$^{-1}$) leads to high density ($n_H \sim$1 – $10^6$ cm$^{-3}$) outflows and high temperatures ($T \sim 50$ – $10^3$ K).

### 1.2.2 Interstellar dust

Even though interstellar dust makes up only 1 % by mass of the ISM, it plays a major role in the chemical evolution of the ISM and hence the formation of stars. It is now known that the formation of $H_2$ molecules is made possible through the catalyzing

[1]The Varian TPS Compact Portable Pumping system in one of our labs pumps down to $10^{-10}$ torr $\sim$ $10^{11}$ molecules cm$^{-3}$(1 torr = 101.325/760 kPa). This converts to a number density at 300 K of $P/(kT) \sim$ $10^8$ cm$^{-3}$.

effect of dust grains (Tielens, 2005). The topic of grain surface chemistry is discussed in detail by Tielens (2005). We can infer the physical conditions of interstellar dust through its interaction with electromagnetic radiation. Observed effects include wavelength dependent attenuation of star light due to absorption and scattering by dust particles in the wavelength region between 0.1 and 20 $\mu$m. Other effects include the polarization dependent attenuation of star light and thermal emission from dust at wavelengths between the submillimeter and 2 $\mu$m.

Even though a model to describe the observed data from interstellar grains has not yet been found, models assuming the composition of dust grains to consist of amorphous silicates and carbonaceous materials have been widely accepted. An example of a successful two component model is that of Mathis et al (Mathis et al., 1977), which assumes silicate and graphite spheres with power law size distributions of the form $n(a) \propto a^{-3.5}$ for 0.005 $\mu$m $<$ a $<$ 0.25 $\mu$m where $a$ is the radius. Polycyclic Aromatic Hydrocarbon (PAH) have been added to form three-component models (e.g. Draine & Li, 2007; Draine & Fraisse, 2009). PAH molecules are composed of carbon atoms arranged into planar hexagonal rings with hydrogen atoms at the boundaries. PAH molecules containing up to hundreds of atoms have been observed. The three-component models have been successful in reproducing observed dust extinction curves.

Big interstellar dust grains ($a$ = 0.01 – 0.1 $\mu$m) (Compiègne et al., 2008) exhibit very small temperature fluctuations after absorbing star light. They then re-radiate the light as continuum emission in the infrared and submillimeter wavelengths. Very small grains ($a$ = 0.001 – 0.01 $\mu$m) exhibit large temperature fluctuations and emit most of their radiation

in the near and mid-infrared wavelengths (25 – 60 $\mu$m). Vibrational relaxation of Far Ultraviolet (FUV)-pumped PAH molecules ($a$ = 0.0004 – 0.001 $\mu$m) result in emission features at 3.3, 6.2, 7.7, 8.6, 11.3 and 12.7 $\mu$m (Draine, 2010).

## 1.3 Present understanding of the earliest stages of star formation

In this section I present the currently accepted theory of formation of low- to intermediate-mass ($M_\star \leq 8$ M$_\odot$) stars. Observations of star forming regions at infrared, millimetre and radio wavelengths, together with theoretical models have led to an improvement of our understanding of the formation of stars. It is commonly accepted that the evolution of stars begins with density enhancements of the interstellar medium to form centrally concentrated cores (e.g. Lada, 1991; Shu et al., 1993; Andre et al., 1993). Gravity causes the core to collapse, forming an infall region feeding a central protostar and a surrounding disk supported by centripetal forces. During collapse, excess angular momentum is dissipated from the system by bipolar outflows (e.g. Shu et al., 1987). The envelope, whose radius is initially about 1000 astronomical unit (AU) or more contains most of the mass, but as the system evolves, most of the material settles into the disk and some is accreted by the central protostar. Eventually, the envelope is depleted of material and is blown away by the powerful stellar outflows leaving behind a young star and a surrounding disk of approximately 100 AU from which planets are believed to form. Figure 1.1 shows the six stages in the formation of low-mass stars. Each stage will be described in the following sections.

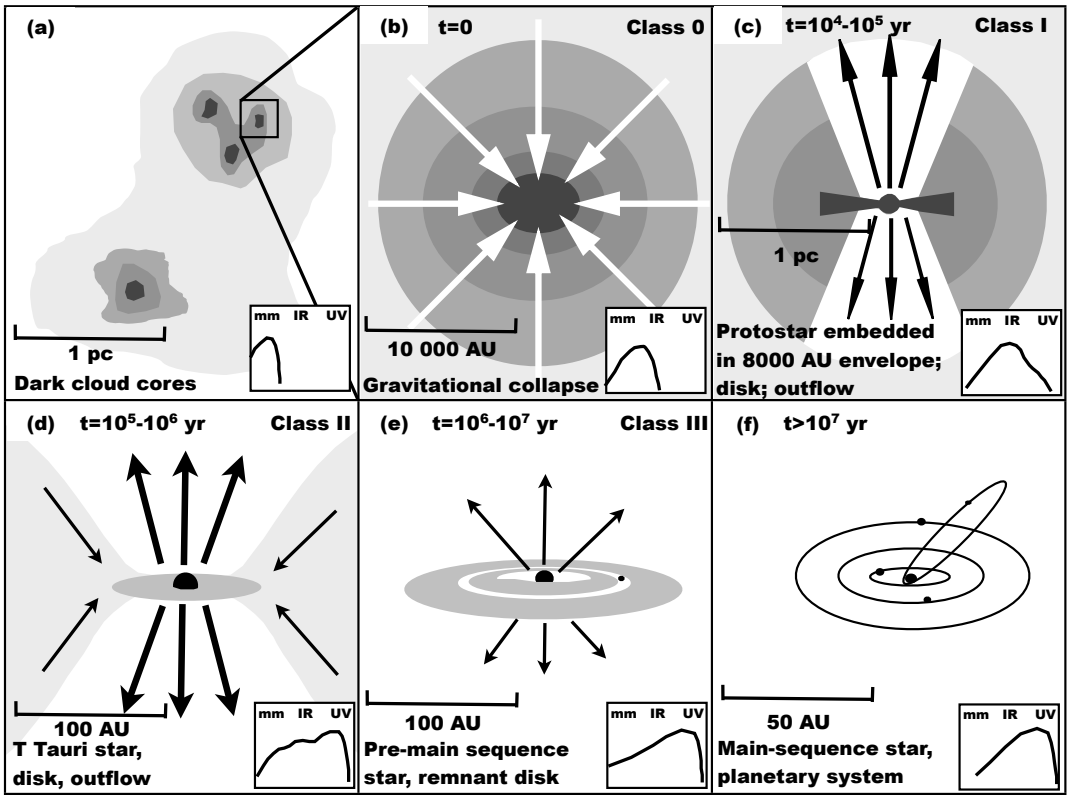


Figure 1.1: A schematic view of the different stages in the formation of stars. Adapted from (Jonkheid, 2006)

### 1.3.1 Molecular Clouds to Clumps

Stars form through gravitational collapse of cold and dense phases of the ISM (mostly in Giant Molecular Clouds (GMCs)). Molecular clouds are obscured in the optical region of the electromagnetic spectrum, but can be observed in the far-infrared and sub-millimeter wavelengths. The processes that cause local density enhancements in molecular clouds are not observable because of the small spatial scales involved, and therefore are not well understood. It is thought that density enhancements may be a result of turbulence,

shocks from colliding clouds, shockwaves from supernova and expanding HII regions. A local density enhancement as shown in Figure 1.1(a) has a relatively large gravitational field than the surrounding regions and will therefore grow by accreting more material. A GMC may have numerous local density enhancement regions, some of which end up forming clumps. Clumps or starless cores are objects with no evidence of embedded protostars that maybe gravitationally bound (e.g. Bodenheimer, 2011).

### 1.3.2 Clumps to Protostars

Under suitable conditions, starless cores may undergo collapse. The Virial Theorem, a theorem that considers the energy balance in an isolated cloud that is in equilibrium, states that, when a cloud collapses, half of the gravitational energy released will go into heating the collapsing material while the other half is radiated away (Ward-Thompson, 2011). The temperature at the centre of the cloud will continue to rise as material keeps falling inwards such that the peak of emission falls in the far-infrared region of the electromagnetic spectrum. Objects that show presence of submillimeter or infrared sources are referred to as protostars. Figure 1.1(b), (c), (d) and (e) shows the four classes of protostars. The classification is based on the spectral slope (or spectral index), $\alpha$, of their continuum spectra (see spectral energy distribution (SED) on the bottom right corner of each diagram in Figure 1.1) between 2 and 20 $\mu$m (Lada & Wilking, 1984; Lada, 1987).

$$\alpha = \frac{d\log(\lambda F_\lambda)}{d\log(\lambda)}. \tag{1.1}$$

Low-mass protostars ($M \lesssim 3$ M$_\odot$) are classified according to their ratio of observed ground-based flux densities in the atmospheric windows at 2.2 $\mu$m (K band) and 10 $\mu$m (N band)

(Draine, 2010):

$$\alpha_{K,N} = \frac{[\log[(\lambda F_\lambda)_{10\ \mu m} - \log[(\lambda F_\lambda)_{2.2\ \mu m}]}{\log(10/2.2)}. \tag{1.2}$$

For a reason why these infrared astronomical bands are important, interested readers are referred to Burke & Graham-Smith (2010).

Class 0 protostars have sizes of about $10^4$ AU and they are heavily obscured such that their spectral energy distribution peaks in the far-infrared region ($\lambda > 100\ \mu m$). These objects may be deeply obscured and may not be visible in the K and N bands. A larger fraction of their luminosity comes from accretion from their envelopes. Typical ages of Class 0 protostars are in the range $1 - 3 \times 10^4$ yr.

Class I protostars are characterized by $\alpha_{K,N} > 0$. This corresponds to blackbodies having temperatures of $T < 870$ K. Class I protostars are surrounded by a disc and circumstellar envelope with combined mass a few tens of solar masses. The planar structure is caused by the initial angular momentum of the cloud due to its rotation around its centre of mass. As collapse continues and in order to conserve angular momentum, the rotation speed of the protostar increases, material falls toward the orbital plane and excess angular momentum is dissipated by bipolar outflows. Some bipolar outflows are highly collimated while others have wide opening angles. The interaction of bipolar outflows with the surrounding envelopes causes shock fronts that generate enough heat to allow excitation of rotational transitions of molecules. A larger fraction of the luminosity of Class I protostars is due to accretion from their disks and envelopes. Typical ages of Class I protostars are in the range $1 \times 10^5 - 2 \times 10^5$ yr.

Class II protostars are characterized by $-1.5 < \alpha_{K,N} < 0$. This corresponds to

blackbodies having temperatures of 870 K $< T <$ 1540 K. Class II protostars have a circumstellar disk from which they are accreting material but have no envelope. Typical ages of Class II protostars are in the range $10^5$ – $10^6$ yr. Class II protostars are also called Classical T Tauri stars, a name that comes after the prototype discovered at optical wavelengths.

Class III protostars are characterized by $\alpha_{K,N} <$ -1.5. This corresponds to blackbodies having temperatures of $T >$ 1540 K. Class III protostars are still undergoing gravitational contraction. At this stage planets have started forming in the disks and so these objects either have little or no evidence of an accretion disk. Typical ages of Class III protostars are in the range $10^6$ – $10^7$ yr.

### 1.3.3 Protostars to Main Sequence stars

As the collapse of the core continues, the temperature increases to high values such that the pressure generated is able to halt core collapse. The maximum temperature reached is dependent on the initial mass of the clump and is a deciding factor whether or not the protostar becomes a main-sequence star. If the maximum temperature reached is lower than that required to ignite the burning of hydrogen in the core, the protostar becomes a brown dwarf which then slowly cools down. In the meantime some material in the disk starts gathering to form planetesimals. If the temperature is high enough to ignite hydrogen fusion, then the protostar becomes a star. The stellar winds from the young star will then blow away the gas and dust in the disk (Figure 1.1(g)) leaving behind the more massive planetesimals which will go on to form planets (Figure 1.1(f)).

## 1.4 A condition for the collapse of molecular clouds: the Jeans Mass

A molecular cloud that is gravitationally unstable will collapse and form a star. In order to calculate the conditions necessary for gravitational instability, consider an infinite static three-dimensional medium with a uniform density $\rho_0$ (Ward-Thompson, 2011). The sound speed in the medium $c_\mathrm{s}$ is assumed to be uniform and isothermal. A small spherical portion of this medium whose radius is $r$ may become slightly more dense that the surrounding medium due to random statistical fluctuations. It can be shown that for such a spherical portion to continue becoming denser and condense, the radius of the sphere, $r$, has to be greater than

$$R_\mathrm{J} = \frac{c_s}{(G\rho_0)^{1/2}}, \tag{1.3}$$

where $G$ is the gravitational constant. If the molecular cloud is assumed to behave as an ideal gas at temperature T, then the sound speed, $c_\mathrm{s}$, is given by

$$c_\mathrm{s} = \sqrt{\frac{kT}{\mu m_\mathrm{H}}}, \tag{1.4}$$

where, $m_\mathrm{H}$ is the mass of a hydrogen atom and $\mu$ is the mean molecular weight of the gas. $R_\mathrm{J}$ is called the Jeans length. The mass associated with the Jeans length is called the Jeans mass and is given by

$$M_\mathrm{J} = \frac{4}{3}\pi\rho_0 R_\mathrm{J}^3 = \frac{4\pi c_s^3}{3(G^3\rho_0)^{1/2}} \tag{1.5}$$

The Jeans mass is the minimum mass required for a uniform density region to collapse. A uniform density region whose mass is greater than the Jeans mass is said to be Jeans unstable and will collapse to form a star. A region whose mass is less than the Jeans mass

is not gravitationally bound and will eventually disperse.

## 1.5 Thesis Summary

This thesis is organized as follows. Chapter 2 discusses the theory required to understand observations of star-forming regions. It is in this chapter that the interaction of electromagnetic radiation with interstellar gas and dust is provided. The propagation of electromagnetic radiation in the interstellar medium is also discussed.

Chapter 3 discusses the derivation of the wavelength dependent beam profile of the SPIRE iFTS. The SPIRE iFTS beam profile was derived by fitting Hermite-Gaussian functions to raster observations of Neptune and Uranus. This was my main contribution to the SPIRE iFTS calibration team. For the past three years, more than 50 % of my time was spent on the characterization of the SPIRE iFTS beam profile and assessing its impact on the observed data.

The application of the beam profile to the calibration of the SPIRE iFTS data is discussed in Chapter 4. Knowledge of the beam profile is important to properly calibrate astronomical sources whose spatial extent falls between that of point-like and extended sources.

Chapters 5 to 7 will discuss SPIRE iFTS observations of sources that fall within the first three phases of star formation as provided in Figure 1.1. Results from analyzing data from three starless cores (L1521E, L1521F and L1689B) are discussed in Chapter 5. In Chapter 6, observations of IRAS16293, a Class 0 protostar are discussed. This is followed by a discussion of a Class I protostar Elias 29 in Chapter 7.

A summary of the thesis and recommendations for future work are provided in Chapter 8.

# Chapter 2

# Probing star formation

The only way of probing physical properties of star forming regions is by observing electromagnetic radiation that these regions emit. There are two types of radiation from star-forming regions, continuum and line radiation. Continuum radiation is distributed over a wide range of frequencies whereas line radiation peaks at specific frequencies. This Chapter will focus on the elementary processes involved in the absorption and emission of electromagnetic radiation by atoms and molecules leading to line radiation and emission by dust particles leading to continuum radiation. The propagation of radiation through absorbing and emitting media will also be described. A more detailed description of the theory presented in this Chapter can be found in Draine (2010); Tielens (2005); Yamada & Winnewisser (2011); Ward-Thompson (2011) and Rybicki & Lightman (2008).

## 2.1 Einstein coefficients

When a ray passes through a medium, its specific intensity $I_\nu$ (in $\mathrm{Wm^{-2}Hz^{-1}sr^{-1}}$) can change as the medium absorbs or emits energy. Figure 2.1 shows a two-level system often used to show that energy can be absorbed or added to the ray by processes of spontaneous and stimulated emission.

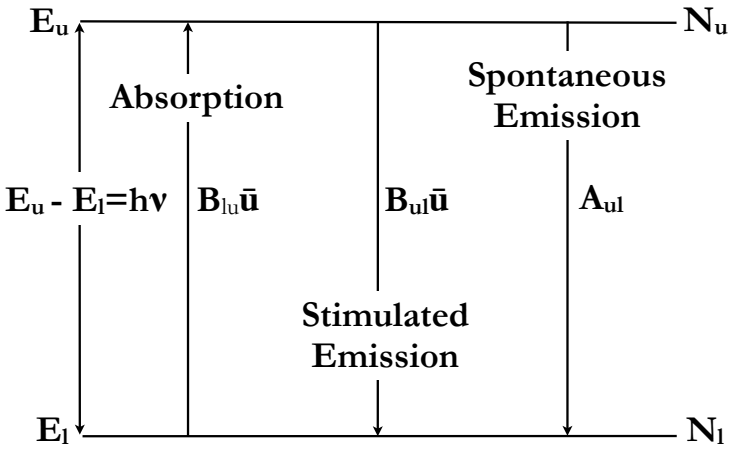


Figure 2.1: The absorption and emission of radiation in a two-level system. The corresponding Einstein A- and B-coefficients are labeled. $\bar{u} = 4\pi\bar{I}/c$ is the mean energy density of the radiation field and $\bar{I}$ is the mean intensity given by $\bar{I} = \int_0^\infty I_\nu \phi(\nu) d\nu$.

The system consists of gas atoms with discrete energy levels $E_\mathrm{u}$ with density $N_\mathrm{u}$ and $E_\mathrm{l}$ with density $N_\mathrm{l}$. According to Einstein, a system in a lower state $E_\mathrm{l}$ will get excited

by absorption of photons of frequency

$$\nu = \frac{E_{\rm u} - E_{\rm l}}{h} \qquad [\rm Hz], \tag{2.1}$$

where $h$ is Planck's constant. A system in an excited state will spontaneously emit photons of frequency $\nu$ with a certain probability $A_{\rm ul}$ to return to lower level $E_{\rm l}$. $A_{\rm ul}$ is known as the Einstein A-coefficient. The number of spontaneous transitions per unit time per unit volume is $N_{\rm u}A_{\rm ul}$. For a single transition, each atom or molecule will contribute an energy $h\nu$ distributed over a $4\pi$ solid angle. The emission coefficient $j_\nu$ of the medium is defined as the energy emitted in a certain frequency range, per unit time, per unit volume, per unit solid angle, i.e.

$$j_\nu = \frac{h\nu}{4\pi} N_{\rm u} A_{\rm ul} \phi(\nu) \qquad [\rm Wm^{-3}Hz^{-1}sr^{-1}], \tag{2.2}$$

where $\phi(\nu)$ is the spectral line profile function describing the emitted line. $\phi(\nu)$ is peaked and normalized such that

$$\int_0^\infty \phi(\nu) d\nu = 1. \tag{2.3}$$

The absorption coefficient $\alpha_\nu$ of the medium is defined as the energy absorbed from the ray in a certain frequency range, per unit time, per unit volume, per unit solid angle, i.e.

$$\alpha_\nu = \frac{h\nu}{4\pi} N_{\rm l} B_{\rm lu} \phi(\nu) \qquad [\rm m^{-1}], \tag{2.4}$$

assuming that absorption is described with the same line profile function as that for emission. $B_{\rm lu}$ is the Einstein B-coefficient. If we incorporate stimulated emission as negative absorption, Equation (2.4) becomes

$$\alpha_\nu = \frac{h\nu}{4\pi} (N_{\rm l} B_{\rm lu} - N_{\rm u} B_{\rm ul}) \phi(\nu) \qquad [\rm m^{-1}], \tag{2.5}$$

## 2.2 Radiative transfer

The term radiative transfer refers to the manner in which radiation from a source interacts with the medium through which it propagates before reaching the observer. Suppose radiation enters a medium of length $S$ at $s$=0 and emerges at $s$=$S$ with intensity $I_\nu(S)$ as shown in Figure 2.2. The change in the intensity of the radiation as it passes though the medium can be described using the equation of radiative transfer

$$\mathrm{d}I_\nu(s) = -\alpha_\nu(s) I_\nu \mathrm{d}s + j_\nu(s)\mathrm{d}s \qquad [\mathrm{Wm}^{-2}\mathrm{Hz}^{-1}\mathrm{sr}^{-1}], \tag{2.6}$$

where $\alpha_\nu(s)$ is the absorption coefficient at frequency $\nu$ in $\mathrm{m}^{-1}$ and $j_\nu(s)$ is the emissivity (or emission coefficient) at frequency $\nu$ in $\mathrm{Wm}^{-3}\mathrm{Hz}^{-1}\mathrm{sr}^{-1}$. The first term on the right hand side of Equation (2.6) represents the attenuation of the intensity due to the effective absorption and the second term represents the increase in intensity due to spontaneous emission in the medium.

Equation (2.6) can be simplified by introducing two new quantities. The first is optical depth, $\tau_\nu$ defined by

$$d\tau_\nu(s) = \alpha_\nu(s) ds, \tag{2.7}$$

such that the optical depth at a point $l$ along the line of sight is given by

$$\tau_\nu(s) = \int_{s'=0}^{s'=l} \alpha_\nu(s') ds'. \tag{2.8}$$

The optical depth measures distances through the medium in units of the local mean free

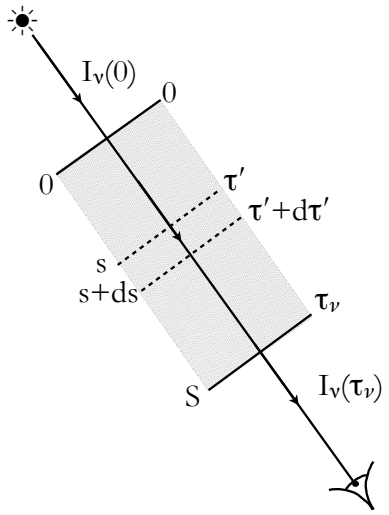


Figure 2.2: A ray traveling through an optically active medium.

path. The second new quantity is the source function, $S_\nu$ defined as

$$S_\nu = \frac{j_\nu}{\alpha_\nu} \qquad [\mathrm{Wm^{-2}Hz^{-1}sr^{-1}}]. \tag{2.9}$$

The radiative transfer equation can now be written in the form

$$dI_\nu(\tau_\nu) = -I_\nu(\tau_\nu)d\tau_\nu + S_\nu(\tau_\nu)d\tau_\nu \qquad [\mathrm{Wm^{-2}Hz^{-1}sr^{-1}}]. \tag{2.10}$$

Equation (2.10) can be integrated by making use of the integrating factor, $e^\tau$, to obtain the equation of radiative transfer in integral form:

$$I_\nu(\tau_\nu) = I_\nu(0)e^{-\tau_\nu} + \int_{\tau_\nu'=0}^{\tau_\nu'=\tau_\nu} e^{-(\tau_\nu-\tau_\nu')}S_\nu(\tau_\nu')d\tau_\nu' \qquad [\mathrm{Wm^{-2}Hz^{-1}sr^{-1}}]. \tag{2.11}$$

The first term on the right hand side of Equation (2.11) is the background intensity $I_\nu(0)$ attenuated by the optical depth $\tau_\nu$ to the required point and the second term represents

emission from all infinitesimal elements of the medium between $\tau_\nu^{'} = 0$ and $\tau_\nu^{'} = \tau_\nu$ each one attenuated by the intervening optical depth $\tau_\nu - \tau_\nu^{'}$. If we consider an infinite slab of uniform medium ($dI_\nu/d\tau_\nu = 0$) whose energy levels have been populated according to a single excitation temperature $T_{\rm ex}$, the radiation field within the slab ($I_\nu$) would be given by the Planck function $B_\nu(T_{\rm ex})$. Equation (2.10) now becomes

$$dI_\nu(\tau_\nu) = 0 = -B_\nu(T_{\rm ex})d\tau_\nu + S_\nu d\tau_\nu \qquad [{\rm Wm^{-2}Hz^{-1}sr^{-1}}], \tag{2.12}$$

and so $S_\nu = B_\nu(T_{\rm ex})$. The emissivity and attenuation coefficient must therefore satisfy Kirchhoff's Law:

$$j_\nu = \alpha_\nu B_\nu(T_{\rm ex}) \qquad [{\rm Wm^{-3}Hz^{-1}sr^{-1}}], \tag{2.13}$$

where $B_\nu(T)$ is the Planck function:

$$B_\nu(T_{\rm ex}) = \frac{2h\nu^3}{c^2}\frac{1}{e^{h\nu/kT_{\rm ex}} - 1} \qquad [{\rm Wm^{-2}Hz^{-1}sr^{-1}}], \tag{2.14}$$

$j_\nu$ and $\alpha_\nu$ are now independent of the geometry of the radiating medium (i.e. the source is much larger than the telescope beam) and depend only on the local properties of the medium. Substituting $B_\nu(T_{\rm ex})$ for $S_\nu$ in Equation (2.11) and integrating we obtain:

$$I_\nu(\tau_\nu) = I_\nu(0)e^{-\tau_\nu} + B_\nu(T_{\rm ex})(1 - e^{-\tau_\nu}) \qquad [{\rm Wm^{-2}Hz^{-1}sr^{-1}}]. \tag{2.15}$$

If emission from the background is negligible compared to emission from the medium then the measured intensity is given by

$$I_\nu(\tau_\nu) = B_\nu(T_{\rm ex})(1 - e^{-\tau_\nu}) \qquad [{\rm Wm^{-2}Hz^{-1}sr^{-1}}]. \tag{2.16}$$

We now apply Equation (2.16) to two extreme cases usually encountered in observational astronomy: optically thin and optically thick emission.

**Optically thin emission**: In this case $\tau_\nu \ll 1$ and the observer receives emission from right through the medium

$$I_\nu(\tau_\nu) \simeq B_\nu(T_{\rm ex})\tau_\nu \qquad [\mathrm{Wm^{-2}Hz^{-1}sr^{-1}}]. \tag{2.17}$$

**Optically thick emission**: In this case $\tau_\nu \gg 1$ and the observer receives emission from a thin layer at the front of the medium

$$I_\nu(\tau_\nu) \simeq B_\nu(T_{\rm ex}) \qquad [\mathrm{Wm^{-2}Hz^{-1}sr^{-1}}]. \tag{2.18}$$

## 2.3 Continuum component

The FIR continuum emission by dust is the major coolant of molecular clouds. Equation (2.16) is important when studying emission from dust. This is because emission from dust dominates over emission from the background. Replacing $T_{ex}$ with dust temperature $T_d$ we obtain

$$I_\nu(\tau_\nu) = B_\nu(T_d)(1 - e^{-\tau_\nu}) \qquad [\mathrm{Wm^{-2}Hz^{-1}sr^{-1}}], \tag{2.19}$$

which is the equation of a greybody. The optical depth $\tau_\nu$ has the form

$$\tau_\nu = \left(\frac{\nu}{\nu_c}\right)^\beta = \left(\frac{\lambda_c}{\lambda}\right)^\beta, \tag{2.20}$$

where $\beta$ is the dust emissivity index ($1 \leq \beta \leq 2$) and $\nu_c$ ($\lambda_c$) is the critical frequency (wavelength) at which the optical depth is unity. The dust temperature and emissivity index can be obtained from fitting measured spectral energy distributions (SEDs) with Equation

2.19. The total dust mass $M_d$ in a cloud can be calculated by first considering a single spherical grain of radius $a$ (surface area $= 4\pi a^2$), density $\rho_d$ and mass $m_d$ $(= 4\pi a^3 \rho_d/3)$ at a temperature $T_d$. If the emission efficiency of the grain at frequency $\nu$ is $Q_\nu$, then its monochromatic luminosity, $L_\nu$, is given by

$$L_\nu = 4\pi a^2 Q_\nu \pi B_\nu(T_d) \qquad [\mathrm{W\ Hz^{-1}}]. \tag{2.21}$$

The number of dust particles in the cloud is given by

$$N_d = \frac{M_d}{m_d} = \frac{M_d}{(4\pi a^3 \rho_d/3)}. \tag{2.22}$$

If the cloud subtends a solid angle $\Omega$ at the observer who is at a distance $d$ and if the column density of dust grains is $n_d = N_d/(d^2\Omega)$, then the optical depth is given by

$$\tau_\nu = \pi a^2 n_d Q_\nu = \frac{3 M_d Q_\nu}{4 a \rho_d d^2 \Omega}. \tag{2.23}$$

Assuming the emission from dust grains is optically thin, the flux density measured by an observer at a distance $d$ is given by

$$F_\nu = \frac{N_d L_\nu}{4\pi d^2} = \frac{3 M_d Q_\nu B_\nu(T_d)}{4 a \rho_d d^2} \qquad [\mathrm{Wm^{-2}Hz^{-1}}]. \tag{2.24}$$

The total mass of the dust is then obtained from

$$M_\mathrm{d} = \frac{4 a \rho_d d^2 F_\nu}{3 Q_\nu B_\nu(T_d)} = \frac{d^2 F_\nu}{\kappa_\nu B_\nu(T_d)} \qquad [\mathrm{g}], \tag{2.25}$$

where $\kappa_\nu = 3Q_\nu/4a\rho_d$ $[\mathrm{cm^2/g}]$ is the emissivity of the dust at frequency $\nu$.

In order to obtain a general equation for all optical depths, we rewrite Equation (2.19) in terms of flux, to obtain

$$F_\nu(\tau_\nu) = \Omega B_\nu(T_d)(1 - e^{-\tau_\nu}) = \Omega B_\nu(T_d) \left[1 - \exp\left(-\frac{3 M_d Q_\nu}{4 a \rho_d d^2 \Omega}\right)\right] \qquad [\mathrm{Wm^{-2}Hz^{-1}}]. \tag{2.26}$$

Rearranging Equation (2.26) we obtain the dust mass as

$$M_d = \frac{d^2\Omega}{\kappa_\nu} \ln\left[1 - \left(\frac{F_\nu}{\Omega B_\nu(T_d)}\right)\right] \qquad [\mathrm{g}], \tag{2.27}$$

which gives Equation (2.25) if the dust emission is optically thin ($\tau_\nu \ll 1$). From this section we see that the observed continuum emission helps us constrain the dust temperature, the emissivity index and the dust mass (see Chapter 5).

## 2.4 Emission line component

A collapsing molecular cloud reaches hydrostatic equilibrium as the gravitational energy is converted to thermal energy. For collapse to continue, the cloud must cool by emitting radiation. This can be achieved through fine structure lines of OI, CI, CII and through rotational lines of molecules like CO, $H_2O$ (e.g. Kaufman et al., 1999; Tielens, 2005; Herbst & van Dishoeck, 2009). Both CI and CO have lines in the Spectral and Photometric Imaging Receiver Array (SPIRE) imaging Fourier transform spectrometer (iFTS) band and will be used as examples in the following discussion. The measured line observations are compared with radiative transfer models to obtain column densities (abundances) of emitting species. From these abundances, physical conditions such as temperature and density of the emitting regions can be constrained.

### 2.4.1 Atomic lines

The gas phase of the Interstellar Medium (ISM) cools mainly by atomic fine structure lines. We use the Russel-Sanders coupling scheme (Tielens, 2005; Yamada & Winnewisser, 2011) to characterize the energy levels of atoms. In the scheme, the coupling of

the orbital angular momenta of all electrons in the atom results in a total angular momentum $L$ given by

$$L = \sum_{i}^{N} l_i, \tag{2.28}$$

The coupling of the spin angular momenta of all electrons in the atom results in a total electron spin $S$ given by

$$S = \sum_{i}^{N} s_i, \tag{2.29}$$

The total angular momentum $J$ is defined as $J = L + S$. The electronic configurations (or electronic terms) of atoms are characterized by $L$, $S$ and $J$ as $^{2S+1}X_J$ where $X$ = S, P, D (for $L$ = 1, 2, 3). $2S + 1$ is the spin multiplicity. The fine structure lines of carbon are discussed here since they fall within the frequency range covered by the SPIRE iFTS and have been observed in the Class 0 and Class I sources discussed in Chapters 6 and 7 respectively. The electronic configuration of carbon is $1s^2 2s^2 2p^2$. Using the Pauli principle, we can see that there are three possible terms: $^1$S, $^1$D and $^3$P. The $^3$P state is a triplet with three fine structure components $^3P_0$, $^3P_1$ and $^3P_2$ corresponding to $J$ = 0, 1 and 2. The fine structure transitions $^3P_1$ – $^3P_0$ and $^3P_2$ – $^3P_1$ are observed in the SPIRE iFTS band at 492 and 809 GHz respectively. They provide information on the intermediate regions between atomic and molecular gas (Tielens, 2005).

### 2.4.2 Molecular lines

The rotational energy levels of molecules are characterized by the rotational quantum number $J$. The energy levels of diatomic and linear molecules can be described by

those allowed for a rigid rotor, i.e.

$$E_J = \frac{h^2}{8\pi^2 I} J(J+1) = BhcJ(J+1), \qquad J = 0, 1, 2, 3, ... \tag{2.30}$$

where B is the rotational constant given by

$$B = \frac{h}{8\pi^2 cI} \qquad [\mathrm{m}^{-1}], \tag{2.31}$$

$h$ is the Planck constant, $c$ is the speed of light (in $\mathrm{ms}^{-1}$). $I$ is the moment of inertia of the molecule given by

$$I = \sum_i m_i r_i^2 \qquad [\mathrm{kg\ m}^2], \tag{2.32}$$

where $m_i$ is the mass of atom $i$ at a distance $r_i$ from the centre of mass. The most common rotational transitions are the electric dipole transitions obeying the selection rule $\Delta J = \pm 1$. The frequency at which a transition can occur is given by

$$\nu = \frac{E_{J+1} - E_J}{h} = 2Bc(J+1) \qquad [\mathrm{s}^{-1}] \tag{2.33}$$

Equation (2.33) tells us that the rotational lines of a linear molecule like CO are evenly spaced in the frequency domain. A discussion of two molecules of interest (CO and $H_2O$) is provided in the following two subsections.

### Carbon monoxide (CO)

CO is the second most abundant molecule in the Universe after hydrogen and its rotational levels are populated mainly by collisions with $H_2$. $H_2$, the most abundant molecule in the Universe does not have a permanent dipole moment and so its electric dipole transitions are forbidden. Therefore CO, instead of $H_2$ is widely used as a tracer of

molecular gas (e.g. Tennyson, 2010; Ward-Thompson, 2011). The SPIRE iFTS was designed to cover CO rotational transitions from $J$=4–3 to $J$=13–12. The CO isotopologues ($^{13}C^{16}O$, $^{12}C^{17}O$ and $^{12}C^{18}O$) are less abundant and therefore tend to be optically thin and so have been used to estimate the total CO and $H_2$ column densities assuming typical [CO/$^{13}$CO] and [CO/$C^{18}O$] abundance ratios (e.g. Wilson & Rood, 1994; Bolatto et al., 2013).

#### Water ($H_2O$)

Water is an asymmetric rotor. Its energy levels are characterized by an irregular set of energy levels characterized by quantum numbers $J_{K_{-1},K_{+1}}$. The two hydrogen atoms of the water molecule can have their nuclear spins either parallel leading to a nuclear spin of 1 or antiparallel leading to a nuclear spin of 0. The parallel spin state is referred to as *ortho* and has an even value of $K_{-1}+K_{+1}$ while the antiparallel spin state is referred to as *para* and has an odd value of $K_{-1}+K_{+1}$. The nuclear spin states do not change in radiative transitions and so *ortho*-$H_2O$ and *para*-$H_2O$ behave like separate species.

The many rotational transitions of water in the far-infrared and sub millimetre wavelengths make it one of the most important coolants of molecular clouds and provide important diagnostics for understanding the early stages of star formation.

### 2.4.3 Rotational diagrams

Rotational diagrams (Goldsmith & Langer, 1999) are based on multi-line observations of a single atomic or molecular species covering a range of upper level energies. The method assumes that the molecule is in local thermodynamic equilibrium (LTE), i.e., the density is large enough that the excitation is mostly caused by collisions. In this case the

level populations of a molecule can be characterized by a single excitation temperature ($T_{\rm ex}$) described by the Boltzmann distribution

$$\frac{N_{\rm u}}{g_{\rm u}} = \frac{N_{\rm tot}}{Q_{\rm ex}} e^{-E_{\rm u}/kT_{\rm ex}} \qquad [{\rm cm}^{-2}], \tag{2.34}$$

where $N_{\rm u}$ is the column density in the upper state, $N_{\rm tot}$ is the total column density summed over all states, $g_u$ is the statistical weight of the upper level given by $2J_{\rm u}$+1, $E_{\rm u}$ is the energy of the upper state, $Q_{\rm ex}$ is the partition function given by $Q_{\rm ex} = kT_{\rm ex}/hcB$. $k$ is the Boltzmann constant, $h$ is the Planck constant, $c$ is the speed of light and $B$ is the rotational constant of the molecular species being considered. The method also assumes that the emission is homogeneous and fills the telescope beam and that the lines are optically thin. The column density for each line is given by

$$\frac{N_{\rm u}}{g_{\rm u}} = \frac{4\pi I_\nu}{h\nu_{ul} A_{\rm ul} g_{\rm u}} = \frac{4\pi}{h\nu_{\rm ul} A_{\rm ul} g_{\rm u}} \int I_\nu d\nu \qquad [{\rm cm}^{-2}], \tag{2.35}$$

where $I_{\rm u} = \int I_\nu d\nu$ is the line flux in Wcm$^{-2}$sr$^{-1}$. Combining Equations (2.34) and (2.35) and applying natural logarithms on both sides we obtain

$$\ln\left(\frac{4\pi}{h\nu_{\rm ul} A_{\rm ul} g_{\rm u}} \int I_\nu d\nu\right) = -\frac{1}{T_{\rm ex}} \frac{E_{\rm u}}{k} + \ln \frac{N_{\rm ex}}{Q_{\rm ex}}. \tag{2.36}$$

The excitation temperature is obtained by plotting a graph of $\ln(N_{\rm u}/g_{\rm u})$ versus $(E_{\rm u}/k)$ and using a linear fit. The obtained excitation (rotational) temperature will be used to calculate the partition function which then enables calculation of the column density from the y-intercept. If all the assumptions stated above are valid, then the temperatures obtained by this method are trustworthy, but column depth effects and non-uniform beam filling affect the derived column densities. In order to calculate the total amount of matter in a cloud,

$N(\mathrm{CO})$ should be converted to the column abundance of hydrogen, $N(\mathrm{H_2})$. A conversion factor of $N(\mathrm{CO})/N(\mathrm{H_2}) = 10^{-4}$ (Wilson & Rood, 1994; van Dishoeck et al., 1995) is usually used. When using $^{13}$CO the conversion factor $^{12}\mathrm{C}/^{13}\mathrm{C} = 65$ derived for nearby (<500 pc) molecular clouds (Langer & Penzias, 1993) is used.

### 2.4.4 Non-LTE models

For many regions in the ISM, the density is too low to attain LTE and so the contribution of radiative decay exceeds that of collisional de-excitation. This leads to excitation temperatures lower than the kinetic temperatures. A commonly used Non-LTE model, RADEX (van der Tak et al., 2007), uses both collisional and radiative processes to calculate level populations of molecules. The collision rates between upper levels $u$ and lower levels $l$ are usually designated $C_{ul}$ and $C_{lu}$. The rate of collisions is given by

$$C_{\mathrm{ul}} = n_{\mathrm{col}}\gamma_{\mathrm{ul}} \qquad \text{and} \qquad C_{\mathrm{lu}} = n_{\mathrm{col}}\gamma_{\mathrm{lu}}, \tag{2.37}$$

where $\gamma_{\mathrm{ul}}(\gamma_{\mathrm{lu}})$ is the downward (upward) collisional rate coefficient (in $\mathrm{cm^3 s^{-1}}$) and $n_{\mathrm{col}}$ is the number density of the collision partner. RADEX assumes statistical equilibrium

$$\frac{dn_{\mathrm{u}}}{dt} = \sum_{l\neq u}^{N} n_{\mathrm{l}} P_{\mathrm{lu}} - n_{\mathrm{u}} \sum_{l\neq u}^{N} P_{\mathrm{ul}} = \mathcal{F}_{\mathrm{u}} - n_{\mathrm{u}}\mathcal{D}_{\mathrm{u}} = 0 \qquad [\mathrm{cm^{-3}s^{-1}}], \tag{2.38}$$

where

$$P_{\mathrm{ul}} = \begin{cases} A_{\mathrm{ul}} + B_{\mathrm{ul}}\bar{u} + C_{\mathrm{ul}} & (u > l) \\ B_{\mathrm{ul}}\bar{u} + C_{\mathrm{ul}} & (u < l) \end{cases} . \tag{2.39}$$

$P_{\mathrm{ul}}$ and $P_{\mathrm{lu}}$ are the destruction and formation rate coefficients respectively, $n_{\mathrm{u}}$ is the number density for level $u$ and $C_{\mathrm{ul}}$ is the sum over all collision partners of the rates of inelastic, collision-induced transitions $u \rightarrow l$. $\mathcal{F}_{\mathrm{u}}$ $[\mathrm{cm^{-3}s^{-1}}]$ and $\mathcal{D}_{\mathrm{u}}$ $[\mathrm{s^{-1}}]$ are the state-specific rates of

Table 2.1: Critical densities ($n_{\rm crit}$) and upper energy levels ($E_{\rm up}$) for a sample of cooling lines in the cold, dense ISM (Lequeux et al., 2005). Collision partners are hydrogen molecules.

| Species | Transition | $n_{\rm crit}$ [cm$^{-3}$] | $E_{\rm up}$ [K] |
|---|---|---|---|
| CO | $J \rightarrow 1-0$ | $3\times10^3$ | 5.53 |
| | $J \rightarrow 2-1$ | $1\times10^4$ | 16.6 |
| | $J \rightarrow 3-2$ | $5\times10^4$ | 33.2 |
| C I | $^3P_1$-$^3P_0$ | $0.5\times10^3$ | 23.6 |
| C I | $^3P_2$-$^3P_1$ | $1.0\times10^3$ | 62.5 |

formation and destruction respectively. An important parameter useful in solving the above equilibrium equation is the critical density, $n_{\rm crit}$, the density at which the radiative decay rate is equal to the collisional de-excitation rate. In the optically thin limit (no radiation trapping), $n_{\rm crit}$ is defined as

$$n_{\rm crit} = \frac{A_{\rm ul}}{\gamma_{\rm ul}} \qquad [{\rm cm}^{-3}]. \tag{2.40}$$

$n_{\rm crit}$ is directly proportional to $\nu^3$ and therefore increases with the energy of transitions. This relationship is important in constraining number densities of detected molecules and transitions. Table 2.1 shows the critical densities ($n_{\rm crit}$) and upper energy levels ($E_{\rm up}$) for some of the major cooling lines in the cold, dense ISM.

## 2.5 Conclusion

This chapter has introduced the processes that lead to emission and absorption of radiation by dust, atoms and molecules. How the radiation propagates from regions where it is emitted to the observer has also been discussed. The examples given in this chapter are those of atoms and molecules whose emission lines fall in the SPIRE iFTS bands. This was carried out to set the stage for a more detailed discussion of the measured spectral lines and dust SEDs in the following three chapters.

# Chapter 3

# The beam profile for the Herschel-SPIRE iFTS

## 3.1 Overview

Flux calibration is one of the most important steps in astronomical data analysis. The measured spectral images are impacted by the wavelength dependent beam profile and source extent. It is therefore important to understand the beam profile of the instrument used in obtaining the data. In this chapter the derivation of the beam profile for the Spectral and Photometric Imaging Receiver Array (SPIRE) imaging Fourier transform spectrometer (iFTS) is discussed. A paper describing this work has been published in the refereed literature and is attached as Appendix A. In this chapter I will describe in more detail the steps taken to derive the beam profile, material that will be used in subsequent chapters into context. The importance of the beam profile of an instrument and its derivation are

described in Section 3.2. The reduction of SPIRE iFTS observations is described in section 3.3. Section 3.4 discusses how the calibration of point and extended sources observed with the SPIRE iFTS is carried out. Sections 3.5 and 3.6 describe the functions used to approximate the SPIRE iFTS beam profile and the algorithm developed to obtain the best fit of the functions to the measured data. The main results are presented in Section 3.7.

## 3.2 Introduction

The role of the primary mirror of a telescope is to provide directionality by focusing electromagnetic radiation from a particular astronomical source onto the instruments and detectors. To calibrate the measured signals, the response of the instrument to a point source as a function of angle should be known. This response is usually referred to as the Point spread function (PSF) or beam profile of the instrument. The response of the instrument to a source of any size is then a convolution of the instrument PSF with the source structure. A bright and isolated point source should be used in the measurement of the instrument beam. This is equivalent to convolving a delta function with the telescope beam. Using a bright and isolated point source ensures that all the measured flux originates from that single object and is contained in the beam shape.

Obtaining the data used to derive the beam profile is achieved by scanning the telescope in a raster pattern around the point source. The measured flux will be highest when the point source is at the centre of the instrument beam. The flux decreases as the telescope is moved away from the point source. The two-dimensional distribution of light in the telescope focal plane is what is called the instrument PSF or beam profile.

Most of the data used in this thesis were obtained using the SPIRE iFTS. A brief description of the SPIRE iFTS is provided in the paper (Makiwa et al., 2013). For a more detailed description of the instrument, the reader is referred to Griffin et al. (2010). The beam profile of the SPIRE iFTS was derived from raster observations of Neptune and Uranus which are described in detail in the paper in Appendix A. The observations were processed as described in the following section.

## 3.3 Data reduction

The Neptune and Uranus raster observations were processed using the Herschel Interactive Processing Environment (HIPE) data pipeline version 7 (Ott, 2010)[1]. A complete description of the SPIRE spectrometer pipeline is provided by Fulton et al. (2013). A block diagram of the SPIRE iFTS data processing pipeline is shown in Figure 3.1. It contains processing modules commonly used to process iFTS data, such as phase correction and Fourier transformation.

The Level-0 product contains raw telemetry data as measured by the instrument. The data are organized into the spectrometer detector timeline (SDT), spectrometer mechanism timeline (SMECT), the nominal housekeeping timeline (NHKT) and the SPIRE pointing product (SPP). Modules common to the Photometer and Spectrometer are applied to the data to yield Level-0.5 products. These initial processing steps convert the raw samples for all the spectrometer detectors into root mean square (RMS) voltage timelines and store them into the Level-0.5 SDT product.

[1] HIPE is a joint development by the Herschel Science Ground Segment Consortium, consisting of European Space Agency (ESA), the National Aeronautics and Space Administration (NASA) Herschel Science Center, and the Heterodyne Instrument for the Far Infrared (HIFI), SPIRE and SPIRE consortia.

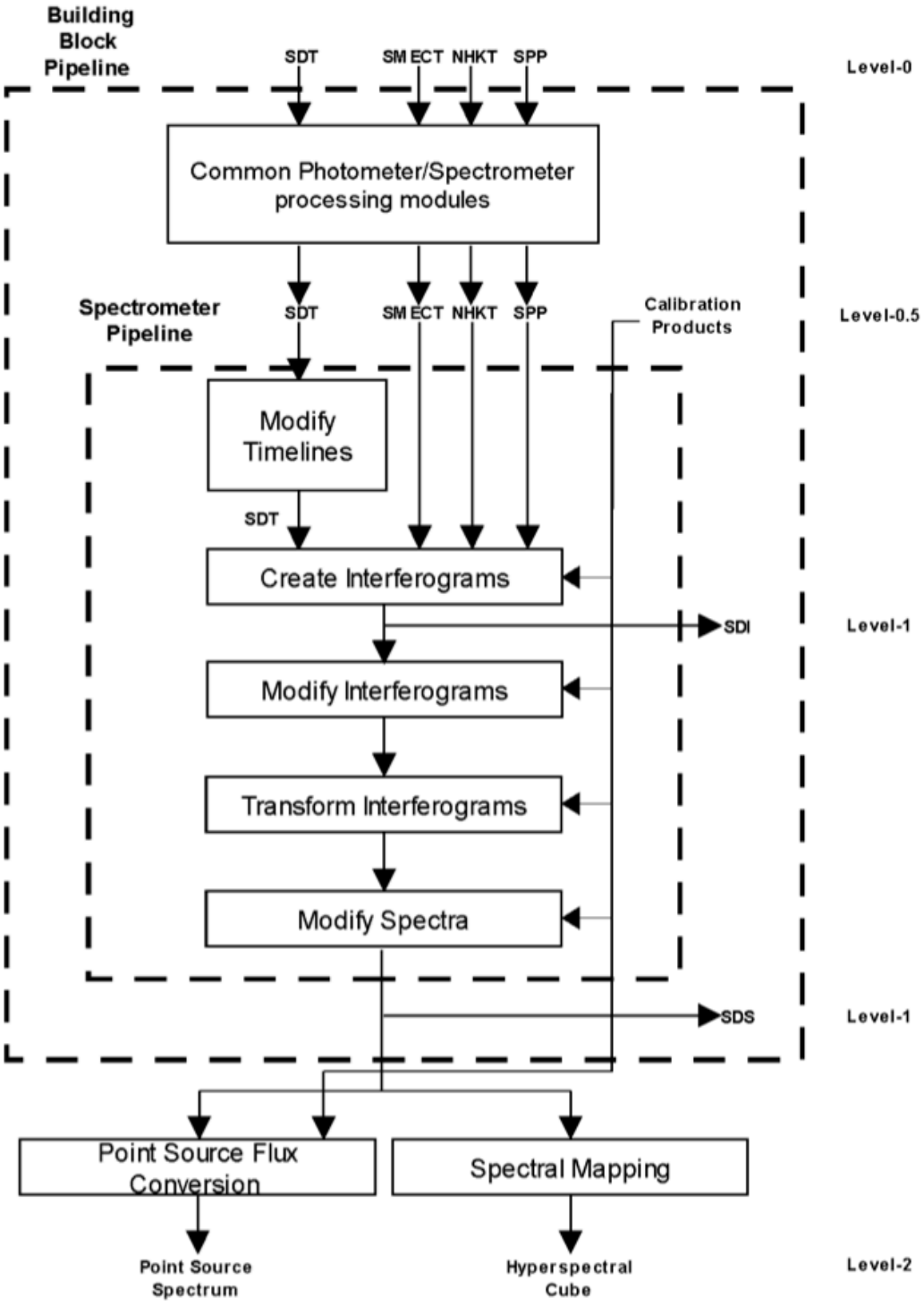


Figure 3.1: The SPIRE iFTS data processing block diagram obtained from Fulton et al. (2013).

The Modify Timelines portion of the the SPIRE Spectrometer building block pipeline performs time domain operations on the spectrometer detector samples. The first operation is first level deglitching where glitches due to cosmic ray hits and other impulse-like events are removed. Processes such as detector non-linearity correction, clipping correction and time domain phase correction are applied in this portion of the pipeline. The pipeline then uses the SMECT, NHKT, SPP and calibration products to create interferograms which are available as Level-1 products. The interferograms are then transformed into spectra which are also saved as Level-1 products. This stage involves using an extended source for which the low emissivity *Herschel* primary mirror provides a reference point. The spectral intensities are converted from quantities with units of Volts/GHz to brightness quantities with units of $\mathrm{Wm^{-2}Hz^{-1}sr^{-1}}$ appropriate for sources uniformly extended in the beam.

The final stages of the processing involve converting the Level-1 spectra into a set of Level-2 spectral products depending on the type of observation. The Level-2 products for all raster and jiggle mapping observations are spectral data cubes with two regularly spaced spatial dimensions and one spectral dimension per pixel in units of $\mathrm{Wm^{-2}Hz^{-1}sr^{-1}}$. The Level-2 products for single pointing sparse sampling observations are point source spectra for the two central detectors (SLWC3 and SSWD4) in units of Jy (1 Jy = $10^{-26}$ $\mathrm{Wm^{-2}Hz^{-1}}$). Converting from $\mathrm{Wm^{-2}Hz^{-1}sr^{-1}}$ to Jy is achieved by applying point source calibration products derived using Uranus observations and models.

Since the raster and cross-scan observations of Neptune and Uranus used in the derivation of the SPIRE iFTS beam profiles were obtained in a special engineering mode where the spacecraft pointing (rather than the beam steering mirror position) was varied to

obtain a map, the data required specialized processing, in which, in addition to all of the processes described above the motion of the planet needs to be taken into account and no gridding was applied to the data.

## 3.4 Point and extended source calibration of the SPIRE iFTS

The processing of the SPIRE iFTS observations has been described in Section 3.3. This section will present how the flux calibration of extended and point sources observed with the SPIRE iFTS is achieved. This is described in detail by Fulton et al. (2013), Wu et al. (2013) and Swinyard et al. (2014).

### 3.4.1 Extended-source calibration

Extended-source calibration is suitable only for uniformly extended sources, those where the solid angle of the source light distribution profile, $\Omega_{\rm source}$, is much larger than that of the SPIRE iFTS beam, $\Omega_{\rm beam}$, at a particular frequency. It is based on observations of a dark region of the sky, i.e. where the detectors are only receiving thermal radiation from the Herschel telescope and SPIRE instrument. The calibration uses models of the telescope and instrument emission constructed using onboard temperature sensors and the telescope mirror emissivity as measured on the ground (Fischer et al., 2004). The relative spectral response function (RSRF) of the telescope $R_{\rm tel}$ is defined as

$$R_{\rm tel} = \frac{(V_{\rm dark} - M_{\rm inst} R_{\rm inst})}{M_{\rm tel}} \quad \left[\frac{\rm V\,GHz^{-1}}{\rm W\ m^{-2}\ sr^{-1}\ Hz^{-1}}\right] \tag{3.1}$$

where $V_{\rm dark}$ (in V GHz$^{-1}$) is the voltage density when observing the dark sky, $R_{\rm inst}$ is the RSRF of the instrument, $M_{\rm tel}$ and $M_{\rm inst}$ (both in Wm$^{-2}$Hz$^{-1}$sr$^{-1}$) are the intensities from

the telescope and instrument calculated based on measured temperatures. $R_{\rm tel}$ is used to convert the observed source voltage density, $V_{\rm obs}$ (in V GHz$^{-1}$) to surface brightness $I_{\rm ext}$.

$$I_{\rm ext} = \frac{(V_{\rm obs} - M_{\rm inst} R_{\rm inst})}{R_{\rm tel}} - M_{\rm tel} \quad [\mathrm{W\ m^{-2}\ sr^{-1}\ Hz^{-1}}] \tag{3.2}$$

### 3.4.2 Point-source calibration

Point source calibration is only suitable when the observed source is point-like. It uses the point-source calibration factor, $C_{\rm point}$, in steradians (sr),

$$C_{\rm point} = \frac{M_{\rm uranus}}{I_{\rm uranus}} \quad [\mathrm{sr}], \tag{3.3}$$

to convert $I_{\rm ext}$ into flux density, $F_{\rm point}$

$$F_{\rm point} = I_{\rm ext}\ C_{\rm point} \quad \mathrm{Jy}], \tag{3.4}$$

where $M_{\rm uranus}$ is the modelled flux density spectrum of Uranus. $I_{\rm uranus}$ is the Level-1 data from the SPIRE observation of Uranus.

## 3.5 Point spread functions

A uniformly illuminated circular aperture produces a diffraction pattern with a bright spot at the centre and concentric rings. The diffraction pattern, characterized by the size of the aperture and the wavelength of the electromagnetic radiation illuminating the circular aperture is called an Airy pattern. The peak of the Airy rings falls rather slowly to zero with increasing distance from the centre. In order to describe the spotsize, a

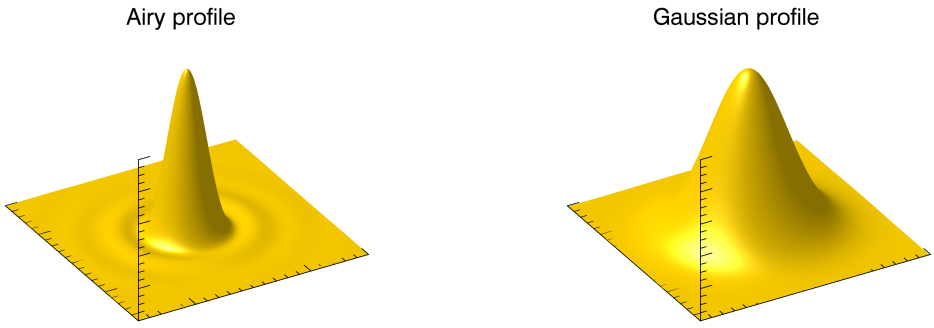


Figure 3.2: 2-D Airy and Gaussian profiles. The Airy profile was generated using an aperture of diameter 3.0 m and at a wavelength of 667 $\mu$m. The Gaussian profile has a FWHM of 30″.

commonly used method is to ignore the relatively small outer rings of the Airy pattern and approximate the central lobe with a Gaussian profile. Using Gaussian profiles enables more detailed analysis such as deconvolution techniques to be applied in a more robust fashion. Another advantage of approximating the beam as Gaussian is that detectors of narrowband instruments that operate in the far-infrared and at radio wavelengths employ single-mode feed-horns whose fundamental mode is Gaussian. Figure 3.2 shows the structure of both Airy and Gaussian profiles.

Multi-moded feed-horns used with broadband instruments have complex beam shapes. Their beam profiles are sometimes represented by Hermite-Gaussian beam profiles (Martin & Bowen, 1993). In order to derive the beam profile for the SPIRE iFTS the measured data were first fitted with Airy and Gaussian PSFs. However, it has been known that the beam is neither Gaussian nor Airy because of the complex nature of the SPIRE

iFTS optical system. We then used Hermite-Gaussian PSFs to describe the beam as stated in our paper. Brief descriptions of Airy and Gaussian PSFs that we used are provided below. Hermite-Gaussian PSF are described in our paper.

### 3.5.1 Airy function

Telescopes have a circular aperture. The resultant intensity, $I(\theta)$, due to diffraction of radiation from a circular aperture of radius, $a$, is given by

$$\frac{I(\theta)}{I(0)} = \left[\frac{2J_1(ka\sin\theta)}{ka\sin\theta}\right]^2, \tag{3.5}$$

where $J_1$ is the Bessel function of the first kind of order one, $k = 2\pi/\lambda$ is the propagation number and $\theta$ is the angle between the axis of the circular aperture and the line from the centre of aperture to point $(x,y)$ on the detector plane. Equation (3.5) is called an Airy function. In order to facilitate the fitting of the Airy function to measured data, Equation (3.5) are expressed in a suitable form as described below. The first minimum for Airy profiles occurs at $\sim 1.22\lambda/D$ ($=1.22\lambda/2a$) where $D$ is the diameter of the aperture. Using the small angle approximation, Equation (3.5) becomes

$$\frac{I(\theta)}{I(0)} = \left[\frac{2J_1(ka\theta)}{ka\theta}\right]^2, \tag{3.6}$$

The half maximum for the central Airy disc, the point where

$$\left[\frac{J_1(ka\theta)}{ka\theta}\right]^2 = \frac{1}{8}, \tag{3.7}$$

occurs when $ka\theta = 1.61633$. The Full Width Half Maximum (FWHM) is therefore given by

$$\frac{2\pi}{\lambda}a\theta_{FWHM} = 2 \times 1.61633. \tag{3.8}$$

Substituting $2 \times 1.61633/\theta_{FWHM}$ for $ka$ and rearranging Equation (3.6) we obtain

$$\frac{I(\theta_{\rm Y},\theta_{\rm Z})}{I(\theta_{\rm Y0},\theta_{\rm Z0})} = \left[ \frac{2J_1\left(3.232660\sqrt{\left(\frac{\theta_{\rm Y}-\theta_{\rm Y0}}{\theta_{\rm FWHM,Y}}\right)^2+\left(\frac{\theta_{\rm Z}-\theta_{\rm Z0}}{\theta_{\rm FWHM,Z}}\right)^2}\right)}{\left(3.232660\sqrt{\left(\frac{\theta_{\rm Y}-\theta_{\rm Y0}}{\theta_{\rm FWHM,Y}}\right)^2+\left(\frac{\theta_{\rm Z}-\theta_{\rm Z0}}{\theta_{\rm FWHM,Z}}\right)^2}\right)} \right]^2 , \tag{3.9}$$

where ($\theta_{\rm Y0}$,$\theta_{\rm Z0}$) and ($\theta_{\rm Y}$,$\theta_{\rm Z}$) are the position of Neptune and any other position on the detector plane respectively. Equation (3.9) is in the appropriate form for use in minimization procedures.

### 3.5.2 Gaussian function

Paraxial waves - waves whose wavefront normals make small angles with the optical axis - must satisfy the paraxial Helmholtz equation:

$$\nabla_T^2 A - j2k\frac{\partial A}{\partial z} = 0, \tag{3.10}$$

where $\nabla_T^2 = \partial^2/\partial x^2 + \partial^2/\partial y^2 + \partial^2/\partial z^2$ is the Laplacian operator and $A(r)$ is the complex envelope of the wave. $r = \sqrt{x^2+y^2}$ is the radial distance from the direction of propagation (the $z$ axis).

One of the most important solutions of the paraxial Helmholtz equation is the Gaussian beam which is described by the function,

$$\frac{I(x,y)}{I(x_0,y_0)} = \exp\left(-\left[\frac{(x-x_0)^2}{2\sigma_x^2}+\frac{(y-y_0)^2}{2\sigma_y^2}\right]\right), \tag{3.11}$$

where $I(x,y)$ and $I(x_0,y_0)$ are the intensity values at points $(x,y)$ and $(x_0,y_0)$ respectively. $(x_0,y_0)$ is the point at which the intensity peak occurs. $\sigma_x$ and $\sigma_y$ are related to the Full Width Half maximum as $FWHM = 2\sqrt{2\ln 2}\sigma$. The PSFs represented by Equations (3.9)

and (3.11) should be normalized such that:

$$A \int\int \frac{I(x,y)}{I(x_0,y_0)} dxdy = \int\int \Psi(x,y) dxdy = 1, \tag{3.12}$$

where $A$ is a normalizing factor and $\Psi(x,y)$ is the normalized PSF.

## 3.6 Minimization

To derive the SPIRE beam profile at each wavelength, the procedure started with an assumed analytical function and performed minimization of the residuals until the best fit was obtained. An Interactive Data Language (IDL) programming script, which uses the Levenberg-Markwardt algorithm to solve least squares problems (Markwardt, 2009), was developed. The first step in the fitting process is to read the 3-D data cubes (2 spatial and 1 spectral dimensions) into IDL. The flux values and their errors were calculated using HIPE as described in Section 3.3. The IDL script then fits the functions described in Section 3.5 while comparing the resulting reduced $\chi^2$ ($\chi^2_R$) values. For the case of Hermite-Gaussian functions we started by fitting the first six modes. The solution that gave lowest $\chi^2_R$ with the fewest number of beam mode terms was selected. The results are presented in the following section.

## 3.7 Results

Since the SPIRE iFTS detectors are feed-horn coupled and the feed-horns are multi-moded, it was decided that the PSFs that would best represent the iFTS beam were the Hermite-Gaussian functions. As is expected, the results from fitting Hermite-Gaussian

PSFs to the data agree very well with those from fitting a pure Gaussian in wavelength regions where the feed horns are expected to be single moded. The results obtained from fitting Hermite-Gaussian functions are described in detail in our paper (Appendix A). The results are presented such that one can reconstruct the wavelength dependent SPIRE iFTS beam. Figure 3.3 shows the results of the fitting performed at 317.5 $\mu$m (944 GHz). At this wavelength, the fitting returned a $\chi^2_R$ of 0.7. The analysis showed that there is no significant improvement in the $\chi^2_R$ from including terms higher than the zeroeth order function (i.e. pure Gaussian) for the spectrometer short wavelength (SSW) band. In contrast, the spectrometer long wavelength (SLW) band requires the first three radially symmetric basis functions.

Generally, the errors from fitting the SLW data are larger than for the SSW data. This is due to the additional higher order terms being fitted. The errors from the fitting of the waist radius are less than 2 % whilst the errors for the coefficients, $c_n$ increase with $n$ up to 20 % for certain wavelengths. This increase in uncertainty arises when the power assigned to higher order terms in the fitting process becomes comparable to the noise level in the data.

Figure 3.4 shows the FWHM (solid curve) determined from the reconstructed composite beam compared to that expected from diffraction theory (dashed line). The long-wavelength end of each SPIRE iFTS band agrees well with diffraction theory as expected since the beam is single-moded in these regions and this approximates well to a Gaussian. However, the beam shows an increasing deviation from diffraction theory as the number of modes increases. The fitting was also applied to a few selected off-centre detectors. The results show that all of the well characterized detectors exhibit a similar mode structure

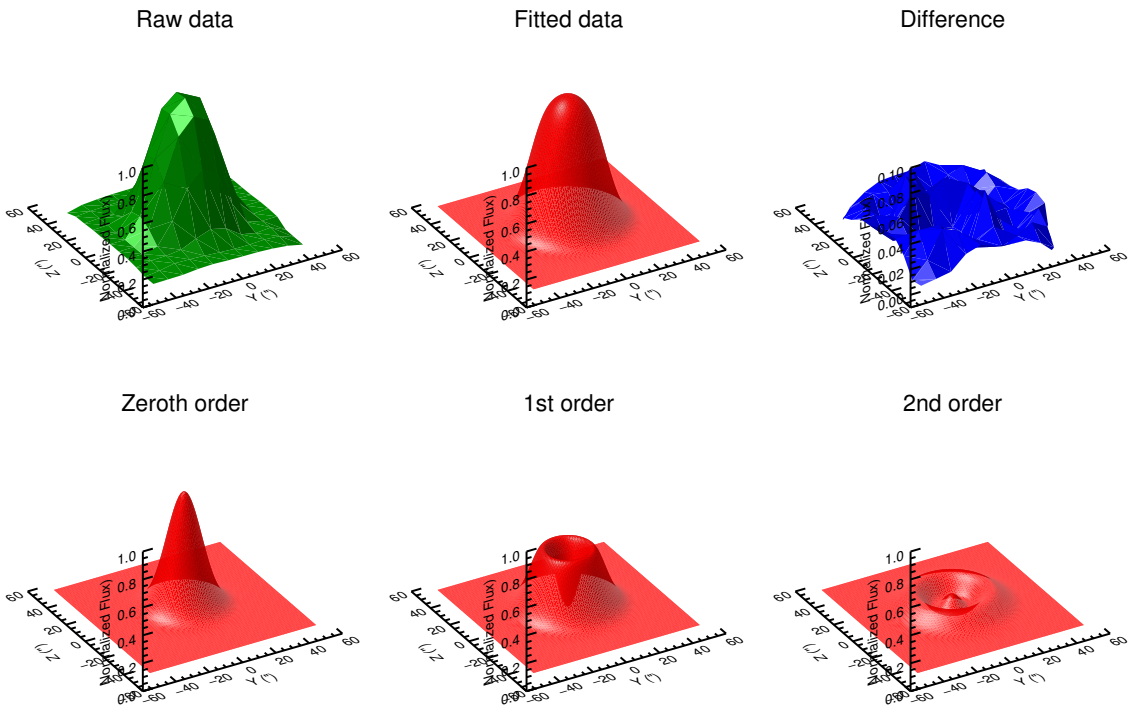


Figure 3.3: Surface plots obtained from fitting Neptune data at 317.5 $\mu$m (944 GHz), the short wavelength end of the SSW band. The top row shows the raw data (left), fitted data (center) and the difference (right). The bottom row shows a decomposition of the fitted data (top center) into the first three modes. See Appendix A for further details.

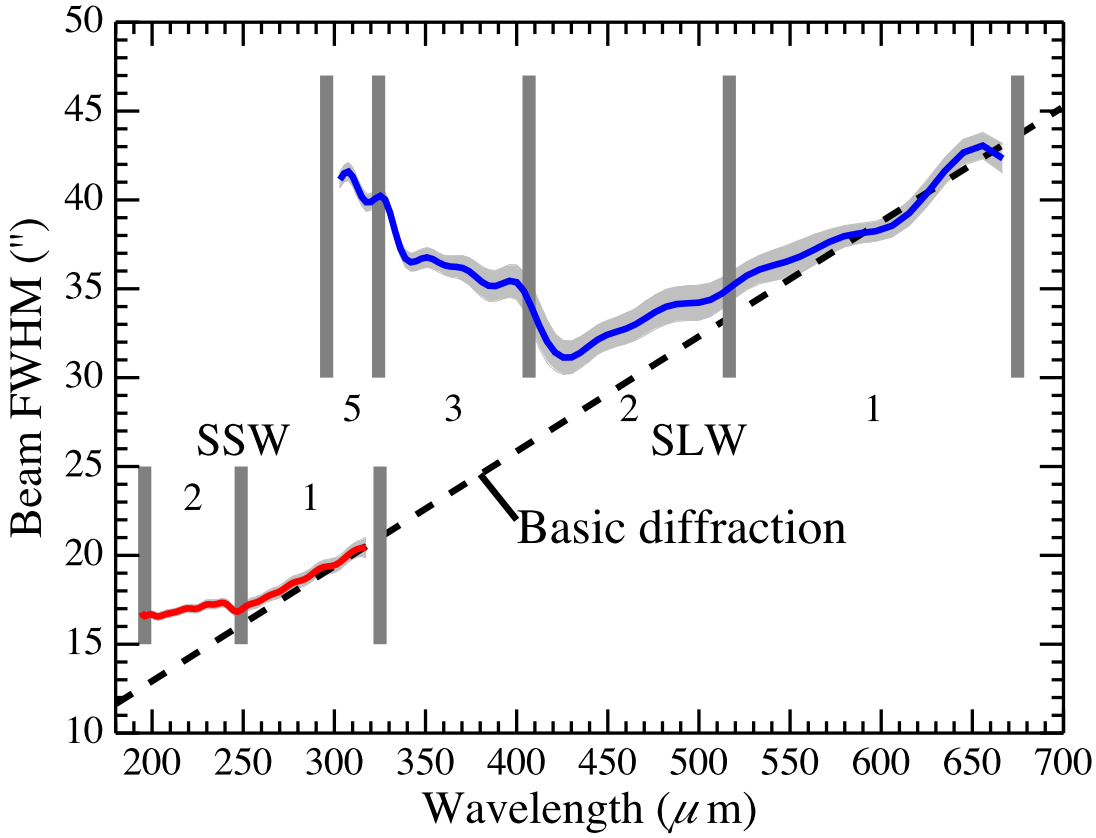


Figure 3.4: The measured FWHM of the central detectors (SLWC3 and SSWD4) compared with diffraction theory. The gray band represents the $3\sigma$ errors in the measured FWHM. The thick vertical lines indicate the cut-on wavelengths for the different feed-horn modes. The expected number of modes present in these regions are also indicated. See Appendix A for further details.

allowing a mean profile to be adopted.

## 3.8 Conclusions

Flux calibration is one of the most important steps in astronomical data analysis. The measured spectra are impacted by the wavelength dependent beam profile and the source extent. In this Chapter we describe the steps followed in the determination of the SPIRE iFTS beam profile. Because the SPIRE iFTS optical components are undersized and the detectors are feed-horn-coupled, the beam profile exhibits a complex dependence on wavelength as the multi-moded feed-horns allow different modes to be enabled at certain wavelengths in the SPIRE iFTS band. All of the well characterized detectors exhibit the same mode structure. In order to simplify the analysis of mapping observations the beam profiles for the centre detectors have been taken as representative of the rest of the detectors.

While allowing for six basis functions, we conclude that the SSW band is best represented by a Gaussian beam which is well behaved in deconvolution applications, whereas the SLW band is more complex with at least three terms identified. The final number of terms was determined after comparing the rms values of the residuals of the fit. Tables of the final wavelength dependent beam parameters are provided in the paper in Appendix A. These profiles have now been adopted by the SPIRE team and have been incorporated in the HIPE processing pipeline.

# Chapter 4

# Applications of the beam profile

## 4.1 Overview

Astronomical objects have varying sizes and shapes. This makes it difficult to design a single data reduction and calibration scheme that can be applied to observations of all astronomical objects. The standard data reduction pipeline for the Spectral and Photometric Imaging Receiver Array (SPIRE) imaging Fourier transform spectrometer (iFTS) was designed to work for two extreme cases of objects: those whose spatial extent is much smaller than the smallest beam and those whose spatial extent is larger than the largest beam. Neither of the calibration schemes is suitable for sources whose spatial extent falls in between the two extremes. In this chapter, the use of the SPIRE iFTS beam profile in correcting spectra for "semi-extended sources" is discussed. A tool developed to carry out this correction has been presented by Wu et al. (2013). Following the introduction in Section 4.2, Section 4.3 discusses the derivation for the correction required for sparsely sampled observations of sources whose spatial extent is neither point-like nor extended. The

importance of the beam profile in the comparison of mapping observations obtained with different instruments is discussed in Section 4.4.1.

## 4.2 Introduction

Accurate calibration of astronomical observations is crucial in the correct interpretation of the respective data. It is therefore common practise to calibrate astronomical observations using sources whose flux densities are well known, or can be well modelled. For the *Herschel Space Observatory* (*Herschel*), brighter point-like sources like Neptune and Uranus are used for this purpose. Calibrating extended sources requires regions in space with uniform flux density distributions and much larger than the instrument beam size. No such sources exist and so *Herschel* uses the telescope itself as a calibrator. Calibration schemes derived this way are limited to those sources with the same spatial extent as the standards. In order to calibrate sources whose spatial extent falls within the extremes mentioned above, knowledge of the SPIRE iFTS beam and the spatial intensity distribution of each source are required. The aim is to calculate beam filling factors which are then used to scale up point-source calibrated flux densities (in Jy) or scale down extended-source calibrated brightness values (in W $m^{-2}$ $Hz^{-1}$ $sr^{-1}$). From here onwards sources that are neither point-like nor extended will be referred to as "semi-extended sources".

One of the challenges with astronomical sources is that they have different shapes and structure and so their flux density distributions within a representative source diameter is not uniform. The "SemiExtendedCorrector" tool in the Herschel Interactive Processing

Environment (HIPE)[1] uses an empirical correction factor required to fix the gap in the overlap region between the spectrometer short wavelength (SSW) and spectrometer long wavelength (SLW) bands to estimate the true source size. In order to do this, the tool uses the SPIRE iFTS beam profiles derived in Chapter 3. Currently the tool can only be used to correct point-source calibrated spectra of semi-extended sources.

## 4.3 Correction for semi-extended source distribution in sparse sampled observations

A large gap and a difference in slope between the SSW and SLW spectra in the overlap region is an indicator that the observation has not correctly taken into account the source size. This is a result of the fact that the beam size for the SLW detectors is almost twice as large as that for the SSW detectors in the overlap region. Figure 4.1 shows the impact of assuming extended- and point-source calibration for an instrument similar to the SPIRE iFTS when viewing a greybody of temperature 15 K and dust emissivity index of 1.45 and where the source size is 50″ (top row), 25″ (centre row) and 15″ (bottom row), respectively. To simplify the problem, it is assumed that the instrument has a constant beam size of 19″ in the SSW and 35″ in the SLW bands, respectively. In each case, the left column shows the brightness expected from the greybody. The middle column shows the spectra produced when using extended-source calibration. The right-most column shows the spectra produced when using point-source calibration.

[1] HIPE is a joint development by the Herschel Science Ground Segment Consortium, consisting of European Space Agency (ESA), the National Aeronautics and Space Administration (NASA) Herschel Science Center, and the Heterodyne Instrument for the Far Infrared (HIFI), SPIRE and SPIRE consortia.

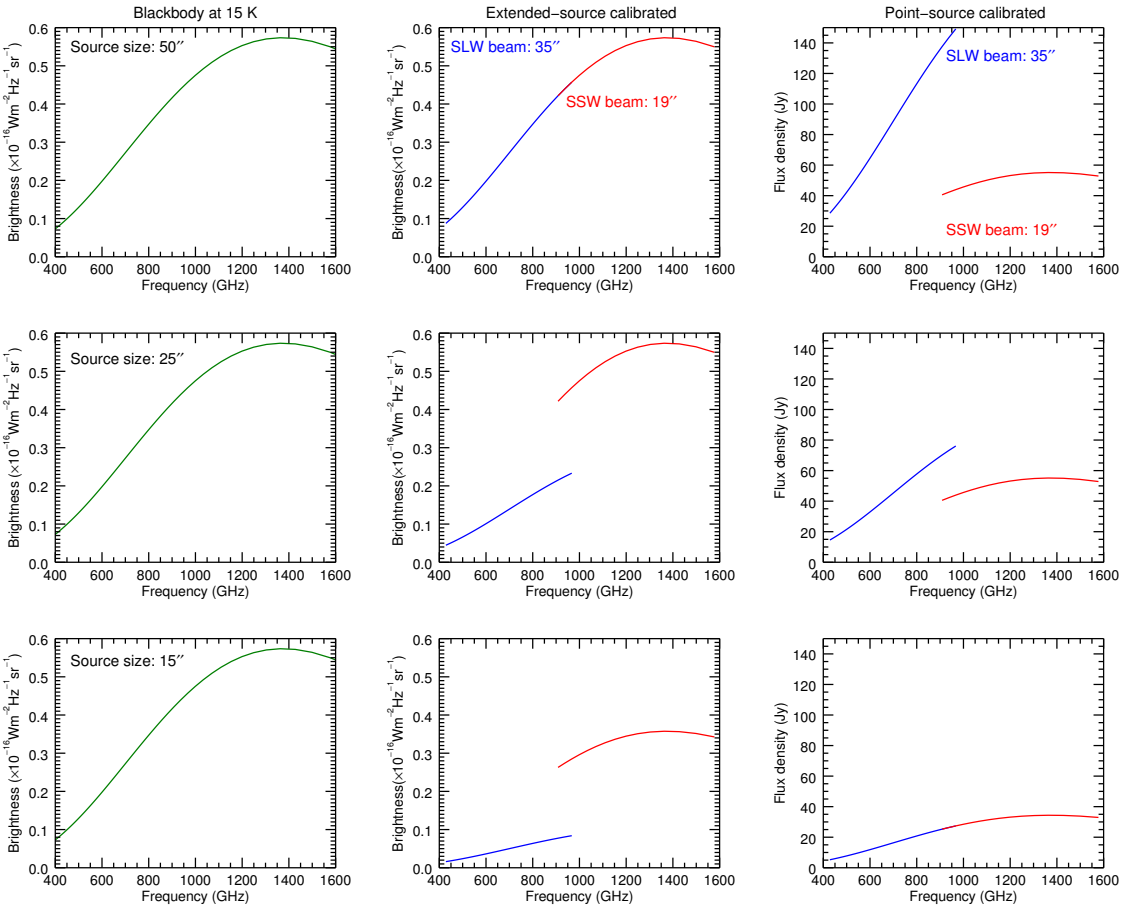


Figure 4.1: The impact of assuming extended- and point-source calibration for an instrument similar to the SPIRE iFTS when viewing a greybody of temperature 15 K and dust emissivity index of 1.45 and where the source size is 50″ (top row), 25″ (centre row) and 15″ (bottom row), respectively. It is assumed that the instrument has a constant beam size of 19″ in the SSW and 35″ in the SLW bands, respectively. See text for a description of the figures.

In the top row, the source size is 50″, which is bigger than the beam sizes for both the SSW and SLW. Since in this case the source will appear extended to both beams, it is appropriate to use the extended source calibration which yields the continuous spectrum as is shown in the top centre figure. However, if the point source calibration was used it would lead to a large gap in the overlap region as shown in the top right figure.

In the centre row, the source size is 25″, which is bigger than the beam size for SSW but smaller than that for SLW. Since in this case the source is extended to SSW and point-like to SLW, it is appropriate to use extended source calibration for SSW and point-source calibration for SLW. In the centre figure, the spectrum shown in red is correct, while the blue spectrum is not. In the right figure, the blue spectrum is correct while the red one is not.

In the bottom row, a source size of 15″ has been assumed. This is smaller than both the SSW and SLW beams. The source appears as a point source to both SSW and SLW and so applying extended-source calibration (centre figure) is not appropriate for both bands. As is expected, applying point-source calibration (bottom right figure) results in a continuous spectrum.

Figure 4.1 shows that important information on the source size is conveyed by studying the overlap region between the SSW and SLW bands. The gap is large when an observation of an extended source is point-source calibrated (top right figure). In this case the larger SLW beam measures more flux than the smaller SSW beam. The gap is smaller for a source size that is extended in the SSW band but point-like in the SLW band (right figure in the centre row). Applying extended-source calibration to an observation of a source

that is extended in the SSW band but point-like in the SLW band (centre figure in the center row) results in a gap where the SLW spectrum is lower than the SSW spectrum.

To illustrate the impact of this on SPIRE iFTS observations of astronomical sources, Figure 4.2 shows measured spectra of three sources of increasing sizes processed with both the extended- and point-source calibration. Figure 4.2 (a) and (d) show the spectra for CRL 618, a point source. CRL 618 is a carbon-rich bipolar Proto-Planetary Nebula (PPN) found at a distance $d = 0.9$ kpc (Tafoya et al., 2013). Applying point-source calibration to the CRL 618 observation produces a reasonable match between the SSW and SLW spectra while applying extended-source calibration leads to a gap and a difference in slope in the overlap region between the SSW and SLW spectra (see bottom row of Figure 4.1). Since the source is point-like, division of the observed flux densities by the beam solid angle leads to larger brightness values for the SSW band than that for the SLW band.

Figure 4.2(c) and (f) show the spectra for the Orion Bar, an extended source. Orion is a nearby ($d \sim 414$ pc) Giant Molecular Cloud (GMC) active in star formation (Draine, 2010). A reasonable match between the SSW and SLW spectra for Orion is obtained by applying extended-source calibration while applying point-source calibration leads to lower flux densities for the SSW band where the beam is smaller (see top row of Figure 4.1). The measured flux densities are directly proportional to the size of the beam. Figure 4.2(b) and (e) show the spectra for M83, a semi-extended source. M83 is a barred spiral galaxy found at a distance $d \sim 4.5$ Mpc (Thim et al., 2003). Neither of the two calibration schemes work for M83 (see centre row of Figure 4.1).

In order to recover the flux density that reached the bolometers, it is necessary to

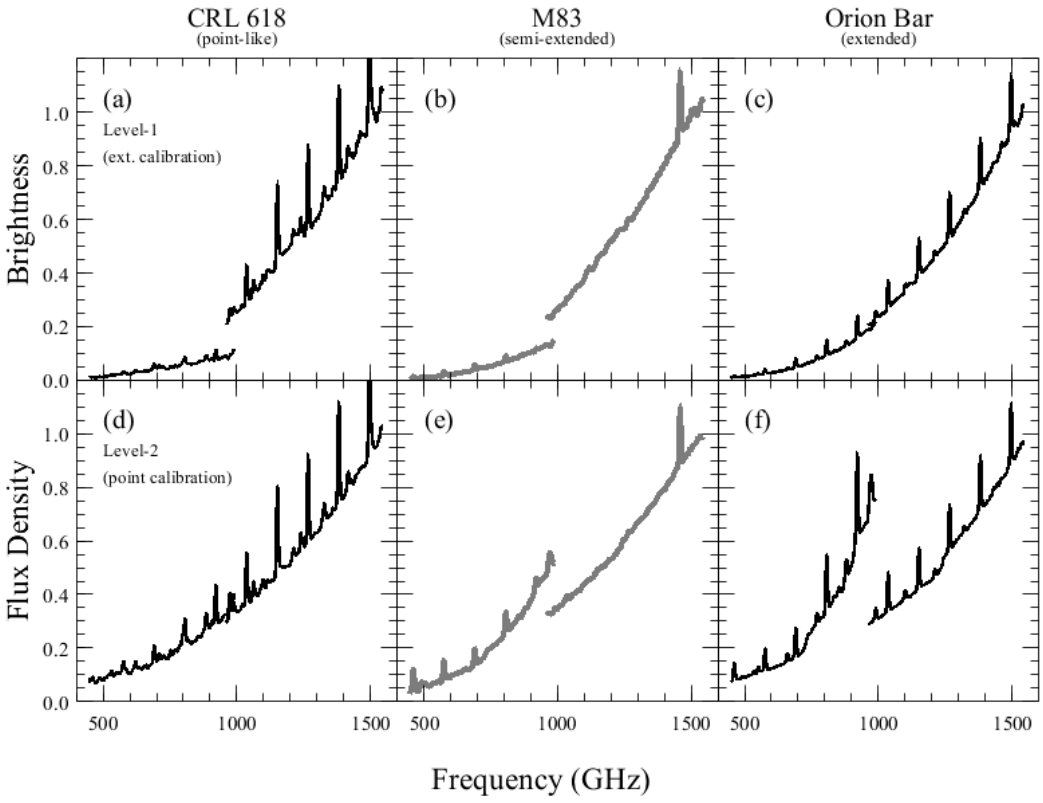


Figure 4.2: Spectra from sources with increasing source size (left to right: CRL 618, M83 and Orion bar). Top row: spectra processed with the extended-source calibration. Bottom row: spectra processed with the point-source calibration. The flux density and brightness are in normalized units. Figure taken from Wu et al. (2013).

calculate a conversion factor, $C_{\rm s}$, similar to $C_{\rm point}$ in Equation 3.3. $C_{\rm s}$ can be expressed as (Wu et al., 2013)

$$C_{\rm s} = \frac{M_{\rm s}}{I_{\rm ext}} \quad [\rm sr], \tag{4.1}$$

where $M_{\rm s}$ is the true integrated flux density of the source and $I_{\rm ext}$ is the surface brightness in W m$^{-2}$ Hz$^{-1}$ sr$^{-1}$. The flux density (in Jy) for the semi-extended source, $F_{\rm s}$ can then be obtained from

$$F_{\rm s} = F_{\rm point}\frac{C_{\rm s}}{C_{\rm point}} \quad [\rm Jy], \tag{4.2}$$

In order to calculate $C_{\rm s}$, knowledge of the beam profile, $\Psi_\nu(\theta,\phi)$, is required. We also need to assume a dimensionless source light distribution, $S_\nu(\theta,\phi)$. These two quantities are related to the solid angles of the source, $\Omega_{\rm source}$, and of the beam, $\Omega_{\rm beam}$, by

$$\Omega_{\rm beam}(\nu) = \iint\limits_{2\pi} \Psi_\nu(\theta,\phi)d\Omega \quad [\rm sr], \tag{4.3}$$

$$\Omega_{\rm source}(\nu) = \iint\limits_{2\pi} S_\nu(\theta,\phi)d\Omega \quad [\rm sr], \tag{4.4}$$

where spherical polar cordinates ($\theta$,$\phi$) have been used to denote positions in a small region of the sky. $M_{\rm s}$ is related to $S_\nu(\theta,\phi)$ by

$$M_{\rm s} = M_0 \iint\limits_{\rm beam} S_\nu(\theta,\phi)d\Omega = M_0\Omega_{\rm source}(\nu) \quad [\rm Jy], \tag{4.5}$$

where $M_0$ (in MJy sr$^{-1}$) is the average surface brightness of the source. An illustration of how the signal from a source, $M_{\rm s}$, is changed by the telescope and by the instruments using the telescope beam before reaching the bolometers is shown in Figure 4.3 (Wu et al., 2013). $\eta_{\rm f}$, the efficiency with which the source couples to the telescope is defined as (Ulich & Haas,

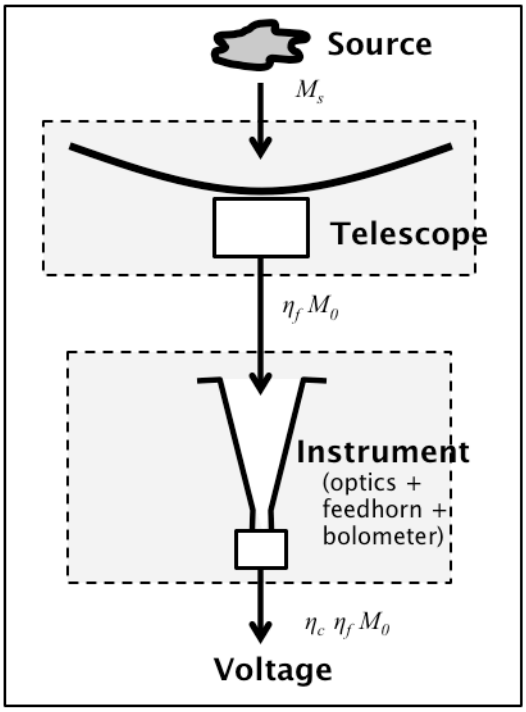


Figure 4.3: Illustration of how the signal from the source is changed by the telescope and by instruments using the telescope beam before reaching the bolometers. Figure taken from (Wu et al., 2013).

1976; Kutner & Ulich, 1981):

$$\eta_{\rm f}(\nu,\Omega_{\rm source}) = \frac{\iint\limits_{2\pi} \Psi_\nu(\theta-\theta_0,\phi-\phi_0)S_\nu(\theta,\phi)d\Omega}{\iint\limits_{2\pi} \Psi_\nu(\theta,\phi)d\Omega}, \tag{4.6}$$

where ($\theta_0$,$\phi_0$) is the position of the centre of the beam on the sky. $\eta_{\rm c}$ is an empirically derived factor introduced to take into account additional effects that Equation (4.6) does not take into account. One such effect is the unknown coupling of the beam profiles to the source distribution. For a point-source, $\eta_{\rm c}(\nu,\Omega_{\rm point}) = 1$. Treating the total source and beam separately, we can express $I_{\rm ext}$ as[2].

$$I_{\rm ext} = M_0 \frac{\eta_{\rm c}(\nu,\Omega_{\rm beam})}{\eta_{\rm c}(\nu,\Omega_{\rm source})}\eta_{\rm f}(\nu,\Omega_{\rm source}) \qquad [\rm W\ m^{-2}\ Hz^{-1}\ sr^{-1}], \tag{4.7}$$

Equation (4.1) can be written as

$$C_{\rm s} = \frac{M_0}{I_{\rm ext}}\Omega_{\rm source} = \frac{\eta_{\rm c}(\nu,\Omega_{\rm source})}{\eta_{\rm c}(\nu,\Omega_{\rm beam})}\frac{\Omega_{\rm source}}{\eta_{\rm f}(\nu,\Omega_{\rm source})} \qquad [\rm sr], \tag{4.8}$$

It can be shown that Equation (4.8) can be reduced to

$$C_{\rm ext} = \Omega_{\rm source} \qquad [\rm sr], \tag{4.9}$$

and

$$C_{\rm point} = \frac{\Omega_{\rm beam}(\nu)}{\eta_{\rm c}(\nu,\Omega_{\rm beam})} \qquad [\rm sr], \tag{4.10}$$

for the case of extended- and point-like sources respectively. Now we can correct the spectra calibrated using either the extended- or point- source flux calibration using

$$F_{\rm s} = \begin{cases} I_{\rm ext}\dfrac{\eta_{\rm c}(\nu,\Omega_{\rm source})}{\eta_{\rm c}(\nu,\Omega_{\rm beam})}\dfrac{\Omega_{\rm source}}{\eta_{\rm f}(\nu,\Omega_{\rm source})} & [\rm Jy] \\ F_{\rm point}\eta_{\rm c}(\nu,\Omega_{\rm source})\dfrac{\Omega_{\rm source}}{\eta_{\rm f}(\nu,\Omega_{\rm source})\Omega_{\rm beam}} & [\rm Jy] \end{cases} \tag{4.11}$$

[2]The following logic is used. For a uniformly extended source, $I_{\rm ext} = \eta_{\rm c}\eta_{\rm f}M_0 = M_0$. Since $\eta_{\rm f}(\nu,\Omega_{\rm source})$ = 1 for extended sources, we must have $\eta_{\rm c} = \eta_{\rm c}(\nu,\Omega_{\rm beam})/\eta_{\rm c}(\nu,\Omega_{\rm source}) = 1$. If $\eta_{\rm c}(\nu,\Omega_{\rm source})$ is known, then the true source intensity of a source whose size is smaller than the beam can be calculated using Equation 4.7.

The "SemiExtendedCorrector" tool is based on Equation (4.11). Figure 4.4 shows the spectra for three starless cores that have been corrected using this tool. These sources are studied in detail in Chapter 5. The top and middle rows show plots for L1521E and L1521F respectively. The bottom row shows plots for L1689B. The left column shows the spectra for each source before and after correction with the "SemiExtendedCorrector" tool and the right column shows the correction required for each source.

Application of the "SemiExtendedCorrector" tool to point-source calibrated spectra for L1521E, L1521F and L1689B returned angular source sizes of 74″, 52″ and 33″, respectively. Since the SPIRE iFTS beam ranges from 16 – 20″ in the SSW band and from 31 – 43″ in the SLW band, the derived source sizes for the starless cores show that L1521E and L1521F are extended sources for both bands while L1689B is an extended source for the SSW band but a point source for the SLW band.

## 4.4 Comparing images observed with different PSFs

### 4.4.1 Mapping observations

SPIRE iFTS Mapping observations with either intermediate (1 beam spacing) or full (1/2 beam spacing) spatial sampling are processed using the "Spectrometer Mapping user pipeline". Full (Nyquist) sampling is achieved by moving the beam steering mirror in a 16-point jiggle pattern. The calibration of each jiggle position is carried out independently before the detector data are resampled onto regular spatial grids with pixel sizes of 9.5″ for SSW and 17.5″ for SLW. The World Coordinate System (WCS) for the two spectral data cubes are different. In order to perform combined analysis of the two data cubes, the pipeline

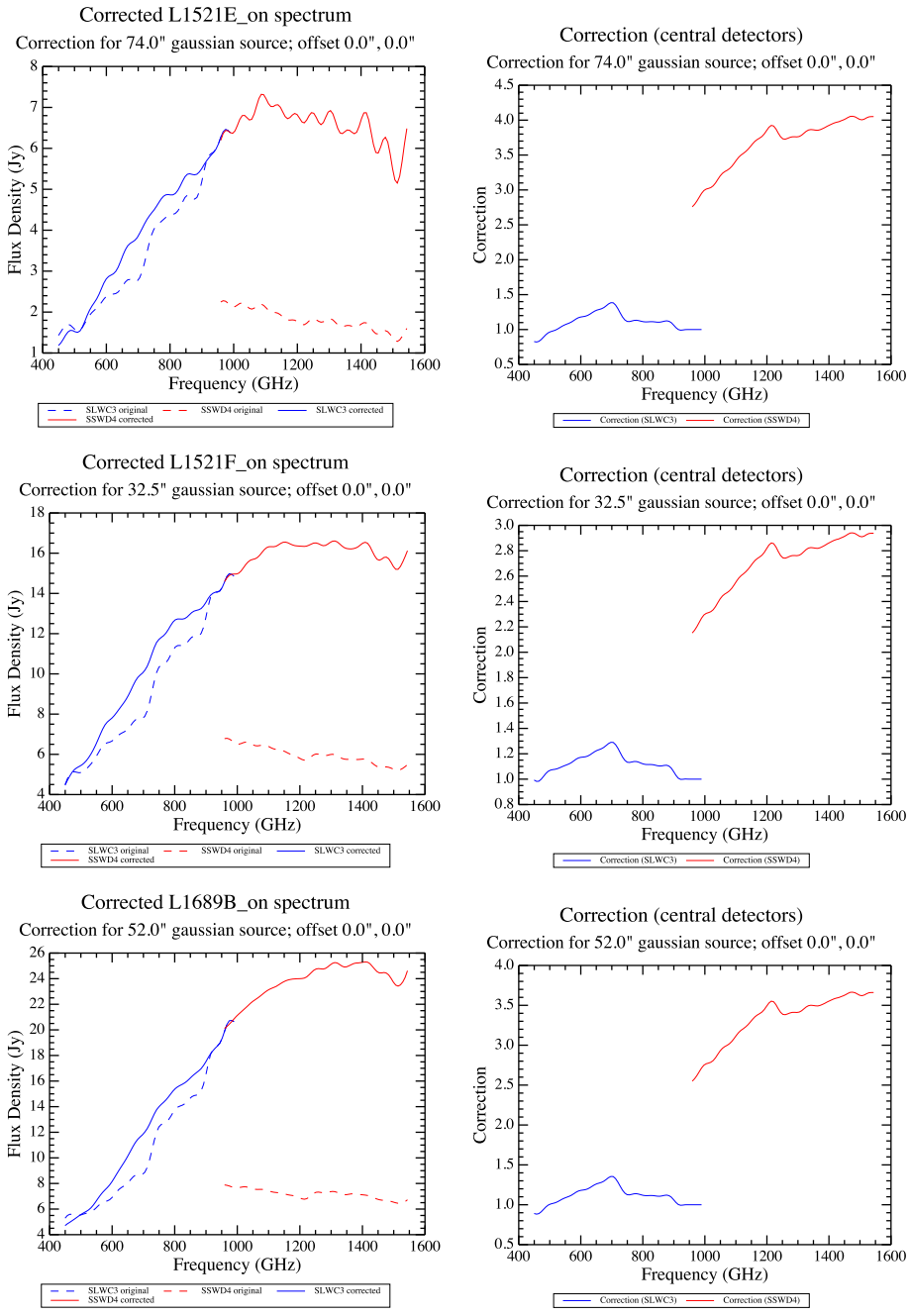


Figure 4.4: Left column: the point-source calibrated SPIRE FTS spectra for L1521E, L1521F and L1689B before (dashed lines) and after (solid lines) correction with the "SemiExtended-Corrector" tool. Right column: The wavelength dependent scaling factor required to fix the gap between the SSW and SLW spectra for each source. The angular source sizes returned by the the "SemiExtendedCorrector" tool is shown on the subtitle of each plot.

has to be adjusted so that the detector data for both SSW and SLW are transformed onto the same WCS and the pixel sizes are the same.

In Chapter 3, it was shown that the beam size of the SPIRE iFTS is wavelength dependent. This variation in beam size has to be taken into account when comparing the SSW and SLW data cubes. This is achieved using the "convolution projection task" in HIPE. The frequency dependent convolution kernel used by this task is Gaussian. While the Point spread function (PSF) for the SSW band is Gaussian, that for the SLW band is not. It consists of Hermite-Gaussian modes and so care must be taken when interpreting SPIRE iFTS maps convolved with the simple Gaussian.

### 4.4.2 Map convolution

Convolving spectral images obtained at different wavelengths to a common beam is necessary in the correct interpretation of the data. Convolution is also used when comparing images taken with different instruments having different PSFs. The process transforms images taken with instruments whose PSFs are smaller into a larger PSF. A brief discussion of the importance of map convolution is provided below. Interested readers are referred to a paper by Aniano et al. (2011) for a detailed discussion of the topic. The paper describes the generation of convolution kernels for the cameras (photometers) of various ground and space-based observatories.

As defined in Chapter 3, the PSF of an instrument, $\Psi(x, y, x', y')$, gives the measured intensity at $(x, y)$ produced by a point source with unit flux at the point $(x', y')$. The cartesian coordinates $(x, y)$ and $(x', y')$ represent the position of a small region of the sky

and source position respectively. This definition ensures that the PSF is normalized as

$$\int\int \Psi(x, y, x', y')dxdy = 1 \tag{4.12}$$

If the PSF is constant across the field of view (FOV) of the instrument, then $\Psi(x, y, x', y')$ $= \Psi(x - x', y - y') = \Psi$. The instrument measures an image $I(x, y)$ which is a convolution of the source $S(x, y)$ with the PSF:

$$I(x, y) = \int\int S(x', y')\Psi(x - x', y - y')dx'dy' = (S * \Psi)(x, y) \tag{4.13}$$

If the PSF of the instrument is wavelength dependent as is the case for the SPIRE iFTS, images of the same source observed at two different wavelengths, $\lambda_{\rm A}$ and $\lambda_{\rm B}$ cannot be compared to each other unless the image obtained with higher spatial resolution is degraded to match the spatial resolution of the other. Suppose the PSFs at $\lambda_{\rm A}$ and $\lambda_{\rm B}$ are $\psi_{\rm A}$ and $\psi_{\rm B}$ respectively. In order to transform the image observed at wavelength $\lambda_{\rm A}$ into an image corresponding to the PSF at $\lambda_{\rm B}$ the convolution kernel must be known. The convolution kernel $K_{AB}$ that transforms an image obtained at $\lambda_{\rm A}$ into an image corresponding to that observed at $\lambda_{\rm B}$ should satisfy:

$$I_B(x, y) = \int\int I_A(x', y')K_{AB}(x - x', y - y')dx'dy' = (I_A * K_{AB})(x, y) \tag{4.14}$$

where $I_A$ and $I_B$ are the images observed at $\lambda_{\rm A}$ and $\lambda_{\rm B}$ respectively. In the discussion above the instrument beam has been assumed to be radially symmetric. If the instrument beam is not radially symmetric then a different PSF is required for each orientation of the detector array.

Equation (4.14) can be written as

$$\Psi_B = (\Psi_A * K_{AB}) \tag{4.15}$$

Taking the 2-D Fourier transform of Equation (4.15) we obtain

$$\mathscr{F}(\Psi_B) = \mathscr{F}(\Psi_A * K_{AB}) = \mathscr{F}(\Psi_A) \times \mathscr{F}(K_{AB}) \tag{4.16}$$

Equation (4.16) can be inverted to obtain

$$K_{AB} = \mathscr{F}^{-1}\left(\mathscr{F}(\Psi_B) \times \frac{1}{\mathscr{F}(\Psi_A)}\right), \tag{4.17}$$

where $\mathscr{F}$ and $\mathscr{F}^{-1}$ are the Fourier transform and inverse Fourier transform, respectively. A condition for the existence of the kernel is that the Fourier components for which $\mathscr{F}(\Psi_A) = 0$ should satisfy $\mathscr{F}(\Psi_B) = 0$ implying that the PSF at $\lambda_{\rm A}$ should be narrower than that at $\lambda_{\rm B}$.

Since the Fourier transform for a Gaussian kernel is also Gaussian, Gaussian kernels are easy to work with and thus find frequent use in this application. The Full Width Half Maximum (FWHM) of the Gaussian kernel ($FWHM_{K_{AB}}$) is the quadrature difference between the FWHM of $\Psi_A$ ($FWHM_{\Psi_A}$) and that for $\Psi_B$ ($FWHM_{\Psi_B}$):

$$FWHM_{K_{AB}} = \sqrt{FWHM^2_{\Psi_B} - FWHM^2_{\Psi_A}}. \tag{4.18}$$

Equation (4.17) is intractable for more complex PSFs such as the Hermite-Gaussian functions used to describe the SPIRE iFTS beam. There is therefore no analytical solution and we have to resort to numerical methods such as the Maximum Entropy (Gull & Skilling, 1984) and the CLEAN algorithm (Högbom, 1974).

Figures 4.5 and 4.6 show two example cases of what happens to the SPIRE FTS spectral data cubes when convolved to a beam of 43″ using a Gaussian kernel[3]. Figure 4.5 shows a mosaic plot of spectra from a SPIRE FTS fully sampled mapping observation

[3]The maximum FWHM of the beam for the SLW detectors is 43″.

of IRAS16293-2422. IRAS16293-2422 was first discovered in a survey undertaken by the *Infrared Astronomical Satellite* (*IRAS*) at 25, 60 and 100 $\mu$m (e.g. Walker et al., 1986). It was later classified as a Class 0 protostar by Andre et al. (1993). In the plot, the right ascension (RA) is on the horizontal axis and increases from right to left, while the declination (Dec) is on the vertical axis and increases from bottom to top. Each box on the plot corresponds to a pixel on the spectral map and has a size of $17.5'' \times 17.5''$. The spectra before convolution are shown in blue while those after convolving the whole map to $43''$ are shown in red.

The discontinuity seen in the SSW and SLW spectra for pixel (5,3) is an example of the phenomena seen in the centre figures of the middle and bottom rows of Figure 4.1. This is an indication that the source size for IRAS16293-2422 is less than the largest beam for the SPIRE iFTS. The data presented in Figure 4.5 are analyzed in detail in Chapter 6 where it has been shown that the continuum and line emission from IRAS16293-2422 are compact ($\sim 15''$). Thus, IRAS16293-2422 will be point-like to both the SSW and SLW bands. Convolving the map to $43''$ does not correct for the spatial extent of continuum emission. Clearly, the beam and source size play an important role in the interpretation of the measured spectra.

Figure 4.6 shows a mosaic plot of spectra from a mapping observation of Elias 29. Elias 29 was first discovered in the infrared survey performed using the Caltech 0.6 m telescope on Mount Wilson (Elias, 1978a). It was classified as a Class I protostar by Wilking et al. (1989). In the plot, the pixel size, the RA and Dec are the same as those described above for IRAS16293-2422. The spectra before convolution are shown in blue while those after convolving the whole map to $43''$ are shown in red. In this plot it can be seen that this

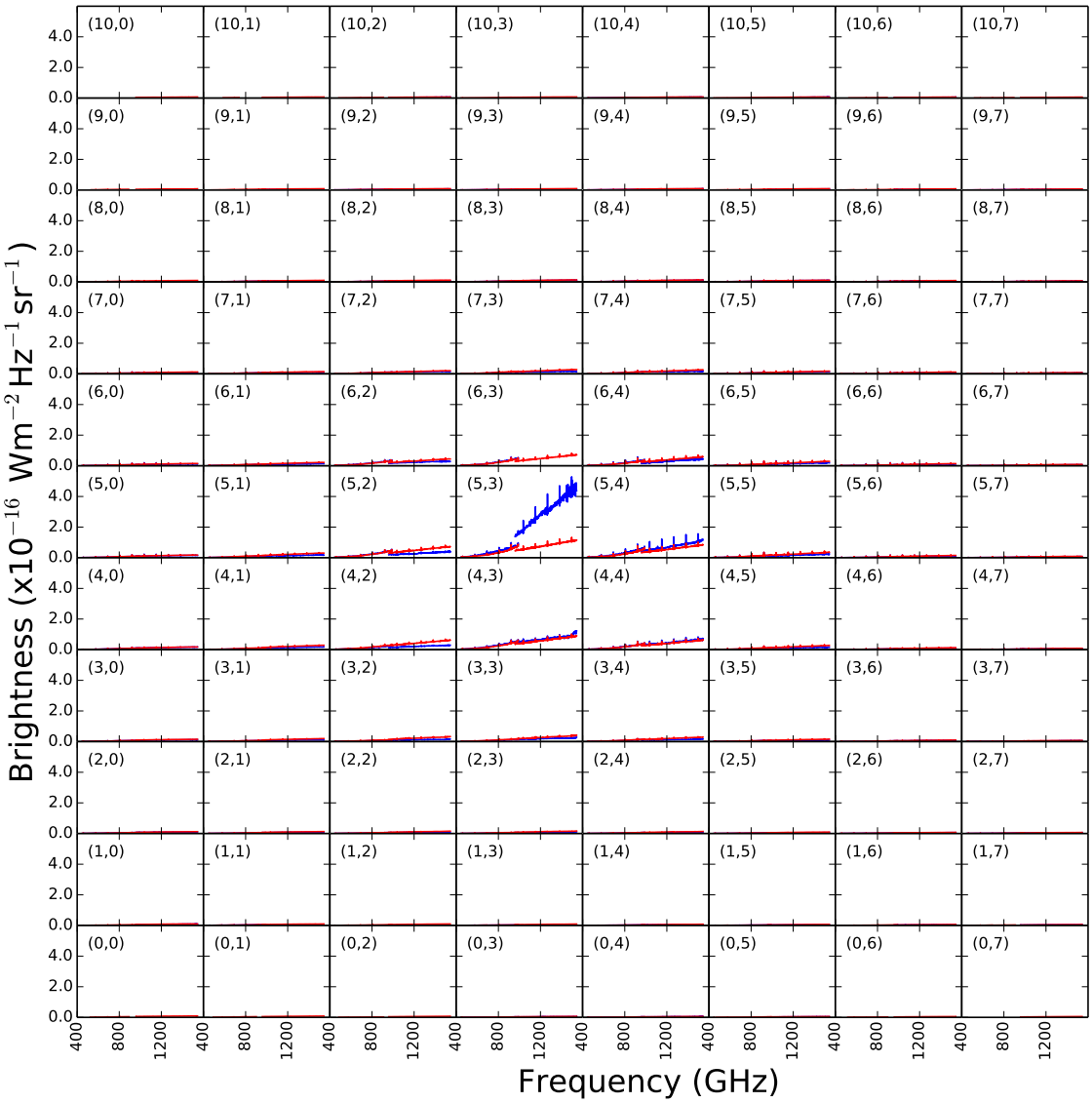


Figure 4.5: Mosiac plot of IRAS16293 spectral data cubes observed with the SPIRE FTS, before (blue) and after (red) convolving to a beam of 43″. The map pixels corresponding to the spectra in each box are shown on the top left corner. There are many pixels where the signal is so faint that it can hardly be seen. The observation was processed using extended-source calibration.

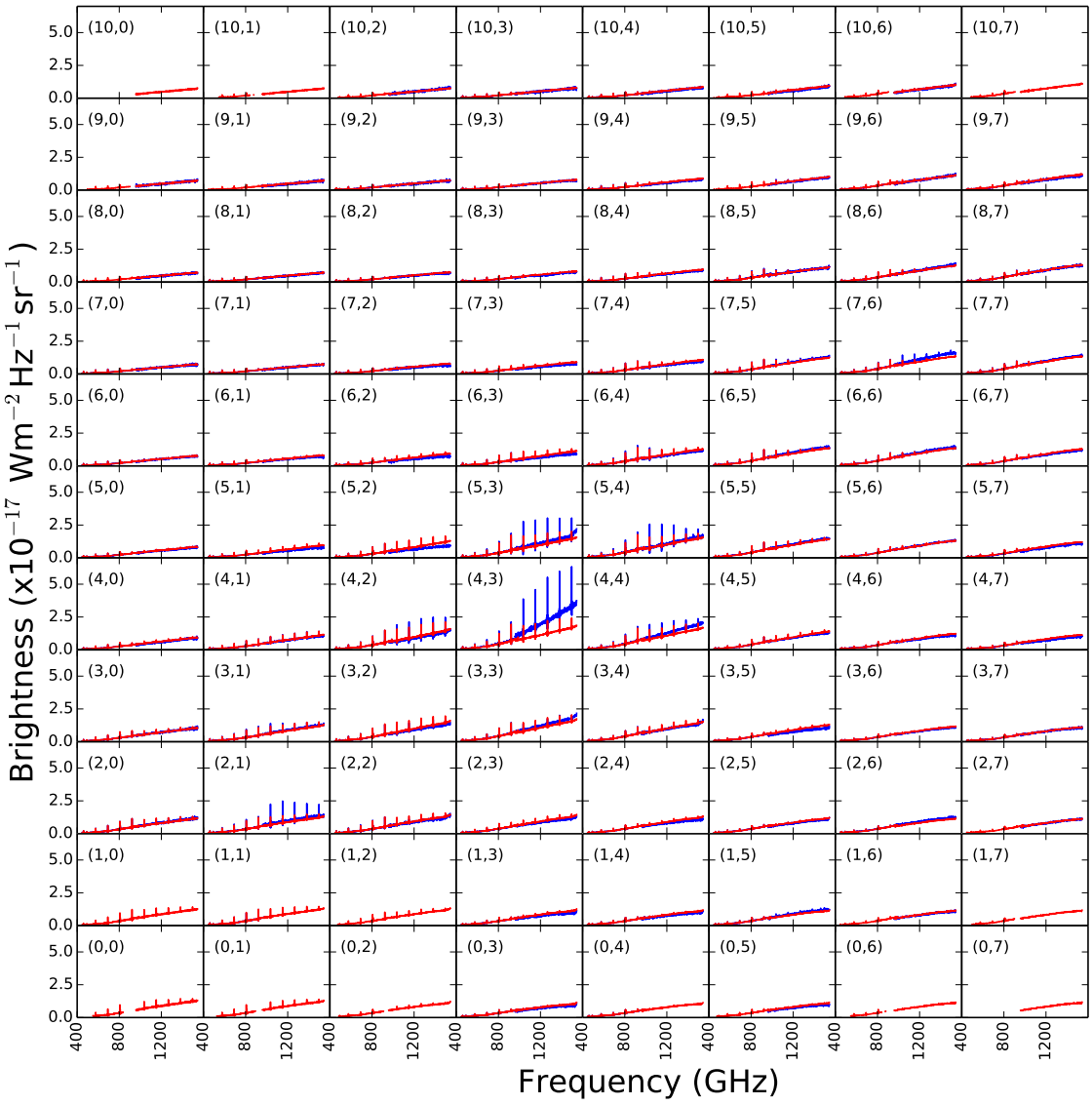


Figure 4.6: Mosiac plot of Elias 29 spectral data cubes observed with the SPIRE FTS, before (blue) and after (red) convolving to a beam of 43″. The map pixels corresponding to the spectra in each box are shown on the top left corner. The observation was processed using extended-source calibration.

region is quite complex. Line emission is not as extended as continuum emission. However, it can be seen that both continuum and line emission for pixel (4,3) are significantly brighter which shows evidence of a source that is compact and hotter than its surroundings.

The discontinuity seen in the SSW and SLW spectra for pixel (4,3) is an example of the phenomena seen in the centre figure of the middle row of Figure 4.1. This is an indication that Elias 29 appears as an extended-source in the SSW band but as a point-source in the SLW band. The data presented in Figure 4.6 has been analyzed in detail in Chapter 7 where it has been shown that the continuum emission from Elias 29 is compact ($\sim 22''$). Convolving the spectral data cubes to $43''$ works well in correcting the continuum from the effect of source coupling to the wavelength dependent beam profiles but does not work for line emission. Again it is clear that the beam profile and source extent should be taken into account when interpreting measured spectra from the SPIRE Fourier transform spectrometer (FTS). A method of solving this problem for the brightest pixels is to process the spectra for those pixels using the point-source calibration and using the "SemiExtendedCorrector" tool to correct for source spatial extent. This will be described in Chapter 6.

## 4.5 Conclusion

In this chapter, the importance of the beam profile of an instrument in the calibration of observed data has been presented. The standard SPIRE iFTS pipeline is applicable only to point-like and fully extended sources. The "SemiExtendedCorrector" tool has been developed to correct spectra for semi-extended sources calibrated using the point-source flux calibration scheme. The tool estimates the source size using the gap in the overlap region

between the SSW and SLW bands and the beam profiles derived in Chapter 3. The importance of the beam profile in comparing images obtained with instruments having different PSFs through convolution has also been discussed. Observations of the three starless cores (L1521E, L1521F and L1689B), a Class 0 protostar (IRAS16293-2422) and a Class I protostar (Elias 29) used as examples in this chapter have been analyzed in detail in Chapters 5, 6 and 7, respectively.

# Chapter 5

# Pre-stellar Cores: L1521E, L1521F and L1689B

## 5.1 Overview

Studying starless cores provides us with knowledge about the initial conditions of star formation. Starless cores that are close to and will go through gravitational collapse are called pre-stellar cores. In this Chapter, an analysis of three pre-stellar cores (Lynds 1521E, 1521F and 1689B hereafter abbreviated as L1521E, L1521F and L1689B) observed with the Spectral and Photometric Imaging Receiver Array (SPIRE) imaging Fourier transform spectrometer (iFTS) is presented. Section 5.2 provides a general introduction to starless cores. Section 5.3 discusses what we currently know about the three starless cores studied in this chapter. A discussion of details concerning the SPIRE iFTS observations of these cores is provided in Section 5.4. The results are presented in Section 5.5. A discussion of

the results is provided in Section 5.6.

## 5.2 Introduction

It has been known for almost three decades now, that stars form in cold ($T <$ 10 K), dense ($n_{\rm H_2} \gtrsim 10^5$ cm$^{-3}$)[1] and quiescent regions of molecular clouds (e.g. Myers & Benson, 1983; Beichman et al., 1986; Benson & Myers, 1989) called dense cores. Evidence for this hypothesis was provided by the association of dense cores to young stars in the *Infrared Astronomical Satellite* (*IRAS*) catalogue. The lack of any sign of protostellar activity such as infrared sources or bipolar outflows in dense cores led them to be designated "starless" cores. The study of starless cores provides us with a chance to probe the initial conditions of star formation.

Dense cores are favourable for the formation of molecules such as $H_2$, CO and complex carbon bearing species (Herbst & van Dishoeck, 2009). The most abundant molecule in starless cores is $H_2$, a homo-nuclear molecule. Because of its symmetry, $H_2$ does not have an electric dipole moment but has weak electric quadrupole transitions between rotational or ro-vibrational levels making it difficult to observe in the quiescent molecular clouds. After $H_2$ the next abundant molecule is CO, a hetero-nuclear molecule. Although $\sim 10^{-4}$ less abundant than $H_2$, CO is the most important molecule used to study the distribution of molecular gas.

Two methods of probing the cold dense molecular clouds are by studying their emission and absorption line spectroscopy which provides information about the chemistry

[1] $n_{\rm H_2}$ is the molecular hydrogen number density in cm$^{-3}$ while $N_{\rm H_2}$ is the molecular hydrogen column density in cm$^{-2}$.

of these regions and by studying thermal (continuum) emission which provides information about the dust. The interpretation of spectral lines is affected by the freezing of CO and other C-bearing molecules onto dust grains (e.g. Caselli et al., 1999; Tafalla et al., 2002). The "freeze-out" increases toward the centres of starless cores where the temperatures are significantly lower. The outer layers of cores are heated by the interstellar radiation field (ISRF) creating an environment where molecules can exist in the gaseous phase.

Studying starless cores using continuum emission is currently accomplished by using spectral energy distributions (SEDs) constructed from a small number of data points (3 or greater) extracted from photometers on ground- and space- based observatories (e.g. Ward-Thompson et al., 2002; Kirk et al., 2007; Schnee et al., 2007). The SED of a particular core is used to derive the dust temperature, emissivity spectral index, column density and dust mass in the core. Schnee et al. (2007) show that in order to accurately derive core parameters from maps obtained at three wavelengths, the noise and calibration errors should be $\lesssim 2\%$. Errors in the derivation of core parameters are however reduced if one uses four or more maps observed at different wavelengths. Photometric observations of starless cores with the *Herschel Space Observatory* (*Herschel*) (Pilbratt et al., 2010) have added six more data points to the SEDs and in addition the spectroscopic capabilities of the SPIRE iFTS in the 447-1545 GHz frequency range with a spectral resolution[2] of 24.9 GHz is equivalent to adding 45 more points.

*Herschel* was designed to cover the far-infrared region of the electromagnetic spectrum using three instruments: SPIRE (Griffin et al., 2010), the Photodetecting Array Cam-

[2]SPIRE iFTS observations were carried out at three spectral resolutions: low resolution ($\Delta\sigma = 0.83$ cm$^{-1}$), medium resolution ($\Delta\sigma = 0.24$ cm$^{-1}$) and high resolution ($\Delta\sigma = 0.398$ cm$^{-1}$)

era and Spectrometer (PACS) (Poglitsch et al., 2010) and the Heterodyne Instrument for the Far Infrared (HIFI) (de Graauw et al., 2010). SPIRE consists of a two-band iFTS and a three-band photometer. The two SPIRE iFTS bands are the spectrometer short wavelength (SSW) array which consists of 37 feed-horn coupled detectors and covers wavelengths from 194–313 $\mu$m (1545–958 GHz) and the spectrometer long wavelength (SLW) array which consists of 19 feed-horn coupled detectors and covers wavelengths from 303–671 $\mu$m (990–447 GHz). The photometer operates at the photometer short wavelength (PSW), photometer medium wavelength (PMW) and photometer long wavelength (PLW) ranges centred at 250 $\mu$m (1199 GHz), 350 $\mu$m (857 GHz) and 500 $\mu$m (600 GHz) respectively.

In this chapter results obtained from the *Herschel* SPIRE continuum observations of three starless cores (L1521E, L1521F and L1689B) are reported. The *Herschel* SPIRE instruments measure near the peak of dust emission from these cold sources and has provided the first accurate view of the SEDs from which trustworthy dust temperatures and emissivity spectral indices are derived.

## 5.3 Background of sources

### 5.3.1 L1521E

L1521E is found in the Taurus star-forming region at a distance of $d$=140 pc (Loinard et al., 2005; Torres et al., 2007). It is a triple-lobed pre-stellar core situated at the south-eastern end of the L1521 filament. Models by Tafalla & Santiago (2004) have shown that L1521E has no $C^{18}O$ depletion. Their models also derive an unusually low $N_2H^+$ abundance. This suggests that L1521E recently contracted to its present density and

is therefore an extremely young starless core with age $\leq 1.5\times10^5$ yr. A modified blackbody fit to the L1521E SED with a fixed dust emissivity index ($\beta = 2$) has resulted in a dust temperature of 8.1 $\pm$ 0.4 K (Kirk et al., 2007). The derived core radius and mass of L1521E traced by $H^{13}CO^+$are 0.031 pc and 2.4 $M_\odot$ respectively (Hirota et al., 2002). The $H_2$ number density measured at the peak position is $n_{H_2} = (1.3–5.6)\times10^5$ cm$^{-3}$.

### 5.3.2 L1521F

L1521F (a.k.a. MC27; Codella et al. 1997; Onishi et al. 1999; Lee et al. 2001) is also found in the Taurus star-forming region. L1521F appears isolated with a strong central condensation as shown from the 160 $\mu$m *Spitzer* map presented by Kirk et al. (2007). It is a dense starless core harbouring a low luminosity ($L = 0.05\ L_\odot$) object L1521F-IRS (Bourke et al., 2006). Due to its low luminosity, L1521F did not appear in the IRAS catalogue (Beichman et al., 1986; Benson & Myers, 1989; Codella et al., 1997) but was observed by the *Spitzer Space Telescope* (Terebey et al., 2006; Bourke et al., 2006). L1521F-IRS together with L1544 (Crapsi et al., 2005) are the best examples of evolved starless cores. Kirk et al. (2005) obtained a dust temperature of 9 $\pm$ 2 K, a mass of 0.4 $\pm$ 0.1 $M_\odot$ and a column density, $N_{H_2}$, of the order of $1\times10^{23}$ cm$^{-2}$ with a typical uncertainity of 20–30 %.

In their mapping surveys of Taurus, Onishi et al. (1999) argued that the high central density ($\sim10^6$ cm$^{-3}$) and infall asymmetry seen in the $H^{13}CO^+$ (3-2) lines from L1521F indicate that the core is in its earliest stages of gravitational collapse with a free-fall timescale of $10^3$ to $10^4$ yr. Besides the high central density and infall asymmetry, L1521F also shows molecular depletion and enhanced deuterium fractionation (Crapsi et al., 2004; Shinnaga et al., 2004). There has been no clear evidence of bipolar outflows from L1521F

but the spatially compact (<30″) line wings seen in $H^{13}CO^+$ (3-2) lines (Onishi et al., 1999) suggest that this may be due to outflow emission similar to that seen from L1014-IRS (Huard et al., 2006). A well-defined bipolar scattered light nebula seen at short wavelengths (<5 $\mu$m) also provides evidence for the presence of molecular outflows similar to those from low-mass protostars (Bourke et al., 2006).

### 5.3.3 L1689B

L1689B is found in the Ophiuchus star-forming region at a distance of $d$=120 pc (Loinard et al., 2008; Lombardi et al., 2008). Millimeter and mid-infrared maps of L1689B have shown that it is a sharp-edged core, elongated in the north-south direction. A modified blackbody fit to the L1689B SED with a fixed dust emissivity index ($\beta$ = 2) has resulted in a dust temperature of 11 ± 2 K (Kirk et al., 2007). For this source, Kirk et al. (2005) derived a core mass of 0.4 ± 0.1 $M_\odot$ and a column density, $N_{H_2}$, of $5\times10^{22}$ cm$^{-2}$, again with a typical uncertainty of 20-30 %.

## 5.4 Observations and data reduction

### 5.4.1 *Herschel*-SPIRE photometer observations

SPIRE Photometer maps of the starless cores (L1521E, L1521F and L1689B) were obtained as part of the Gould Belt guaranteed time key programmes for the study of star formation (André et al., 2010) using the SPIRE and PACS photometers on *Herschel*. Large area observations of the L1688 cloud in the rho Ophiuchus star forming region and the L1521 cloud in the Taurus star forming region were obtained. Two cross scans (Observation

Identification Number (OBSID) = 1342205093 and 1342205094 for L1688 and OBSID = 1342190616 and 1342202090 for L1521) were obtained. The publicly available SPIRE photometer cross-scan observations for each cloud were downloaded, reprocessed and merged using the Herschel Interactive Processing Environment (HIPE)[3] version 11 (Ott, 2010).

### 5.4.2 *Herschel*-SPIRE spectrometer observations

The starless cores (L1521E, L1521F and L1689B) were observed as part of the "Evolution of Interstellar dust" key program under the ISM Specialist Astronomy Group (SAG4) (Abergel et al., 2010) using the SPIRE spectrometer on board *Herschel*. These objects were observed in sparse sampling mode. The L1521E observation (OBSID:1342191211) was centred at $\alpha_{2000} = 4^{\rm h}29^{\rm m}14.2^{\rm s}$, $\delta_{2000} = 26°15'10.0''$. The L1521F observation (OBSID:1342191208) was centred at $\alpha_{2000} = 4^{\rm h}28^{\rm m}39.8^{\rm s}$, $\delta_{2000} = 26°52'33.9''$ and the L1689B observation (OBSID:1342191221) was centred at $\alpha_{2000} = 16^{\rm h}34^{\rm m}48.3^{\rm s}$, $\delta_{2000} = -24°38'03.1''$. These source positions are slightly offset from the positions listed in Table 2 of Kirk et al. (2007). The SPIRE iFTS data were also reduced using HIPE version 11.

The calibration of the SPIRE iFTS is achieved using solar system objects and other astronomical targets as outlined by Swinyard et al. (2010, 2014). As was mentioned in Chapter 4, the standard data reduction pipeline for the SPIRE iFTS was designed to work for two extreme cases of objects: those whose spatial extent is smaller than the beam and those whose spatial extent is much larger than the beam. The calibration scheme for the former is referred to as point-source calibration and that for the later is referred to as extended-

[3]HIPE is a joint development by the Herschel Science Ground Segment Consortium, consisting of ESA, the NASA Herschel Science Center, and the HIFI, PACS and SPIRE consortia.

source calibration. All sparse sampled SPIRE iFTS observations are processed using the "Spectrometer Single Pointing user pipeline" which applies point source flux calibration. Since continuum emission from the sample of starless cores studied in this thesis is not point-like, the resultant spectra have a large gap between the overlap region.

The "SemiExtendedCorrector" tool (Wu et al., 2013) (see Chapter 4) was used to correct for source spatial extent. The derived effective Full Width Half Maximum (FWHM) source sizes are 74″, 33″ and 52″ which correspond to source diameters of 0.050, 0.022 and 0.030 pc for L1521E, L1521F and L1689B respectively. These source sizes are in agreement with those derived by Kirk et al. (2005).

## 5.5 Results

### 5.5.1 Far-infrared photometry

To place results from this work in context, the SPIRE spectroscopic and photometric data have been combined with other photometry data from ground and space instruments. A brief introduction of these instruments is provided below.

The Multiband Imaging Photometer for Spitzer (MIPS) (Rieke et al., 2004) is a far-infrared camera on the *Spitzer Space Telescope* (*Spitzer*) (Werner et al., 2004). *Spitzer*, an 85 cm diameter cryogenically cooled telescope was designed to operate from 3 to 160 $\mu$m. MIPS covered three wavebands at 24, 70 and 160 $\mu$m with telescope-limited resolutions of 6″, 18″ and 40″ respectively. Although *Spitzer* ran out of its on-board supply of liquid cryogens in May 2009, its Infrared Array Camera (IRAC) which provides some of the photometry data used in this chapter continues to be used in the *Spitzer* Warm Mission phase.

The Submillimeter Common-User Bolometer Array (SCUBA) (Holland et al., 1999) operated on the James Clerk Maxwell Telescope (JCMT) before it was retired in 2005. It consisted of the Short-Wave (SW) array with 91 pixels operating in the 450 $\mu$m atmospheric transmission window and the Long-Wave (LW) array with 37 pixels operating at 850 $\mu$m.

The source positions for the three sources studied in this thesis have been listed in Table 5.1. The main challenge faced when comparing data from ground and space based instruments was background subtraction. The challenge in comparing data from MIPS and SCUBA is that, unlike *Spitzer* that is sensitive to the entire dynamic range and spatial scale of the source emission, the JCMT has a chopping secondary mirror that is used to reject bright atmospheric emission (Kirk et al., 2007). As a result, the flux density values from SCUBA are only reliable for small scale spatial features and will underestimate large scale emission. Flux density values observed with the larger SPIRE beam are therefore expected to be greater than those from SCUBA.

In order to compare flux density values from MIPS and SCUBA, Kirk et al. (2007) had to subtract a large background from the *Spitzer* data integrated from a 150″ size aperture. This method has its own challenges in that different ways of obtaining the background lead to different results since the cores are usually not found in isolation and are not symmetrical in shape. To illustrate this point, Table 5.1 shows flux density values from the PSW band of the SPIRE photometer obtained using the "annularSkyAperturePhotometry" task in HIPE from an annular aperture of size 150″. Source positions listed are those from Kirk et al. (2007) since they are closer to the peak of the continuum emission than the iFTS pointings. For this reason, all photometric flux density values recorded from here onwards

Table 5.1: Flux density values for L1521E, L1521F and L1689B obtained from the PSW map using annular sky apertures of different inner and outer radii. The first three columns list the source names and the corresponding RA and Dec. The fourth and fifth columns list the background subtracted flux densities obtained by using inner/outer radii of 400″/450″ and 100″/120″ respectively, from which it can be seen that flux densities for these sources clearly depend on what region is used for background subtraction.

| Source | RA (2000) ($^h$ $^m$ $^s$) | Dec (2000) ($^\circ$ $'$ $''$) | $S_{250}$ 400/450 (Jy) | 100/120 (Jy) |
|---|---|---|---|---|
| L1521E | 04 29 13.6 | 26 14 05 | 32(6) | 21(5) |
| L1521F | 04 28 39.2 | 26 51 36 | 59(8) | 33(6) |
| L1689B | 16 34 48.2 | -24 38 04 | 119(11) | 52(7) |

were obtained from annular sky apertures centred at these positions.

The background was calculated by varying the inner and outer radii of the annular sky aperture. Using inner and outer radii of 400″ and 450″ respectively resulted in flux density values that are almost twice those obtained from inner and outer radii of 100″ and 120″ respectively. The respective inner and outer radii of 400″ and 450″ appear to be suitable for the calculation of the background since they are far enough from all the three cores studied here. These radii were used to calculate backgrounds and the obtained SPIRE photometer flux density values are recorded in Tables 5.2, 5.3 and 5.4.

Table 5.2 shows photometer data points for L1521E obtained at various wavelengths. Columns 4 and 5 lists the instrument beam and aperture size over which the flux is measured. Most of the the flux densities were obtained from a aperture of size 150″. The only exception is that of flux densities from IRAC shown in Table 5.3. These were obtained

Table 5.2: Photometer flux values for L1521E. The first three columns show the wavelength, observed flux ($F$) and errors ($\Delta F$). Errors include statistical measurement errors and uncertainties in the absolute calibration. Columns 4 and 5 show the beam sizes for the instrument ($\theta_{\rm beam}$) used to obtain the data (column 5) and the size of the aperture ($\theta_{\rm aperture}$) over which the flux is measured. Columns 6 and 7 show the instrument used to obtain the data and the reference from which the data were taken. Refs.–(1) Kirk et al. (2007); (2) this work.

| $\lambda$ [$\mu$m] | $F$ [mJy] | $\Delta F$ [mJy] | $\theta_{\rm beam}['']$ | $\theta_{\rm aperture}['']$ | Instrument | Ref. |
|---|---|---|---|---|---|---|
| 24 | $<$2.6 | – | 5.7 | 150 | MIPS | 1 |
| 70 | $<$67 | – | 17 | 150 | MIPS | 1 |
| 160 | 660 | 230 | 40 | 150 | MIPS | 1 |
| 250 | 32022 | 5700 | 17.6 | 150 | SPIRE | 2 |
| 350 | 25454 | 5000 | 23.9 | 150 | SPIRE | 2 |
| 450 | 4000 | 1400 | 7.8 | 150 | SCUBA | 1 |
| 500 | 12505 | 3500 | 35.2 | 150 | SPIRE | 2 |
| 850 | 1400 | 200 | 13.8 | 150 | SCUBA | 1 |

with a small size aperture.

### 5.5.2 Morphology of far-infrared emission

Figure 5.1 shows the SPIRE photometer maps for each of the three sources with each map measuring $6'\times6'$ and centred on the source. For each source, the far-infrared images show that there is a similarity in the diffuse emission, evidence that the 250, 350 and 500 $\mu$m wavelengths are tracing the same dust component. All sources are extended with respect to the largest SPIRE photometer spatial resolution of $38.2'' = 5350$ AU $= 0.026$ pc at 500 $\mu$m and at a distance of 140 pc.

Table 5.3: Photometer flux values for L1521F. The first three columns show the wavelength, observed flux ($F$) and errors ($\Delta F$). Errors include statistical measurement errors and uncertainties in the absolute calibration. Columns 4 and 5 show the beam sizes for the instrument ($\theta_{\rm beam}$) used to obtain the data (column 5) and the size of the aperture ($\theta_{\rm aperture}$) over which the flux is measured. Columns 6 and 7 show the instrument used to obtain the data and the reference from which the data were taken. Refs.–(1) Bourke et al. (2006); (2) Kirk et al. (2007); (3) this work.

| $\lambda$ [$\mu$m] | $F$ [mJy] | $\Delta F$ [mJy] | $\theta_{\rm beam}[''']$ | $\theta_{\rm aperture}[''']$ | Instrument | Ref. |
|---|---|---|---|---|---|---|
| 3.6 | 0.42 | 0.06 | 1.7 | 1.7 | IRAC | 1 |
| 4.5 | 0.54 | 0.08 | 1.7 | 1.7 | IRAC | 1 |
| 5.8 | 0.34 | 0.05 | 1.9 | 1.9 | IRAC | 1 |
| 8.0 | 0.45 | 0.07 | 2.0 | 2.0 | IRAC | 1 |
| 24 | 35 | 4 | 5.7 | 150 | MIPS | 2 |
| 70 | 290 | 60 | 17 | 150 | MIPS | 2 |
| 160 | 4400 | 900 | 40 | 150 | MIPS | 2 |
| 250 | 59161 | 7700 | 17.6 | 150 | SPIRE | 3 |
| 350 | 55519 | 7500 | 23.9 | 150 | SPIRE | 3 |
| 450 | 12000 | 4000 | 7.8 | 150 | SCUBA | 2 |
| 500 | 29305 | 5400 | 35.2 | 150 | SPIRE | 3 |
| 850 | 3200 | 400 | 13.8 | 150 | SCUBA | 2 |

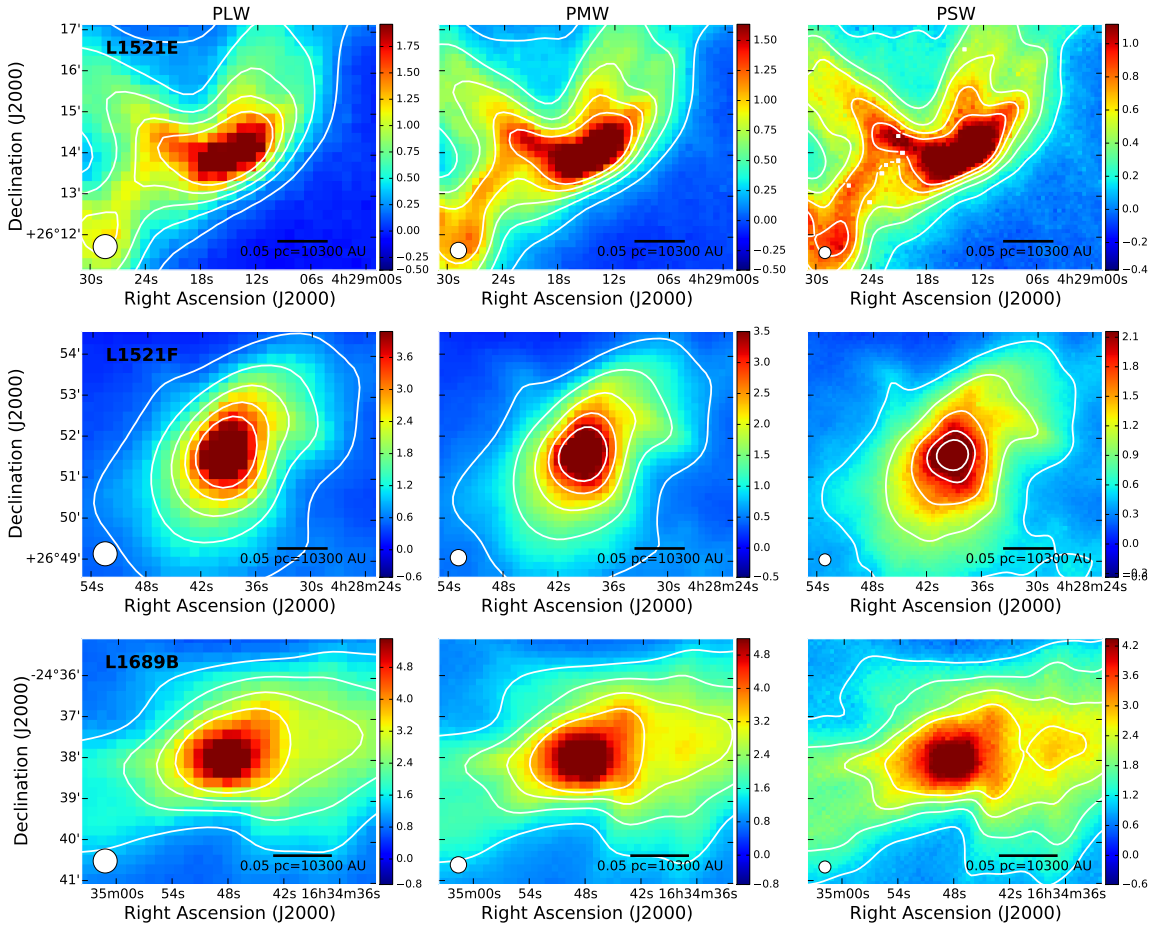


Figure 5.1: The SPIRE PSW (250 $\mu$m), PMW (350 $\mu$m) and PLW (500 $\mu$m) maps for L1521E, L1521F and L1689B. Contours are shown at 10, 20, 30, 40 and 50 % of the peak in each map. The contour at 10 % for L1689B falls outside the map. The circle at the bottom left corner of each map represents the photometer beam size at that wavelength. A scale bar is shown at the bottom right corner of each plot. The maps show that all three sources are quite extended and have different shapes.

Table 5.4: Photometer flux values for L1689B. The first three columns show the wavelength, observed flux ($F$) and errors ($\Delta F$). Errors include statistical measurement errors and uncertainties in the absolute calibration. Columns 4 and 5 show the beam sizes for the instrument ($\theta_{\rm beam}$) used to obtain the data (column 5) and the size of the aperture ($\theta_{\rm aperture}$) over which the flux is measured. Columns 6 and 7 show the instrument used to obtain the data and the reference from which the data were taken. Refs.–(1) Kirk et al. (2007); (2) this work.

| $\lambda$ [$\mu$m] | $F$ [mJy] | $\Delta F$ [mJy] | $\theta_{\rm beam}['']$ | $\theta_{\rm aperture}['']$ | Instrument | Ref. |
|---|---|---|---|---|---|---|
| 24 | <15 | – | 5.7 | 150 | MIPS | 1 |
| 70 | <330 | – | 17 | 150 | MIPS | 1 |
| 160 | 35000 | 7000 | 40 | 150 | MIPS | 1 |
| 250 | 118615 | 11000 | 17.6 | 150 | SPIRE | 2 |
| 350 | 77540 | 8800 | 23.9 | 150 | SPIRE | 2 |
| 450 | 18000 | 6000 | 7.8 | 150 | SCUBA | 1 |
| 500 | 34597 | 5900 | 35.2 | 150 | SPIRE | 2 |
| 850 | 3100 | 400 | 13.8 | 150 | SCUBA | 1 |

### 5.5.3 Analysis of SEDs

In the limit of small optical depth, emission from dust particles can be described using a modified blackbody (Equation 2.17):

$$F_\nu = \tau_\nu B_\nu(T_{\rm d})\Omega = \mu m_{\rm H} N_{\rm H} \kappa_\nu B_\nu(T_{\rm d})\Omega \qquad [\rm Jy] \tag{5.1}$$

where $F_\nu$ is the flux density per beam in Jy (1 Jy=$1\times10^{-26}$ W m$^{-2}$ Hz$^{-1}$) and $B_\nu(T_{\rm d})$ is the Planck blackbody function at the dust temperature, $T_{\rm d}$. $B_\nu(T_{\rm d})$ is given by

$$B_\nu(T_{\rm d}) = \frac{2h\nu^3}{c^2}\frac{1}{\exp\left(h\nu/kT_{\rm d}\right)-1} \qquad [\rm W\ m^{-2}\ Hz^{-1}\ sr^{-1}], \tag{5.2}$$

$\tau_\nu$ is the optical depth. $\tau_\nu$ can be expressed in terms of the specific opacity $\kappa_\nu$ (in cm$^2$ g$^{-1}$), the density of the gas-dust mixture $\rho$, and the path length $L$ by (Smith, 2004; Irwin, 2007)

$$\tau_\nu = \kappa_\nu \rho L \tag{5.3}$$

$$= \kappa_\nu \mu m_{\rm H} N_{\rm H} \tag{5.4}$$

$$= \sigma_\nu N_{\rm H}. \tag{5.5}$$

$\kappa_\nu$ is the emissivity of the dust (specific opacity) at frequency $\nu$:

$$\kappa_\nu = \kappa_{230} \left( \frac{\nu}{230 \text{ GHz}} \right)^\beta \qquad [\text{cm}^2 \text{ g}^{-1}]. \tag{5.6}$$

$\mu$ ( = 1.38) is the mean molecular weight of interstellar material in a molecular cloud per hydrogen atom, $m_{\rm H}$ is the mass of the hydrogen atom, $N_{\rm H}$ is the hydrogen column density[4], $\Omega$ is the beam solid angle and $\sigma_\nu$ is the dust absorption cross section in units of cm$^2$ per H atom. $h$ is the Planck constant, $k$ is the Boltzmann constant, $c$ is the speed of light, $\kappa_{230}$ = 0.009 cm$^2$/g is the emissivity of dust grains at a frequency of 230 GHz and a gas density of $10^6$ cm$^{-3}$ (Ossenkopf & Henning, 1994) and $\beta$ is the dust emissivity index.

Equation 5.1 can be expressed as

$$F_\nu = \mu m_{\rm H} N_{\rm H} \Omega \kappa_\nu B_\nu(T_{\rm d}) = \frac{M_{\rm d}}{d^2} \kappa_\nu B_\nu(T_{\rm d}) = \text{constant} \times \kappa_\nu B_\nu(T_{\rm d}), \tag{5.7}$$

which shows that fitting a greybody function to the SEDs returns a constant that contains information about the dust mass and molecular hydrogen column density. The gas mass $M_{\rm H}$ is subsequently obtained by assuming a gas-to-dust ratio of 100.

The data in Tables 5.2, 5.3 and 5.4 was used to construct SEDs shown in Figures 5.2, 5.3 and 5.4. The data from Kirk et al. (2007) and that from the SPIRE iFTS and

[4]It is often assumed that in these dense and cold environments all the gas exists in molecular form and so $N_{\rm H} \approx 2N_{\rm H_2}$

photometer were fit separately with a single greybody function (Equation 5.1). Flux density values obtained at wavelengths shorter than 100 $\mu$m were not considered in the fitting since they do not appear to be coming from regions where the dust is cold and some in Table 5.3 were obtained using a smaller aperture.

As was mentioned before, the SPIRE iFTS spectra were obtained with a wavelength dependent beam. The point-source calibrated spectra were then corrected for source extent using the semi-extended corrector tool (Wu et al., 2013). Since the derived source sizes are less than the aperture size used to obtain the photometric points, it was found necessary to scale the SPIRE iFTS spectra by the appropriate ratio of aperture areas (150/(source size)$^2$). For the case of L1521E, the derived source size was 74″. The SPIRE iFTS spectra was therefore multiplied by $(150/74)^2 = 4.11$. After this scaling, the resulting spectrum matches well with flux densities from the SPIRE photometer. However, for L1521F and L1689B, it was discovered that the expected scaling factors of 21 and 8, respectively, were too large. A factor of 4.11 was required to scale both spectra. Multiplying the SPIRE iFTS spectrum with the ratio of aperture areas assumes that the sources are uniformly extended which is not the case for the starless cores in our sample. This explains why the required scaling factors for L1521F and L1689B are less than expected.

Another reason why flux densities from the SPIRE iFTS are scaled to those for the photometer and not the other way round is that whereas the beam profile for the SPIRE iFTS is wavelength dependent and multi-moded, that for the photometer is single moded and well defined (SPIRE Observers Manual, 2011). Furthermore, the photometer band is well known. This makes flux densities from the photometer more reliable.

The fitting was carried out by fixing all the parameters in Equation (5.1) except $\beta$ and $T_{\rm d}$. In each plot the SPIRE iFTS spectrum is shown as a solid blue line. The diamond points represent flux densities from the SPIRE photometer. Flux densities from *Spitzer* and SCUBA (Kirk et al., 2007) are represented with red symbols (squares and 'pins'). Although they are upper limits, the 'pins', are not useful constraints and so were not taken into account during fitting. The results derived from the fits are summarized in Table 5.5. Also shown in Table 5.5 are the calculated Jeans masses of the three cores. Assuming a gas to dust ratio of 100 it is clear that all three cores are Jeans unstable and so will collapse to form stars.

It is important to note that SEDs from *Spitzer* and SCUBA always fall below those from SPIRE data. The reason for that is in the way SCUBA operates which results in it underestimating flux densities on large spatial scales. This was explained in Section 5.5.1. In order to compare SCUBA and *Spitzer* data, Kirk et al. (2007) had to process the *Spitzer* data in a way to remove the effective background emission. The current best estimate in combining data from *Spitzer* and SCUBA which is to subtract a large background from the *Spitzer* data results in lower flux densities.

## 5.6 Discussion

### 5.6.1 L1521E

Fitting to the L1521E SED from SPIRE iFTS and photometer flux densities resulted in a temperature and dust emissivity index of 11.1 $\pm$ 0.2 K and 2.2 $\mp$ 0.1 respectively. Fitting to the SED from SCUBA and background subtracted *Spitzer* flux density points resulted in a temperature and dust emissivity index of 9.0 $\pm$ 0.2 K and 1.5 $\mp$ 0.2 respectively.

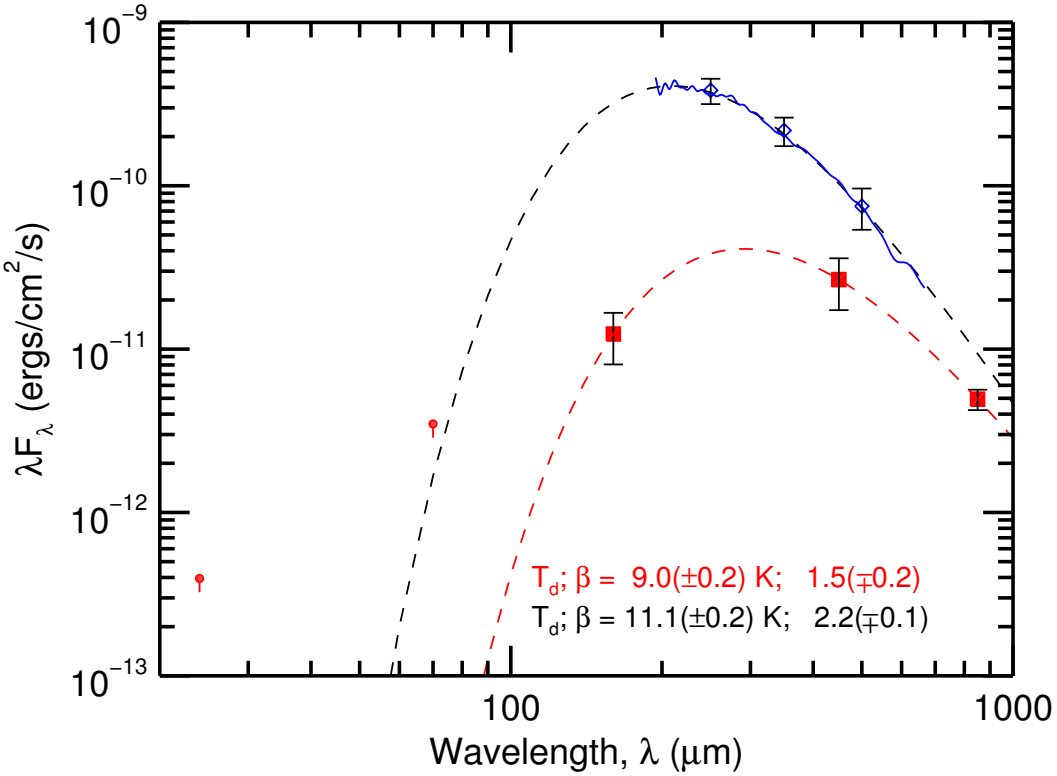


Figure 5.2: Spectral energy distribution for L1521E. The open diamonds and the blue spectrum represent flux densities from the SPIRE FTS and photometer respectively, while the red squares and pins represent flux densities from *Spitzer* and SCUBA (Kirk et al., 2007). The pins represent upper limits. The greybody fit to the SPIRE data is shown as a black dashed line while the fit to *Spitzer* and SCUBA data is shown as a red dashed line. The disparity between the SPIRE data and that from *Spitzer* and SCUBA is due to how SCUBA operates and also due to the way in which Kirk et al. (2007) processed the *Spitzer* data to remove the effective background emission as is explained in Section 5.5.1. The analysis by Kirk et al. (2007) underestimates the flux densities.

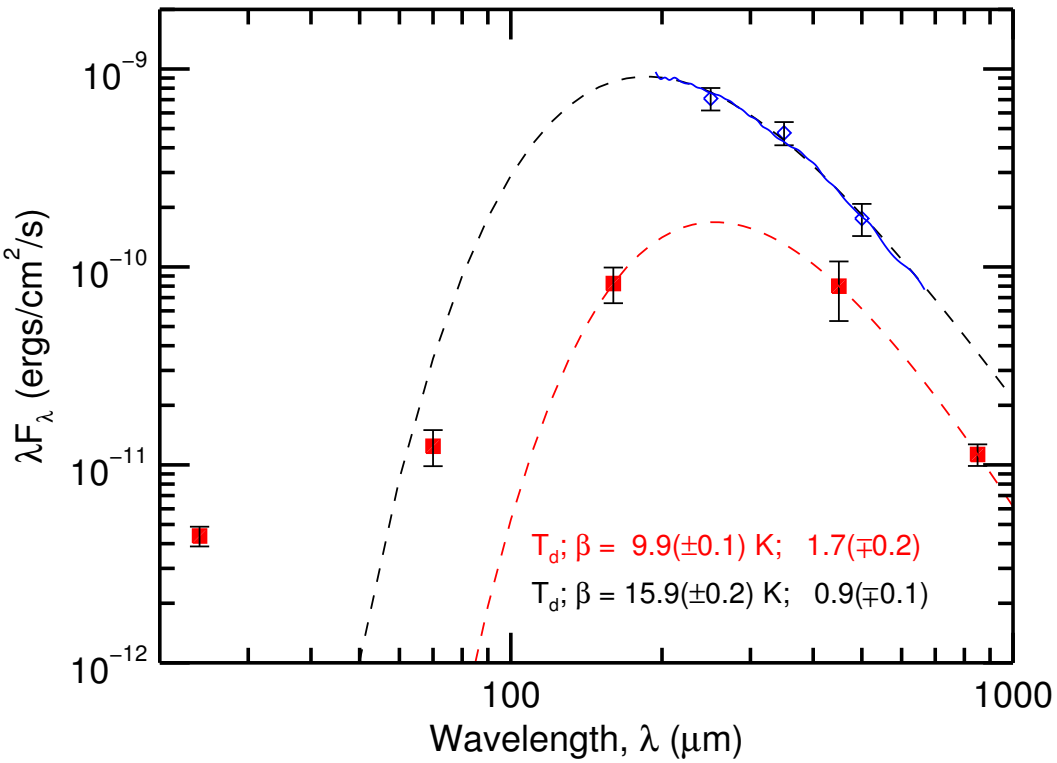


Figure 5.3: Spectral energy distribution for L1521F. The open diamonds and the blue spectrum represent flux densities from the SPIRE FTS and photometer respectively, while the red squares represent flux densities from *Spitzer* and SCUBA (Kirk et al., 2007). The grey-body fit to the SPIRE data is shown as a black dashed line while the fit to *Spitzer* and SCUBA data is shown as a red dashed line. The disparity between the SPIRE data and that from *Spitzer* and SCUBA is due to how SCUBA operates and also due to the way in which Kirk et al. (2007) processed the *Spitzer* data to remove the effective background emission as is explained in Section 5.5.1. The analysis by Kirk et al. (2007) underestimates the flux densities.

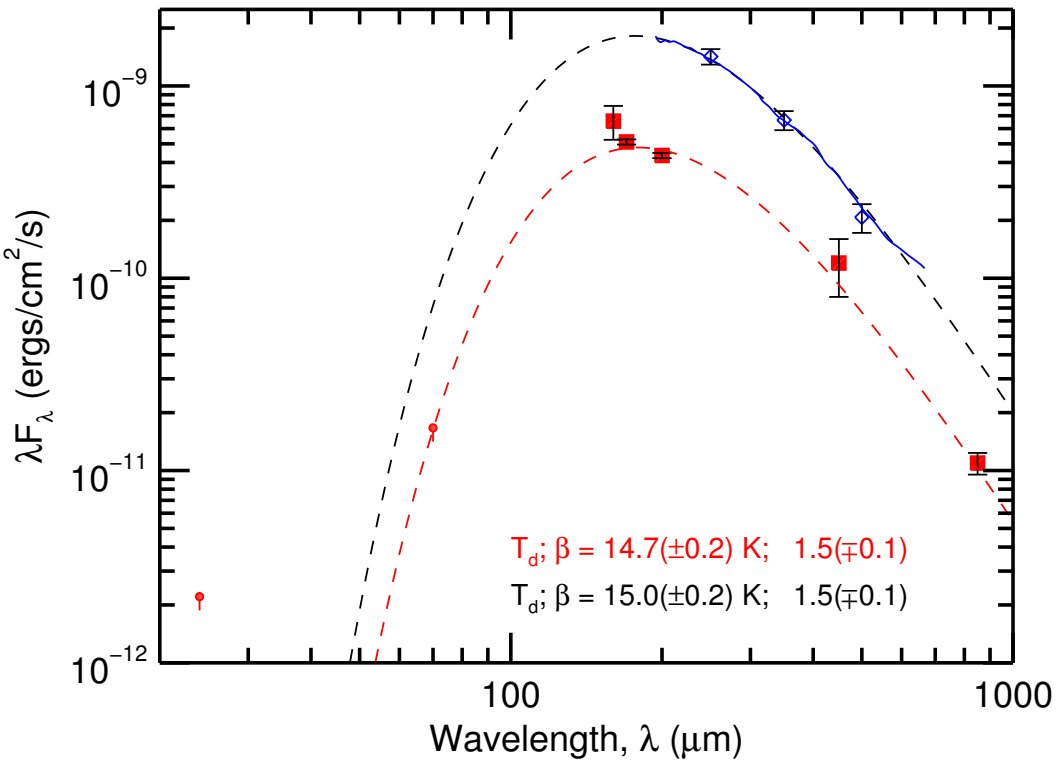


Figure 5.4: Spectral energy distribution for L1689B. The open diamonds and the blue spectrum represent flux densities from the SPIRE FTS and photometer respectively, while the red squares and pins represent flux densities from *Spitzer* and SCUBA (Kirk et al., 2007). The pins represent upper limits. The greybody fit to the SPIRE data is shown as a black dashed line while the fit to *Spitzer* and SCUBA data is shown as a red dashed line. The disparity between the SPIRE data and that from *Spitzer* and SCUBA is due to how SCUBA operates and also due to the way in which Kirk et al. (2007) processed the *Spitzer* data to remove the effective background emission as is explained in Section 5.5.1. The analysis by Kirk et al. (2007) underestimates the flux densities.

Table 5.5: Results obtained from fitting greybody functions to the SEDs for L1521E, L1521F and L1689B. The first two rows list the temperature and dust emissivity indices obtained from fitting SPIRE FTS and photometer data (column A: this work) and from other instruments (column B; Kirk et al., 2007). The third and fourth rows list the wavelengths and optical depths at which the peak of the SEDs occur. The fifth and sixth rows list the masses and H column densities of the cores. The last row lists the Jeans masses calculated using the recorded temperatures and column densities.

| | L1521E | | L1521F | | L1689B | |
|---|---|---|---|---|---|---|
| | A | B | A | B | A | B |
| $T$ [K] | 11.1(0.2) | 9.0(0.2) | 15.9(0.2) | 9.9(0.1) | 15.0(0.2) | 14.7(0.2) |
| $\beta$ | 2.2(0.1) | 1.5(0.2) | 0.9(0.1) | 1.7(0.2) | 1.5(0.1) | 1.5(0.1) |
| $\lambda_{\rm peak}$ [$\mu$m] | 250 | 360 | 240 | 310 | 220 | 220 |
| $\tau_{\lambda_{\rm peak}}$ [$\times 10^{-3}$] | 44(6) | 9(2) | 20(1) | 25(5) | 46(4) | 14(2) |
| $M_d$ [$M_\odot$] | 0.44(0.02) | 0.5(0.1) | 1.74(0.02) | 0.8(0.2) | 1.34(0.02) | 0.39(0.03) |
| $N_{\rm H}$ [$\times$ $10^{22}$ cm$^{-2}$] | 5.6(0.2) | 6(1) | 21.9(0.3) | 10(3) | 16.9(0.3) | 5.0(0.4) |
| $M_J$ [$M_\odot$] | 1.4 | | 0.8 | | 1.0 | |

The temperature derived from SPIRE data is slightly greater than that reported by Kirk et al. (2007) obtained by fixing the dust emissivity index to 2. The degeneracy between $T_{\rm d}$ and $\beta$ results in a decrease in $T_{\rm d}$ as $\beta$ is increased and vice versa. In the case of L1521E, it was noted that $T_{\rm d}$ derived in this work is high even though the derived $\beta$ is greater than 2. The small difference between the temperatures obtained from fitting to the SCUBA and background subtracted *Spitzer* data is also due to the fact that in this work, the fitting was carried out by taking $\beta$ as a free parameter whereas it was fixed to 2 in Kirk et al. (2007).

As is expected, the fitting to the SEDs from SCUBA and *Spitzer* carried out in this work resulted in the same wavelength ($\lambda_{\rm peak}$= 360 $\mu$m) for the peak of emission as that reported by Kirk et al. (2007). The SED from SPIRE data were peaked at a shorter wavelength of $\lambda_{\rm peak}$= 250 $\mu$m.

The derived optical depths are $\ll 1$ as is expected in these cold and dense environments. The derived dust masses from the two data sets ($M_{\rm d}$ = 0.44 $\pm$ 0.02 $M_{\odot}$ and 0.5 $\pm$ 0.1 $M_{\odot}$) are in agreement with each other. The column densities ($N_{\rm H_2}$ = 5.6 $\pm$ 0.2 $\times$ $10^{22}$ cm$^{-2}$ and 6 $\pm$ 1 $\times$ $10^{22}$ cm$^{-2}$) are also in agreement. Using the derived core diameter of 0.05 pc, the derived column density can be converted to a density of $n_{\rm H_2}$ = 3.9 $\pm$ 0.6 $\times$ $10^5$ cm$^{-3}$ which is in the range of $n_{\rm H_2}$ = 1.3 – 5.6 $\times$ $10^5$ cm$^{-3}$ derived by Hirota et al. (2002).

### 5.6.2 L1521F

There is a largest discrepancy in the derived temperature and dust emissivity indices for L1521F. Fitting to the SPIRE SED results in a temperature of 15.9 $\pm$ 0.2 K and a dust emissivity index of 0.9 $\mp$ 0.1 while fitting to the SED from SCUBA and *Spitzer* data results in a lower temperature of 9.9 $\pm$ 0.1 K and a dust emissivity index of 1.7 $\mp$

0.2. The temperature derived from the SPIRE data is also greater than that derived by Kirk et al. (2007) which was obtained by keeping the dust emissivity index constant at 2. Using the same dust emissivity index of 2 when fitting to the SPIRE data results in a lower dust temperature of 12 K, almost consistent with 9 ± 2 K derived by Kirk et al. (2005). Although the evidence is not totally compelling, tantalizingly, the higher temperature from the SPIRE data could be explained by the existence of the protostar in the L1521F core as reported by Bourke et al. (2006).

The fitting to SCUBA and *Spitzer* SED resulted in the same $\lambda_{\rm peak}$ (= 360 $\mu$m) as that reported in Kirk et al. (2007). However, fitting to the SPIRE SED resulted in $\lambda_{\rm peak}$ = 240 $\mu$m. The derived optical depths are in agreement. The differences in the derived temperatures and dust emissivity indices resulted in dust masses and column densities derived from SPIRE SED that are almost twice those from SCUBA and *Spitzer* SED. The derived mass and column density from SPIRE data are 1.74 ± 0.02 $M_\odot$ and 21.9 ± 0.3 × $10^{22}$ cm$^{-2}$. Those from SCUBA and *Spitzer* SED were 0.8±0.2 $M_\odot$ and 10 ± 2 × $10^{22}$ cm$^{-2}$. The mass derived from SPIRE data is lower and falls just outside the error range of $M_{\rm d}$ = 2.6 ± 0.8 $M_\odot$ derived by Kirk et al. (2005) in a 150″ aperture. The derived column density in this work is almost twice as large as 10 ± 3 × $10^{22}$ cm$^{-2}$ reported by Kirk et al. (2005).

### 5.6.3 L1689B

Values for the dust temperatures and emissivity indices for L1689B obtained using the two data sets were consistent. Fitting to the SPIRE SED results in a temperature of 15.0 ± 0.2 K and a dust emissivity index of 1.5 ∓ 0.1 consistent with a temperature of 14.7 ± 0.2 K and a dust emissivity index of 1.5 ∓ 0.1 obtained from fitting to the SED from

SCUBA and *Spitzer* data. Dust temperatures derived in this work are comparable to but slightly greater than 11 ± 2 K derived by Kirk et al. (2005) obtained by keeping the dust emissivity index constant at 2. Keeping the dust emissivity index constant at 2 when fitting to the SPIRE data lowers the dust temperature to 11.4 K which is consistent with their value.

The same wavelength for the peak of the SEDs was obtained in this work. The derived value of $\lambda_{\rm peak} = 220$ $\mu$m is slightly less than that reported by Kirk et al. (2007). As is the case for the other two cores discussed above, the derived optical column depths are comparable and $\ll 1$. Fitting to the SPIRE SED resulted in a mass of $1.34 \pm 0.02$ $M_\odot$ and a column density of $16.9 \pm 0.3 \times 10^{22}$ cm$^{-2}$. The calculated mass and column density from fitting to the SCUBA and *Spitzer* SED are $0.39 \pm 0.03$ $M_\odot$ and $5.0 \pm 0.4 \times 10^{22}$ cm$^{-2}$. While the mass calculated from fitting to the SPIRE data is close to 1.4 $M_\odot$ reported by Kirk et al. (2005), the column density from this work is twice as large.

## 5.7 Conclusion

In this chapter, results from fitting greybody functions to SEDs constructed from two sets of data have been compared. SEDs for three starless cores were constructed from SPIRE photometer data and low-spectral resolution spectra obtained using the SPIRE iFTS. Results have been compared with SEDs from data previously published by Kirk et al. (2007). In this work, the fitting was performed by keeping both the dust temperature and emissivity spectral index as free parameters whereas Kirk et al. (2007) fixed the emissivity spectral index at 2. The flux densities from the SPIRE instruments and those reported in Kirk

et al. (2007) are inconsistent. The reason for this is that prior to *Herschel*, SEDs were constructed by combining data from different ground- and space-based instruments having different beams, each sensitive to structure on a different scale. In order to combine data from different instruments, Kirk et al. (2007) had to use different assumptions about the spatial extent of the sources. This was challenging and results in lower flux densities than reported in this thesis for the SPIRE iFTS.

For the first time, *Herschel* provides a unique facility that is not affected by the Earth's atmosphere and that has a cooled primary mirror to minimize background emission. The SPIRE photometer and spectrometer use the same telescope and provide internally consistent results and furthermore measure near the peak of emission of these cold sources. *Herschel* has thus removed the ambiguity of combining SCUBA and *Spitzer* flux densities which are lie far from the peak of emission. This has led to more accurate values of dust emissivity index and temperature from which more accurate core masses have been calculated. For all the three sources analyzed, there is emission at lower wavelengths that cannot be fit with a single greybody function. Detailed radiative transfer modelling is required to explain this emission. The more accurate core properties derived from this work will improve radiative transfer models of starless and pre-stellar cores.

# Chapter 6

# Class 0 Protostar: IRAS16293-2422

## 6.1 Overview

A collapsing pre-stellar core develops into a Class 0 protostar (see Section 1.4). One of the characteristics of protostars is that they often exhibit bipolar outflows. The change in the physical and chemical properties of the parent cloud induced by bipolar outflows (e.g. Pineda et al., 2008; Friesen et al., 2010) can be studied using continuum and line emission. This chapter will focus on Spectral and Photometric Imaging Receiver Array (SPIRE) imaging Fourier transform spectrometer (iFTS) and photometer observations of IRAS16293-2422, a well studied Class 0 protostar. Section 6.2 provides an introduction to Class 0 sources and what information about these sources one can obtain from SPIRE iFTS and photometer observations. Our current understanding of IRAS16293-2422 is presented in Section 6.3. The details concerning the SPIRE iFTS observations of IRAS16293-2422 and data reduction are discussed in Section 6.4. The results are presented in Section 6.5.

## 6.2 Introduction

Class 0 protostars are surrounded and obscured by cold and dense envelopes making them observable only at millimetre and far-infrared wavelengths. The inner regions of the cold envelopes are heated by the central forming star raising the temperatures to enable evaporation of ice mantles of dust grains. Molecules such as CO and $H_2O$ are released back into the gas phase where they can be detected by their rotational emission lines. It is also well known that these deeply embedded protostars have high velocity outflows which supports the thesis that outflow and infall motions happen simultaneously (Bachiller, 1996).

Molecules such as water and CO also form in regions where bipolar outflows and winds from protostars meet with the surrounding material in envelopes (Kaufman & Neufeld, 1996). Molecular line emission is therefore used to trace outflowing gas. An interesting example is how CO has been used to trace the red and blue shifted lobes of a Class 0 protostar IRAS 20386+6751 (Bachiller et al., 2001). IRAS 20386+6751 is found in the L1157 molecular cloud and is one of the most illustrative cases of bipolar outflows (Bachiller et al., 2001). The basic theoretical concepts of these outflows are well understood but further observations are required to understand how the flows are driven (Bjerkeli et al., 2009). A challenge in the interpretation of observations of protostars is in the characterization of their lines of sight. In addition to emission from gas and ices in the envelopes and disks of protostars there might be emission from quiescent foreground material.

The results from the analysis of observations of IRAS-16293-2422 (hereafter referred to as IRAS16293), obtained using the SPIRE iFTS on board the *Herschel Space Observatory* (*Herschel*) (Griffin et al., 2010; Pilbratt et al., 2010), are presented in this chapter. The

SPIRE iFTS covers frequencies from ∼450 to 1550 GHz. This spectral band covers a number of emission lines from CO, C I, $H_2O$ and $HCO^+$ enabling us to study molecular outflows and inner regions of envelopes. However, the large beam of the SPIRE iFTS (Makiwa et al., 2013) does not provide sufficient spatial resolution to distinguish emission from the envelope, outflows and the central forming star. The largest SPIRE iFTS beam is 43″ which corresponds to ∼ 5160 astronomical unit (AU) (=0.025 pc) at the distance of 120 pc.

## 6.3 Source Background

IRAS16293 is a solar-type Class 0 protostar with a luminosity of 22 $L_\odot$ (Crimier et al., 2010) found in the L1689N molecular cloud in the nearby $\rho$ Ophiuchus star forming region. The distance to the $\rho$ Ophiuchus star forming region has previously been considered to be 160 pc (Whittet, 1974) but has recently been revised to 120 pc (Knude & Hog, 1998; Loinard et al., 2008; Lombardi et al., 2008). In this chapter we use the revised distance of 120 pc. Figure 6.1 shows images of IRAS16293 obtained at 450 and 850 $\mu$m. The images from the Submillimeter Common-User Bolometer Array (SCUBA) observations obtained in August 1999 are publicly available on the James Clerk Maxwell Telescope (JCMT) archive.

Our current understanding of IRAS16293 is that it is a low-mass protobinary system (Mundy et al., 1986) deeply embedded in a 2 $M_\odot$ envelope of size $\lesssim$ 1500 AU with a bolometric luminosity of 22 $L_\odot$ (Crimier et al., 2010). The two sources inside the envelope – source A which is located South-East ($\alpha_{2000} = 16^h32^m22.85^s$, $\delta_{2000} = -24°28'35.5''$) with a mass of ∼ 0.6 $M_\odot$ and source B located North-West ($\alpha_{2000} = 16^h32^m22.6^s$, $\delta_{2000} = -24°28'33''$) with a mass of ∼ 0.9 $M_\odot$ – are separated by about 4″ corresponding to a dis-

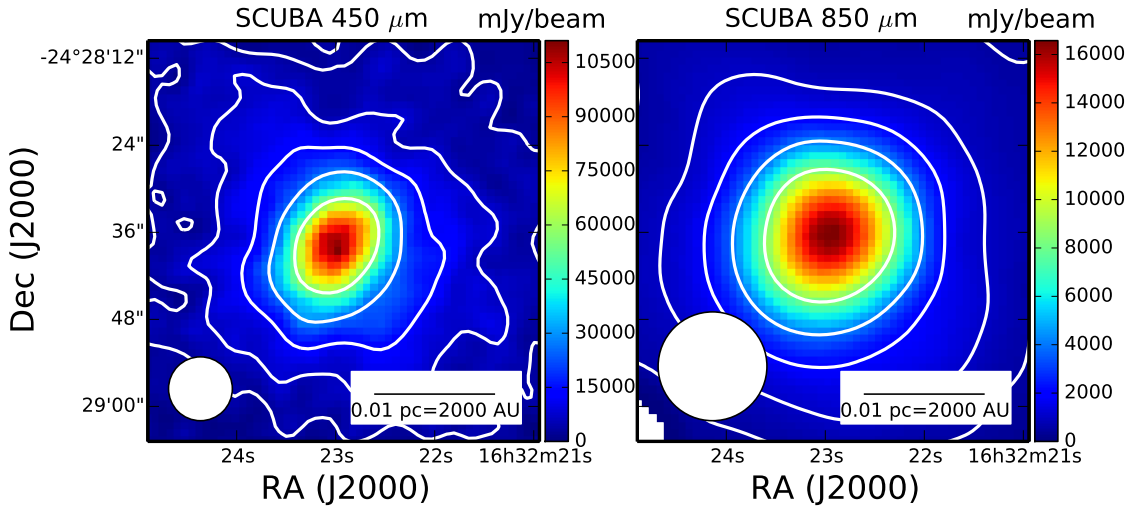


Figure 6.1: Images of IRAS16293 at 450 and 850 $\mu$m obtained with SCUBA in August 1999. The size of the beam and a linear scale are shown on the bottom left and right corners of each plot respectively. The intensity scale is in mJy/beam. The contours closest to the brightest point in each map are at half of the peak intensity and decrease by half going outwards.

tance of about 480 AU in the plane of the sky (Wootten, 1989; Mundy et al., 1992). Figure 6.2 shows a high spatial resolution image of IRAS16293 from the Atacama Large Millimeter Array (ALMA) showing the two protostars (A and B) and directions of the two outflows from source A (Loinard et al., 2013). Source A is more complex with two centimetre sources (A1 and A2) and two submillimeter sources (Aa and Ab) having been detected towards it (Wootten, 1989; Chandler et al., 2005; Walker et al., 1993). No substructure has been detected for source B at these wavelengths. Stark et al. (2004) have suggested that source B is a young T Tauri star[1] but recent high spectral resolution and high sensitivity observations

[1]A T Tauri star is at a later evolutionary stage than a Class 0 protostar.

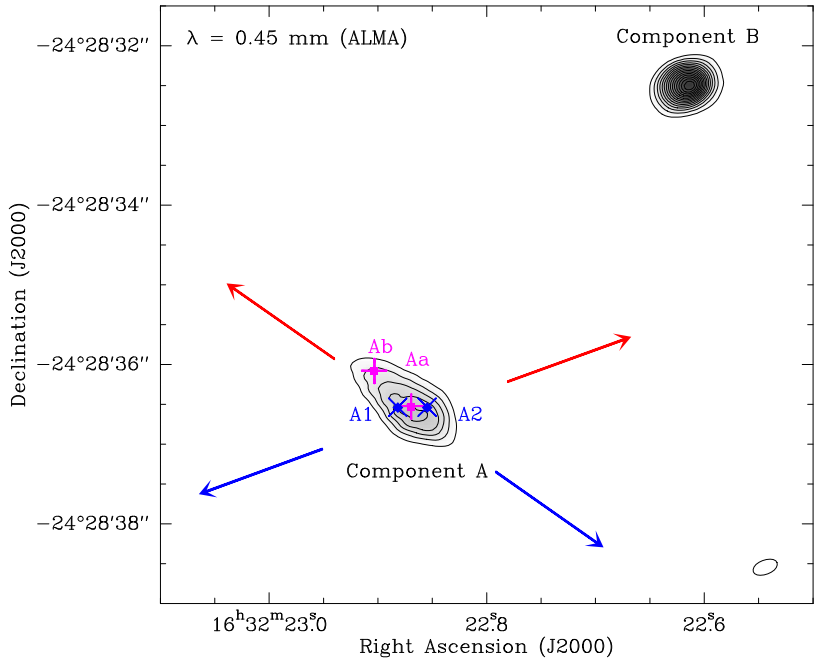


Figure 6.2: The image of IRAS16293 at 0.45 mm from ALMA. Sources A and B together with two outflow directions from source A (Mizuno et al., 1990) are labeled. Also shown are the submillimeter peaks Aa and Ab from (Chandler et al., 2005) and centimetre sources A1 and A2. Contours run from 0.2 to 4 Jy beam$^{-1}$ in steps of 0.2 Jy beam$^{-1}$. The circle at the bottom right corner represents the synthesized beam (0.32″ × 0.18″; -69°). Figure taken from Loinard et al. (2013).

obtained with the ALMA interferometer rules out this possibility (Pineda et al., 2012).

IRAS16293 has a rich chemistry, with hot-core-like (hot-corino) properties at small scales ($\sim$ 100 AU) (e.g. Ceccarelli et al., 1998; Caux et al., 2011; Coutens, A. et al., 2012; Pineda et al., 2012). Zhou (1995) has claimed that infall and outflow occur simultaneously in IRAS16293 and this agrees well with the general paradigm of star formation. Figure 6.1 shows that the outflows of IRAS16293 have a quadrupolar shape suggesting that the individual outflows of source A and source B are perpendicular (Walker et al., 1988; Mizuno et al., 1990; Walker et al., 1993).

## 6.4 Observations and data reduction

### 6.4.1 *Herschel*-SPIRE photometer observations

SPIRE Photometer maps of IRAS16293 were obtained as part of the Gould Belt guaranteed time key programmes for the study of star formation (André et al., 2010). Using the SPIRE and Photodetecting Array Camera and Spectrometer (PACS) photometers, a large area observation of the L1689 star forming cloud in the $\rho$ Ophiuchus star forming region was obtained. The SPIRE photometer operates at the photometer short wavelength (PSW), photometer medium wavelength (PMW) and photometer long wavelength (PLW) ranges centred at 250 $\mu$m (1199 GHz), 350 $\mu$m (857 GHz) and 500 $\mu$m (600 GHz) respectively. Two cross scans (Observation Identification Numbers (OBSIDs) = 1342205093 and 1342205094) were obtained. The two observations were processed using Herschel Interactive Processing Environment (HIPE) version 11 (HIPE, Ott 2010)[2] and merged using a Photometer Merging

[2]HIPE is a joint development by the Herschel Science Ground Segment Consortium, consisting of European Space Agency (ESA), the National Aeronautics and Space Administration (NASA) Herschel Science

script.

### 6.4.2 *Herschel*-SPIRE spectrometer observations

The Class 0 protostar IRAS16293 was observed as part of the "Evolution of Interstellar dust" key program under the Interstellar Medium (ISM) Specialist Astronomy Group (SAG4) (Abergel et al., 2010) using the SPIRE spectrometer on board the Herschel Space Observatory. The spectrometer operates at the spectrometer short wavelength (SSW) and the spectrometer long wavelength (SLW) covering wavelengths from 194-331 $\mu$m (1546 to 906 GHz) and 303-671 $\mu$m (989 to 447 GHz) respectively. The observations can be carried out in the high $\sim$1.2 GHz) spectral resolution (HR) and low $\sim$25 GHz) spectral resolution (LR) modes. Our observation was carried out on Operational Day 494 (OD494: 20 September 2010) and the OBSID is 1342204898.

We obtained a fully sampled spectral map of IRAS16293 centred on $\alpha_{2000} = 16^{\rm h}32^{\rm m}23.0^{\rm s}$, $\delta_{2000} = -24°28'33.0''$ and measuring an area of $\sim 3' \times 3'$. To achieve fully Nyquist sampled images, the beam steering mirror of the SPIRE iFTS is moved in a 16-point jiggle resulting in a beam spacing of 9.5″ and 17.5″ for SSW and SLW respectively. Figure 6.3 shows the actual positions observed on the sky for the IRAS16293 fully sampled observation for SSW (black squares) and SLW (white circles). The centre of the SSW map is not well sampled because the interferogram from some of the detectors pointings close to the peak of emission were saturated at the point of zero optical path difference. Efforts to correct for the saturation of the detectors have not been successful. The observation had 13 scans in high and low spectral resolution (4 scans in HR and 9 scans in LR) mode for

Center, and the Heterodyne Instrument for the Far Infrared (HIFI), SPIRE and SPIRE consortia.

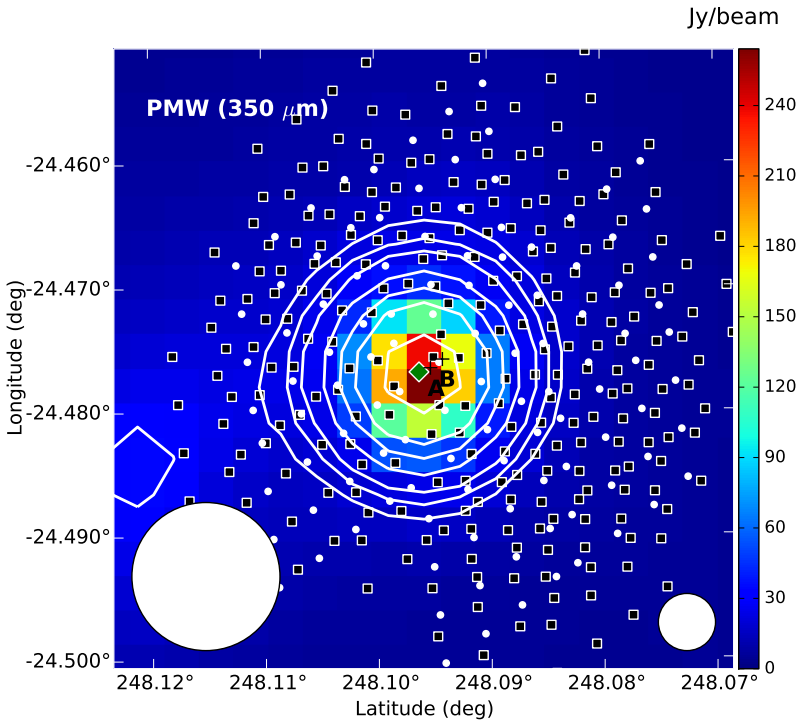


Figure 6.3: Actual positions observed on the sky for the IRAS16293 fully sampled FTS observation over-plotted on the 350 $\mu$m SPIRE photometer map. Pointings for the SSW detectors are represented by black squares while pointings for SLW detectors are represented by white circles. The green diamond represents the brightest point on the SPIRE photometer maps (to be shown in Figure 6.7). The plus signs labelled A and B represent the positions for IRAS16293A and IRAS16293B. The large and small circles on the bottom left and right sides of the image represent the largest and smallest FTS beams. Contours are at 30, 25, 20, 15, 12.5, 10 and 6.25 % of the peak flux.

a total integration time of 11491 s. The observation was processed using the Spectrometer Mapping Pipeline in HIPE version 11.

### 6.4.3 Map making

The standard Spectrometer Mapping Pipeline in HIPE version 11 uses a simple algorithm to regrid measured detector data into spectral data cubes with square pixels of sizes 9.5″ and 17.5″ for SSW and SLW respectively. In order to make a fair comparison of SSW and SLW spectra, they should be presented with the same pixel sizes and World Coordinate System (WCS). The size of the pixels was therefore fixed to half the SLW beam (17.5″) with the brightest pixels (position determined from SPIRE photometer maps at 250 $\mu$m) centred on $\alpha_{2000} = 16^{\mathrm{h}}32^{\mathrm{m}}23.09^{\mathrm{s}}$, $\delta_{2000} = -24°28'36.66''$ for both SSW and SLW maps. During the processing, we noticed that the shape of the spectra for semi-extended sources changes with the size of the pixels. This is due to the averaging of spectra coming from different regions of the same source. This problem can be solved by reducing the size of pixels. However, it is not possible to obtain information for pixels smaller than the Nyquist sampling and so the algorithm returns no values.

Since IRAS16293 is not uniformly extended, the processed spectra have a discontinuity in the overlap region between the SSW and SLW bands as shown in Figure 6.4. Applying point-source calibration to the spectral data cubes is also not useful since IRAS16293 is not a point source. Each box in Figure 6.4 represents a 17.5″ ×17.5″ pixel on the SSW and SLW spectral maps. The right ascension (RA) is on the horizontal axis and increases from right to left. The declination (Dec) is on the vertical axis and increases from bottom to top. A zoom-in of spectra for pixels close to the peak of emission is shown in Figure 6.5. The brightest pixel (pixel 5,3) shows a mismatch in the slopes for SSW and SLW spectra.

In an attempt to correct for the mismatch in the slopes of the spectra and the

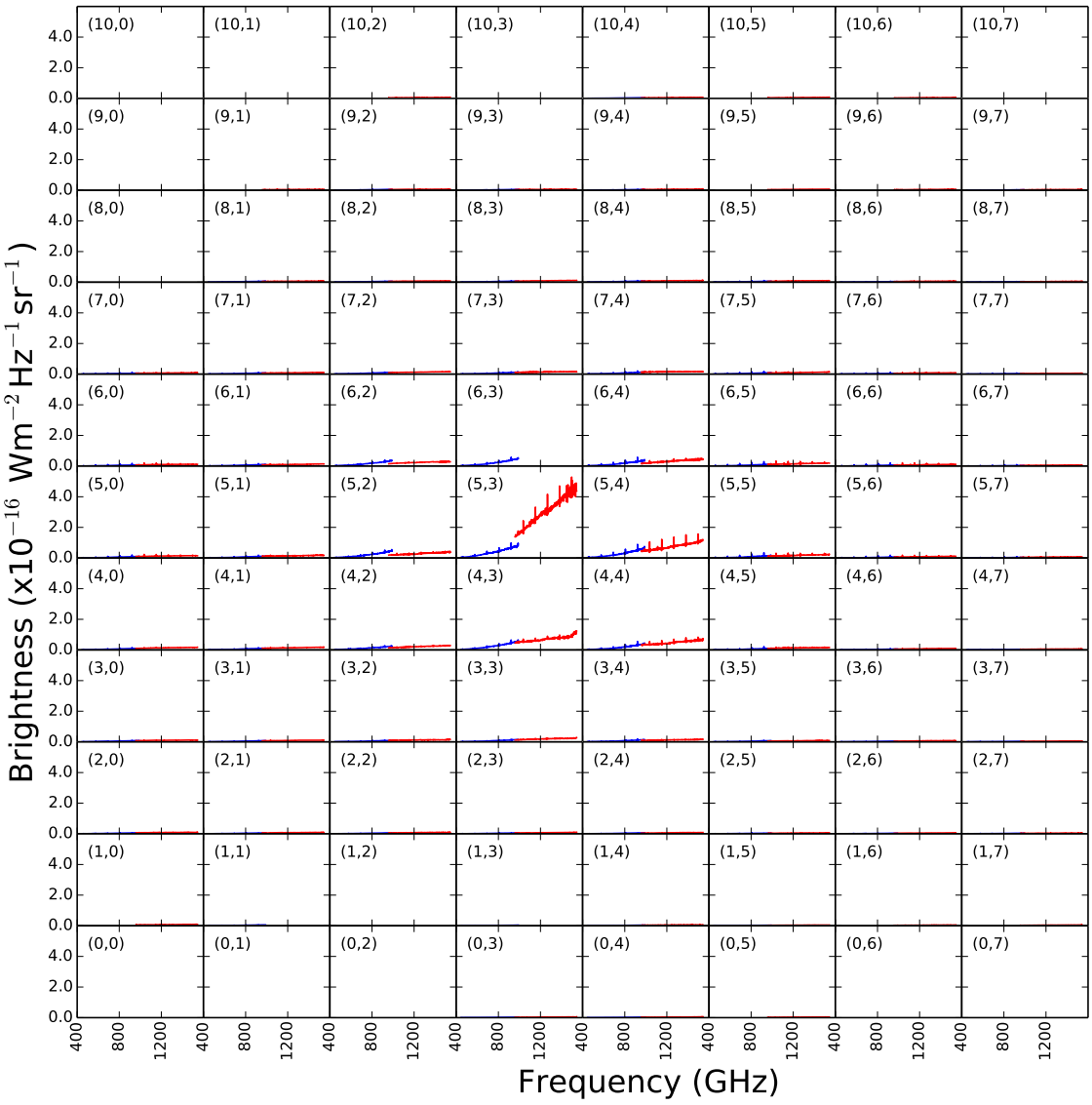


Figure 6.4: The combined SSW (red) and SLW (blue) spectra for all the pixels on the observed IRAS16293 maps. The map pixels corresponding to the spectra in each box are shown on the top left corner. There are many pixels where the signal is too faint to be seen.

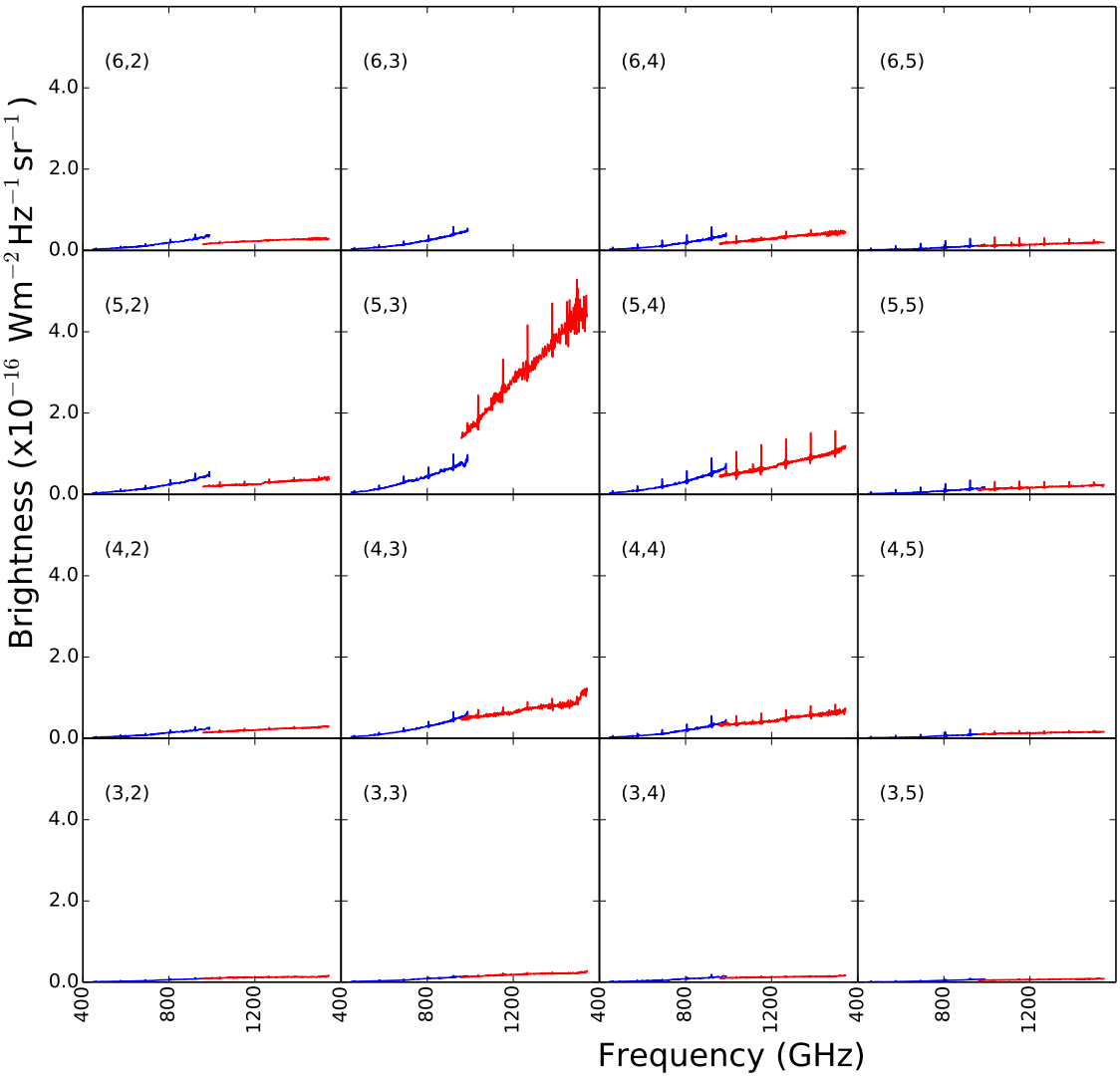


Figure 6.5: The combined SSW (red) and SLW (blue) spectra for pixels close to the peak of emission (Figure 6.4). The map pixels corresponding to the spectra in each box are shown on the top left corner.

gap in the overlap band, the maps were convolved to a common beam using beam profiles derived by Makiwa et al. (2013). A Gaussian kernel whose width is a quadrature difference between the maximum SPIRE iFTS beam and the beam at each frequency was used. This method does not resolve the discontinuity seen in the overlap region of SSW and SLW as was shown in Section 4.4.2. The SPIRE iFTS beam can be described by a 2-D Gaussian function in the SSW band and by complex 2-D Hermite-Gaussian functions in the SLW band. Therefore considering the SPIRE iFTS beam as Gaussian is expected to work only for the SSW band but not for the SLW band. A numerical method to properly convolve SPIRE iFTS and photometer maps to a common beam has been developed by Ayasso et al. (in prep) and is currently undergoing tests.

### 6.4.4 Line fitting

As stated before, the output spectra from HIPE sometimes exhibit a large mismatch in the overlap region between the SSW and SLW bands. In order to extract line information, the spectra for the brightest pixels in both bands were extracted from the maps and reprocessed using the point source flux calibration script. The point source calibrated spectra are represented by red lines in the top panel of Figure 6.6. The semi-extended corrector tool (Wu et al., 2013), was used to correct spectra from effects introduced by point source flux calibration. As described in Chapter 4, the tool uses the overlap region between the SSW and SLW bands and knowledge of the SPIRE iFTS beam profile (Makiwa et al., 2013) to estimate source extent and make a correction to the spectra. The source size required to correct for the gap between the SSW and SLW spectra was 15″ which corresponds to a source diameter of 1800 AU. This is in agreement with the envelope size of 1500 AU

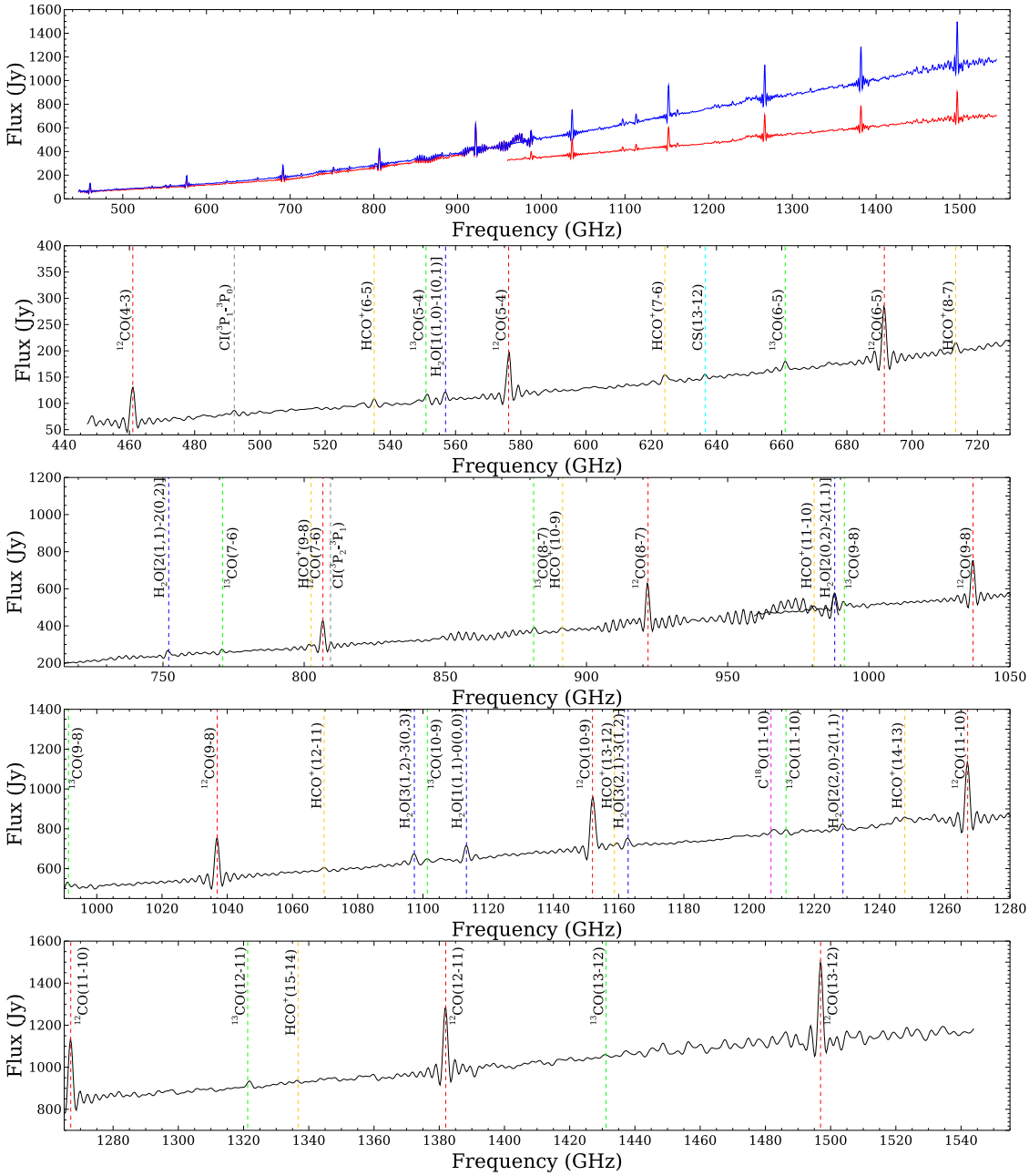


Figure 6.6: Top row: The spectrum for the brightest pixel of the IRAS16293 spectral map calibrated as a point source (red) and after correcting for source extent (blue). Bottom rows: Magnified sections of the corrected spectrum. Superimposed on the continuum is line emission of which the brightest lines belong to the $^{12}$CO ladder.

reported by Crimier et al. (2010) and with the extent seen in the SCUBA 450 $\mu$m maps (Figure 6.1). The corrected spectra are represented by blue lines in the top row of Figure 6.6. The plots in the bottom rows show the spectrum corrected for source extent divided into four regions to reveal the spectral lines and the predominantly sinc instrumental line profile. All identified lines are labelled and listed in Table 6.1. Line fitting was then carried out using the Spectrometer Line Fitting tool in HIPE.

In order to investigate the spatial extent of line emission, the Spectrometer Line Fitting tool was modified to loop through all the pixels in the maps transformed onto the same WCS as described in Section 6.4.3. The Spectrometer Line Fitting tool extracts the spectrum at a specified pixel, corrects it to the local standard of rest (LSR) frame using the satellite radial velocity, fits a polynomial to the continuum and uses user defined line positions to fit sinc profiles to the unapodized spectra. If the user enters the redshift and velocity of the source, the rest frequencies are shifted appropriately before line fitting. The user can also change the degree of the polynomial to be fit to the continuum. The results from the fit include the central frequency, amplitude and line width from which the integrated line fluxes can be calculated. At present the line width of the sinc profiles is fixed at 0.377 GHz (=1.1845/$\pi$ GHz) and efforts are underway to set the line width as a free parameter. In this case, fixing the line width is appropriate since the lines are intrinsically narrower than 1 GHz.

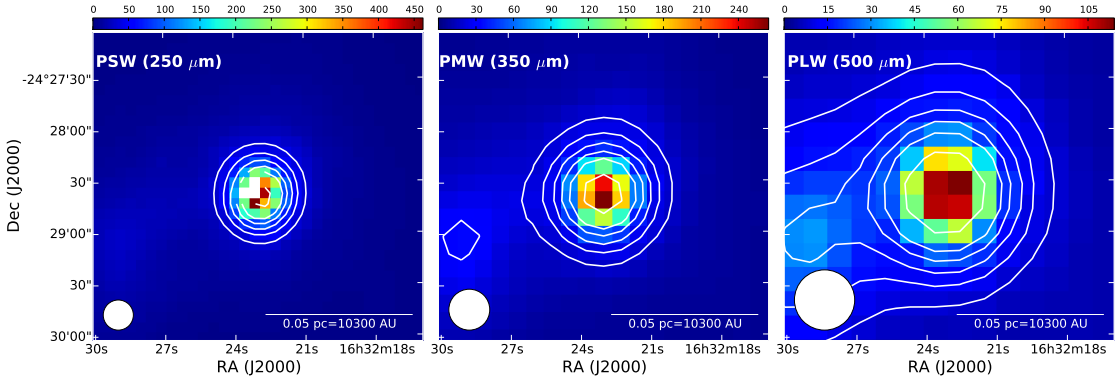


Figure 6.7: The SPIRE Photometer images of the region surrounding IRAS16293. On the left is the PSW image observed at 250 $\mu$m. At the centre is the PMW image observed at 350 $\mu$m and on the right side is the PLW image observed at 500 $\mu$m. The beam size in each spectral band is represented by the hatched circles on the bottom left corner of each image. A scale bar is shown on the bottom right corner of each image. Contours are at 10, 15, 20, 25, 30 and 50 % of the peak flux value in each map. This same region measuring $\sim 3' \times 3'$ (21600 AU $\times$ 21600 AU) was observed by the FTS in the full sampling mode.

## 6.5 Results

### 6.5.1 SPIRE photometer maps of IRAS16293

Figure 6.7 shows maps of IRAS16293 obtained with the SPIRE photometer. The photometer beam is shown on the bottom left corner of each map. Some bright pixels in the PSW map have been clipped. This is similar to what was seen for the centre detector in the SSW band of the iFTS. The same region was observed by the iFTS in the full sampling mode. The contour lines show that the source size compares to the beam size. The protobinary system, separated by $\sim 4''$ cannot be resolved by the SPIRE photometer. The maps confirm

that the protobinary system is closer to being a point source than being a fully extended source. In order to calibrate sources like IRAS16293, one has to consider the source spatial extent.

### 6.5.2 Line detections

We detect a wealth of molecular line emission from IRAS16293. The vertical coloured lines in Figure 6.6 show the different transitions from CO (red), $^{13}$CO (green), C$^{18}$O (magenta), C I (grey), $H_2O$ (blue), $HCO^+$ (orange) and CS (cyan). The results from line fitting are presented in Table 6.1. The upper level energies, $E_{\rm up}$, for each transition are listed. The $H_2O$ $2_{02}$-$1_{11}$ line appears in both the SSW and SLW bands. For this line, the recorded line flux value was obtained by fitting the SSW band which is less noisy.

Table 6.1: Line flux values for the brightest pixel on the IRAS16293 spectral data cubes.

| Species | Transition | $\nu_{\rm rest}$ [GHz] | $E_{\rm up}$ [K] | $\int F_\nu d\nu$ [$10^{-17}$W m$^{-2}$] | $\int F_\nu d\upsilon$ [$10^3$Jy km s$^{-1}$] |
|---|---|---|---|---|---|
| $^{12}$CO | 4-3 | 461.0 | 55.3 | 75.2±6.1 | 49.4±4.0 |
| | 5-4 | 576.3 | 83.0 | 91.0±6.0 | 47.9±3.2 |
| | 6-5 | 691.5 | 116.2 | 112.9±6.0 | 49.5±2.6 |
| | 7-6 | 806.7 | 154.9 | 173.6±6.0 | 65.2±2.3 |
| | 8-7 | 921.8 | 199.1 | 254.2±6.0 | 83.6±2.0 |
| | 9-8 | 1036.9 | 248.9 | 240.4±6.4 | 70.3±1.9 |
| | 10-9 | 1152.0 | 304.2 | 314.4±8.8 | 82.7±2.3 |
| | 11-10 | 1267.0 | 365.0 | 342.5±6.3 | 81.9±1.5 |
| | 12-11 | 1382.0 | 431.3 | 355.8±6.3 | 78.0±1.4 |
| | 13-12 | 1496.9 | 503.1 | 432.9±6.4 | 87.6±1.3 |
| $^{13}$CO | 5-4 | 550.9 | 79.3 | 16.9±6.0 | 9.3±3.3 |
| | 6-5 | 661.1 | 111.1 | 17.4±6.0 | 8.0±2.8 |
| | 7-6 | 771.2 | 148.1 | 23.1±6.0 | 9.1±2.4 |

Continued on next page

Table 6.1 – continued from previous page

| Species | Transition | $\nu_{\rm rest}$ [GHz] | $E_{\rm up}$ [K] | $\int F_\nu d\nu$ [$10^{-17}$W m$^{-2}$] | $\int F_\nu d\upsilon$ [$10^3$Jy km s$^{-1}$] |
|---|---|---|---|---|---|
| | 8-7 | 881.3 | 190.4 | 28.7±6.0 | 9.9±2.1 |
| | 9-8 | 991.3 | 237.9 | 30.3±6.5 | 9.3±2.0 |
| | 10-9 | 1101.3 | 290.8 | 17.9±6.4 | 4.9±1.8 |
| | 11-10 | 1211.3 | 348.9 | 25.0±6.3 | 6.3±1.6 |
| | 12-11 | 1321.3 | 412.3 | 21.0±6.4 | 4.8±1.5 |
| | 13-12 | 1431.2 | 481.0 | 16.9±6.3 | 3.6±1.3 |
| [C I ] | $^3P_1$-$^3P_0$ | 492.2 | 23.6 | 8.9±6.0 | 5.5±2.8 |
| | $^3P_2$-$^3P_1$ | 809.3 | 62.5 | 7.6±6.0 | 3.7±2.8 |
| $H_2O$ | $1_{10}$-$1_{01}$ | 556.9 | 61.0 | 18.2±6.1 | 9.9±3.3 |
| | $2_{11}$-$2_{02}$ | 752.0 | 137.0 | 36.3±6.0 | 14.6±2.4 |
| | $2_{02}$-$1_{11}$ | 987.9 | 100.8 | 73.9±6.0 | 22.7±1.8 |
| | $3_{12}$-$3_{03}$ | 1097.4 | 249.4 | 55.5±6.4 | 15.3±1.8 |
| | $1_{11}$-$0_{00}$ | 1113.3 | 53.4 | 76.5±6.4 | 20.8±1.7 |
| | $3_{12}$-$2_{21}$ | 1153.1 | 249.4 | 99.3±8.0 | 26.1±2.1 |
| | $3_{21}$-$3_{12}$ | 1162.9 | 305.2 | 53.5±6.3 | 13.9±1.6 |
| | $2_{20}$-$2_{11}$ | 1228.8 | 195.9 | 29.4±6.3 | 7.3±1.6 |
| $HCO^+$ | 6-5 | 535.1 | 89.8 | 14.3±6.0 | 8.0±3.4 |
| | 7-6 | 624.2 | 119.8 | 13.4±6.0 | 6.5±2.9 |
| | 8-7 | 713.3 | 154.1 | 11.1±6.0 | 4.7±2.5 |
| | 9-8 | 802.5 | 192.6 | 28.8±6.0 | 10.9±2.3 |
| | 10-9 | 891.6 | 235.4 | 14.6±6.0 | 5.0±2.0 |
| | 11-10 | 980.6 | 282.4 | 24.7±6.3 | 7.6±1.9 |
| | 12-11 | 1069.7 | 333.8 | 14.8±6.2 | 4.2±1.8 |
| | 13-12 | 1158.7 | 389.4 | 23.3±6.3 | 6.1±1.6 |
| | 14-13 | 1247.7 | 449.3 | 43.1±6.2 | 10.5±1.5 |

Notes: The rest frequencies ($\nu_{\rm rest}$) and upper level energies ($E_{\rm up}$) were obtained from the JPL database (Pickett et al. (1998), http://spec.jpl.nasa.gov/). The $1\sigma$ uncertainties in the table are from line fitting and do not include those related to absolute calibration, which are $\sim 7\,\%$ for the mapping mode (Swinyard et al., 2014). Converting from W m$^{-2}$ to Jy km s$^{-1}$ was achieved using $\int F_\nu d\upsilon$ (Jy km s$^{-1}$) = $\int F_\nu d\nu$ (W m$^{-2}$) $\times$ 0.3 $\times$ $10^{23}$ $\nu_{\rm GHz}^{-1}$.

Figure 6.8 shows the $^{12}$CO and $^{13}$CO rotational diagrams (Section 2.4.3) for IRAS16293. The rotational temperatures were derived by fitting a line to the integrated line intensities, with the slope of the line being equal to $1/T_{\rm rot}$. Clearly, data for $^{12}$CO cannot be fit by a single temperature, and so the $J_{\rm up}$ $\leq$6 and $J_{\rm up}$ >6 lines were fit separately. Data for $^{13}$CO was fit with a single temperature. The selection of the breakpoint in fitting two components to the $^{12}$CO rotational diagrams is arbitrary and so has an effect on the final results.

The derived temperatures from the $^{12}$CO line fluxes are $T_{\rm rot}$ = 36 K for $E_{\rm up} \leq$ 116.2 K and 153 K for $E_{\rm up}$ > 116.2 K. The fit to the $^{13}$CO data produced a rotational temperature $T_{\rm rot}$ = 86 K. The lower temperature $J_{\rm up}$ $\leq$6 $^{12}$CO transitions are tracing the colder outer layers of the envelope. The higher $^{12}$CO transitions originate from inner regions of the envelope and disk of the protobinary system. These regions are heated by the central forming star. The less optically thick $^{13}$CO lines seem to originate from inner regions of the envelope, at least further than the lowest $J$ $^{12}$CO ones with $T_{\rm rot}$ = 36 K. However, it is well understood that optical depth effects and varying temperature regimes makes intepreting results from rotation diagrams quite challenging. Fortunately, the Fourier transform spectrometer (FTS) also measured isotopic lines, like $^{13}$CO, which are generally optically thin.

### 6.5.3 Spatial distribution of lines

In this section, the spatial distribution of emission lines detected in the spectral cube of IRAS16293 are discussed. The maps were constructed using Level-2 data cubes transformed onto the same WCS and no convolution was carried out. In order to make a fair comparison of the transitions at different frequencies, source extent and the wavelength

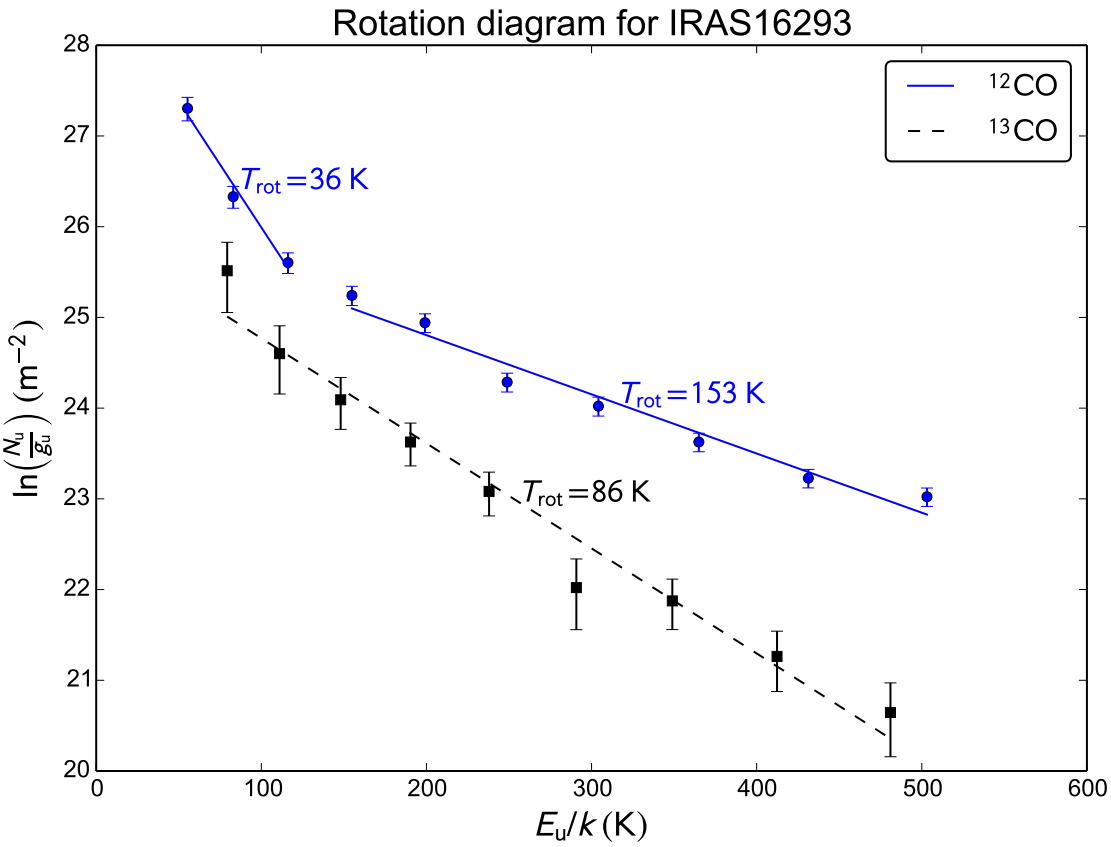


Figure 6.8: Rotational diagram for $^{12}$CO (blue circle points and solid line) and $^{13}$CO (black square points and dashed line) in IRAS16293. Error bars include errors from fitting and the 7 % calibration uncertainty (Swinyard et al., 2014). Solid lines indicate the best linear fit to selected data points.

dependent SPIRE iFTS beam should be taken into account.

### Carbon Monoxide

Figure 6.9 shows line intensity maps for all 10 $^{12}$CO transitions measured in the SPIRE band. Since Full Width Half Maximum (FWHM) is a measure of source size, the first contour on the maps was set at 50 %. However, since the region of emission is greater than one pixel for only the first two transitions that we detect, there is no 50 % contour on the maps for transitions above $J = 5 - 4$. Maps for lines in the SSW band only show the contour at 10 % (and at 20 % in the case of the $J = 9 - 8$ transition).

These line intensity maps together with photometer maps show that the gas and dust in IRAS16293 are both resolved. It is clearly seen that the low-J transitions which trace cold gas are extended and high-J transitions which are susceptible to opacity effects originate from a compact region. $^{13}$CO maps shown in Figure 6.10 also show the same trend. While this may be considered as evidence that the different transitions are tracing different regions of IRAS16293, it could also be due to beam dilution since the beam sizes for the SLW band are much larger than those for the SSW band.

The brighter and more extended emission from the lower transitions make it difficult to see elongated emission in the North-West direction. There is stronger evidence for elongated emission in the higher $^{12}$CO transitions. The maps for lower $^{12}$CO transitions peak at a position that is to the west of the peak position for higher $^{12}$CO and all $^{13}$CO transitions. Only five $^{13}$CO transitions (four in SLW and one in SSW) were detected. The higher transitions in the band were faint and the fit returned integrated line intensities of the same order as the noise level.

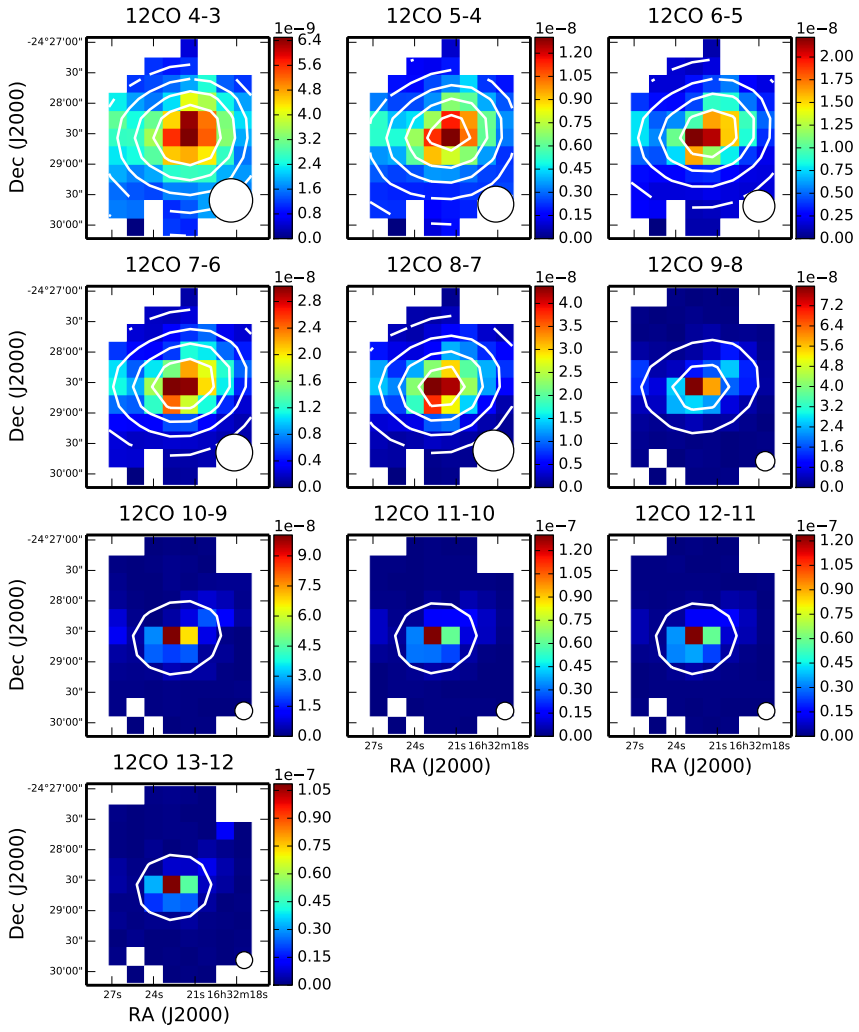


Figure 6.9: $^{12}$CO (J = 4 – 3 to 13 – 12) integrated line intensity maps for IRAS16293. The units for the colour bars are $\mathrm{Wm^{-2}sr^{-1}}$. The circle on the bottom right corner represents the SPIRE iFTS beam at each $^{12}$CO transition. Contours are at 10, 20, 30, 40 and 50 % of the peak flux in each map. In this figure, it is clearly seen that emission from low-J transitions which probe cold gas is extended and that from high-J transitions which are less susceptible to opacity effects is point-like.

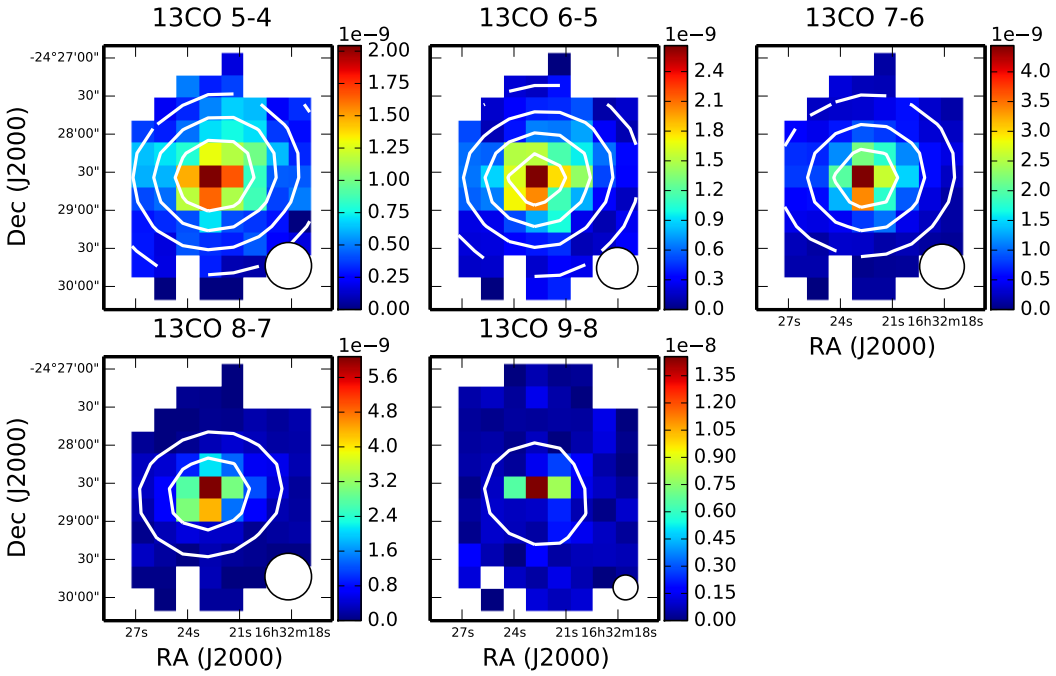


Figure 6.10: $^{13}$CO (J=5-4 to 9-8) integrated line intensity maps for IRAS16293. The units for the colour bars are $\mathrm{Wm^{-2}sr^{-1}}$. The circle on the bottom right corner represents the SPIRE iFTS beam at each $^{13}$CO transition. Contours are at 10, 20, 30 and 40 % of the peak flux value in each map. In this figure, it is clearly seen that emission from low-J transitions which probe cold gas is extended and that from high-J transitions, which are less susceptible to opacity effects, is more point-like.

### Neutral carbon

Figure 6.11 shows intensity maps for the two C I transitions in the SPIRE iFTS band. The map for the $^3P_1$ – $^3P_0$ transition peaks at the same position as the higher $^{12}$CO transitions. $^3P_2$-$^3P_1$ emission appears to be much more extended than the $^3P_1$-$^3P_0$ transition. A likely reason for this difference is that the $^3P_2$ – $^3P_1$ line is blended with an often strong $^{12}$CO J = 7 – 6 line making it a challenge to extract more accurate integrated line intensities. To illustrate this point, Figure 6.12 shows the region of the spectrum where the $^{12}$CO J = 7 – 6 and $^3P_2$ – $^3P_1$ lines are found. The measured spectrum is shown in blue while the best fit to all lines in the spectrum is shown in black. The two sinc profiles shifted from the zero line show the fit to the $^{12}$CO J = 7 – 6 line (green) and the fit to the $^3P_2$ – $^3P_1$ line (red). When the $^3P_2$ – $^3P_1$ line is faint the uncertainty in the derived parameters for this line increases. Thus caution should be exercised in interpreting the C I $^3P_2$ – $^3P_1$ map for IRAS16293 where the line emission is weak.

### Water

Absorption of radiation by water vapour in the Earth's atmosphere make measurements of water with ground-based telescopes impossible. A total of nine water lines shown in Table 6.1 have been observed in the SPIRE FTS spectrum for IRAS16293. Line intensity maps for eight of the water lines are shown in Figure 6.11. Of all the water emission lines detected, emission from the ground state transition ($1_{10}$-$1_{01}$) which occurs at 557 GHz is the most extended. This line has been observed in a number of Class 0 and I protostars with HIFI (de Graauw et al., 2010) on *Herschel* as part of the Water in star-forming regions with

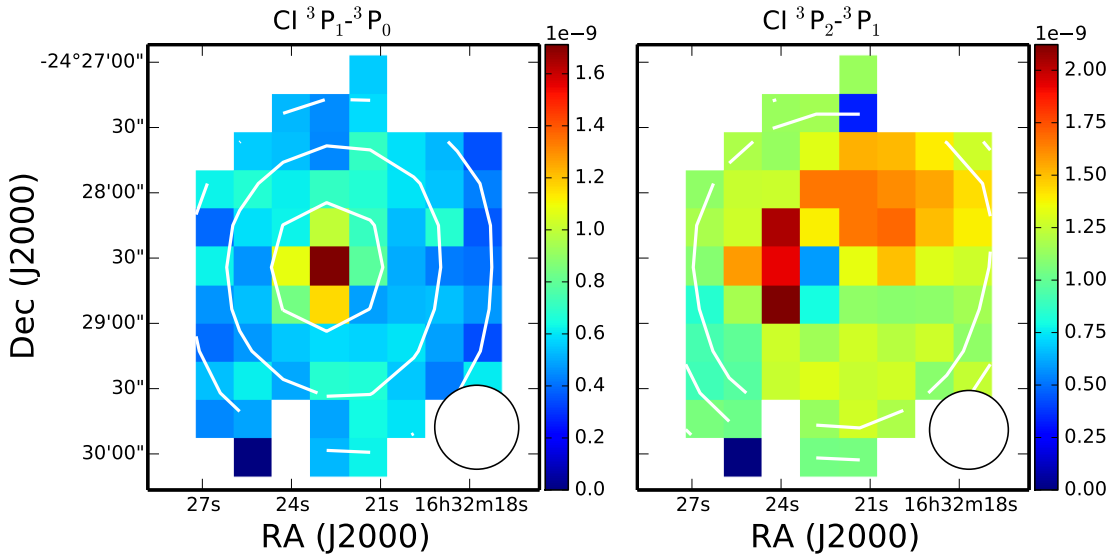


Figure 6.11: C I ($^3P_1 - {}^3P_0$ and $^3P_2 - {}^3P_1$) integrated line intensity maps for IRAS16293. The units for the colour bars are $Wm^{-2}sr^{-1}$. The circle on the bottom right corner represents the SPIRE iFTS beam at each C I transition. Contours are at 20, 30 and 40 % of the peak flux value in each map. In this figure, it is clearly seen that emission from $^3P_1 - {}^3P_0$ transition is point-like suggesting that it originates from the envelope + disk system of IRAS16293. Emission from the $^3P_2 - {}^3P_1$ transition is quite extended. However, the uncertainties in the integrated line intensities for the $^3P_2 - {}^3P_1$ line are larger since the line is blended with an often strong $^{12}$CO J = 7 – 6 line.

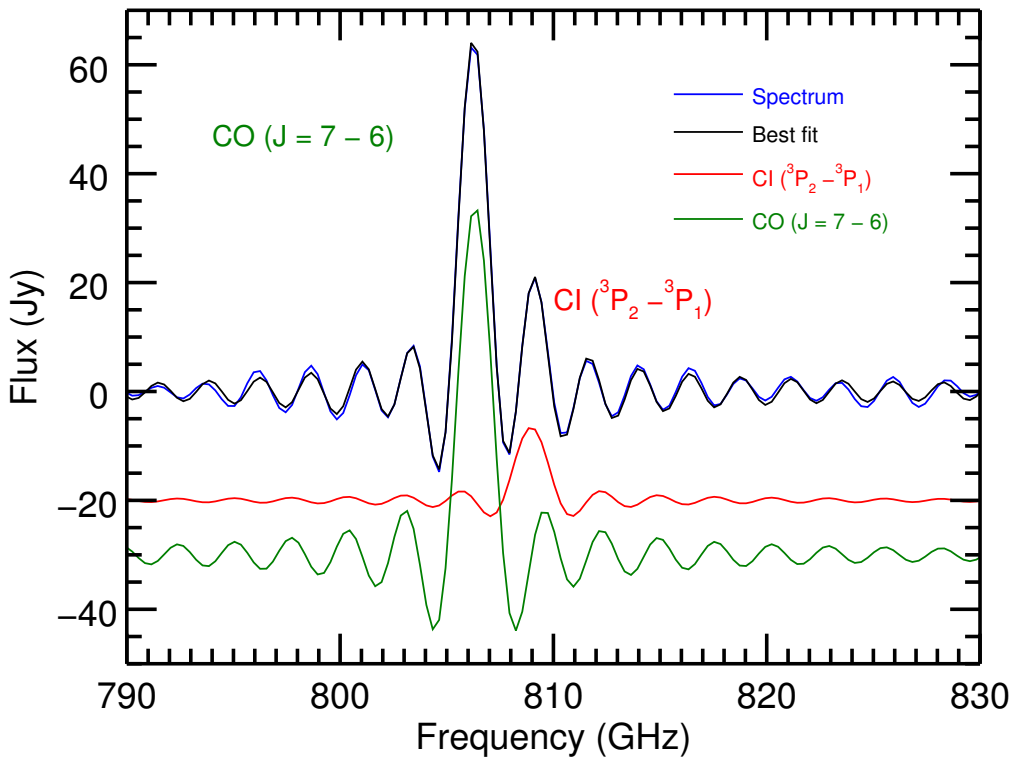


Figure 6.12: Line fitting for the blended $^{12}$CO J = 7 – 6 and C I $^3$P$_2$ – $^3$P$_1$ lines. The continuum subtracted spectrum is shown in blue and the total fit to all identified lines in the spectrum is in black. The fit to the $^{12}$CO J = 7 – 6 line is shown in green and that to the C I $^3$P$_2$ – $^3$P$_1$ line is shown in red. For clarity, the fits to the $^{12}$CO J = 7 – 6 and C I $^3$P$_2$ – $^3$P$_1$ lines have been shifted from the zero line.

Herschel (WISH) program (Kristensen et al., 2012).

The high spectral resolution HIFI instrument has detected absorption and emission lines of water from IRAS16293 that are a mixture of emission and absorption (Emmanuel Caux, private communication). This structure is completely diluted in our low spatial resolution SPIRE iFTS spectra. This makes modelling of the water lines from our results more challenging. However, when combined with spectrally resolved lines from HIFI, our maps provide the spatial extent that help in constraining radiative transfer models.

Water is directly associated with the emergence of life on Earth and the search for it in space has become one of the key priorities in our search for habitable exosolar planets. The water observed in protostars will probably go into the protoplanetary disks and ultimately end up on comets and eventually on planets.

### $HCO^+$

Figure 6.14 shows the intensity maps for $HCO^+$. The emission is peaks at the location of IRAS16293 just like in other molecular line emission maps discussed above. The intensity map for the 713 GHz $HCO^+$ 8-7 emission line appears more confined and its peak intensity is greater than that for higher transitions of the same molecule. This is not physical and might be due to problems in the linefitting. $HCO^+$ emission lines have been detected in the envelopes of a number of low-mass Young Stellar Objectss (YSOs) (Gregersen et al., 1997). The 357 GHz $HCO^+$ 4-3 emission line (not in the SPIRE band) is less optically thick than the 557 GHz $1_{10}$-$1_{01}$ water line and therefore has been used as a tracer of the collapse structure of YSOs (Gregersen et al., 1997).

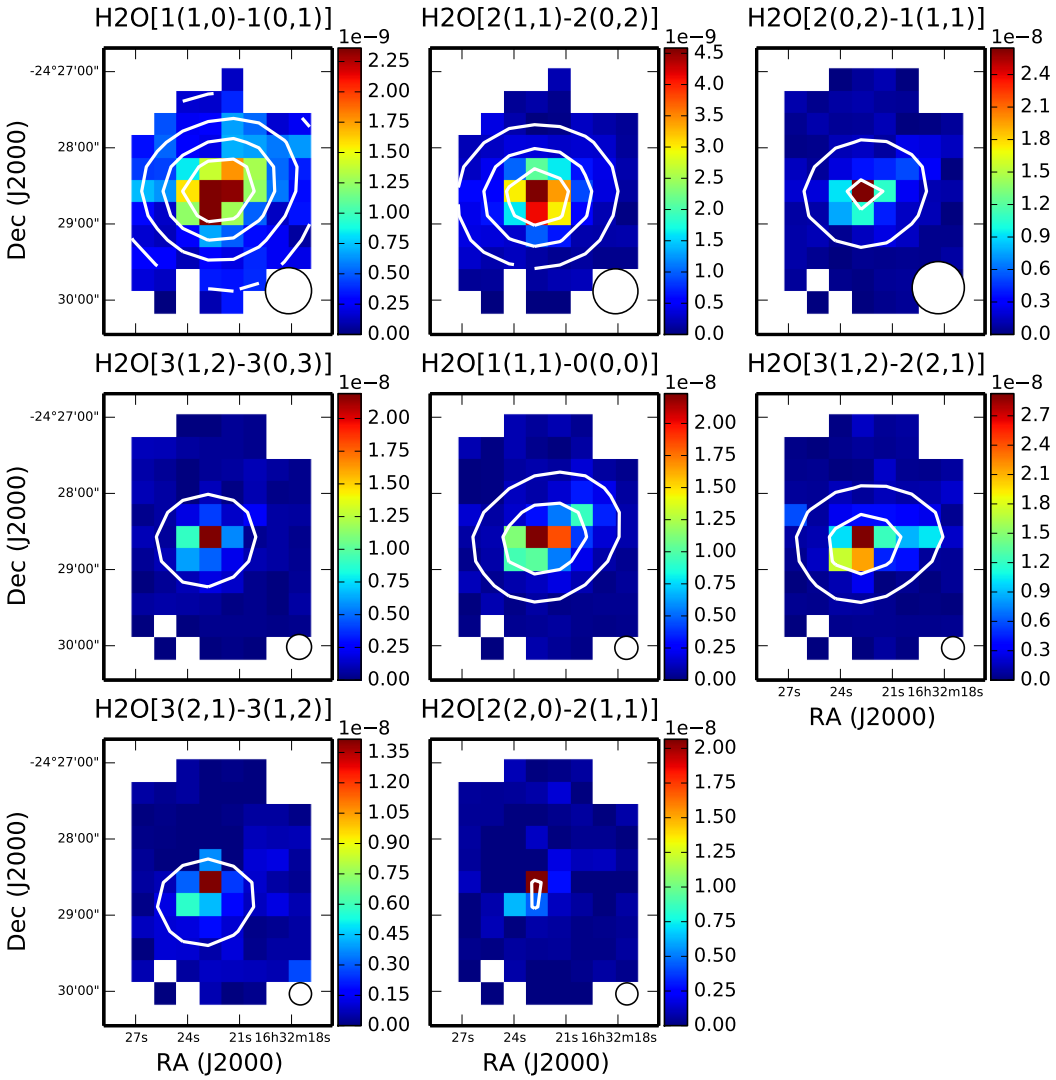


Figure 6.13: $H_2O$ integrated line intensity maps for IRAS16293. The units for the colour bars are $Wm^{-2}sr^{-1}$. The circle on the bottom right corner represents the SPIRE iFTS beam at each $H_2O$ transition. Contours are at 10, 20, 30 and 40 % of the peak flux value in each map. It is clearly seen that emission from water is point-like suggesting it originates from the envelope + disk system.

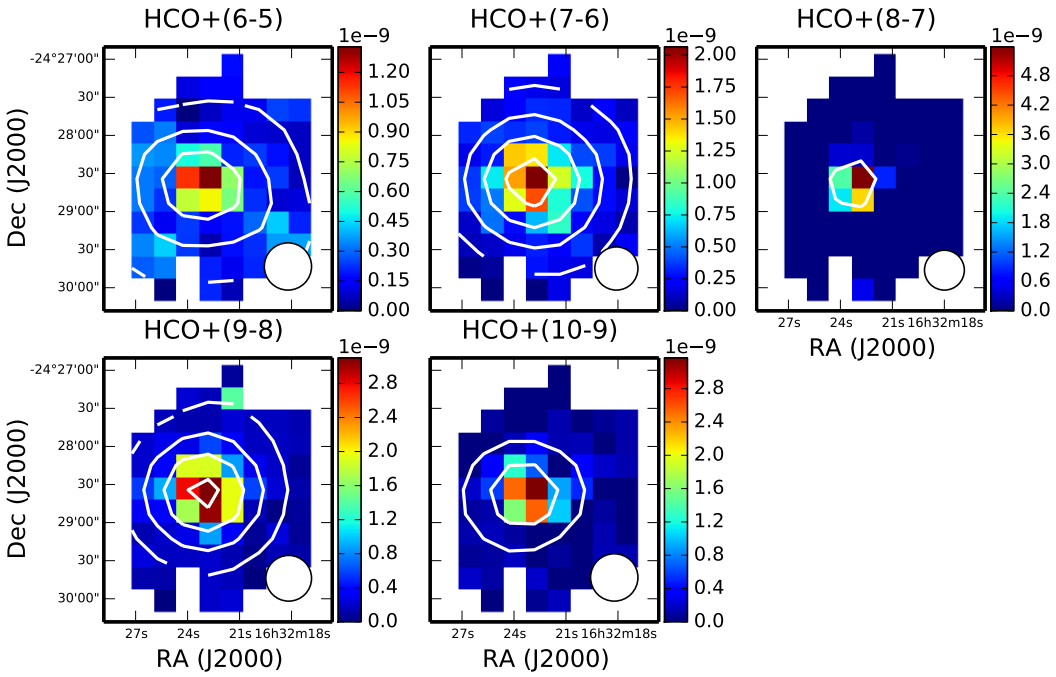


Figure 6.14: $HCO^+$ integrated line intensity maps for IRAS16293. The units for the colour bars are $Wm^{-2}sr^{-1}$. The circle on the bottom right corner represents the SPIRE iFTS beam at each $HCO^+$ transition. Contours are at 20, 30 and 40 % of the peak flux value in each map. The figure shows that emission from $HCO^+$ is also point-like.

### 6.5.4 SED of IRAS16293

Figure 6.15 shows the spectral energy distribution (SED) for IRAS16293. In order to construct the SED, we obtained data from many ground- and space-based instruments (see Table 6.2). Converting the data to a common beam is a challenge. Fortunately, in the case of IRAS16293, the source size is $\sim 15''$ which is smaller than any of the apertures used in extracting the photometer flux values. The spectrum for IRAS16293 obtained by the *Infrared Space Observatory* (*ISO*) long wavelength spectrometer (LWS) was binned into ten data points, each one representing one detector (Correia et al., 2004). These were then entered into Table 6.2 as if they were photometric data points. The UKT14 data points were obtained from Sandell (1994). There is good agreement between the SPIRE iFTS spectral data and the flux values from other instruments.

The black diamond shaped points in Figure 6.15 represent flux values from the various instruments. Spectra from the SPIRE iFTS are shown in blue. The black dashed line shows the best greybody fit to the data (see Section 2.3). The derived dust temperature and emissivity index are $T_{\rm dust} = 27.8 \pm 0.3$ K and $\beta = 1.45 \mp 0.01$. Although the data is fit well at longer wavelengths, the fit does not represent the data well at wavelengths $\leq 100$ $\mu$m. As was seen in Figure 6.9 where emission from low-J $^{12}$CO transitions is more extended than that for high-J transitions, this further confirms that the next level in understanding IRAS16293 is to use models that take into account various temperature and density regimes.

The above method of fitting a greybody to the SED assumes that the source can be described by a single temperature and a uniform density. However, it is known that beside the evolutionary state of the object, various parameters like viewing angle have an effect

Table 6.2: Photometer flux values for IRAS16293. The first three columns show the wavelength, observed flux ($F$) and errors ($\Delta F$). Errors include statistical measurement errors and uncertainties in the absolute calibration. Columns 4 and 5 show the beam sizes for the instrument ($\theta_{\rm beam}$) used to obtain the data and the size of the aperture ($\theta_{\rm aperture}$) over which the flux is measured. Columns 6 and 7 show the photometer used to obtain the data and the reference from which the data was taken. Refs.–(1) Correia et al. (2004); (2) IRAS Point Source Catalogue ; (3) Sandell (1994); (4) Walker et al. (1990); (5) *Spitzer* catalogue; (6) Crimier et al. (2010); (7) Saraceno et al. (1996).

| $\lambda$ [$\mu$m] | $F$ [mJy] | $\Delta F$ [mJy] | $\theta_{\rm beam}['']$ | $\theta_{\rm aperture}['']$ | Instrument | Ref. |
|---|---|---|---|---|---|---|
| 23.7 | 0.6 | 0.1 | 6.0 | 80 | MIPS | 5 |
| 25 | 1.8 | 0.7 | 80.0 | 80 | *IRAS* | 2,6 |
| 50 | 150 | 45 | 80 | 80 | *ISO*-LWS | 1 |
| 60 | 255 | 122 | 160.0 | 80 | *IRAS* | 2,6 |
| 60 | 350 | 105 | 80 | 80 | *ISO*-LWS | 1 |
| 70 | 640 | 196 | 80 | 80 | *ISO*-LWS | 1 |
| 80 | 940 | 282 | 80 | 80 | *ISO*-LWS | 1 |
| 90 | 1180 | 354 | 80 | 80 | *ISO*-LWS | 1 |
| 100 | 1032.0 | 412 | 237.0 | 80 | *IRAS* | 2,6 |
| 100 | 1320 | 396 | 80 | 80 | *ISO*-LWS | 1 |
| 125 | 1590 | 477 | 80 | 80 | *ISO*-LWS | 1 |
| 150 | 1590 | 477 | 80 | 80 | *ISO*-LWS | 1 |
| 175 | 1360 | 408 | 80 | 80 | *ISO*-LWS | 1 |
| 190 | 1100 | 330 | 80 | 80 | *ISO*-LWS | 1 |
| 250 | 645 | 25 | 17.6 | 80 | SPIRE | 1 |
| 350 | 368 | 19 | 23.9 | 80 | SPIRE | 1 |
| 350 | 235 | 19 | 19.5 | 19.5 | UKT14 | 3 |
| 350 | 500 | 250 | 9.0 | 19.5 | UKT14 | 3 |
| 450 | 270 | 108 | 7.8 | 40 | SCUBA | 6 |
| 450 | 119 | 11 | 18.5 | 18.5 | UKT14 | 3 |
| 500 | 129 | 11 | 35.2 | 80 | SPIRE | 1 |
| 750 | 28.1 | 1.5 | 17.5 | 17.5 | UKT14 | 3 |
| 800 | 18.5 | 0.5 | 13.5 | 13.5 | UKT14 | 3 |
| 800 | 21.1 | 0.5 | 17.5 | 17.5 | UKT14 | 3 |
| 850 | 20.2 | 8.0 | 14.5 | 40 | SCUBA | 1 |
| 850 | 17.3 | 0.9 | 17.5 | 17.5 | UKT14 | 3 |
| 1100 | 8.4 | 0.3 | 17.5 | 18.5 | UKT14 | 3 |
| 1300 | 6.97 | 2.24 | 30.0 | | NRAO | 4 |
| 1300 | 6.4 | 2.6 | 22.0 | 22 | UKT14 | 3 |
| 2000 | 2.4 | 0.2 | 27 | 27 | UKT14 | 3 |
| 2730 | 0.55 | 0.08 | 60.0 | | NRAO | 4 |

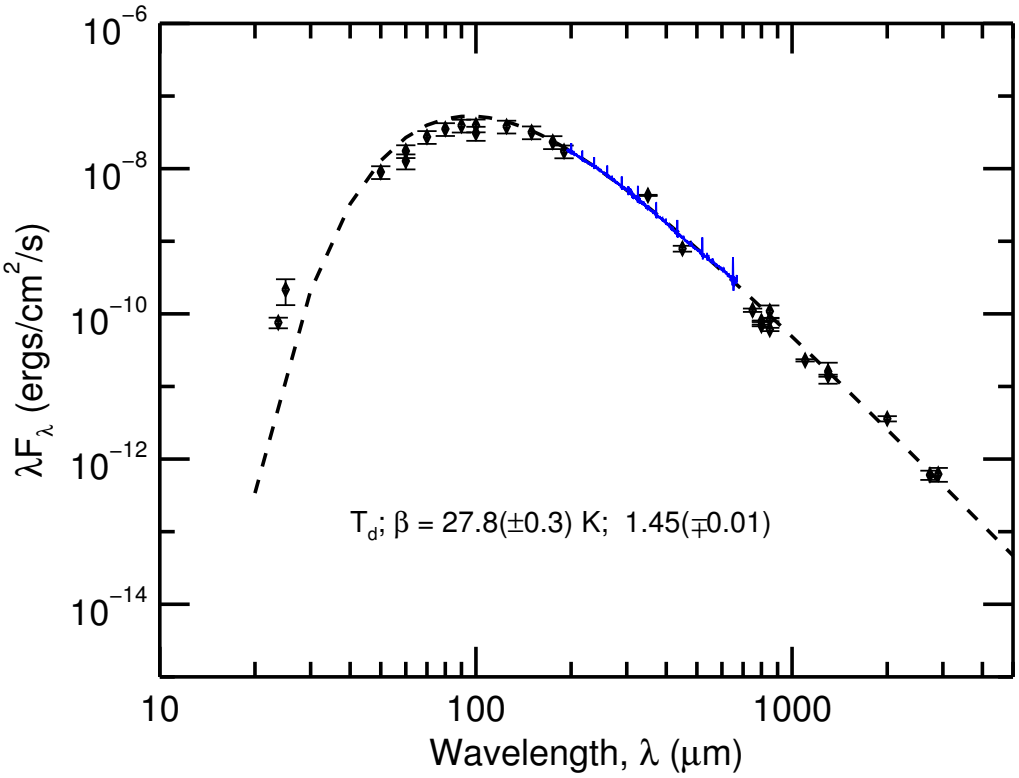


Figure 6.15: Spectral energy distribution for IRAS16293. The solid blue line shows the SPIRE FTS spectra (SSW and SLW) and the black diamond points with error bars are flux densities from other instruments. The dashed line is the best greybody fit to all the data in Table 6.2.

on the observed SED. In order to fit the data accurately and derive these parameters, the SED is fitted with precomputed two-dimensional (2D) radiative transfer models of Robitaille et al. (2007). Robitaille et al. (2007) have computed over 20 000 YSO models, with SEDs computed at ten viewing angles. The models span a large range of evolutionary stages, stellar masses, disk masses, envelope masses and envelope infall rates to mention just a few. Figure 6.16 shows the best fit radiative transfer model to the IRAS16293 SED in bright colors with different colours representing different apertures. The faded colours show subsequent good fits. The data are well fit and a summary of the results is provided in Table 6.3. We obtain a total luminosity of 28.9 $L_{\odot}$. This is in agreement with 29.3 $L_{\odot}$ obtained by Walker et al. (1990) and with 27 $L_{\odot}$ obtained by Mundy et al. (1986).

Another interesting result from our model is that at the centre of IRAS16293 is a $3 \times 10^3$ yr 0.63 $M_{\odot}$ star whose photosphere has a temperature of 3785 K. Results from high spatial resolution interferometric observations of radio and millimetre continuum emission have showed that IRAS16293 is a binary protostar (Mundy et al., 1986) with a total mass of 1.5 $M_{\odot}$ which is greater than the mass that we obtain here. Our model results also show that the star is surrounded by a 6910 AU envelope whose mass is 9.76 $M_{\odot}$. This is also outside the circumstellar mass range of 0.9-6 $M_{\odot}$ estimated by Mundy et al. (1986). We obtain a high accretion rate of $\dot{M} = 1.85 \times 10^{-4}$ $M_{\odot}$/yr. This is even higher than a value of $\dot{M} = 5 \times 10^{-5}$ $M_{\odot}$/yr obtained from radiative transfer modelling by Schöier et al. (2002).

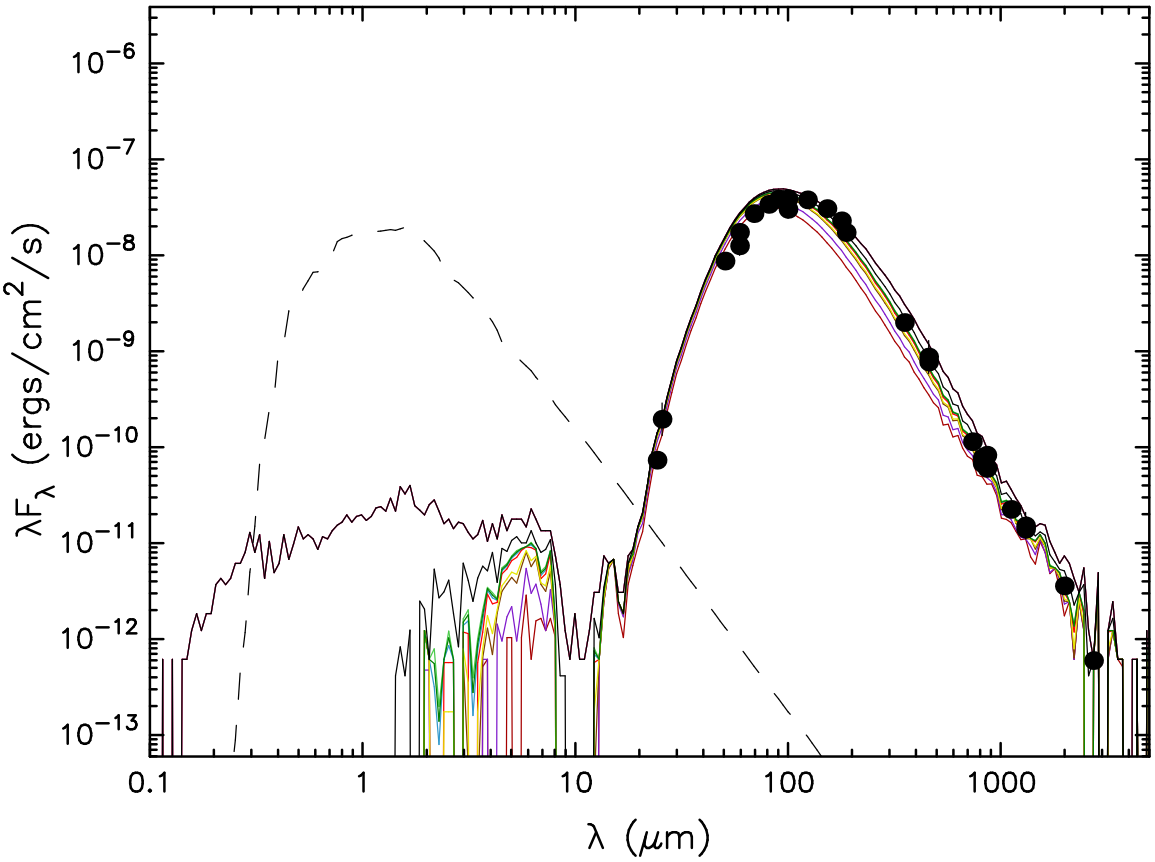


Figure 6.16: Best fit model SED for IRAS16293 obtained from fitting the photometer data in Table 6.2 with precomputed two-dimensional (2D) radiative transfer models of Robitaille et al. (2007). The filled circles show the input fluxes. The brightest colored lines show the best fit, with each color representing a different aperture. The faded colors show subsequent good fits. The dashed line shows the stellar photosphere corresponding to the central source of the best fitting model, as it would look in the absence of circumstellar dust (but including interstellar extinction).

Table 6.3: Parameters from the best fit SED model of IRAS16293.

| Item | Value |
|---|---|
| Stellar age [yr] | $2.99 \times 10^3$ |
| Stellar mass [$M_\odot$] | 0.63 |
| Stellar radius [$R_\odot$] | 7.82 |
| Stellar temperature [K] | 3785 |
| Envelope accretion rate [$M_\odot$/yr] | $1.85 \times 10^{-4}$ |
| Envelope outer radius [AU] | $6.91 \times 10^3$ |
| Envelope cavity angle [degrees] | 10.0 |
| Envelope inner radius [$R_{sub}$] | 1.00 |
| Disk mass [$M_\odot$] | $6.87 \times 10^{-2}$ |
| Disk outer radius [AU] | 11.6 |
| Disk inner radius [$R_{sub}$] | 1.00 |
| Disk inner radius [AU] | 0.341 |
| Disk scaleheight factor | 0.719 |
| Disk flaring power | 1.079 |
| Disk accretion alpha | $3.40 \times 10^{-2}$ |
| Envelope cavity density [cgs] | $2.20 \times 10^{-20}$ |
| Ambient density [cgs] | $4.05 \times 10^{-22}$ |
| Disk accretion rate [$M_\odot$/yr] | $7.89 \times 10^{-6}$ |
| $A_v$ [circumstellar] [mag] | $1.30 \times 10^3$ |
| Total luminosity [$L_\odot$] | 28.9 |
| Disk scaleheight at 100AU | 5.55 |
| Envelope mass [$M_\odot$] | 9.76 |

## 6.6 Conclusion

Results from SPIRE observations of IRAS16293 have been presented. SPIRE photometric data have been combined with data from other instruments to provide an SED with better spectral coverage. The iFTS spectra are in agreement with photometric data. The physical structure of IRAS16293 has been derived by fitting the SEDs with radiative transfer models developed by Robitaille et al. (2007). The results are in agreement with previous studies by other authors. The stellar age and mass of the protobinary system are ∼3 $\times$ $10^3$ yr and 0.63 $M_\odot$ respectively. IRAS16293 has a disk of mass 0.07 $M_\odot$and is accreting material from a $\sim$ 9000 AU radius envelope at a rate of 1.85 $M_\odot$/yr. The total luminosity of the system is 28.9 $L_\odot$.

A wealth of molecular line emission from $^{12}$CO, $^{13}$CO, C$^{18}$O, C I, $H_2O$, $HCO^+$ and CS has been detected. This is the first time $^{12}$CO, $^{13}$CO emission lines from $E_{up} \sim$ 50-500 K have been observed from IRAS16293. We have also been able to determine the spatial extent of the line emission. It is now possible to determine the chemical properties of IRAS16293 using detailed radiative transfer modelling of the observed molecular line emissions.

# Chapter 7

# Class I Protostar: EL29

## 7.1 Overview

The previous chapter described observations of a Class 0 protostar IRAS16293-2422. As the envelope of a Class 0 protostar is depleted of material due to accretion onto the protostar, the peak of the spectral energy distribution (SED) continues its shift towards Ultra-violet (UV) wavelengths (see Figure 1.1). The object develops into a Class I protostar. This chapter will focus on Spectral and Photometric Imaging Receiver Array (SPIRE) imaging Fourier transform spectrometer (iFTS) observations of Elias 29, a Class I protostar. Section 7.2 provides an introduction to Class I protostars and what information about these protostars can be obtained from SPIRE iFTS observations. Our current understanding of Elias 29 is presented in Section 7.3. The details concerning the SPIRE iFTS observations of Elias 29 and data reduction are discussed in Section 7.4. The results are presented in Section 7.5.

## 7.2 Introduction to Class I protostars

As discussed in previous chapters, the formation of low-mass stars begins with the gravitational collapse of dense and cold clouds of gas, dust and ices referred to as pre-stellar or starless cores (Beichman et al., 1986). Due to their low temperatures (T$\sim$10 – 15 K), pre-stellar cores can only be studied at far-infrared and sub-millimeter wavelengths. At these low temperatures molecules like CO and $H_2O$ are frozen onto dust particles in the form of ice mantles. The collapse of a pre-stellar core leads to the formation of a Class 0 protostar characterized by a central hot object that is surrounded by a disk and an envelope.

As collapse proceeds, more material from the envelope settles onto the disk from where it is accreted onto the central object. The protostar enters a Class I stage when the envelope has been depleted enough to allow near-infrared radiation to escape from the central core. At this stage the temperature of the central object has increased to above 100 K allowing the ice mantles within the inner parts of the disk to evaporate releasing water and other molecules into the gaseous phase (Ceccarelli et al., 1996; Fraser et al., 2001). Molecular gases are also formed in regions where bipolar outflows and winds from protostars meet with surrounding material in envelopes (Kaufman & Neufeld, 1996). Bombardment by cosmic rays and ultraviolet irradiation also play a part in returning molecules to the gas phase (e.g. Tielens & Charnley, 1997; van Dishoeck & Blake, 1998). Molecular species therefore play an important part in the evolution of stars and their study allows us to probe the environmental properties of the regions in which they exist. The *Herschel Space Observatory* (*Herschel*) has enabled us to probe star forming regions by studying their dust and molecular emission at the far-infrared wavelengths.

This chapter presents recent observations of a young protostar, Elias 29, carried out with the SPIRE iFTS onboard *Herschel*. We obtained spectral maps of the Elias 29 region measuring $\sim 3'' \times 3''$.

## 7.3 Source Background

Elias 29, also called WL 15, YLW 7 (Elias, 1978b; Wilking & Lada, 1983; Young et al., 1986) is a Class I protostar found in the $\rho$ Ophiuchus cloud complex. Elias 29 has a bolometric luminosity ($L_{\rm bol}$) of 26 $L_\odot$ (Bontemps et al., 2001). Its accretion luminosity has been determined by Muzerolle et al. (1998) using the Br$\gamma$ emission line to be $\sim 15 - 18$ $L_\odot$. The relatively short distance, $d \sim 120$ (Loinard et al., 2008; Lombardi et al., 2008) to the $\rho$ Ophiuchus cloud complex makes it an important astronomical region for studies aimed at answering various questions related to the formation of stars.

Elias 29 has been extensively studied by Boogert et al. (2000, 2002) and Ceccarelli et al. (2002), who have identified three emission components in addition to the central object. They used heterodyne spectral line observations carried out with the Digital Autocorrelation Spectrometer (DAS) and acousto-optical spectrometer (AOS) back ends on the James Clerk Maxwell Telescope (JCMT) and Caltech Submillimeter Observatory (CSO)[1] (Carlstrom et al., 1994) and the autocorrelator backend on the National Radio Astronomy Observatory (NRAO) (User's Manual for the NRAO 12 M Millimeter-wave Telescope, Kitt Peak, Arizona, 2000). They also constructed a SED for Elias 29 using spectra obtained with the *Infrared Space Observatory* (*ISO*) short wavelength spectrometer (SWS) and long

[1]The JCMT and CSO can be used as an interferometer (Carlstrom et al., 1994) but in this case the telescopes were used separately.

wavelength spectrometer (LWS) instruments covering wavelengths from 2.4 – 45 $\mu$m and 45 – 195 $\mu$m, respectively and whose apertures had sizes of 25″ and 80″ respectively (Kessler et al., 1996). From their line observations, they identified emission components at velocities of $v_{\rm LSR}$ = 2.7 km s$^{-1}$ and $v_{\rm LSR}$ = 3.8 km s$^{-1}$ and associated them with cold foreground clouds. A third emission component with a velocity of $v_{\rm LSR}$ = 5.0 km s$^{-1}$ was associated with the dense ridge of $HCO^+$-rich material (see Figure 7.1) to which most of the nearby sources belong. Using interferometric observations of the $^{13}$CO $J$ = 1 – 0 obtained with the Owens Valley Radio Observatory (OVRO) millimeter array (Padin et al., 1991), an envelope/disk system centred on Elias 29, but deeply embedded within the ridge and having the same rest velocity as that of the ridge, was resolved.

The outflows of the Elias 29 region have been reported by Bontemps et al. (1996), Khanzadyan et al. (2004), Ybarra et al. (2006) and Bussmann et al. (2007). A blue-shifted component with a velocity of $V_{\rm LSR}$ = - 4 – 1 km s$^{-1}$ and a redshifted component with a velocity of $V_{\rm LSR}$ = 7 – 12 km s$^{-1}$ have been identified and attributed to Elias 29 (Bontemps et al., 1996). Outflows from a nearby protostar LFAM have also been discovered in the same region. These contributions from nearby sources make analyzing data from Elias 29 challenging. Figure 7.2 shows the S-shaped symmetry of the outflow from Elias 29 traced by the $H_2$ emission (Ybarra et al., 2006) observed using the Persson's Auxiliary Nasmyth Infrared Camera (PANIC) on the Baade 6.5 m telescope at Las Campanas Observatory (Martini et al., 2004). In this image, the blue-shifted and red-shifted lobes point towards the northwest and southeast, respectively.

Ceccarelli et al. (2002) have analyzed $^{13}$CO $J = 6 \rightarrow 5$ and $J \geq 15$ transitions from

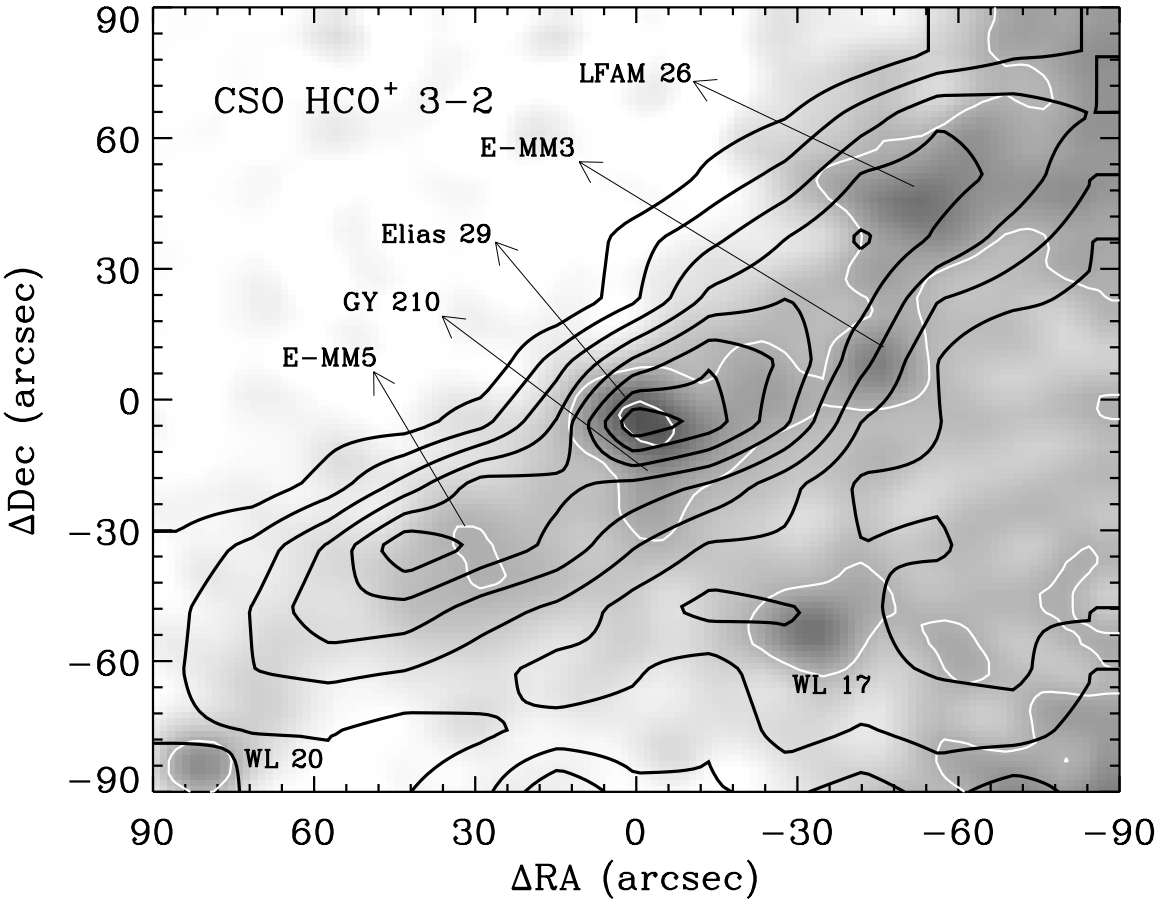


Figure 7.1: Overlay of IRAM 30 m 1.3 mm continuum map (gray scale and two white contours; Motte et al. (1998)) and integrated CSO $HCO^+$ emission (black contours) of Elias 29. White contours are at 7 and 14 $\sigma$, with $\sigma$ = 10 mJy per 15″ beam[2], and $\int T_{MB} dv$ = 1.1, 1.6, ..., 4.6 K kms$^{-1}$ for $HCO^+$ 3-2 ($\sigma$=0.2 K kms$^{-1}$). Figure taken from Boogert et al. (2002).

observations of Elias 29 obtained with the JCMT and *ISO* SWS respectively. They found evidence of a super-heated surface disk layer and derived a gas temperature and mass similar to that found in Herbig AeBe stars (Thi et al., 2001). They speculate that the super-heated

[2] $\sigma$ is the standard deviation of the noise in the measure signal.

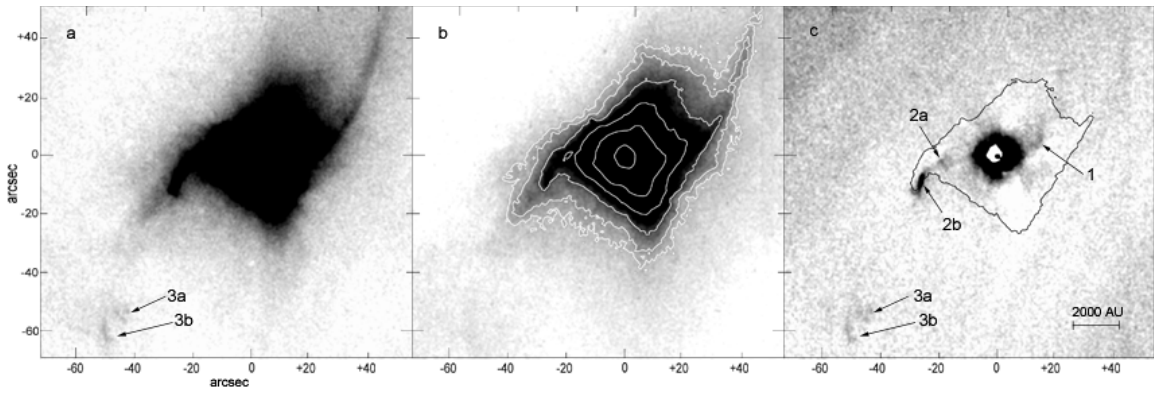


Figure 7.2: Narrowband images of Elias 29 obtained with PANIC showing offsets from $\alpha_{2000} = 16^{\rm h}27^{\rm m}09.43^{\rm s}$, $\delta_{2000} = -24°37'18.7''$. (a) Elias 29 observed through the narrowband $H_2$ filter with PANIC. (b) Elias 29 imaged with the Br$\gamma$ filter with PANIC (Martini et al., 2004); contour levels are at 3, 5, 10, 20, 50 and 500 $\sigma$. (c) Pure $H_2$ emission line image of Elias 29, obtained by subtracting the Br$\gamma$ image from the PANIC $H_2$ filter image with the Br$\gamma$ 10$\sigma$ contour superposed. The pure $H_2$ emission objects labeled 1, 2a, 2b, 3a, and 3b are discussed in Ybarra et al. (2006). In these images, North is up and East is on the left. Figure taken from Ybarra et al. (2006).

gas may be partly caused by the high energy UV and X-ray radiation from the central hot object. Their analysis suggests that Elias 29 could be a transition object between class I and class II or a deeply embedded Herbig AeBe star. The reason why Elias 29 does not appear as a T Tauri or Herbig AeBe star (optically visible) has been attributed, by Boogert et al. (2002), to a column of foreground clouds which have a high visual extinction. The measured flat SED of Elias 29 between 10 and 200 $\mu$m has been attributed to the disk that is thought to be oriented at angles less than 60°. This is in agreement with the speculation that Elias 29 could be a T Tauri or Herbir AeBe star.

Elias 29 has also recently been observed by the Photodetecting Array Camera and Spectrometer (PACS) (Poglitsch et al., 2010) on Herschel under the Dust, Ice and Gas in Time (DIGIT) key program (Green et al., 2013). PACS covers wavelengths from 55 to 210 $\mu$m and therefore covers $^{12}$CO rotational lines from $J$=14-13 up to $J$=40-39. These highly excited CO emission lines are thought to originate from hot shocked gas (Green et al., 2013). From a sample of 30 Class 0 and Class I protostars, Elias 29 had the richest spectrum. These authors also used SEDs constructed with photometry data from Two Micron All Sky Survey (2MASS) (Skrutskie et al., 2006), *Spitzer Space Telescope* (*Spitzer*) – Infrared Array Camera (IRAC), *Infrared Astronomical Satellite* (*IRAS*) (Werner et al., 2004), *ISO* and *Spitzer* – Multiband Imaging Photometer for Spitzer (MIPS) to calculate new bolometric luminosities for their sample observations. They obtained $L_{\rm bol} \sim 20.1$ L$_\odot$ for Elias 29 which is lower than 26 L$_\odot$ reported by (Bontemps et al., 2001). A reason for this could be that (Green et al., 2013) used few photometric points on their SED compared to the broadband *ISO* spectrum used by (Bontemps et al., 2001). A rotational diagram of the $^{12}$CO lines observed by PACS

showed the presence of two temperature components of $T_{\rm rot}$ = 423 ± 63 K and $T_{\rm rot}$ = 690 ± 129 K.

## 7.4 Observations and data reduction

### 7.4.1 *Herschel*-SPIRE photometer observations

SPIRE Photometer maps of Elias 29 were obtained as part of the Gould Belt guaranteed time key programmes for the study of star formation (André et al., 2010). Using the SPIRE and PACS photometers, a large area observation of the L1688 star forming cloud in the $\rho$ Ophiuchus star forming region was obtained. Two cross scans (Observation Identification Numbers (OBSIDs) = 1342205093 and 1342205094) were obtained. The two observations were processed using the Herschel Interactive Processing Environment (HIPE)[3] version 11 and merged using the "Photometer Merging script" also found in HIPE.

### 7.4.2 *Herschel*-SPIRE spectrometer observations

Elias 29 was observed with the SPIRE iFTS as part of the "Evolution of Interstellar dust" key program under the Interstellar Medium (ISM) Specialist Astronomy Group (SAG4, Abergel et al. (2010)). Fully sampled maps of Elias 29 centred on $\alpha_{2000} = 16^{\rm h}27^{\rm m}09.3^{\rm s}$, $\delta_{2000} = -24°37'01.1''$ were obtained. The observation had a total of 13 scans in high and low resolution (4 scans in HR and 9 scans in LR) mode for a total integration time of 11491 s. The data were reduced using the "Spectrometer Mapping Pipeline" also in HIPE version 11.

[3]HIPE is a joint development by the Herschel Science Ground Segment Consortium, consisting of European Space Agency (ESA), the National Aeronautics and Space Administration (NASA) Herschel Science Center, and the Heterodyne Instrument for the Far Infrared (HIFI), SPIRE and SPIRE consortia.

### 7.4.3 Map making

The same procedure as that described for IRAS16293-2422 in Section 6.4.3 was followed during map making for Elias 29 data cubes. The size of the pixels was fixed to half the spectrometer long wavelength (SLW) beam (17.5″) with the brightest pixels centred on $\alpha_{2000} = 16^{h}27^{m}09.46^{s}$, $\delta_{2000} = -24°37'24.12''$ for both spectrometer short wavelength (SSW) and SLW maps. This position is the brightest pixel in the SPIRE 250 $\mu$m photometer map of Elias 29.

Figure 7.3 shows a mosaic plot of all the spectra on the measured data cubes. Each box in the figure represents a 17.5″ ×17.5″ pixel on the SSW and SLW spectral maps. The right ascension (RA) is on the horizontal axis and increases from right to left. The declination (Dec) is on the vertical axis and increases from bottom to top. A zoom-in of spectra for pixels close to the peak of emission is shown in Figure 7.4.

### 7.4.4 Line fitting

In order to extract line information, the spectra for the brightest pixels in both SSW and SLW bands were extracted from the maps and reprocessed using the "pointsource-conversion" task in HIPE. The point source calibrated spectra were then corrected for source spatial extent. This was achieved using the semi-extended corrector tool (Wu et al., 2013). The source size required to correct for the gap in the overlap region of SSW and SLW was 22″ which corresponds to a source diameter of 2640 astronomical unit (AU). This is comparable to a Full Width Half Maximum (FWHM) of ∼17″ obtained from 1.3 mm maps by Andre & Montmerle (1994). The top panel of Figure 7.5 shows the point source calibrated

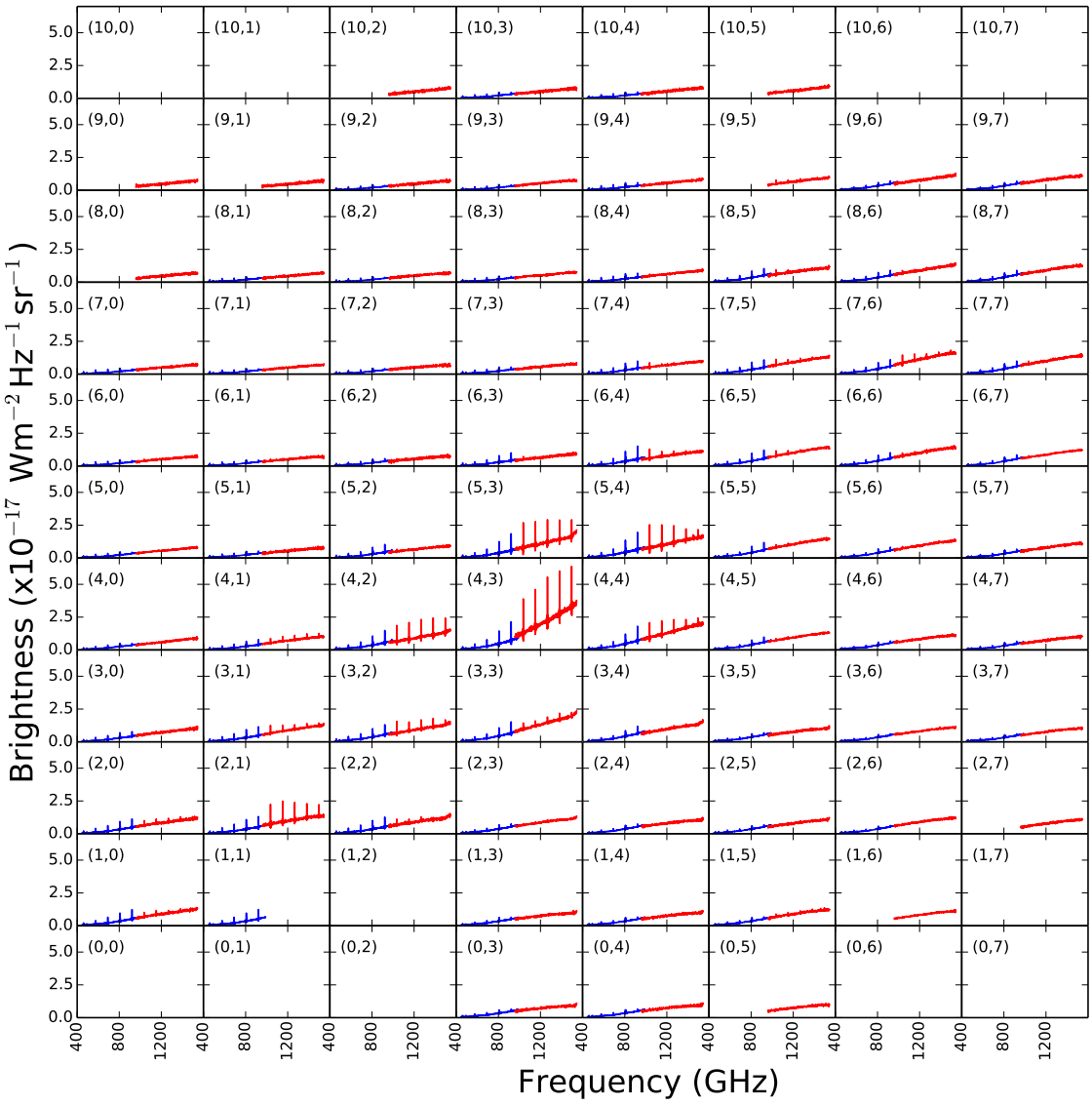


Figure 7.3: The combined SSW (red) and SLW (blue) spectra for all the pixels on the observed Elias 29 maps. The map pixels corresponding to the spectra in each box are shown on the top left corner.

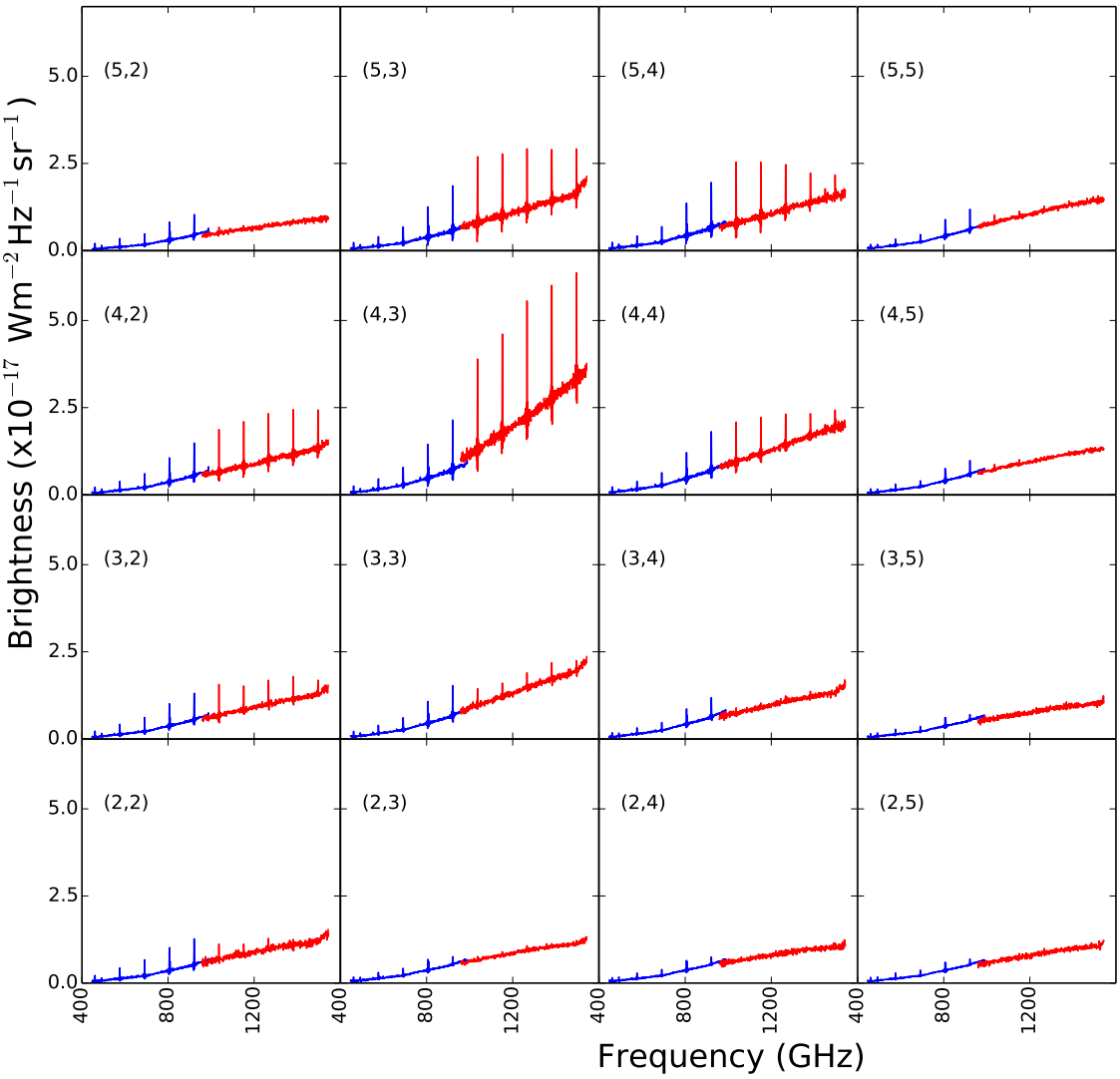


Figure 7.4: The combined SSW (red) and SLW (blue) spectra for pixels close to the peak of emission (Figure 7.3). The map pixels corresponding to the spectra in each box are shown on the top left corner.

spectra before (red lines) and after (blue lines) correcting for spatial extent. The plots in the bottom rows show the spectrum corrected for source extent divided into four regions to reveal the spectral lines and the sinc instrumental line profile. All identified lines are labelled and listed in Table 7.1. For this spectrum, line fitting was carried out using the "Spectrometer Line Fitting" tool in HIPE.

In order to investigate the spatial extent of line emission in Elias 29, the "Spectrometer Line Fitting" tool was modified to loop through all the pixels in the maps transformed onto the same World Coordinate System (WCS) as described in Section 7.4.3.

## 7.5 Results

### 7.5.1 Photometer maps of Elias 29

Figure 7.6 shows the SPIRE photometer maps of the region surrounding Elias 29. The map shows a ridge running from North-West to South-East. The protostar LFAM 26 and protostellar condensation E-MM5 shown on the map are two of the many sources found along the ridge. A fully sampled spectral map of the region enclosed by the black square was obtained with the SPIRE iFTS.

### 7.5.2 Line detections and rotational diagrams

The spectrum of Elias 29 shown in Figure 7.5 shows a number of lines from $^{12}$CO (red), $^{13}$CO (green), C I (grey) and $H_2O$ (blue). Results from line fitting are presented in Table 7.1 which also shows the rest frequencies and upper level energies $E_{\rm up}$ for each transition.

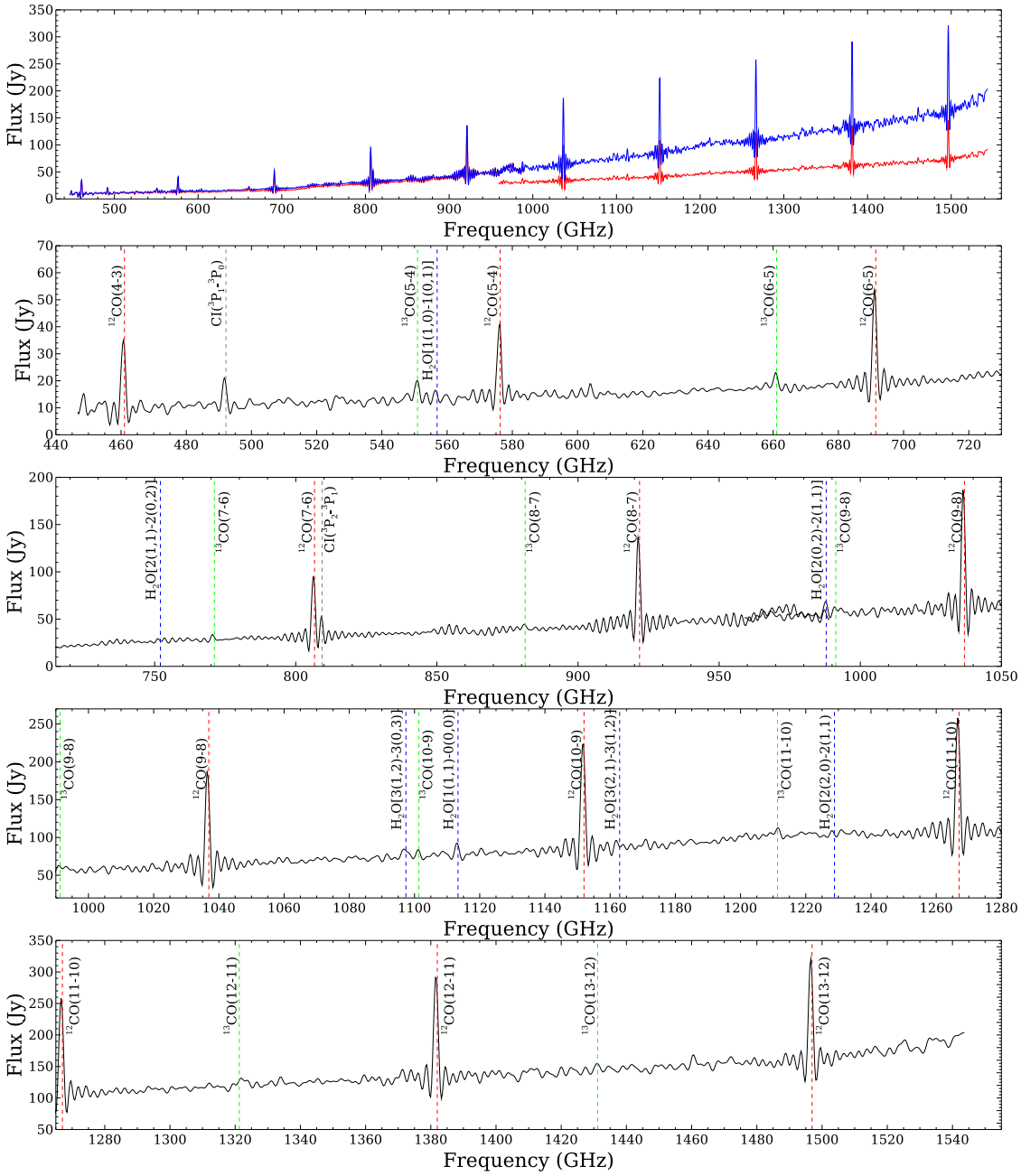


Figure 7.5: Top panel: the spectrum for the brightest pixel of the Elias 29 spectral map calibrated as a point source (red) and after correcting for source extent (blue). Bottom panels: magnified sections of the corrected spectrum. Superposed on the continuum is line emission of which the brightest lines belong to the $^{12}$CO ladder.

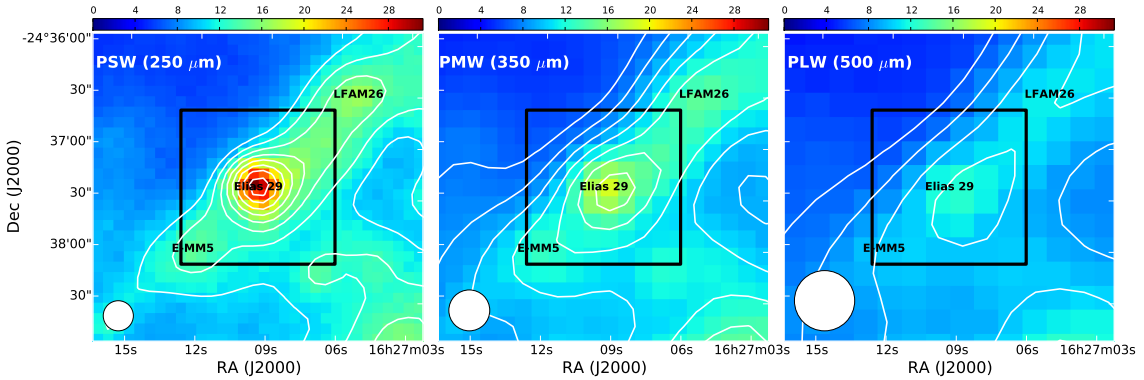


Figure 7.6: The SPIRE Photometer images of the region surrounding Elias 29. SPIRE iFTS spectral maps were obtained for the region inside the black square measuring $3' \times 3'$ ($\sim$21600 AU $\times$ 21600 AU). On the left is the photometer long wavelength image observed at 500 $\mu$m. At the centre is the PMW image observed at 350 $\mu$m and on the right side is the PSW image observed at 250 $\mu$m. The colour scales for all three images have been fixed at 0-30 Jy/beam for ease of comparison. All images show a ridge running from the North West to South East of the image. Contour lines are at 40, 30, 25, 20, 15, 12.5, 10, 6.25 % of the maximum flux for each image.

Table 7.1: Line flux values for the brightest pixel of the Elias 29 spectral data cubes.

| Species | Transition | $\nu_{\rm rest}$ [GHz] | $E_{\rm up}$ [K] | $\int F_\nu d\nu$ [$10^{-17}$W m$^{-2}$] | $\int F_\nu d\upsilon$ [$10^3$Jy km s$^{-1}$] |
|---|---|---|---|---|---|
| $^{12}$CO | 4-3 | 461.0 | 55.3 | 30.3±1.2 | 19.7±0.8 |
| | 5-4 | 576.3 | 83.0 | 31.4±1.2 | 16.3±0.6 |
| | 6-5 | 691.5 | 116.2 | 38.7±1.2 | 16.8±0.5 |
| | 7-6 | 806.7 | 154.9 | 75.8±1.2 | 28.2±0.5 |
| | 8-7 | 921.8 | 199.1 | 108.5±1.2 | 35.3±0.4 |
| | 9-8 | 1036.9 | 248.9 | 146.8±2.2 | 42.5±0.6 |
| | 10-9 | 1152.0 | 304.2 | 166.7±2.2 | 43.4±0.6 |
| | 11-10 | 1267.0 | 365.0 | 174.4±2.2 | 41.3±0.5 |
| | 12-11 | 1382.0 | 431.3 | 191.9±2.2 | 41.7±0.6 |
| | 13-12 | 1496.9 | 503.1 | 182.7±2.2 | 36.6±0.4 |
| $^{13}$CO | 5-4 | 550.9 | 79.3 | 9.0±1.2 | 4.9±0.7 |
| | 6-5 | 661.1 | 111.1 | 6.3±1.2 | 2.8±0.5 |
| | 7-6 | 771.2 | 148.1 | 6.6±1.2 | 2.6±0.5 |
| | 8-7 | 881.3 | 190.4 | 5.5±1.2 | 1.9±0.4 |
| | 9-8 | 991.3 | 237.9 | 6.4±2.2 | 1.9±0.7 |
| | 10-9 | 1101.3 | 290.8 | 9.3±2.2 | 2.5±0.6 |
| | 11-10 | 1211.3 | 348.9 | 15.2±2.2 | 3.8±0.5 |
| | 12-11 | 1321.3 | 412.3 | 10.9±2.2 | 2.5±0.5 |
| | 13-12 | 1431.2 | 481.0 | 16.1±2.2 | 3.4±0.5 |
| [C I ] | $^3P_1$-$^3P_0$ | 492.2 | 23.6 | 11.1±1.2 | 6.8±0.7 |
| | $^3P_2$-$^3P_1$ | 809.3 | 62.5 | 15.9±1.2 | 5.9±0.5 |
| $H_2O$ | $1_{10}$-$1_{01}$ | 556.9 | 61.0 | 3.3±1.2 | 1.8±0.7 |
| | $2_{11}$-$2_{02}$ | 752.0 | 137.0 | 3.5±1.2 | 1.4±0.5 |
| | $2_{02}$-$1_{11}$ | 987.9 | 100.8 | 16.1±2.2 | 4.9±0.7 |
| | $3_{12}$-$3_{03}$ | 1097.4 | 249.4 | 12.5±2.2 | 3.4±0.6 |
| | $1_{11}$-$0_{00}$ | 1113.3 | 53.4 | 16.1±2.2 | 4.3±0.6 |
| | $2_{20}$-$2_{11}$ | 1228.8 | 195.9 | 6.3±2.2 | 1.5±0.5 |

Notes: The rest frequencies ($\nu_{\rm rest}$) and upper level energies ($E_{\rm up}$) were obtained from the JPL database (http://spec.jpl.nasa.gov/). The $1\sigma$ uncertainties in the table are from line fitting and do not include those related to absolute calibration, which are $\sim 7\,\%$ for the mapping mode (Swinyard et al., 2014). Converting from W m$^{-2}$ to Jy km s$^{-1}$ was achieved using $\int F_\nu d\upsilon$ (Jy km s$^{-1}$) = $\int F_\nu d\nu$ (W m$^{-2}$) $\times$ 0.3 $\times$ $10^{23}$ $\nu_{\rm GHz}^{-1}$.

A simple way of extracting the gas temperature and column abundance is rotational diagram analysis (Goldsmith & Langer, 1999). Using rotational diagrams is based on assumptions that the medium is isothermal, in local thermodynamic equilibrium, is optically thin and fills the beam. Figure 7.7 shows the $^{12}$CO and $^{13}$CO rotational diagrams for Elias 29. The rotational temperatures were derived by fitting a line to the integrated line intensities, with the slope of the line being equal to $1/T_{\rm rot}$. Clearly, data for each molecule cannot be fitted by a single temperature, and so for $^{12}$CO the $J_{\rm up} \leq 6$ and $J_{\rm up} > 6$ lines were fit separately, while for $^{13}$CO the $J_{\rm up} \leq 8$ and $J_{\rm up} > 8$ lines were also fit separately. The rotational temperature obtained from low- and high-$J$ $^{12}$CO lines are $T_{\rm rot}$ = 33 K and $T_{\rm rot}$ =154 K respectively. The rotational temperature obtained from low- and high-$J$ $^{13}$CO lines are $T_{\rm rot}$ = 39 K and $T_{\rm rot}$ =230 K respectively. These results are consistent with the presence of many components along the line of sight as will be discussed in the following section.

### 7.5.3 Spatial distribution of lines

One of the advantages of the SPIRE iFTS is its capability to map large regions of space in a relatively short period of time enabling the study of spatial extent of line and continuum emission. A mosaic plot of all the spectra on the observed data cubes for the region surrounding Elias 29 has already been presented in Figure 7.3. It shows that the dust is relatively extended throughout the field of view. There is evidence of hot gas at the position of Elias 29 (pixel (4,3) and a few surrounding pixels). Line emission is confined to the position of Elias 29 and along the ridge running from north-west to south-east. A closer look at the spectra for pixel (4,3) shows that there is a discontinuity in the continuum and in

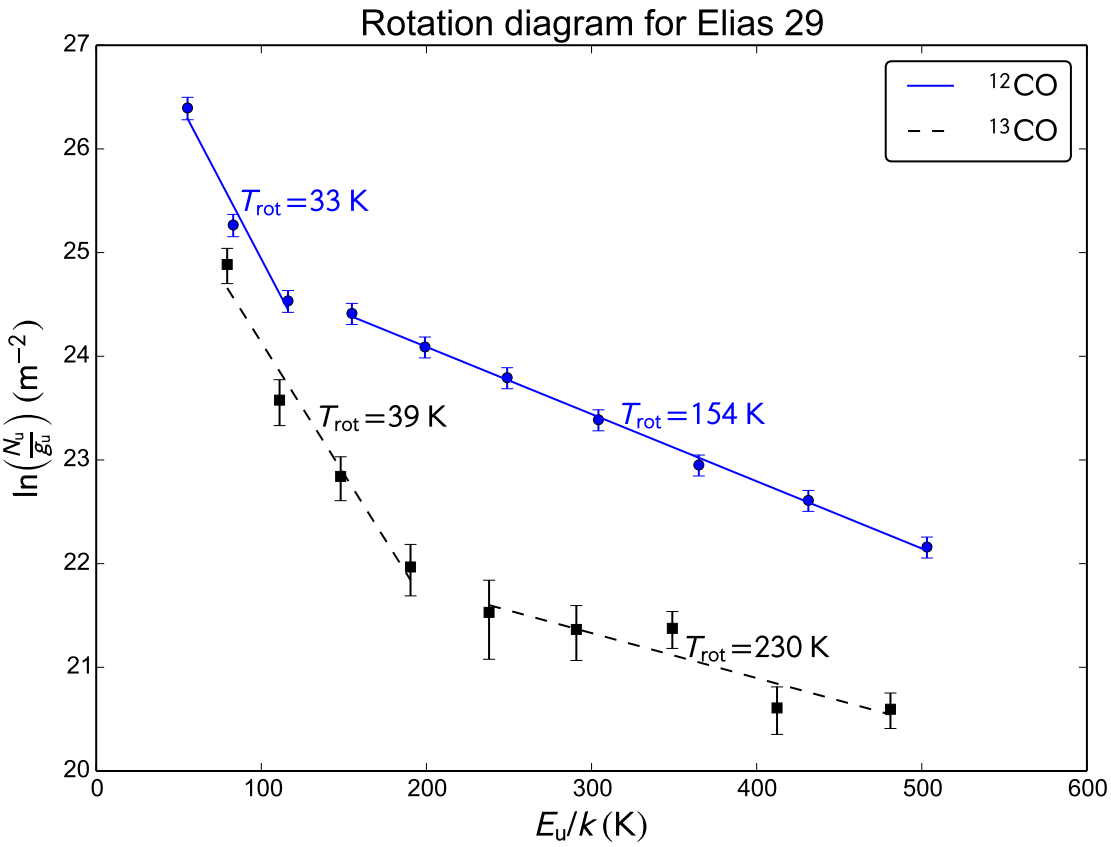


Figure 7.7: Rotational diagram for $^{12}$CO (blue square point and solid line) and $^{13}$CO (red circle point and dashed line) in Elias 29. Errors bars include errors from fitting and the 6 % calibration uncertainty (Swinyard et al., 2014). Solid and dashed lines indicate the best linear fit to data points for $^{12}$CO and $^{13}$CO, respectively.

the line peaks between the SSW and SLW bands. This is due to the differences in the SSW and SLW beam sizes and also to the fact that line emission is not as extended as that of the continuum. This discussion will now be continued using integrated line intensity maps. It is important to note that the integrated line intensity maps presented in this section were derived from spectral data cubes produced as described in Section 7.4.3. The integrated line intensity maps were not convolved to the same beam due to challenges discussed in Chapter 4 and so the comparison of maps for different transitions should be carried out with caution.

### Carbon Monoxide

Figure 7.8 shows the CO integrated line intensity maps for all the ten CO lines identified in the spectrum for Elias 29. Low-$J$ transitions are much more extended that high-$J$ transitions, providing evidence that the CO lines are tracing different components of the region surrounding Elias 29, in agreement with Boogert et al. (2002). The low-$J$ transitions are tracing the much more extended foreground clouds which are thought to be associated with the $\rho$ Ophiuchus cloud complex. The ridge, elongated in the north west - south east direction and reported to be rich in $HCO^+$ is clearly seen in the mid-$J$ $^{12}CO$ transitions. The envelope + disk system is seen as a confined source at high-$J$ transitions. It is clear that $^{12}CO$ is optically thick and this needs to be taken into account when modelling emission from Elias 29.

Figure 7.9 shows the $^{13}CO$ integrated line intensity maps for four transitions in which reasonable maps could be obtained. Although we identified nine $^{13}CO$ lines in the spectrum for the brightest point, emission from high-$J$ $^{13}CO$ transitions are close to the noise level and the maps are not trustworthy. The maps shown indicate that emission from

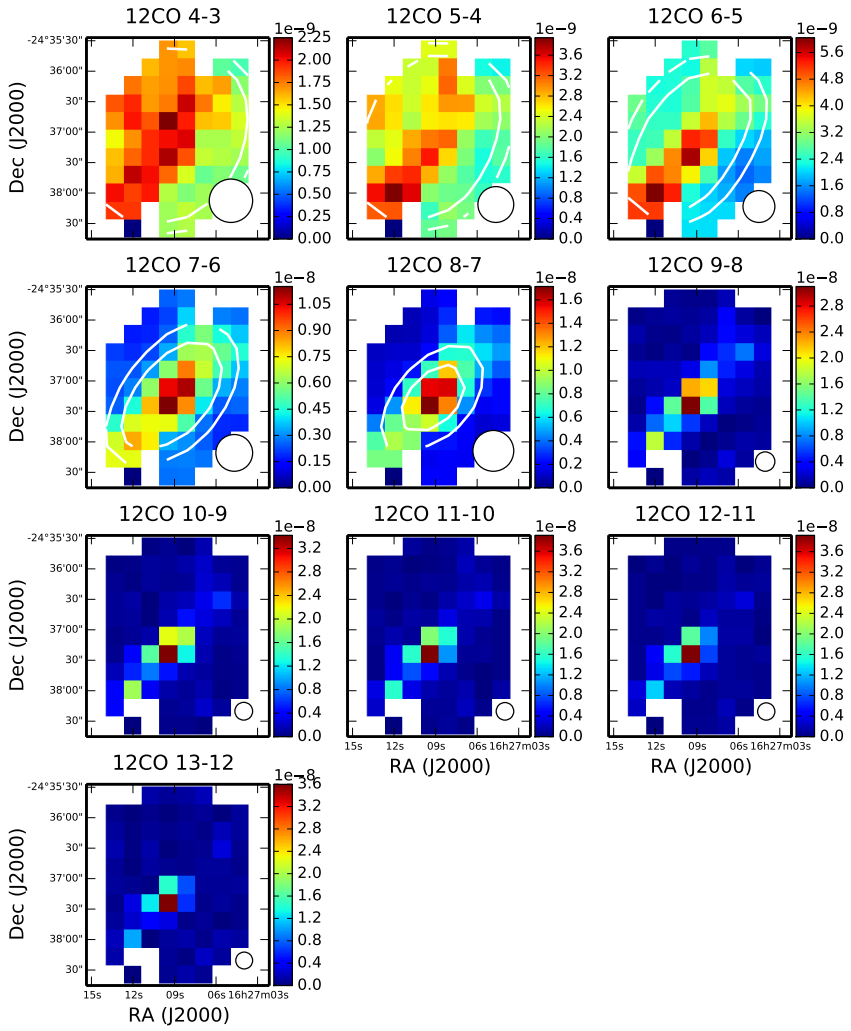


Figure 7.8: $^{12}$CO (J=4-3 to 13-12) integrated line intensity maps for Elias 29. The units for the colour bar are W m$^{-2}$ sr$^{-1}$. The circle on the bottom right corner represents the SPIRE iFTS beam at each $^{12}$CO transition. Contours are shown at 40 and 30 % of the peak flux value in each map. In this figure, it is clearly seen that emission from low-J transitions which probe cold gas is extended and that from high-J transitions which are less susceptible to opacity effects is point-like. The lines trace different components of the region around Elias 29.

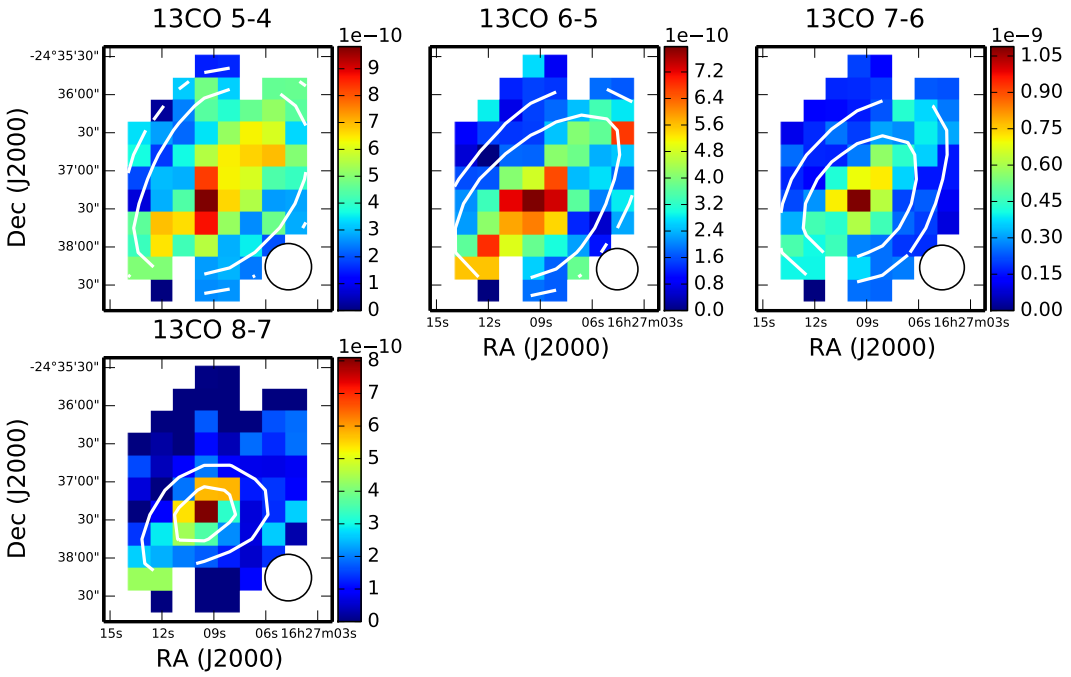


Figure 7.9: $^{13}$CO (J=4-3 to 13-12) integrated line intensity maps for Elias 29. The units for the colour bar are W m$^{-2}$ sr$^{-1}$. The circle on the bottom right corner represents the SPIRE iFTS beam at each $^{13}$CO transition. Contours are shown at 40 and 30 % of the peak flux value in each map. In this figure, it is seen that emission from $^{13}$CO is probing the ridge.

low-$J$ transitions is more extended compared to that for high-$J$ transitions. The dense ridge can be seen in maps for the lower three transitions. Based on these results, $^{12}$CO and $^{13}$CO should be taken as separate tracers.

### Neutral carbon

Figure 7.10 shows C I ($^3$P$_1$-$^3$P$_0$ and $^3$P$_2$-$^3$P$_1$) integrated line intensity maps. One of the striking features from the C I fine-structure emission maps is that they are as extended as the continuum. These lines play an important role in the cooling of the ISM and originate

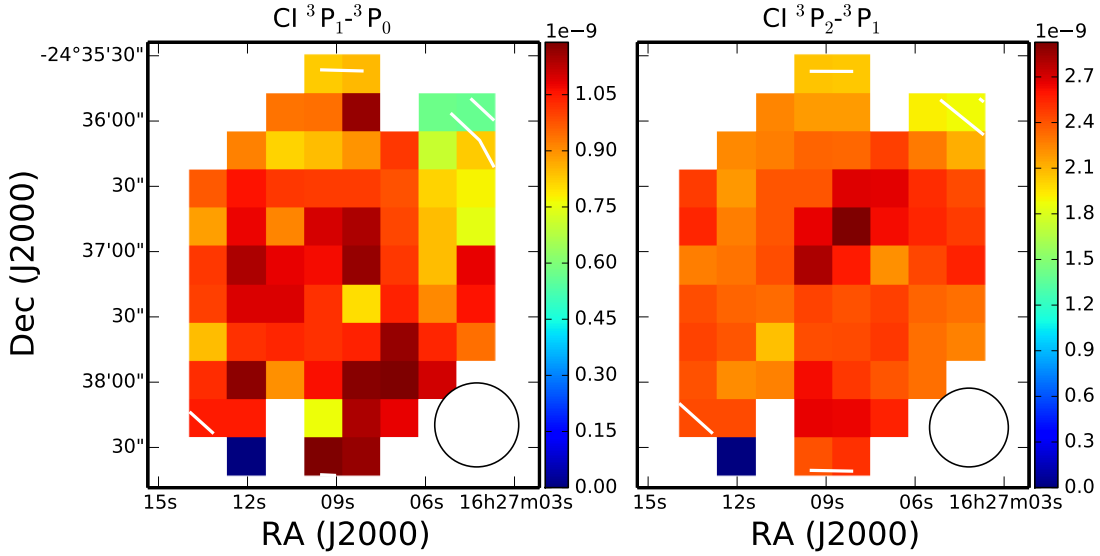


Figure 7.10: C I ($^3P_1$-$^3P_0$ and $^3P_2$-$^3P_1$) integrated line intensity maps for Elias 29. The units for the colour bar are W m$^{-2}$ sr$^{-1}$. The circle on the bottom right corner represents the SPIRE iFTS beam at each C I transition. Contours are shown at 40 and 30 % of the peak flux value in each map. This figure shows that C I is more extended suggesting it originates from foreground clouds.

from an intermediate region between atomic and molecular gas (Tielens, 2005). This suggests that the observed extended emission from C I could be coming from the foreground clouds. Measurements of line of sight rest velocities of the C I lines from high spectral resolution observations are required to confirm the origin of these emission lines.

**Water**

Five water lines shown in Table 7.1 have been observed in the SPIRE SSW and SLW bands. This is not the first time water has been detected from Elias 29. Boogert et al.

(2000) detected hot water vapour ($T_{\rm ex} > 300$ K) at high abundances on scales a few hundred AU. Figure 7.11 shows the integrated line intensity maps for water. Emission from water is not structured at all. However, the pixel located at the position of Elias 29 is bright in all maps suggesting that emission from water is associated with the envelope + disk system. This supports results from Boogert et al. (2000) that water emission is confined to a few hundred AU.

The 557 GHz $1_{10}$-$1_{01}$ water line has been observed in a number of Class 0 and I protostars with the HIFI instrument (de Graauw et al., 2010) on *Herschel* as part of the Water in star-forming regions with Herschel (WISH) program (Kristensen et al., 2012). It has been shown that the lines are complex and rich in various dynamic components. The regular and inverse P-Cygni profiles in observations of Class 0 and I protostars indicate the presence of simultaneous expansion and infall, respectively. The SPIRE iFTS does not have sufficiently high spectral resolution to spectrally resolve the line features. However, the detection of water is itself a key result as this water may end up in oceans on planetary systems formed as the objects evolve to become "solar-type" main-sequence stars.

### 7.5.4 SED of Elias 29

Figure 7.12 shows the broadband dust continuum SED of Elias 29 constructed from spectra obtained using *ISO* (SWS and LWS instruments) covering wavelengths from 2.4 to 195 $\mu$m and using SPIRE iFTS covering wavelengths from 194 to 671 $\mu$m. The *ISO* spectra were originally published by Boogert et al. (2002). Our SPIRE iFTS spectrum provides confirmation that the drop-off of the SED is around 200 $\mu$m. Fitting a greybody function to the SPIRE iFTS spectrum, with a fixed dust emissivity index ($\beta = 2$) results in a dust

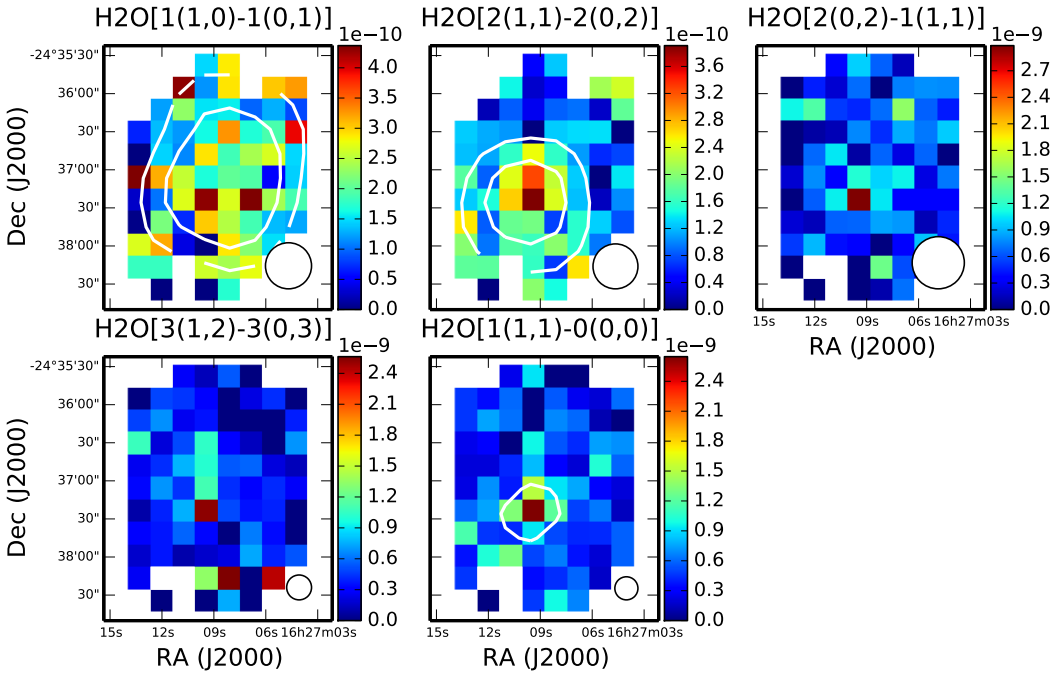


Figure 7.11: $H_2O$ integrated line intensity maps for Elias 29. The units for the colour bar are W $m^{-2}$ $sr^{-1}$. The circle on the bottom right corner represents the SPIRE iFTS beam at each $H_2O$ transition. Contours are shown at 40 and 30 % of the peak flux value in each map. This figure shows that emission from water is not structured. The pixel located at the position of Elias 29 is bright in all maps suggesting that emission from water is associated with the envelope + disk system.

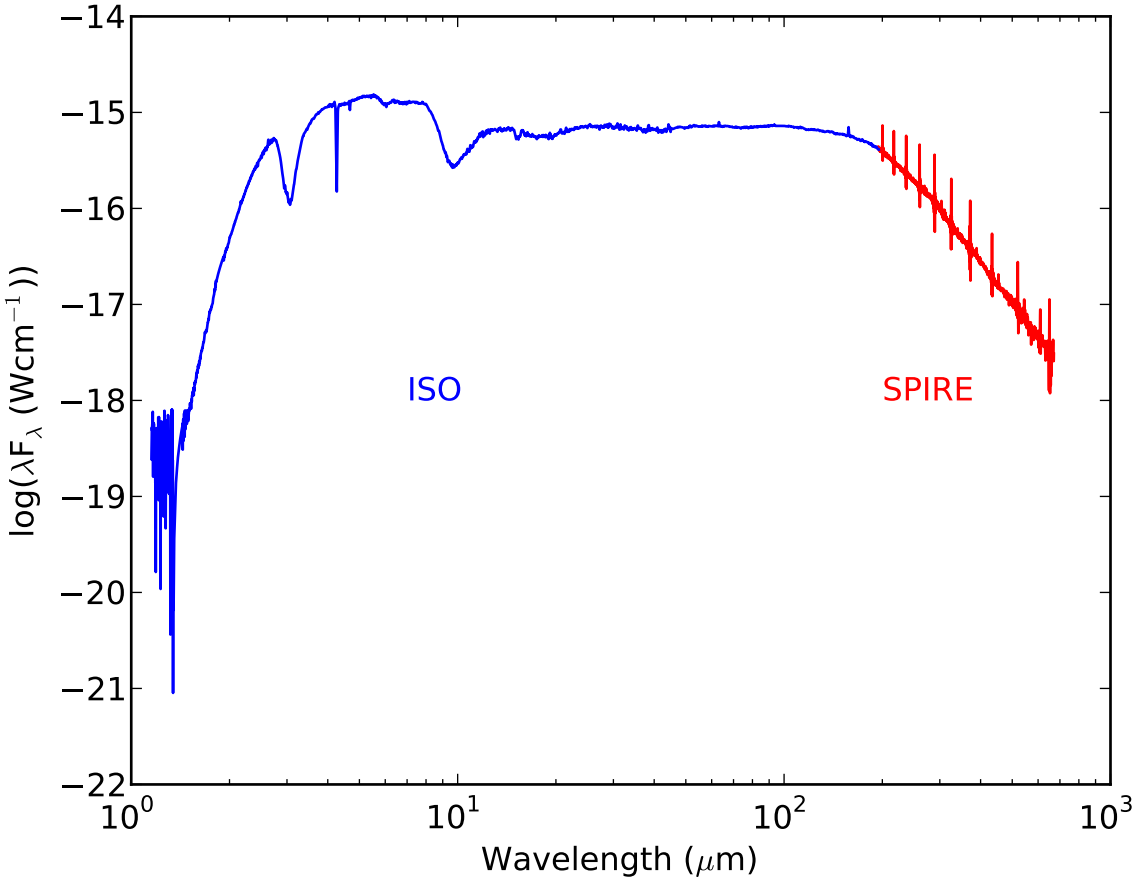


Figure 7.12: The SED of Elias 29 constructed using spectra from ISO and SPIRE FTS instruments. The SED is almost flat between the 4 to 200 $\mu$m band. It then falls off in a region where there are strong CO emission lines.

temperature of 22 $\pm$ 1 K. This is slightly greater but close to a value of 19 K reported by Boogert et al. (2002) for the foreground clouds.

## 7.6 Conclusion

Integrated line intensity maps for $^{12}$CO and $^{13}$CO have have confirmed that there are three components in the observed region of Elias 29. Emission from low-$J$ transitions originates from an extended region and is associated with foreground clouds. A ridge, elongated in the north west - south east direction is seen in the emission from mid-$J$ transitions. The high-$J$ transitions originate from a confined region that is associated with the envelope + disk system. The presence of a number of components in the line of sight has also been confirmed by a rotation diagram which shows that both $^{12}$CO and $^{13}$CO integrated line intensities cannot be fit with single temperature lines. The rotation diagram approach uses the assumption that the medium is isothermal and in thermodynamic equilibrium. It is clear that this assumption is not met and so more detailed modelling of the emitting region is required.

Although the integrated line intensity maps for water do not show any structure, they are interesting in that there is relatively strong emission from the envelope + disk system. This is the first time that integrated line intensity maps for C I have been shown for Elias 29. The emission is more extended suggesting that it originates from the foreground clouds.

The results presented in this chapter will help future research to constrain radiative transfer models for Elias 29.

# Chapter 8

# Conclusions and Future Work

## 8.1 Conclusions

This thesis has presented *Herschel*-SPIRE observations of astronomical objects that belong to the earliest stages of stellar evolution. The study of these objects helps us better understand the processes involved in the formation of stars. This is the first time these objects have been observed with a broadband instrument working in the far-infrared region of the electromagnetic spectrum.

An introduction to the thesis was provided in Chapter 1 where a discussion of the ISM and our current understanding of the initial stages of stellar evolution were presented. It has been known for almost three decades now that the process of star formation begins with density enhancements of the ISM leading to the formation of centrally concentrated cores, which we refer to as "starless cores". The study of starless cores offers an opportunity to better understand the basic principles and evolution of star formation physics. A core that is gravitationally unstable collapses to form a Class 0 protostar, which then evolves to

become a Class I protostar. The evolution sequence proceeds as discussed in Chapter 1. In this thesis I have only discussed SPIRE iFTS observations of three starless cores, one Class 0 protostar and one Class I protostar. I have combined these SPIRE iFTS observations with observations from a variety of other facility instruments including the Submillimeter Common-User Bolometer Array (SCUBA) on the JCMT and MIPS together with IRAC on *Spitzer*.

The theoretical background required to understand observations of astronomical objects has been presented in Chapter 2. The chapter focused primarily on the elementary processes involved in the absorption and emission of electromagnetic radiation. Absorption and emission by atoms and molecules leads to line radiation and that by dust particles lead to continuum radiation. The propagation of this radiation through absorbing and emitting media has also been discussed. Example cases given in the chapter were based on molecules that have emission lines in the SPIRE band and have been identified in the SPIRE iFTS spectra for Class 0 and Class I protostars discussed in the later chapters of the thesis.

Chapters 3 and 4 present my contribution to the calibration of the SPIRE iFTS. Chapter 3 describes the derivation of the beam profile for the SPIRE iFTS. A discussion of the data reduction pipeline for the SPIRE iFTS is presented in Sections 3.3 and 3.4. Chapter 4 discusses applications of the beam profiles derived in Chapter 3. One of the applications is the correction of point-source calibrated observations of semi-extended sources. The other application discussed is the convolution of maps observed with instruments having different Point spread functions (PSFs) to a common beam for more meaningful comparison and interpretation.

Chapter 5 presents the analysis of SPIRE iFTS observations of three starless cores, L1521E, L1521F and L1689B. This is the first time the broadband far-infrared spectra of a starless core has been observed. Prior to *Herschel*, these objects were studied using SEDs derived from ∼3 –5 photometric points. Our SPIRE iFTS observations helped constrain the peak of the SEDs and, therefore the dust temperature and emissivity indices for these cores. The dust masses and column densities for the cores were also derived.

Chapter 6 presented the results derived from observations of IRAS16293-2422, a Class 0 protostar. A wealth of molecular line emission from $^{12}$CO, $^{13}$CO, C$^{18}$O, C I, $H_2O$, $HCO^+$ and CS was detected. We obtained spectral maps of IRAS16293-2422 which enabled study of the spatial extent of line emission. Combining these observations with those from other instruments, an SED was constructed enabling the derivation of dust temperature and emissivity index.

Chapter 7 presents results from the SPIRE iFTS mapping observations of Elias 29, a Class I protostar. The spectra were rich with emission lines from $^{12}$CO, $^{13}$CO, C I and $H_2O$. Integrated line intensities were derived from the brightest pixel on the spectral maps. Integrated line intensity maps from the detected emission lines confirm the presence of three components along the line of sight: foreground clouds, the ridge and envelope + disk system. The spatial extent of line emission can now be used together with high resolution spectral line information from instruments like the *Herschel* HIFI to derive physical properties of Elias 29.

## 8.2 Future Work

For the SPIRE iFTS sparsely sampled observations of pre-stellar cores (Chapter 5), there is a spectrum for almost each of the bolometers in the SSW and SLW bands. There are only two bolometers in the SSW band that are not functional. In this thesis, I only used spectra from the central bolometers in both bands. Further study will investigate the use of spectra from unvignetted and co-aligned bolometers in the construction of SEDs that can be used to study the spatial distribution of dust temperature and emissivity index.

Information about the spatial extent of line emission provided by the mapping observations is a useful constraint to radiative transfer models. Further study of IRAS16293 and Elias 29 (Chapters 6 and 7) will involve using the spatial extent of line emission from this work together with high resolution spectra from instruments like HIFI and Atacama Large Millimeter Array (ALMA) to constrain radiative transfer models. The Line Modeling Engine (LIME) (Brinch & Hogerheijde, 2010) and 1D radiative transfer code DUSTY (Ivezic & Elitzur, 1997) can now be used to derive the dust temperature and density profiles of these protostars.

This work, along with the proposed future study will serve to increase our knowledge of the physics of star formation.

# Appendix A

# The beam profile for the SPIRE FTS

Originally published in Applied Optics, 52, 3864-3875 (2013)

# The Beam Profile for the Herschel-SPIRE Fourier Transform Spectrometer

Gibion Makiwa,[1] David A. Naylor,[1] Marc Ferlet,[2] Carl Salji,[3] Bruce Swinyard,[2,3] Edward Polehampton[1,2] and Matthijs H. D. van der Wiel[1]

[1]*Institute for Space Imaging Science, Department of Physics and Astronomy, University of Lethbridge, 4401 University Drive, Lethbridge, AB, T1K 3M4, Canada*

[2]*RAL Space, Rutherford Appleton Laboratory, Didcot OX11 0QX, UK*

[3]*Department of Physics and Astronomy, University College London, Gower Street, London, WC1E 6BT, UK*

[*]*Corresponding author: gibion.makiwa@uleth.ca*

One of the instruments on board the Herschel Space Observatory is the Spectral and Photometric Imaging Receiver (SPIRE). SPIRE employs a Fourier transform spectrometer with feed-horn coupled bolometers to provide imaging spectroscopy. To interpret the resultant spectral images requires knowledge of the wavelength dependent beam, which in the case of SPIRE is complicated by the use of multi-moded feed-horns. In this paper we describe a series of observations and the analysis conducted to determine the wavelength dependence of the SPIRE spectrometer beam profile. 

*OCIS codes:* 350.6090, 120.6085, 350.1260, 120.6200

## 1. Introduction

It is now known that approximately half of the radiant energy emitted by the universe occurs in the infrared spectral range [1]. Most of the infrared wavelength region is inaccessible from the ground primarily due to absorption by the Earth's atmosphere, which necessitates the use of space borne instrumentation. Moreover, to minimize the effects of thermal emission from the infrared instruments themselves, which would otherwise dominate the weak astronomical signal, instruments must be cooled, often to liquid helium temperatures. In the first infrared space telescopes (Infrared Astronomical Satellite (IRAS) [2], Infrared Space Observatory (ISO) [3]) this was achieved by placing the entire telescope in a cryostat, limiting

the diameters of primary mirrors to 60 cm. While these pioneering missions provided our first view of the far-infrared universe their small aperture resulted in relatively low angular resolution.

On May 14, 2009, the European Space Agency launched the Herschel Space Observatory [4] which, with its 3.5 m diameter passively cooled primary mirror, provides a major advance in spatial resolution. Herschel is the largest infrared space telescope to-date and is designed to provide unfettered access to the far-infrared region by means of three instruments which are themselves cooled to $\leq 4$ K by an on board supply of liquid helium.

One of Herschel's instruments is the Spectral and Photometric Imaging Receiver (SPIRE) [5]. SPIRE is comprised of a three-band imaging photometer and a two-band imaging Fourier Transform Spectrometer (FTS). The SPIRE FTS uses feed-horn coupled spider-web bolometers that are cooled to $\approx 300$ mK [6], to provide imaging spectroscopy over the range from 194 to 671 $\mu$m.

A feature common to all interferometers is that they have two input and two output ports. In the case of the SPIRE FTS, one input views the astronomical source while the other views an internal blackbody calibration source. The two complementary output ports feed the Short Wavelength (SSW) array which consists of 37 detectors and covers wavelengths from 194-313 $\mu$m and the Long Wavelength (SLW) array which consists of 19 detectors and covers wavelengths from 303-671 $\mu$m.

A schematic view of the SPIRE FTS detectors is shown in Figure 1 [7]. The detector arrays themselves consist of hexagonally close-packed feed-horn-coupled spider-web bolometers [6]. Each feed-horn consists of a conical concentrator in front of a circular waveguide (see Section 2). The feed-horns for each array are optimized for the two spectral bands. Since the spectral ranges are too broad to be covered by a feed-horn coupled waveguide operating in a single mode, the waveguides propagate different transverse electric (TE) and transverse magnetic (TM) modes [8–10] as a function of wavelength. The cut-off frequency for each mode is dependent on the diameter of the waveguide. In this paper we examine the effect of this "multi-moded" response, as modified by the SPIRE optics, on the effective beam size of the SPIRE instrument. We present the wavelength dependent SPIRE FTS beam profile determined from raster observations of Neptune and Uranus, which, as will be shown, are good approximations to point sources.

## 2. Optical design of the Herschel-SPIRE FTS

In order to place the results presented in this paper in context, a brief review of the Herschel-SPIRE spectrometer is presented below. For more detailed information the reader is referred to papers by Dohlen *et al.* [11], Griffin *et al.* [12] and Naylor *et al.* [13].

Herschel is a classical Cassegrain telescope with the primary mirror having a diameter of

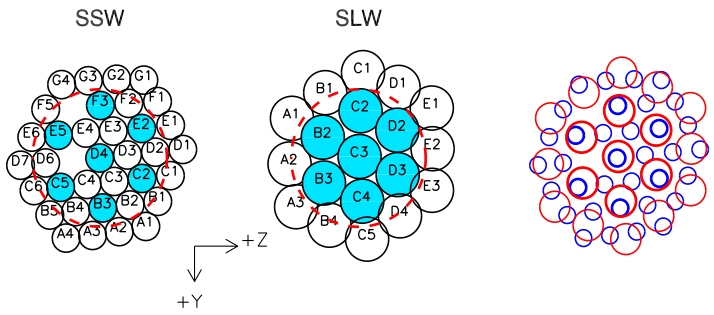


Fig. 1. A schematic view of the SPIRE FTS detector arrays and the spacecraft (Y,Z) coordinate system. The circles represent feed-horns for each detector. Circles shaded in blue represent SSW and SLW detectors that have the maximum overlap on the sky. The two empty spaces on the SSW array represent dead detectors. The 2.6′ unvignetted field of view for each detector array is delineated by a red dashed line. The rightmost figure shows the overlap on the sky of the SSW (blue circles) and SLW (red circles) detector arrays with circle sizes corresponding to a representative full width half maximum (FWHM) of the beam.

3.5 m and an “undersized" secondary mirror yielding an effective primary aperture of 3.29 m. The Herschel primary mirror was designed to have a fast f-ratio (f/0.5) to fit within the envelope of the launch vehicle. The resulting focal ratio of the Herschel telescope is f/8.68 [11, 12] which produces a curved focal surface at the entrance to the spectrometer.

Figure 2 shows the optical design of the SPIRE instrument [11, 12]. The photometer and spectrometer are mounted on opposite sides of a common optical bench. A mirror directs light from the telescope to either instrument. Before the beam reaches the FTS it passes through an undersized cold pupil stop located between the pick-off mirror and the input fold mirror. This pupil stop helps to minimize stray light from reaching the detectors. The SPIRE FTS is of the Mach-Zehnder configuration [13] which employs collimating mirrors within arms of the interferometer to control beam divergence and minimize the volume occupied. The beam enters the FTS through one of the input ports. A thermal calibration source is placed at the pupil image of the second input port. The source was designed such

that its temperature and emissivity could be adjusted to match the background emission from the telescope and thus reduce the interferogram modulation at zero path difference albeit at the cost of additional photon noise. However, three months after launch, during the commissioning phase of Herschel, it was found that the emissivity of the telescope was so low that the calibration source was not required.

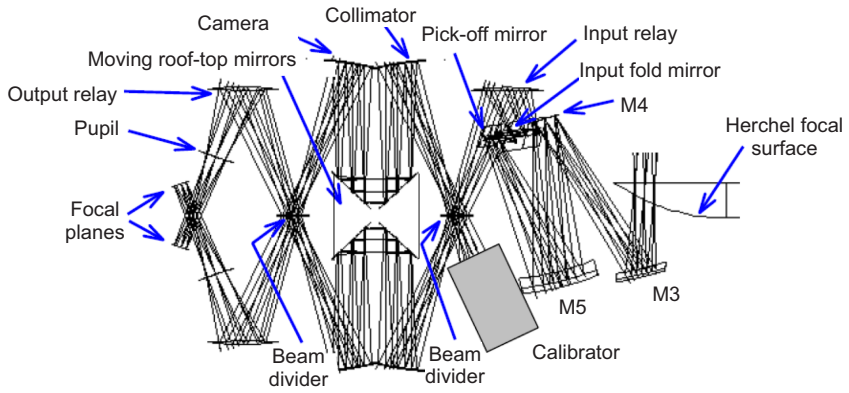


Fig. 2. The ray diagram of the SPIRE FTS. The design was constrained by the requirement to fit the instrument into the available space. For further details, the reader is refered to Griffin *et al.* [12].

Upon entering the FTS, the beam is brought to an intermediate focus just after the first intensity beam divider. It is then collimated and directed to the roof-top mirrors which create the optical path difference between the two interferometer beams. The SPIRE FTS can be operated at three spectral resolutions (Low, Medium and High Resolutions with designations LR, MR and HR respectively) corresponding to $\Delta\sigma$=0.83, 0.24 and 0.0398 cm$^{-1}$ respectively [7]. These resolutions were specifically chosen to match the science programs. From the roof-top mirrors, the beam is directed to the camera mirrors producing an image just before the second intensity beam divider. Finally, relay mirrors reimage the beam onto the feed-horns of the detector arrays.

Conical feed-horns, shown in Figure 3, are used to couple the large telescope beam onto the individual detectors. The feed-horns are hexagonally close-packed (Figure 1) and were chosen to have a center to center spacing of 2F$\lambda$ (where F is the final focal ratio), which was a compromise between increased individual detector sensitivity and spatial sampling. The

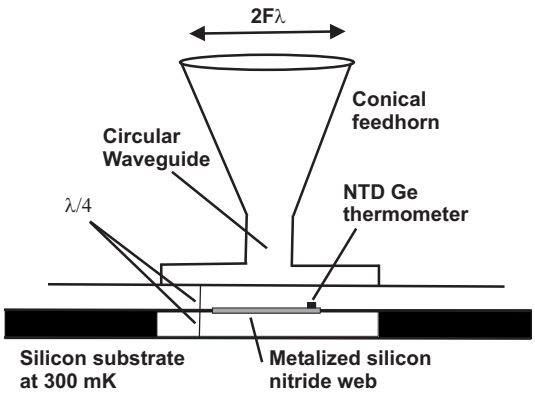


Fig. 3. The SPIRE feed-horn and cavity design. [9]. The metalized silicon nitride web absorber is located at the center of the integrating cavity, a distance of $\lambda/4$ below the front, and above the bottom surfaces.

feed-horns are terminated in circular wave-guides which are followed by integrating cavities. The bolometer itself is located at the center of the integrating cavity with a spacing of $\lambda/2$ between the front and rear surfaces of the cavity.

## 3. Observations

The wavelength dependent beam profile can be determined by obtaining a spectrum at each spatial position as a point source is raster scanned across the field of view of the spectrometer. Neptune and Uranus, both good approximations of point sources were used for this purpose; Neptune and Uranus having average diameters of 2.3″ and 3.5″ respectively, small when compared to the minimum predicted pre-launch beam sizes (17" for SSW and 30" for SLW [7]). Moreover, Neptune and Uranus are bright in the infrared, which leads to a high signal-to-noise ratio in measurements. The observation details are shown in Table 1. Herschel observations are classed according to the operational day on which they were taken (e.g. OD1234 for operational day 1234). The Neptune observation on OD210 consisted of medium spectral resolution ($\triangle\sigma$ = 0.24 cm$^{-1}$) FTS scans with two repetitions (i.e. 4 interferograms) per raster position, which yielded spectra with typical peak signal-to-noise ratios of ∼700 and ∼900 for SLW and SSW, respectively. The duration of the observation was 4.8 hours. The relative signal values and their errors were calculated using the Herschel Interactive Processing Environment (HIPE) data pipeline version 7 [14].

Table 1. Observation details of the data used to determine the SPIRE beam profile. [OD: Operational Day from the launch of the telescope, OBSID: OBServation IDentification number, Res: Spectral Resolution, LR: Low resolution, MR: Medium resolution, HR: High resolution, Reps: Number of repetitions, DOO: Duration of Observation, SS is the source size at the time of observation. More information about some of these parameters can be obtained from the SPIRE Observer's Manual [7].]

| Source | OD | OBSID | Res | Reps | DOO (s) | Raster grid size | Step size (″) | SS (″) |
|---|---|---|---|---|---|---|---|---|
| Neptune | 210 | 0x50002990 | MR | 2 | 17260 | 90″x90″ | 9 | 2.24 |
| | 742 | 0x5000AD8A | LR | 6 | 20983 | 84″x84″ | 7 | 2.26 |
| Uranus | 410 | 0x500055D6 | MR | 2 | 16528 | 70″x70″ | 7 | 3.50 |
| | 767 | 0x5000B216 | HR | 4 | 17036 | Cross (90″) | 7.5 | 3.46 |
| | 767 | 0x5000B217 | HR | 4 | 17036 | Cross (90″) | 7.5 | 3.46 |

The underlying processing of bolometer signals has not changed in more recent versions of HIPE and so updated processing would not change the results presented here (which depend only on the relative signal level between different raster positions). Since this observation was done in a special engineering mode where the spacecraft pointing (rather than the beam steering mirror position) was varied to obtain a map, the data required specialized processing. The data were produced in the form of a 3-D cube with two angular coordinates (RA and Dec) and one spectral coordinate, resulting in a complete SPIRE FTS spectrum at each of the points on the 11x11 (90″x90″) raster grid. Figure 4 shows the raster grid in the equatorial coordinate system (left) and in the spacecraft coordinate frame (right), which are related through a rotation matrix determined from the orientation of the spacecraft at the time of observation. The Neptune OD742 and Uranus OD410 observations have similar but smaller raster grids and different step sizes (see Table 1). The time required to measure the beam profile of all pixels in the arrays was prohibitive. For this reason the last two observations of Uranus were cross-rasters centered on two off-center detectors (SLWC2 for 0x5000B216 and SLWC4 for 0x5000B217). This produced two one-dimensional cuts of length 90″ along each of the two angular coordinates to allow us to investigate the beam profile of some of the other detectors and to verify that they were in good agreement with the center detectors in each array. In this paper we present the analysis of the Neptune OD210 observation, which has the largest raster grid and therefore enabled us to explore contributions from

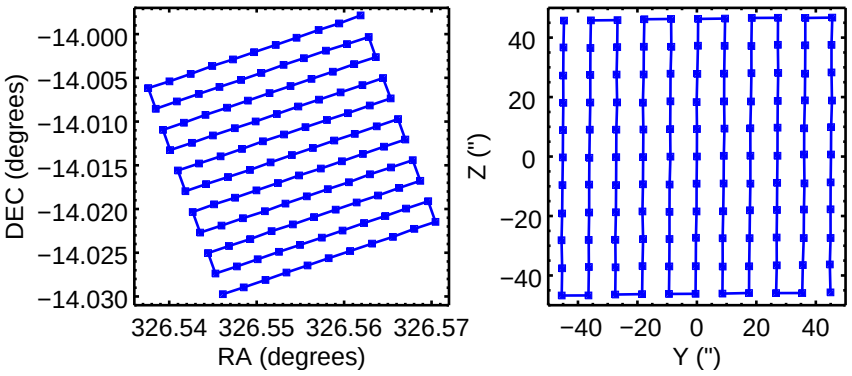


Fig. 4. The raster grid for the Neptune OD210 observation, corrected for proper motion of the planet, before (left) and after (right) rotation for alignment with the spacecraft Y and Z axes. Neptune was close to the center of the grid during the observation.

the wings of the beam profile. We also present the results from cross-raster observations of Uranus obtained on OD767. All of the other observations have been analyzed and confirm the results presented in this paper.

## 4. Hermite-Gaussian functions

End-to-end modeling of a complex optical system such as the SPIRE FTS, which includes 18 mirrors, 2 beamsplitters, several filters, a dichroic, a lens and an undersized pupil stop, is impractical. Moreover, some clipping of the divergent beam in the two arms of the FTS is inevitable since the location of the intermediate pupil image changes as the interferometer is scanned. Thus, even though the feed-horn modes themselves are well known [9], we cannot apply time reversal of the instrument beam from first principles.

In order to derive the SPIRE FTS beam, a linear superposition of Hermite-Gaussian functions was fitted to the data. The Hermite-Gaussian functions form a complete set of solutions to the paraxial Helmholtz equation [15, 16]. Another set of solutions which could have been used are Laguerre-Gaussian functions. We chose Hermite-Gaussian over Laguerre-Gaussian decomposition because it would be more instructive to reference the Cartesian frame of the instrument should clear asymmetries be present. Hermite-Gaussian basis functions are commonly used to describe systems with rectangular symmetry and are computationally

convenient. The decomposition adapted here should not be taken as directly representing the expected TE and TM modes but as a convenient mathematical representation.

The solutions of the Helmholtz equation represent the electromagnetic field and so the expression of the resulting intensity due to a superposition of Hermite-Gaussian basis functions is non-trivial. While we did explore contributions for individual basis functions, the experimental errors on the measurements prevented us from being able to confirm any asymmetries. As a result the final analysis assumed radially symmetric basis functions. The intensity distribution in the beam, $S(r,\lambda)$, was expressed as [15, 16],

$$S(r,\lambda) = \sum_{n=0}^{\infty} c_n(\lambda)|\varphi_n(r,\lambda)|^2. \tag{1}$$

where $c_n(\lambda)$ are the coefficients which indicate the intensity contribution from each basis function of order $n$. $r = \sqrt{x^2+y^2}$ where $x$ and $y$ are orthogonal angular coordinates. $\varphi_n(r,\lambda)$ are the radial basis functions of order $n$ and are given by the product of a Gaussian function and a Hermite polynomial:

$$\varphi_n(r,\lambda) = \left(\frac{2}{\pi}\right)^{1/4} \cdot \frac{1}{\sqrt{w_0(\lambda)}} \cdot \frac{1}{\sqrt{2^n \cdot n!}} \cdot H_n\left(\sqrt{2}\frac{r}{w_0(\lambda)}\right) e^{-r^2/w_0^2(\lambda)}. \tag{2}$$

$\varphi_n(r,\lambda)$ has been normalized such that $\int_{-\infty}^{+\infty} |\varphi_n(r,\lambda)|^2 dr = 1$. $w_0(\lambda)$ is the beam waist radius. For a Gaussian beam, $w_0(\lambda)$ is related to the full width half maximum (FWHM) by $w_0(\lambda)$ =FWHM/$\sqrt{2\ln 2}$. The relationship is more complex for a multi-moded beam. $H_n\left(\sqrt{2}\frac{r^2}{w_0(\lambda)}\right)$ are the Hermite polynomials of order $n$, the first three of which are given by

$$\begin{aligned} H_0(x) &= 1, \\ H_1(x) &= 2x, \\ H_2(x) &= 4x^2 - 2. \end{aligned} \tag{3}$$

To derive the analytical form of the SPIRE beam profile, the 2-D data at each wavelength was fitted using the first six terms of Equation (1) to extract optimum values of $c_n$ and $w_0$. The solution that gave lowest reduced chi-square, $\chi^2_R$, with the least number of terms was selected.

### 5. The effect of finite source size

The relatively small angular sizes of Neptune (diameter=2.3″) and Uranus (diameter=3.5″), when compared to the expected beam sizes for both SSW ($\sim$ 19″) and SLW ($\sim$35″) bands, is expected to incur negligible error. To confirm this we compared the convolution of the reconstructed beam and a cylinder representing the size of the Neptune disc with the raw data, and minimized the residuals. Table 2 shows a comparison of resulting beam widths,

Table 2. A comparison of the waist radii for the beam profile at a few frequencies in the SPIRE SSW band before and after correcting for the finite size of Neptune. The average errors for the uncorrected and corrected values are ± 0.06″ and ± 0.18″ respectively.

| Frequency (GHz) | Uncorrected $w_0(″)$ | Corrected $w_0(″)$ |
|---|---|---|
| 1349 | 14.43 | 14.34 |
| 1379 | 14.40 | 14.44 |
| 1409 | 14.27 | 14.22 |
| 1439 | 14.18 | 14.28 |
| 1469 | 14.06 | 13.98 |
| 1499 | 14.15 | 14.05 |

$w_0$, with and without the correction for the effect of the finite size of the planet. Values shown here are for the shortest wavelength (highest frequency) end of the SSW band where the effect is expected to be greatest. The effect, predicted to be 1.1 %, is dominated by the errors from the fitting process ($\sim \pm$ 2 %) and justifies our assumption that Neptune is a point source in the determination of the beam profile.

## 6. Results

### *6.A. Center detectors*

The results from fitting the radially symmetric basis functions (Equation (1)) are presented in the Appendix (Tables 3 and 4). With these results, one can reconstruct the wavelength dependent SPIRE FTS beam. The analysis showed that there is no significant improvement in the $\chi^2_R$ from including terms higher than the zeroeth order function (i.e. pure Gaussian) for the SSW band. In contrast, the SLW band requires the first three radially symmetric basis functions. Generally, the errors from fitting the SLW data are larger than for the SSW data. This is due to the additional higher order terms being fitted. The errors from the fitting of the waist radius are less than 2 % whilst the errors for the coefficients, $c_n$ increase with $n$ up to 20 % for certain wavelengths. This increase in uncertainty arises when the power assigned to higher order terms in the fitting process becomes comparable to the noise level in the data. Figures 5 and 6 show the results of the fitting performed at the edges of the SLW wavelength band; at 317.5 $\mu$m (944 GHz) and at 645.2 $\mu$m (464 GHz) respectively. At these wavelengths, the fitting returned $\chi^2_R$ values of 0.7 and 0.02, respectively.

Figure 7 shows the FWHM (solid curve) determined from the reconstructed composite

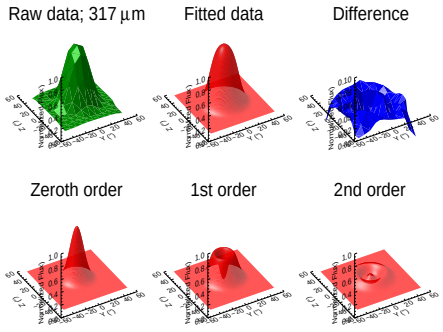


Fig. 5. Surface plots obtained from fitting Neptune data at 317.5 $\mu$m (944 GHz), the short wavelength end of the SLW band. The top row shows the raw data (left), fitted data (center) and the difference (right). The bottom row shows a decomposition of the fitted data (top center) into the first three modes.

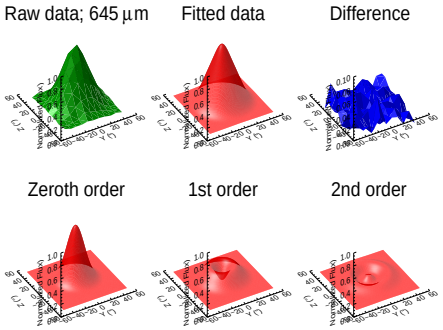


Fig. 6. Surface plots obtained from fitting Neptune OD210 data at 645.2 $\mu$m (464 GHz), the long wavelength end of the SLW band. The format of this figure is the same as that of Figure 5.

beam compared to that expected from diffraction theory (dashed line). The longer wavelength end of each SPIRE FTS band agrees well with diffraction theory. This is due to the fact

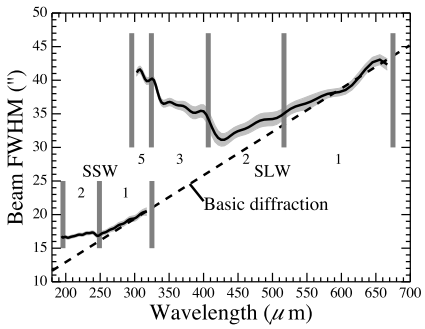


Fig. 7. The measured FWHM of the central detectors (SLWC3 and SSWD4) compared with diffraction theory. The gray band represents the $3\sigma$ errors in the measured FWHM. The thick vertical lines indicate the cut-on wavelengths for the different feed-horn modes. The expected number of modes present in these regions are also indicated.

that the beam is single-moded in these regions. As expected, the beam shows an increasing deviation from diffraction theory as the number of modes increases.

### *6.B. Off-center detectors*

Unfortunately, time precluded scanning Neptune over all of the detectors. While we lack complete spatial coverage for most of the off-center detectors, fitting was attempted on the partial data available. This allows us to comment on the variation in beam profile from one detector to another. The results are presented in Figures 8 and 9. In general, there is good agreement between different detectors. However, in the longer wavelength region of the SLW band (above 570 $\mu$m), there is a large spread in the FWHM. This is the region where the beam is large and so a large part of the profile fell outside the measured grid leading to fitting results with a larger $\chi^2_R$ value. An example of the fitting procedure applied to a detector where the peak of the measured signal lay close to the edge of the raster grid is shown in Figure 8. At this wavelength, the fit gave a $\chi^2_R$ value of 1.0.

It was therefore not meaningful to average the results and provide the SPIRE FTS users with a single set of parameters for the beam. We therefore recommend taking the beam profile for the center detectors provided in the Appendix as representative of other detectors. It can be seen that the FWHM for SSWE4 is slightly shifted from the other detectors. This may

be due to a manufacturing variance as each waveguide was custom made. There is however no clear confirmation in the manufacturing record for the feed-horns that this might be the case [17]. Figure 10 shows the FWHM obtained from fitting the Uranus OD767 cross-raster

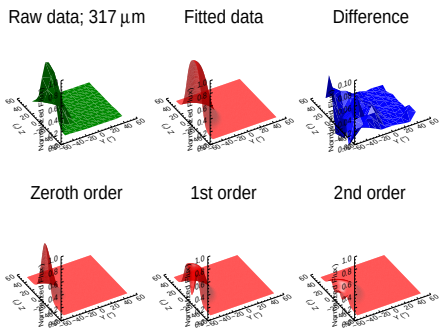


Fig. 8. Surface plots obtained from fitting Neptune OD210 data for detector SLWC2 at 317.5 $\mu$m (944 GHz) showing that the peak of the profile is close to the edge of the measured grid. The format of this figure is the same as that of Figure 5.

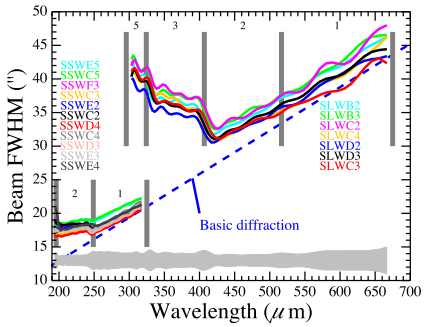


Fig. 9. The measured FWHM for selected off-center detectors. The grey band represents the standard deviation from the mean (not shown here) of the FWHM for all detectors shown.

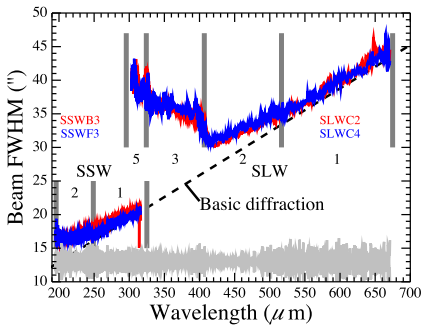


Fig. 10. The measured FWHM for selected off-center detectors from the Uranus cross-raster observations. The plot appears noisy since the observations were done in high spectral resolution. The gray band represents the mean $3\sigma$ errors in the measured FWHM.

observations with radially symmetric functions of the same form as Equation (1) for the four detectors on which the observations were centered. These results are in agreement with those for the center detectors presented in Figure 7. Moreover, since these observations were obtained at high spectral resolution, they serve to show that the derived beam parameters do not change significantly from medium to high spectral resolution.

## 7. Applications

In order to extract the maximum information from the spectral images obtained with the SPIRE FTS, it is important to take into account the effects of beam variation with wavelength. The efficiency with which the different feed-horn modes couple to the incoming radiation pattern from a source of finite size is dependent on source distribution [18–20] and so impacts the intepretation of measured flux values. The calibration of sources can be divided into three main categories: point like, semi-extended and extended sources. Point-like sources are defined as those with a size much smaller than the beam at all wavelengths. Extended sources have a source distribution much wider than the beam at all wavelengths. Semi-extended sources are found in-between these extremes. They partially fill the beam and their flux calibration is usually difficult since it requires prior knowledge of source extent and distribution.

The observed images represent a convolution of the source, be it point-like or extended,

and instrument point spread function (PSF). In many cases, facility instruments at major observatories have sufficiently small bandwidth that the variation of beam size with wavelength is generally insignificant. The trend to increase the bandwidth of instruments (for example the SPIRE FTS) means that an understanding of the beam profile is essential, not only to compare observations at different wavelengths within the SPIRE band, but also to compare the SPIRE results with those obtained with different instruments operating on different telescopes. The accurate wavelength dependent beam profile for the SPIRE FTS described in this paper can be used to explore deconvolution techniques such as the Maximum Entropy method [21], with the goal of improving the spatial resolution of spectral images [22, 23]. Conversely, knowledge of the beam profile can be used to convolve the SPIRE FTS data to a common beam size. Finally, the beam profile can be used to calculate the coupling integral with a model source distribution to disentangle the effects of source extent from the measured spectrum [20].

## 8. Summary and Conclusions

Flux calibration is one of the most important steps in astronomical data analysis. The measured spectra are impacted by the wavelength dependent beam profile and the source extent. In this paper we describe the steps followed in the determination of the SPIRE FTS beam profile. Because the SPIRE FTS optical components are undersized and the detectors are feed-horn-coupled, the beam profile exhibits a complex dependence on wavelength as the multi-moded feed-horns allow different modes to be enabled at certain wavelengths in the SPIRE band. All of the well characterized detectors exhibit the same mode structure. In order to simplify the analysis of mapping observations where the spatial extent of the source is provided by off-center detectors, the beam profiles for the center detectors can be taken as representative of the rest of the detectors. While allowing for six basis functions, we conclude that the SSW band is best represented by a Gaussian beam which is well behaved in deconvolution applications, whereas the SLW band is more complex with at least three terms identified. The final number of terms was determined after comparing the rms values of the residuals of the fit. Tables of the final wavelength dependent beam parameters are provided in the Appendix.

*Acknowledgments*

Herschel is an ESA space observatory with science instruments provided by European-led Principal Investigator consortia and with important participation from NASA. SPIRE has been developed by a consortium of institutes led by Cardiff Univ. UK and including Univ. Lethbridge (Canada); NAOC (China); CEA, LAM (France); IFSI, Univ. Padua (Italy); IAC (Spain); Stolkholm Observatory (Sweden); Imperial College London, RAL, UCL-MSSL,

UKATC, Univ. Sussex (UK); Caltech, JPL, NHSC, Univ.Colorado (USA). This development has been supported by national funding agencies: CSA (Canada); NAOC (China); CEA, CNES, CNRS (France); ASI (Italy); MCINN (Spain); SNSB (Sweden); STFC (UK); and NASA (USA).

The authors would like to acknowledge Peter Imhof and Trevor Fulton of Bluesky Spectroscopy for providing the HIPE processed data from Neptune and Uranus observations and also the conversion matrix from RA/Dec to the spacecraft (Y,Z) coordinate system for both planets. G.M., D.A.N. and M.H.D.vdW. acknowledge support from the CSA and NSERC.

**References**

1. M. G. Hauser and E. Dwek, "The cosmic infrared background: Measurements and Implications," Annu. Rev. Astron. Astr. **39**(1), 249-307 (2001).
2. G. Neugebauer, H. J. Habing, R. van Duinen, H. H. Aumann, B. Baud, C. A. Beichman, D. A. Beintema, N. Boggess, P. E. Clegg, T. de Jong, J. P. Emerson, T. N. Gautier, F. C. Gillett, S. Harris, M. G. Hauser, J. R. Houck, R. E. Jennings, F. J. Low, P. L. Marsden, G. Miley, F. M. Olnon, S. R. Pottasch, E. Raimond, M. Rowan-Robinson, B. T. Soifer, R. G. Walker, P. R. Wesselius and E. Young, "The Infrared Astronomical Satellite (IRAS) mission," Astrophys. J. **278**, L1-L6 (1984).
3. M. F. Kessler, J. A. Sreinz, M. E. Anderegg, J. Clavel, G. Drechsel, P. Estaria, J. Faelker, J. R. Riedinger, A. Robson, B. G. Taylor, S. Ximénez de Ferrán, "The Infrared Space Observatory (ISO) mission," Astron. Astrophys. **315**, L27-L31 (1996).
4. G. L. Pilbratt, J. R. Riedinger, T. Passvogel, G. Crone, D. Doyle, U. Gageur, A. M. Heras, C. Jewell, L. Metcalfe, S. Ott and M. Schmidt, "Herschel Space Observatory - An ESA facility for far-infrared and submillimetre astronomy," Astron. Astrophys. **518**, L1, 3-8 (2010).
5. M. J. Griffin, A. Abergel, A. Abreu, P. A. R. Ade, P. André, J.-L. Augueres, T. Babbedge, Y. Bae, T. Baillie, J.-P. Baluteau, M. J. Barlow, G. Bendo, D. Benielli, J. J. Bock, P. Bonhomme, D. Brisbin, C. Brockley-Blatt, M. Caldwell, C. Cara, N. Castro-Rodriguez, R. Cerulli, P. Chanial, S. Chen, E. Clark, D. L. Clements, L. Clerc, J. Coker, D. Communal, L. Conversi, P. Cox, D. Crumb, C. Cunningham, F. Daly, G. R. Davis, P. De Antoni, J. Delderfield, N. Devin, A. Di Giorgio, I. Didschuns, K. Dohlen, M. Donati, A. Dowell, C. D. Dowell, L. Duband, L. Dumaye, R. J. Emery, M. Ferlet, D. Ferrand, J. Fontignie, M. Fox, A. Franceschini, M. Frerking, T. Fulton, J. Garcia, R. Gastaud, W. K. Gear, J. Glenn, A. Goizel, D. K. Griffin, T. Grundy, S. Guest, L. Guillemet, P. C. Hargrave, M. Harwit, P. Hastings, E. Hatziminaoglou, M. Herman, B. Hinde, V. Hristov, M. Huang, P. Imhof, K. J. Isaak, U. Israelsson, R. J. Ivison, D. Jennings, B. Kiernan, K. J. King, A. E. Lange, W. Latter, G. Laurent, P. Laurent, S. J. Leeks, E. Lellouch, L. Leven-

son, B. Li, J. Li, J. Lilienthal, T. Lim, S. J. Liu, N. Lu, S. Madden, G. Mainetti, P. Marliani, D. McKay, K. Mercier, S. Molinari, H. Morris, H. Moseley, J. Mulder, M. Mur, D. A. Naylor, H. Nguyen, B. O'Halloran, S. Oliver, G. Olofsson, H.-G. Olofsson, R. Orfei, M. J. Page, I. Pain, P. Panuzzo, A. Papageorgiou, G. Parks, P. Parr-Burman, A. Pearce, C. Pearson, I. Pérez-Fournon, F. Pinsard, G. Pisano, J. Podosek, M. Pohlen, E. T. Polehampton, D. Pouliquen, D. Rigopoulou, D. Rizzo, I. G. Roseboom, H. Roussel, M. Rowan-Robinson, B. Rownd, P. Saraceno, M. Sauvage, R. Savage, G. Savini, E. Sawyer, C. Scharmberg, D. Schmitt, N. Schneider, B. Schulz, A. Schwartz, R. Shafer, D. L. Shupe, B. Sibthorpe, S. Sidher, A. Smith, A. J. Smith, D. Smith, L. Spencer, B. Stobie, R. Sudiwala, K. Sukhatme, C. Surace, J. A. Stevens, B. M. Swinyard, M. Trichas, T. Tourette, H. Triou, S. Tseng, C. Tucker, A. Turner, M. Vaccari, I. Valtchanov, L. Vigroux, E. Virique, G. Voellmer, H. Walker, R. Ward, T. Waskett, M. Weilert, R. Wesson, G. J. White, N. Whitehouse, C. D. Wilson, B. Winter, A. L. Woodcraft, G. S. Wright, C. K. Xu, A. Zavagno, M. Zemcov, L. Zhang and E. Zonca, "The Herschel-SPIRE instrument and its in-flight performance," Astron. Astrophys. **518**, L3, 21-27 (2010).

6. A. D. Turner, J. J. Bock, J. W. Beeman, J. Glenn, P. C. Hargrave, V. V. Hristov, H T. Nguyen, F. Rahman, S. Sethuraman, and A. L. Woodcraft, "Silicon nitride micromesh bolometer array for submillimeter astrophysics," Appl. Opt. **40**(28), 4921-4932 (2001).
7. SPIRE Observer's Manual v2.4. 2011, Herschel Science Centre, HERSCHEL-DOC-0798.
8. J. A. Murphy and R. Padman, "Radiation patterns of few-moded horns and condensing lightpipes," Infrared Phys. **31**(3), 1676-1690 (1993)
9. G. Chattopadhyay, J. Glenn, J. J. Bock, B. K. Rownd, M. Caldwell, M. J. Griffin, "Feed horn coupled bolometer arrays for SPIRE - design, simulations, and measurements," IEEE Trans. Microwave Theory Tech. **51**(10), 2139-2146 (2003).
10. B. Rownd, J. J. Bock, G Chattopadhyay, J. Glenn and M. J. Griffin, "Design and performance of feedhorn-coupled bolometer arrays for SPIRE," *Millimeter and Submillimeter Detectors for Astronomy*, Thomas G. Phillips, Jonas Zmuidzinas, Eds, Proc. SPIE **4855**, 510-519 (2002).
11. K. Dohlen, A. Origné, D. Pouliquen and B. Swinyard, "Optical design of the SPIRE instrument for First," *UV, Optical, and IR Space Telescopes and Instruments*, J. B. Breckinridge, P. Jakobsen, Eds, Proc. SPIE **4013**, 119-128 (2000).
12. M. Griffin, A. Abergel, P. Ade, P. André, J-P. Baluteau, J. Bock, A. Franceschini, W. Gear, J. Glenn, D. Griffin, K. King, E. Lellouch, D. Naylor, G. Olofsson, I. Perez-Fournon, M. Rowan-Robinson, P. Saraceno, E. Sawyer, A. Smith, B. Swinyard, L. Vigroux, G. Wright, "Herschel-SPIRE: design, performance, and scientific capabilities," *Space Telescopes and Instrumentation I: Optical, Infrared, and Millimeter*, Edited by

John. C. Mather, H. A. MacEwen, M. W. M. de Graauw, Proc. SPIE **6265**, 62650A-62650A-12 (2006).

13. D. A. Naylor, B. G. Gom, I. Schofield, G. Tompkins and G. R. Davis, "Mach-Zehnder Fourier transform spectrometer for astronomical spectroscopy at submillimeter wavelengths," Proc. SPIE **4855**, 540-551 (2003).
14. S. Ott, "The Herschel Data Processing System - HIPE and Pipelines - Up and Running Since the Start of the Mission," Astronomical Data Analysis Software and Systems XVIII, ASP Conference Series **434**, 139-142 (2010).
15. L. Mandel and E. Wolf, *Optical Coherence and quantum optics* (Cambridge University Press, 1995).
16. D. H. Martin and J. W. Bowen, "Long-wave optics," IEEE Trans. Microwave Theory Tech. **41**(10), 1676-1690 (1993)
17. J. J. Bock, Jet Propulsion Laboratory, M/S 169-327, 4800 Oak Grove Drive, Pasadena, CA 91109, USA (private communication, 2013)
18. P. Panuzzo, N. Rangwala, A. Rykala, K. G. Isaak, J. Glenn, C. D. Wilson, R. Auld, M. Baes, M. J. Barlow, G. J. Bendo, J. J. Bock, A. Boselli, M. Bradford, V. Buat, N. Castro-Rodríguez, P. Chanial, S. Charlot, L. Ciesla, D. L. Clements, A. Cooray, D. Cormier, L. Cortese, J. I. Davies, E. Dwek, S. A. Eales, D. Elbaz, T. Fulton, M. Galametz, F. Galliano, W. K. Gear, H. L. Gomez, M. Griffin, S. Hony, L. R. Levenson, N. Lu, S. Madden, B. O'Halloran, K. Okumura, S. Oliver, M. J. Page, A. Papageorgiou, T. J. Parkin, I. Pérez-Fournon, M. Pohlen, E. T. Polehampton, E. E. Rigby, H. Roussel, N. Sacchi, M. Sauvage, B. Schulz, M. R. P. Schirm, M. W. L. Smith, L. Spinoglio, J. A. Stevens, S. Srinivasan, M. Symeonidis, B. Swinyard, M. Trichas, M. Vaccari, L. Vigroux, H. Wozniak, G. S. Wright and W. W. Zeilinger, "Probing the molecular interstellar medium of M82 with Herschel-SPIRE spectroscopy," Astron. Astrophys. **518**, L37, 199-203 (2010).
19. B. M. Swinyard, P. Ade, J.-P. Baluteau, H. Aussel, M. J. Barlow, G. J. Bendo, D. Benielli, J. Bock, D. Brisbin, A. Conley, L. Conversi, A. Dowell, D. Dowell, M. Ferlet, T. Fulton, J. Glenn, A. Glauser, D. Griffin, M. Griffin, S. Guest, P. Imhof, K. Isaak, S. Jones, K. King, S. Leeks, L. Levenson, T. L. Lim, N. Lu, G. Makiwa, D. Naylor, H. Nguyen, S. Oliver, P. Panuzzo, A. Papageorgiou, C. Pearson, M. Pohlen, E. Polehampton, D. Pouliquen, D. Rigopoulou, S. Ronayette, H. Roussel, A. Rykala, G. Savini, B. Schulz, A. Schwartz, D. Shupe, B. Sibthorpe, S. Sidher, A. J. Smith, L. Spencer, M. Trichas, H. Triou, I. Valtchanov, R. Wesson, A. Woodcraft, C. K. Xu, M. Zemcov and L. Zhang, "In-flight calibration of the Herschel-SPIRE instrument," Astron. Astrophys. **518**, L4, 28-33 (2010).
20. R. Wu, Commissariat À l´Ènergie Atomique, Service d´Astrophysique, Saclay, 91191

Gif-sur Yvette, France, E. Polehampton, M. Etxaluze, G. Makiwa *et al.* are preparing a manuscript to be called, "Derivation of the Herschel Semi-Extended Correction Tool (SECT)."

21. S. F. Gull and G. J. Daniell, "Image reconstruction from incomplete and noisy data," Nature. **272**, 686 - 690 (1978).
22. H. Ayasso, T. Rodet and A. Abergel, "A variational approach for unsupervised super-resolution using mixture models of point and smooth sources applied to astrophysical mapmaking," Inverse Problems, **28**, 125005 (2012).
23. H. Ayasso, MCF Université Joseph Fourier/UFR PhITEM, BP 46 - 38402 Saint Martin d´Hères Cedex, France, *et al.* are preparing a manuscript to be called, "SUPREME: a SUPer REsolution Mapmaker for Extended emission based on an unsupervised Variational Bayesian approach."

**Appendix**

This appendix contains the wavelength dependent beam parameters required for reconstruction of the SPIRE FTS beam. There are two tables, one for each of the SPIRE FTS bands. The FWHM values provided in the tables were determined from the reconstructed beams and do not imply the beam is Gaussian throughout the wavelength range. The wavelength dependent beam can be reconstructed using Equations (1), (2) and (3) and the parameters given in this Appendix. The following example shows how to calculate the area normalized beam at a wavelength of 317.5 $\mu$m (944 GHz).

$$\begin{aligned} S(r, 944\text{GHz}) &= 0.533\left[\left(\frac{2}{\pi}\right)^{1/4}\cdot\frac{1}{\sqrt{18.72}}\cdot\frac{1}{\sqrt{2^0\cdot 0!}}\cdot(1)\cdot e^{-r^2/18.72^2}\right]^2 \\ &\quad +0.355\left[\left(\frac{2}{\pi}\right)^{1/4}\cdot\frac{1}{\sqrt{18.72}}\cdot\frac{1}{\sqrt{2^1\cdot 1!}}\cdot\left(2\sqrt{2}\frac{r}{18.72}\right)\cdot e^{-r^2/18.72^2}\right]^2 \\ &\quad +0.112\left[\left(\frac{2}{\pi}\right)^{1/4}\cdot\frac{1}{\sqrt{18.72}}\cdot\frac{1}{\sqrt{2^2\cdot 2!}}\cdot\left(4(\sqrt{2}\frac{r}{18.72})^2-2\right)\cdot e^{-r^2/18.72^2}\right]^2 \quad (4) \end{aligned}$$

The radial distance $r$ (in arcseconds) is calculated from the center of a 2-D array generated by the user.

Table 3: Parameters required to generate the SPIRE FTS SLW beam profiles using Equation (1). These parameters were derived from the central detector, SLWC3. [$f$: frequency; $w_0$: waist radius; $\triangle w_0$: error in $w_0$; $c_n$: coefficients of Hermite-Gaussian terms; $\triangle c_n$: error in $c_n$, FWHM:Full Width at Half Maximum; $\triangle$ FWHM: error in FWHM.]

| $f$ (GHz) | $w_0$ ($''$) | $\triangle\ w_0$ ($''$) | $c_0$ | $\triangle\ c_0$ | $c_1$ | $\triangle\ c_1$ | $c_2$ | $\triangle\ c_2$ | FWHM ($''$) | $\triangle$ FWHM ($''$) |
|---|---|---|---|---|---|---|---|---|---|---|
| 442 | 24.01 | 0.55 | 0.643 | 0.021 | 0.192 | 0.013 | 0.164 | 0.016 | 39.5 | 0.3 |
| 449 | 24.68 | 0.43 | 0.642 | 0.015 | 0.219 | 0.008 | 0.139 | 0.012 | 42.3 | 0.3 |
| 457 | 24.90 | 0.34 | 0.646 | 0.012 | 0.230 | 0.006 | 0.125 | 0.009 | 43.1 | 0.2 |
| 464 | 24.80 | 0.32 | 0.652 | 0.011 | 0.231 | 0.005 | 0.116 | 0.008 | 42.7 | 0.2 |
| 472 | 24.45 | 0.32 | 0.659 | 0.012 | 0.228 | 0.005 | 0.112 | 0.008 | 41.6 | 0.3 |
| 479 | 23.91 | 0.32 | 0.663 | 0.012 | 0.224 | 0.005 | 0.112 | 0.008 | 40.4 | 0.3 |
| 487 | 23.31 | 0.30 | 0.662 | 0.011 | 0.222 | 0.005 | 0.116 | 0.008 | 39.3 | 0.2 |
| 494 | 22.79 | 0.28 | 0.657 | 0.011 | 0.221 | 0.005 | 0.121 | 0.008 | 38.6 | 0.2 |

Continued on next page

Table 3 – continued from previous page

| $f$ (GHz) | $w_0$ ($''$) | $\triangle\ w_0$ ($''$) | $c_0$ | $\triangle\ c_0$ | $c_1$ | $\triangle\ c_1$ | $c_2$ | $\triangle\ c_2$ | FWHM ($''$) | $\triangle$ FWHM ($''$) |
|---|---|---|---|---|---|---|---|---|---|---|
| 502 | 22.44 | 0.26 | 0.652 | 0.011 | 0.223 | 0.005 | 0.125 | 0.008 | 38.2 | 0.2 |
| 509 | 22.24 | 0.26 | 0.650 | 0.010 | 0.226 | 0.005 | 0.124 | 0.008 | 38.1 | 0.2 |
| 517 | 22.12 | 0.26 | 0.653 | 0.011 | 0.230 | 0.005 | 0.118 | 0.008 | 38.0 | 0.2 |
| 524 | 21.98 | 0.29 | 0.659 | 0.012 | 0.233 | 0.005 | 0.108 | 0.009 | 37.6 | 0.2 |
| 532 | 21.78 | 0.34 | 0.666 | 0.014 | 0.237 | 0.006 | 0.097 | 0.010 | 37.2 | 0.3 |
| 539 | 21.52 | 0.36 | 0.669 | 0.015 | 0.241 | 0.006 | 0.090 | 0.011 | 36.8 | 0.3 |
| 547 | 21.25 | 0.36 | 0.668 | 0.015 | 0.245 | 0.006 | 0.088 | 0.011 | 36.5 | 0.3 |
| 554 | 21.01 | 0.33 | 0.664 | 0.014 | 0.247 | 0.006 | 0.089 | 0.010 | 36.3 | 0.3 |
| 562 | 20.82 | 0.32 | 0.662 | 0.014 | 0.248 | 0.006 | 0.090 | 0.010 | 36.1 | 0.3 |
| 569 | 20.68 | 0.31 | 0.663 | 0.014 | 0.247 | 0.006 | 0.090 | 0.010 | 35.7 | 0.3 |
| 577 | 20.55 | 0.31 | 0.669 | 0.014 | 0.244 | 0.006 | 0.087 | 0.010 | 35.3 | 0.3 |
| 584 | 20.44 | 0.33 | 0.676 | 0.015 | 0.241 | 0.006 | 0.082 | 0.010 | 34.7 | 0.3 |
| 592 | 20.35 | 0.36 | 0.682 | 0.016 | 0.240 | 0.006 | 0.078 | 0.011 | 34.4 | 0.3 |
| 599 | 20.29 | 0.36 | 0.684 | 0.016 | 0.241 | 0.007 | 0.075 | 0.011 | 34.2 | 0.3 |
| 607 | 20.23 | 0.36 | 0.684 | 0.016 | 0.242 | 0.006 | 0.074 | 0.011 | 34.2 | 0.3 |
| 614 | 20.14 | 0.36 | 0.683 | 0.016 | 0.244 | 0.006 | 0.073 | 0.011 | 34.1 | 0.3 |
| 622 | 20.01 | 0.36 | 0.682 | 0.017 | 0.246 | 0.007 | 0.072 | 0.011 | 34.0 | 0.3 |
| 629 | 19.81 | 0.36 | 0.683 | 0.017 | 0.247 | 0.007 | 0.070 | 0.011 | 33.7 | 0.3 |
| 637 | 19.60 | 0.35 | 0.683 | 0.016 | 0.248 | 0.006 | 0.069 | 0.011 | 33.3 | 0.3 |
| 644 | 19.41 | 0.33 | 0.684 | 0.016 | 0.248 | 0.006 | 0.068 | 0.010 | 33.0 | 0.3 |
| 652 | 19.30 | 0.31 | 0.684 | 0.015 | 0.247 | 0.006 | 0.069 | 0.010 | 32.7 | 0.3 |
| 659 | 19.26 | 0.30 | 0.685 | 0.015 | 0.244 | 0.006 | 0.070 | 0.009 | 32.6 | 0.3 |
| 667 | 19.21 | 0.30 | 0.687 | 0.014 | 0.243 | 0.006 | 0.071 | 0.009 | 32.4 | 0.3 |
| 674 | 19.10 | 0.30 | 0.688 | 0.015 | 0.241 | 0.006 | 0.071 | 0.009 | 32.1 | 0.3 |
| 682 | 18.90 | 0.32 | 0.689 | 0.016 | 0.241 | 0.006 | 0.069 | 0.010 | 31.8 | 0.3 |
| 689 | 18.68 | 0.33 | 0.691 | 0.016 | 0.242 | 0.007 | 0.067 | 0.010 | 31.4 | 0.3 |
| 697 | 18.58 | 0.33 | 0.694 | 0.017 | 0.242 | 0.007 | 0.063 | 0.010 | 31.1 | 0.3 |
| 704 | 18.73 | 0.34 | 0.702 | 0.017 | 0.239 | 0.007 | 0.059 | 0.010 | 31.1 | 0.3 |
| 712 | 19.23 | 0.36 | 0.715 | 0.018 | 0.232 | 0.008 | 0.053 | 0.010 | 31.4 | 0.4 |
| 719 | 19.99 | 0.41 | 0.729 | 0.019 | 0.223 | 0.008 | 0.048 | 0.011 | 32.0 | 0.4 |
| 726 | 20.73 | 0.43 | 0.734 | 0.019 | 0.218 | 0.009 | 0.048 | 0.011 | 32.9 | 0.4 |
| 734 | 21.18 | 0.41 | 0.725 | 0.018 | 0.221 | 0.008 | 0.054 | 0.010 | 34.0 | 0.4 |
| 741 | 21.34 | 0.38 | 0.710 | 0.016 | 0.229 | 0.006 | 0.061 | 0.010 | 34.9 | 0.4 |

Continued on next page

Table 3 – continued from previous page

| $f$ (GHz) | $w_0$ ($''$) | $\triangle\ w_0$ ($''$) | $c_0$ | $\triangle\ c_0$ | $c_1$ | $\triangle\ c_1$ | $c_2$ | $\triangle\ c_2$ | FWHM ($''$) | $\triangle$ FWHM ($''$) |
|---|---|---|---|---|---|---|---|---|---|---|
| 749 | 21.33 | 0.35 | 0.699 | 0.015 | 0.236 | 0.006 | 0.065 | 0.009 | 35.4 | 0.3 |
| 756 | 21.22 | 0.33 | 0.694 | 0.014 | 0.239 | 0.005 | 0.067 | 0.009 | 35.4 | 0.3 |
| 764 | 21.08 | 0.32 | 0.693 | 0.014 | 0.241 | 0.005 | 0.066 | 0.009 | 35.3 | 0.3 |
| 771 | 20.95 | 0.32 | 0.693 | 0.014 | 0.242 | 0.005 | 0.065 | 0.009 | 35.2 | 0.3 |
| 779 | 20.85 | 0.32 | 0.690 | 0.014 | 0.245 | 0.005 | 0.065 | 0.009 | 35.2 | 0.3 |
| 786 | 20.75 | 0.32 | 0.683 | 0.014 | 0.250 | 0.005 | 0.067 | 0.009 | 35.4 | 0.3 |
| 794 | 20.63 | 0.31 | 0.673 | 0.014 | 0.257 | 0.005 | 0.070 | 0.009 | 35.7 | 0.3 |
| 801 | 20.46 | 0.29 | 0.661 | 0.013 | 0.264 | 0.005 | 0.075 | 0.009 | 36.0 | 0.3 |
| 809 | 20.28 | 0.27 | 0.651 | 0.012 | 0.269 | 0.005 | 0.080 | 0.009 | 36.2 | 0.2 |
| 816 | 20.09 | 0.25 | 0.644 | 0.011 | 0.273 | 0.005 | 0.084 | 0.008 | 36.2 | 0.2 |
| 824 | 19.94 | 0.24 | 0.638 | 0.011 | 0.275 | 0.004 | 0.087 | 0.008 | 36.3 | 0.2 |
| 831 | 19.82 | 0.23 | 0.632 | 0.011 | 0.278 | 0.004 | 0.090 | 0.008 | 36.3 | 0.2 |
| 839 | 19.74 | 0.23 | 0.627 | 0.011 | 0.281 | 0.004 | 0.092 | 0.008 | 36.5 | 0.2 |
| 846 | 19.65 | 0.23 | 0.621 | 0.011 | 0.286 | 0.005 | 0.093 | 0.008 | 36.7 | 0.2 |
| 854 | 19.54 | 0.23 | 0.616 | 0.011 | 0.290 | 0.005 | 0.094 | 0.009 | 36.8 | 0.2 |
| 861 | 19.38 | 0.23 | 0.612 | 0.011 | 0.293 | 0.005 | 0.094 | 0.009 | 36.7 | 0.2 |
| 869 | 19.21 | 0.22 | 0.609 | 0.011 | 0.296 | 0.005 | 0.095 | 0.009 | 36.6 | 0.2 |
| 876 | 19.05 | 0.21 | 0.605 | 0.011 | 0.299 | 0.005 | 0.097 | 0.008 | 36.5 | 0.2 |
| 884 | 18.94 | 0.20 | 0.597 | 0.010 | 0.303 | 0.004 | 0.099 | 0.008 | 36.7 | 0.2 |
| 891 | 18.88 | 0.20 | 0.585 | 0.010 | 0.311 | 0.005 | 0.104 | 0.008 | 37.3 | 0.2 |
| 899 | 18.87 | 0.19 | 0.567 | 0.010 | 0.323 | 0.005 | 0.110 | 0.008 | 38.2 | 0.1 |
| 906 | 18.88 | 0.19 | 0.549 | 0.010 | 0.336 | 0.005 | 0.115 | 0.008 | 39.3 | 0.1 |
| 914 | 18.88 | 0.19 | 0.536 | 0.010 | 0.346 | 0.005 | 0.118 | 0.009 | 40.0 | 0.1 |
| 921 | 18.86 | 0.19 | 0.531 | 0.010 | 0.351 | 0.005 | 0.118 | 0.009 | 40.2 | 0.2 |
| 929 | 18.82 | 0.19 | 0.533 | 0.010 | 0.352 | 0.005 | 0.116 | 0.009 | 40.1 | 0.2 |
| 936 | 18.78 | 0.20 | 0.535 | 0.010 | 0.352 | 0.005 | 0.113 | 0.009 | 39.9 | 0.2 |
| 944 | 18.72 | 0.20 | 0.533 | 0.010 | 0.355 | 0.005 | 0.112 | 0.009 | 39.9 | 0.2 |
| 951 | 18.65 | 0.20 | 0.524 | 0.011 | 0.362 | 0.005 | 0.113 | 0.010 | 40.2 | 0.2 |
| 959 | 18.57 | 0.21 | 0.510 | 0.011 | 0.373 | 0.006 | 0.117 | 0.010 | 40.7 | 0.2 |
| 966 | 18.50 | 0.20 | 0.496 | 0.011 | 0.383 | 0.006 | 0.121 | 0.010 | 41.3 | 0.2 |
| 974 | 18.47 | 0.19 | 0.489 | 0.010 | 0.388 | 0.006 | 0.123 | 0.010 | 41.6 | 0.2 |
| 981 | 18.48 | 0.18 | 0.492 | 0.010 | 0.386 | 0.005 | 0.123 | 0.009 | 41.5 | 0.2 |
| 989 | 18.54 | 0.17 | 0.501 | 0.009 | 0.379 | 0.005 | 0.120 | 0.008 | 41.1 | 0.1 |

Table 4: Parameters required to generate the SPIRE FTS SSW beam profile using Equation (1). These parameters were derived from the central detector, SSWD4. [$f$: frequency; $w_0$: waist radius; $\triangle w_0$: error in $w_0$; $c_n$: coefficients of Hermite-Gaussian terms; $\triangle c_n$: error in $c_n$, FWHM:Full Width at Half Maximum; $\triangle$ FWHM: error in FWHM.]

| $f$ (GHz) | $w_0(''$) | $\triangle$ $w_0(''$) | $c_0$ | $\triangle$ $c_0$ | FWHM($''$) | $\triangle$ FWHM($''$) |
|---|---|---|---|---|---|---|
| 936 | 17.36 | 0.27 | 1.000 | 0.016 | 20.4 | 0.3 |
| 944 | 17.35 | 0.16 | 1.000 | 0.010 | 20.4 | 0.2 |
| 951 | 17.34 | 0.13 | 1.000 | 0.008 | 20.4 | 0.2 |
| 959 | 17.28 | 0.12 | 1.000 | 0.007 | 20.3 | 0.1 |
| 966 | 17.17 | 0.12 | 1.000 | 0.007 | 20.2 | 0.1 |
| 974 | 17.01 | 0.12 | 1.000 | 0.007 | 20.0 | 0.1 |
| 981 | 16.83 | 0.12 | 1.000 | 0.007 | 19.8 | 0.1 |
| 989 | 16.65 | 0.12 | 1.000 | 0.007 | 19.6 | 0.1 |
| 996 | 16.53 | 0.12 | 1.000 | 0.007 | 19.5 | 0.1 |
| 1004 | 16.47 | 0.12 | 1.000 | 0.007 | 19.4 | 0.1 |
| 1011 | 16.45 | 0.12 | 1.000 | 0.007 | 19.4 | 0.1 |
| 1019 | 16.42 | 0.11 | 1.000 | 0.007 | 19.3 | 0.1 |
| 1026 | 16.35 | 0.11 | 1.000 | 0.007 | 19.2 | 0.1 |
| 1034 | 16.23 | 0.11 | 1.000 | 0.007 | 19.1 | 0.1 |
| 1041 | 16.08 | 0.11 | 1.000 | 0.007 | 18.9 | 0.1 |
| 1049 | 15.94 | 0.11 | 1.000 | 0.007 | 18.8 | 0.1 |
| 1056 | 15.84 | 0.11 | 1.000 | 0.007 | 18.6 | 0.1 |
| 1064 | 15.78 | 0.11 | 1.000 | 0.007 | 18.6 | 0.1 |
| 1071 | 15.74 | 0.11 | 1.000 | 0.007 | 18.5 | 0.1 |
| 1079 | 15.68 | 0.10 | 1.000 | 0.007 | 18.5 | 0.1 |
| 1086 | 15.60 | 0.10 | 1.000 | 0.007 | 18.4 | 0.1 |
| 1094 | 15.49 | 0.10 | 1.000 | 0.007 | 18.2 | 0.1 |
| 1101 | 15.37 | 0.10 | 1.000 | 0.007 | 18.1 | 0.1 |
| 1109 | 15.27 | 0.10 | 1.000 | 0.007 | 18.0 | 0.1 |
| 1116 | 15.20 | 0.10 | 1.000 | 0.007 | 17.9 | 0.1 |
| 1124 | 15.15 | 0.10 | 1.000 | 0.007 | 17.8 | 0.1 |

Continued on next page

Table 4 – continued from previous page

| $f$ (GHz) | $w_0(\prime\prime)$ | $\triangle\ w_0(\prime\prime)$ | $c_0$ | $\triangle\ c_0$ | FWHM($\prime\prime$) | $\triangle$ FWHM($\prime\prime$) |
|---|---|---|---|---|---|---|
| 1131 | 15.09 | 0.09 | 1.000 | 0.007 | 17.8 | 0.1 |
| 1139 | 15.02 | 0.09 | 1.000 | 0.007 | 17.7 | 0.1 |
| 1146 | 14.93 | 0.09 | 1.000 | 0.007 | 17.6 | 0.1 |
| 1154 | 14.84 | 0.09 | 1.000 | 0.007 | 17.5 | 0.1 |
| 1161 | 14.76 | 0.09 | 1.000 | 0.007 | 17.4 | 0.1 |
| 1169 | 14.71 | 0.09 | 1.000 | 0.007 | 17.3 | 0.1 |
| 1176 | 14.67 | 0.09 | 1.000 | 0.007 | 17.3 | 0.1 |
| 1184 | 14.63 | 0.09 | 1.000 | 0.007 | 17.2 | 0.1 |
| 1191 | 14.55 | 0.08 | 1.000 | 0.006 | 17.1 | 0.1 |
| 1199 | 14.45 | 0.08 | 1.000 | 0.006 | 17.0 | 0.1 |
| 1206 | 14.35 | 0.08 | 1.000 | 0.006 | 16.9 | 0.1 |
| 1214 | 14.29 | 0.08 | 1.000 | 0.006 | 16.8 | 0.1 |
| 1221 | 14.31 | 0.08 | 1.000 | 0.006 | 16.8 | 0.1 |
| 1229 | 14.40 | 0.08 | 1.000 | 0.006 | 17.0 | 0.1 |
| 1236 | 14.53 | 0.07 | 1.000 | 0.006 | 17.1 | 0.1 |
| 1244 | 14.64 | 0.07 | 1.000 | 0.005 | 17.2 | 0.1 |
| 1251 | 14.71 | 0.07 | 1.000 | 0.005 | 17.3 | 0.1 |
| 1259 | 14.71 | 0.07 | 1.000 | 0.005 | 17.3 | 0.1 |
| 1266 | 14.68 | 0.07 | 1.000 | 0.005 | 17.3 | 0.1 |
| 1274 | 14.65 | 0.07 | 1.000 | 0.005 | 17.2 | 0.1 |
| 1281 | 14.63 | 0.07 | 1.000 | 0.005 | 17.2 | 0.1 |
| 1289 | 14.63 | 0.07 | 1.000 | 0.005 | 17.2 | 0.1 |
| 1296 | 14.64 | 0.07 | 1.000 | 0.005 | 17.2 | 0.1 |
| 1304 | 14.63 | 0.07 | 1.000 | 0.005 | 17.2 | 0.1 |
| 1311 | 14.59 | 0.07 | 1.000 | 0.005 | 17.2 | 0.1 |
| 1319 | 14.53 | 0.07 | 1.000 | 0.005 | 17.1 | 0.1 |
| 1326 | 14.47 | 0.07 | 1.000 | 0.005 | 17.0 | 0.1 |
| 1334 | 14.43 | 0.07 | 1.000 | 0.005 | 17.0 | 0.1 |
| 1341 | 14.42 | 0.07 | 1.000 | 0.005 | 17.0 | 0.1 |
| 1349 | 14.43 | 0.07 | 1.000 | 0.005 | 17.0 | 0.1 |
| 1356 | 14.44 | 0.07 | 1.000 | 0.005 | 17.0 | 0.1 |
| 1364 | 14.45 | 0.07 | 1.000 | 0.005 | 17.0 | 0.1 |
| 1371 | 14.43 | 0.06 | 1.000 | 0.005 | 17.0 | 0.1 |
| 1379 | 14.40 | 0.06 | 1.000 | 0.005 | 17.0 | 0.1 |

Continued on next page

Table 4 – continued from previous page

| $f$ (GHz) | $w_0(\prime\prime)$ | $\triangle\ w_0(\prime\prime)$ | $c_0$ | $\triangle\ c_0$ | FWHM($\prime\prime$) | $\triangle$ FWHM($\prime\prime$) |
|---|---|---|---|---|---|---|
| 1386 | 14.37 | 0.06 | 1.000 | 0.005 | 16.9 | 0.1 |
| 1394 | 14.33 | 0.06 | 1.000 | 0.005 | 16.9 | 0.1 |
| 1401 | 14.30 | 0.06 | 1.000 | 0.005 | 16.8 | 0.1 |
| 1409 | 14.27 | 0.06 | 1.000 | 0.005 | 16.8 | 0.1 |
| 1416 | 14.24 | 0.06 | 1.000 | 0.005 | 16.8 | 0.1 |
| 1424 | 14.22 | 0.06 | 1.000 | 0.005 | 16.7 | 0.1 |
| 1431 | 14.21 | 0.06 | 1.000 | 0.005 | 16.7 | 0.1 |
| 1439 | 14.18 | 0.06 | 1.000 | 0.005 | 16.7 | 0.1 |
| 1446 | 14.16 | 0.06 | 1.000 | 0.005 | 16.7 | 0.1 |
| 1453 | 14.13 | 0.06 | 1.000 | 0.005 | 16.6 | 0.1 |
| 1461 | 14.09 | 0.06 | 1.000 | 0.005 | 16.6 | 0.1 |
| 1468 | 14.06 | 0.06 | 1.000 | 0.005 | 16.6 | 0.1 |
| 1476 | 14.06 | 0.06 | 1.000 | 0.005 | 16.5 | 0.1 |
| 1483 | 14.07 | 0.06 | 1.000 | 0.005 | 16.6 | 0.1 |
| 1491 | 14.11 | 0.06 | 1.000 | 0.005 | 16.6 | 0.1 |
| 1498 | 14.15 | 0.06 | 1.000 | 0.005 | 16.7 | 0.1 |
| 1506 | 14.16 | 0.06 | 1.000 | 0.005 | 16.7 | 0.1 |
| 1513 | 14.14 | 0.06 | 1.000 | 0.005 | 16.6 | 0.1 |
| 1521 | 14.10 | 0.06 | 1.000 | 0.005 | 16.6 | 0.1 |
| 1528 | 14.07 | 0.06 | 1.000 | 0.005 | 16.6 | 0.1 |
| 1536 | 14.11 | 0.06 | 1.000 | 0.005 | 16.6 | 0.1 |
| 1543 | 14.26 | 0.07 | 1.000 | 0.005 | 16.8 | 0.1 |
| 1551 | 14.56 | 0.07 | 1.000 | 0.005 | 17.1 | 0.1 |

# Bibliography

Abergel A., Arab H., Compiègne M., Kirk J. M., Ade P., Anderson L. D., André P., Baluteau J.-P., Bernard J.-P., Blagrave K., et al., 2010, Astronomy and Astrophysics, 518

André P., Men'shchikov A., Bontemps S., Könyves V., Motte F., Schneider N., Didelon P., Minier V., Saraceno P., Ward-Thompson D., et al., 2010, Astronomy and Astrophysics, 518, L102

Andre P., Montmerle T., 1994, The Astrophysical Journal, 420, 837

Andre P., Ward-Thompson D., Barsony M., 1993, The Astrophysical Journal, 406, 122

Aniano G., Draine B. T., Gordon K. D., Sandstrom K., 2011, Publications of the Astronomical Society of the Pacific, 123, 1218

Bachiller R., 1996, Annual Review of Astronomy and Astrophysics, 34, 111

Bachiller R., Gutiérrez M. P., Kumar M. S. N., Tafalla M., 2001, Astronomy and Astrophysics, 372, 899

Beichman C. A., Myers P. C., Emerson J. P., Harris S., Mathieu R., Benson P. J., Jennings R. E., 1986, The Astrophysical Journal, 307, 337

Benson P. J., Myers P. C., 1989, the Astrophysical Journal Supplement Series, 71, 89

Bjerkeli P., Liseau R., Olberg M., Falgarone E., Hjalmarson Å., Klotz A., Larsson B., Olofsson A. O. H., Olofsson G., Ristorcelli I., et al., 2009, Astronomy and Astrophysics

Bodenheimer P. H., 2011, Principles of star formation. Springerverlag Berlin Heidelberg

Bolatto A. D., Wolfire M., Leroy A. K., 2013, Annual Review of Astronomy and Astrophysics, 51, 207

Bontemps S., Andre P., Kaas A. A., Nordh L., Olofsson G., Huldtgren M., Abergel A., Blommaert J., Boulanger F., Burgdorf M., et al., 2001, Astronomy and Astrophysics, 372, 173

Bontemps S., Andre P., Terebey S., Cabrit S., 1996, Astronomy and Astrophysics, 311, 858

Boogert A. C. A., Hogerheijde M. R., Ceccarelli C., other 2002, The Astrophysical Journal, 570, 708

Boogert A. C. A., Tielens A. G. G. M., Ceccarelli C., Boonman A. M. S., van Dishoeck E. F., Keane J. V., Whittet D. C. B., de Graauw T., 2000, Astronomy and Astrophysics, 360, 683

Bourke T. L., Myers P. C., Evans N. J., Dunham M. M., Kauffmann J., Shirley Y. L., Crapsi A., Young C. H., Huard T. L., Brooke T. Y., et al., 2006, Astrophysical Journal, 649, L37

Brinch C., Hogerheijde M. R., 2010, Astronomy and Astrophysics, 523, 25

Burke B. F., Graham-Smith F., 2010, An introduction to radio astronomy. Cambridge University Press

Bussmann R. S., Wong T. W., Hedden A. S., Kulesa C. A., Walker C. K., 2007, The Astrophysical Journal Letters, 657, L33

Carlstrom J. E., Hills R. E., Lay O. P., Force B., Hall C. G., Phillips T. G., Schinckel A. E., 1994, in IAU Colloq. 140: Astronomy with Millimeter and Submillimeter Wave Interferometry Vol. 59, The cso-jcmt submillimeter interferometer. pp 35–40

Caselli P., Walmsley C. M., Tafalla M., Dore L., Myers P. C., 1999, The Astrophysical Journal Letters, 523, L165

Caux E., Kahane C., Castets A., Coutens A., Ceccarelli C., Bacmann A., Bisschop S., Bottinelli S., Comito C., Helmich F., et al., 2011, Astronomy and Astrophysics, 532, A23

Ceccarelli C., Boogert A. C. A., Tielens A. G. G. M., Caux E., Hogerheijde M. R., Parise B., 2002, Astronomy and Astrophysics, 395, 863

Ceccarelli C., Castets A., Loinard L., Caux E., Tielens A. G. G. M., 1998, Astronomy and Astrophysics, 338, L43

Ceccarelli C., Hollenbach D. J., Tielens A. G. G. M., 1996, The Astrophysical Journal, 471, 400

Chandler C. J., Brogan C. L., Shirley Y. L., Loinard L., 2005, The Astrophysical Journal, 632, 371

Codella C., Welser R., Henkel C., Benson P. J., Myers P. C., 1997, Astronomy and Astrophysics, 324, 203

Compiègne M., Abergel A., Verstraete L., Habart E., 2008, Astronomy and Astrophysics, 491, 797

Correia J. C., Griffin M., Saraceno P., 2004, Astronomy and Astrophysics, 418, 607

Coutens, A. Vastel, C. Caux, E. Ceccarelli, C. Bottinelli, S. Wiesenfeld, L. Faure, A. Scribano, Y. Kahane, C. 2012, Astronomy and Astrophysics, 539, A132

Crapsi A., Caselli P., Walmsley C., Tafalla M., Lee C., Bourke T., Myers P., 2004, Astronomy and Astrophysics, 420, 957

Crapsi A., Caselli P., Walmsley C. M., Myers P. C., Tafalla M., Lee C. W., Bourke T. L., 2005, the Astrophysical Journal, 619, 379

Crimier N., Ceccarelli C., Maret S., Bottinelli S., Caux E., Kahane C., Lis D., Olofsson J., 2010, Astronomy and Astrophysics, 519, 65

de Graauw T., Helmich F. P., Phillips T. G., Stutzki J., Caux E., Whyborn N. D., Dieleman P., Roelfsema P. R., Aarts H., Assendorp R., et al., 2010, Astronomy & Astrophysics, 518, 1

Draine B. T., 2010, Physics of the interstellar and intergalactic medium. Princeton University Press

Draine B. T., Fraisse A. A., 2009, The Astrophysical Journal, 696, 1

Draine B. T., Li A., 2007, The Astrophysical Journal, 657, 810

Elias J. H., 1978a, The Astrophysical Journal, 224, 453

Elias J. H., 1978b, The Astrophysical Journal, 223, 859

Fischer J., Klaassen T., Hovenier N., Jakob G., Poglitsch A., Sternberg O., 2004, Applied Optics, 43, 3765

Fraser H. J., Collings M. P., McCoustra M. R., Williams D. A., 2001, Monthly Notices of the Royal Astronomical Society, 327, 1165

Friesen R. K., Di Francesco J., Myers P. C., Belloche A., Shirley Y. L., Bourke T. L., André P., 2010, The Astrophysical Journal, 718, 666

Fulton T., Naylor D. A., Baluteau J.-P., Griffin M. J., et al., 2013, Astronomy and Astrophysics (in preparation)

Goldsmith P. F., Langer W. D., 1999, The Astrophysical Journal, 517, 209

Green J. D., Evans N. J., Jørgensen J. K., Herczeg G. J., Kristensen L. E., Lee J.-E., Dionatos O., Yildiz U. A., Salyk C., Meeus G., et al., 2013, The Astrophysical Journal, 770, 123

Gregersen E. M., Evans II N. J., Zhou S., Choi M., 1997, the Astrophysical Journal, 484, 256

Griffin M. J., Abergel A., Abreu A. *et al.*., 2010, Astronomy and Astrophysics, 518

Gull S. F., Skilling J., 1984, Communications, Radar and Signal Processing, IEE Proceedings F, 131, 646

Herbst E., van Dishoeck E. F., 2009, Annual Review of Astronomy and Astrophysics, 47, 427

Hirota T., Ito T., Yamamoto S., 2002, The Astrophysical Journal, 565, 359

Högbom J. A., 1974, Astronomy and Astrophysics Supplement Series, 15, 417

Holland W. S., Robson E. I., Gear W. K., Cunningham C. R., Lightfoot J. F., Jenness T., Ivison R. J., Stevens J. A., Ade P. A. R., Griffin M. J., et al., 1999, Monthly Notices of the Royal Astronomical Society, 303, 659

Huard T. L., Myers P. C., Murphy D. C., Crews L. J., Lada C. J., Bourke T. L., Crapsi A., Evans N. J., McCarthy Jr D. W., Kulesa C., et al., 2006, The Astrophysical Journal, 640, 391

Irwin J. A., 2007, Astrophysics: decoding the cosmos. John Wiley & Sons

Ivezic Z., Elitzur M., 1997, Monthly Notices of the Royal Astronomical Society, 287, 799

Jonkheid B. J., 2006, PhD thesis, Faculty of Mathematics and Natural Sciences, Leiden University

Kaufman M. J., Neufeld D. A., 1996, The Astrophysical Journal, 456, 611

Kaufman M. J., Wolfire M. G., Hollenbach D. J., Luhman M. L., 1999, The Astrophysical Journal, 527, 795

Kessler M. F., Steinz J. A., Anderegg M. E., Clavel J., Drechsel G., Estaria P., Faelker J., Riedinger J. R., Robson A., Taylor B. G., et al., 1996, Astron. Astrophys, 315, L27

Khanzadyan T., Gredel R., Smith M. D., Stanke T., 2004, Astronomy and Astrophysics, 426, 171

Kirk J. M., Ward-Thompson D., André P., 2005, Monthly Notices of the Royal Astronomical Society, 360, 1506

Kirk J. M., Ward-Thompson D., André P., 2007, Monthly Notices of the Royal Astronomical Society, 375, 843

Knude J., Hog E., 1998, Astronomy and Astrophysics, 338, 897

Kristensen L. E., Van Dishoeck E. F., Bergin E. A., Visser R., Yildiz U. A., San Jose-Garcia I., Jorgensen J. K., Herczeg G. J., Johnstone D., Wampfler S. F., et al., 2012, Astronomy and Astrophysics, 542, A8

Kutner M. L., Ulich B. L., 1981, The Astrophysical Journal, 250, 341

Lada C. J., 1987, in Star Forming Regions Vol. 115, Star formation-from ob associations to protostars. pp 1–17

Lada C. J., 1991, in , The Physics of Star Formation and Early Stellar Evolution. Springer, pp 329–364

Lada C. J., Wilking B. A., 1984, the Astrophysical Journal, 287, 610

Langer W. D., Penzias A. A., 1993, The Astrophysical Journal, 408, 539

LeBlanc F., 2011, An introduction to stellar astrophysics. Wiley

Lee C. W., Myers P. C., Tafalla M., 2001, the Astrophysical Journal Supplement Series, 136, 703

Lequeux J., Falgarone E., Ryter C., 2005, The interstellar medium. Springer

Loinard L., Mioduszewski A. J., Rodríguez L. F., González R. A., Rodríguez M. I., Torres R. M., 2005, The Astrophysical Journal Letters, 619, L179

Loinard L., Torres R. M., Mioduszewski A. J., Rodríguez L. F., 2008, The Astrophysical Journal Letters, 675, L29

Loinard L., Zapata L. A., Rodríguez L. F., Pech G., Chandler C. J., Brogan C. L., Wilner D. J., Ho P. T. P., Parise B., Hartmann L. W., et al., 2013, Monthly Notices of the Royal Astronomical Society: Letters, 430, L10

Lombardi M., Lada C. J., Alves J., 2008, Astronomy and Astrophysics, 480, 785

Makiwa G., Naylor D. A., Ferlet M., Salji C., Swinyard B., Polehampton E., van der Wiel M. H. D., 2013, Appl. Opt., 52, 3864

Markwardt C. B., 2009, in Astronomical Society of the Pacific Conference Series Vol. 411, Astronomical Data Analysis Software and Systems XVIII. p. 251

Martin D. H., Bowen J. W., 1993, Microwave Theory and Techniques, IEEE Transactions on, 41, 1676

Martini P., Persson S. E., Murphy D. C., Birk C., Shectman S. A., Gunnels S. M., Koch E., 2004, in Astronomical Telescopes and Instrumentation Panic: a near-infrared camera for the magellan telescopes. pp 1653–1660

Mathis J. S., Rumpl W., Nordsieck K. H., 1977, The Astrophysical Journal, 217, 425

Mizuno A., Fukui Y., Iwata T., Nozawa S., Takano T., 1990, The Astrophysical Journal, 356, 184

Motte F., André P., Neri R., 1998, Astronomy and Astrophysics, 336, 150

Mundy L. G., Myers S. T., Wilking B. A., 1986, The Astrophysical Journal, 311, L75

Mundy L. G., Wootten A., Wilking B. A., Blake G. A., Sargent A. I., 1992, The Astrophysical Journal, 385, 306

Muzerolle J., Hartmann L., Calvet N., 1998, The Astronomical Journal, 116, 2965

Myers P. C., Benson P. J., 1983, The Astrophysical Journal, 266, 309

Neugebauer G., Habing H., van Duinen R. *et al.*., 1984, The Astrophysical Journal, 278, L1

Onishi T., Mizuno A., Fukui Y., 1999, Publications of the Astronomical Society of Japan, 51, 257

Ossenkopf V., Henning T., 1994, Astronomy and Astrophysics, 291, 943

Ott S., 2010, in Astronomical Society of the Pacific Conference Series Vol. 434, Astronomical Data Analysis Software and Systems XIX. p. 139

Padin S., Scott S. L., Woody D. P., Scoville N. Z., Seling T. V., Finch R. P., Giovanine C. J., Lawrence R. P., 1991, Publications of the Astronomical Society of the Pacific, 103, 461

Pickett H. M., Poynter R. L., Cohen E. A., Delitsky M. L., Pearson J. C., Müller H. S. P., 1998, Journal of Quantitative Spectroscopy and Radiative Transfer, 60, 883

Pilbratt G. L., Riedinger J. R., Passvogel T. *et al.*., 2010, Astronomy and Astrophysics, 518

Pineda J. E., Caselli P., Goodman A. A., 2008, The Astrophysical Journal, 679, 481

Pineda J. E., Maury A. J., Fuller G. A., Testi L., García-Appadoo D., Peck A. B., Villard E., Corder S. A., van Kempen T. A., Turner J. L., et al., 2012, Astronomy and Astrophysics, 544, L7

Poglitsch A., Waelkens C., Geis N., Feuchtgruber H., Vandenbussche B., Rodriguez L., Krause O., Renotte E., van Hoof C., Saraceno P., et al., 2010, Astronomy and Astrophysics, 518, L2

Rieke G. H., Young E. T., Engelbracht C. W., Kelly D. M., Low F. J., Haller E. E., Beeman J. W., Gordon K. D., Stansberry J. A., Misselt K. A., et al., 2004, The Astrophysical Journal Supplement Series, 154, 25

Robitaille T. P., Whitney B. A., Indebetouw R., Wood K., 2007, The Astrophysical Journal Supplement Series, 169, 328

Rybicki G. B., Lightman A. P., 2008, Radiative processes in astrophysics. John Wiley & Sons

Sandell G., 1994, Monthly Notices of the Royal Astronomical Society, 271, 75

Saraceno P., André P., Ceccarelli C., Griffin M., Molinari S., 1996, Astronomy and Astrophysics, 309, 827

Schnee S., Kauffmann J., Goodman A., Bertoldi F., 2007, The Astrophysical Journal, 657, 838

Schöier F. L., Jørgensen J. K., van Dishoeck E. F., Blake G. A., 2002, Astronomy and Astrophysics, 390, 1001

Shinnaga H., Ohashi N., Lee S.-W., Moriarty-Schieven G. H., 2004, the Astrophysical Journal, 601, 962

Shu F., Najita J., Galli D., Ostriker E., Lizano S., 1993, in Protostars and Planets III Vol. 1, The collapse of clouds and the formation and evolution of stars and disks. pp 3–45

Shu F. H., Adams F. C., Lizano S., 1987, Annual Review of Astronomy and Astrophysics, 25, 23

Skrutskie M. F., Cutri R. M., Stiening R., Weinberg M. D., Schneider S., Carpenter J. M., Beichman C., Capps R., Chester T., Elias J., et al., 2006, The Astronomical Journal, 131, 1163

Smith M. D., 2004, The origin of stars. World Scientific

SPIRE Observers Manual 2011, HERSCHEL-HSC-DOC-0789 accessed from http://herschel.esac.esa.int/Documentation.shtml

Stark R., Sandell G., Beck S. C., Hogerheijde M. R., van Dishoeck E. F., van der Wal P., van der Tak F. F. S., Schäfer F., Melnick G. J., Ashby M. L. N., et al., 2004, The Astrophysical Journal, 608, 341

Swinyard B., Polehampton E., Hopwood R., et al., 2014, Monthly Notices of the Royal Astronomical Society (Accepted)

Swinyard B. M., Ade P., Baluteau J.-P., Aussel H., Barlow M. J., Bendo G. J., Benielli D., Bock J., Brisbin D., Conley A., et al., 2010, Astronomy and Astrophysics, 518

Tafalla M., Myers P. C., Caselli P., Walmsley C. M., Comito C., 2002, the Astrophysical Journal, 569, 815

Tafalla M., Santiago J., 2004, Astronomy and Astrophysics, 414, L53

Tafoya D., Loinard L., Fonfría J. P., Vlemmings W. H. T., Martí-Vidal I., Pech G., 2013, Astronomy and Astrophysics, 556, 35

Tennyson J., 2010, Astronomical spectroscopy: An introduction to the atomic and molecular physics of astronomical spectra. World Scientific

Terebey S., Fich M., Noriega-Crespo A., Padgett D. L., Sullivan A., Team T. S. D., 2006, in Protostars and Planets V Vol. 1, Spitzer detection of a low-luminosity infrared source in a pre stellar core in the taurus molecular cloud. p. 8568

Thi W. F., Van Dishoeck E. F., Blake G. A., Van Zadelhoff G. J., Horn J., Becklin E. E., Mannings V., Sargent A. I., van den Ancker M. E., Natta A., et al., 2001, The Astrophysical Journal, 561, 1074

Thim F., Tammann G. A., Saha A., Dolphin A., Sandage A., Tolstoy E., Labhardt L., 2003, The Astrophysical Journal, 590, 256

Tielens A. G. G. M., 2005, The physics and chemistry of the interstellar medium. Cambridge University Press

Tielens A. G. G. M., Charnley S. B., 1997, in , Planetary and Interstellar Processes Relevant to the Origins of Life. Springer, pp 23–51

Torres R. M., Loinard L., Mioduszewski A. J., Rodríguez L. F., 2007, The Astrophysical Journal, 671, 1813

Ulich B. L., Haas R. W., 1976, The Astrophysical Journal Supplement Series, 30, 247

User's Manual for the NRAO 12 M Millimeter-wave Telescope, Kitt Peak, Arizona 2000, Available from http://aro.as.arizona.edu/12m_docs/12m_userman.pdf

van der Tak F. F. S., Black J. H., Schöier F. L., Jansen D. J., van Dishoeck E. F., 2007, Astronomy and Astrophysics, 468, 627

van Dishoeck E. F., Blake G. A., 1998, Annual Review of Astronomy and Astrophysics, 36, 317

van Dishoeck E. F., Blake G. A., Jansen D. J., Groesbeck T. D., 1995, The Astrophysical Journal, 447, 760

Walker C. K., Adams F. C., Lada C. J., 1990, The Astrophysical Journal, 349, 515

Walker C. K., Carlstrom J. E., Bieging J. H., 1993, The Astrophysical Journal, 402, 655

Walker C. K., Lada C. J., Young E. T., Maloney P. R., Wilking B. A., 1986, The Astrophysical Journal, 309, L47

Walker C. K., Lada C. J., Young E. T., Margulis M., 1988, The Astrophysical Journal, 332, 335

Ward-Thompson D., 2011, An introduction to star formation. Cambridge University Press

Ward-Thompson D., André P., Kirk J. M., 2002, Monthly Notices of the Royal Astronomical Society, 329, 257

Werner M. W., Roellig T. L., Low F. J., Rieke G. H., Rieke M., Hoffmann W. F., Young E., Houck J. R., Brandl B., Fazio G. G., et al., 2004, The Astrophysical Journal Supplement Series, 154, 1

Whittet D. C. B., 1974, Monthly Notices of the Royal Astronomical Society, 168, 371

Wilking B., Lada C. J., 1983, The Astrophysical Journal, 274, 698

Wilking B. A., Lada C. J., Young E. T., 1989, The Astrophysical Journal, 340, 823

Wilson T. L., Rood R., 1994, Annual Review of Astronomy and Astrophysics, 32, 191

Wootten A., 1989, The Astrophysical Journal, 337, 858

Wu R., Polehampton E. T., Etxaluze M., Makiwa G., Naylor D. A., Salji C., Swinyard B. M., Ferlet M., van der Wiel M. H., Smith A. J., et al., 2013, Astronomy and Astrophysics, 556, A116

Yamada K. M. T., Winnewisser G., 2011, Interstellar Molecules: Their Laboratory and Interstellar Habitat. Vol. 241, Springer

Ybarra J. E., Barsony M., Haisch Jr K. E., Jarrett T. H., Sahai R., Weinberger A. J., 2006, The Astrophysical Journal Letters, 647, L159

Young E. T., Lada C. J., Wilking B. A., 1986, The Astrophysical Journal, 304, L45

Zhou S., 1995, The Astrophysical Journal, 442, 685